



UNIVERSITAT POLITÈCNICA
DE CATALUNYA
BARCELONATECH

Historical copper and iron coloured glazes and glasses

Mingyue Yuan

ADVERTIMENT La consulta d'aquesta tesi queda condicionada a l'acceptació de les següents condicions d'ús: La difusió d'aquesta tesi per mitjà del repositori institucional UPCommons (<http://upcommons.upc.edu/tesis>) i el repositori cooperatiu TDX (<http://www.tdx.cat/>) ha estat autoritzada pels titulars dels drets de propietat intel·lectual **únicament per a usos privats** emmarcats en activitats d'investigació i docència. No s'autoritza la seva reproducció amb finalitats de lucre ni la seva difusió i posada a disposició des d'un lloc aliè al servei UPCommons o TDX. No s'autoritza la presentació del seu contingut en una finestra o marc aliè a UPCommons (*framing*). Aquesta reserva de drets afecta tant al resum de presentació de la tesi com als seus continguts. En la utilització o cita de parts de la tesi és obligat indicar el nom de la persona autora.

ADVERTENCIA La consulta de esta tesis queda condicionada a la aceptación de las siguientes condiciones de uso: La difusión de esta tesis por medio del repositorio institucional UPCommons (<http://upcommons.upc.edu/tesis>) y el repositorio cooperativo TDR (<http://www.tdx.cat/?locale-attribute=es>) ha sido autorizada por los titulares de los derechos de propiedad intelectual **únicamente para usos privados enmarcados** en actividades de investigación y docencia. No se autoriza su reproducción con finalidades de lucro ni su difusión y puesta a disposición desde un sitio ajeno al servicio UPCommons No se autoriza la presentación de su contenido en una ventana o marco ajeno a UPCommons (*framing*). Esta reserva de derechos afecta tanto al resumen de presentación de la tesis como a sus contenidos. En la utilización o cita de partes de la tesis es obligado indicar el nombre de la persona autora.

WARNING On having consulted this thesis you're accepting the following use conditions: Spreading this thesis by the institutional repository UPCommons (<http://upcommons.upc.edu/tesis>) and the cooperative repository TDX (<http://www.tdx.cat/?locale-attribute=en>) has been authorized by the titular of the intellectual property rights **only for private uses** placed in investigation and teaching activities. Reproduction with lucrative aims is not authorized neither its spreading nor availability from a site foreign to the UPCommons service. Introducing its content in a window or frame foreign to the UPCommons service is not authorized (*framing*). These rights affect to the presentation summary of the thesis as well as to its contents. In the using or citation of parts of the thesis it's obliged to indicate the name of the author.



UNIVERSITAT POLITÈCNICA
DE CATALUNYA
BARCELONATECH

PhD program in Computational and Applied Physics

Historical copper and iron coloured glazes and glasses

Doctoral thesis by:
Mingyue Yuan

Thesis advisor:
Trinitat Pradell Cara

A thesis presented for the degree of Doctor at the
Universitat Politècnica de Catalunya
Department of Physics
Barcelona, July 2023

Acknowledgement

Finally, my doctoral study is approaching the end.

I am filled with deep gratitude for the invaluable support and guidance I have received from numerous individuals and institutions throughout these four years.

First and foremost, I want to express my heartfelt gratitude to my supervisor, Prof. Trinitat Pradell. She is an incredibly kind, knowledgeable, and enthusiastic person, always energized and passionate about research, and equally kind to everyone she interacts with. Under her expert and professional guidance, I have gained extensive knowledge in the field of historical ceramics and glass, expanded my horizons, and deeply mastered characterization techniques. Her encouragement during moments of frustration and genuine care for my well-being in daily life have been a constant source of strength. Both my academic pursuits and personal growth have significantly improved during these four years, and the cherished memories shared with her will forever hold a special place in my heart. It is with immense gratitude and honour that I acknowledge her mentorship, and I feel truly privileged to have been her student.

Then I want to extend my thanks to Prof. Nigel Wood from the University of Oxford for his generous support in providing the imperial yellow samples of the Ming and the Qing dynasty. Thanks to Ms. Jiayu Hou from the Palace Museum for her invaluable support in obtaining the Jun ware samples and the Changsha ware samples. Thanks to Mr. Jordi Bonet from J.M. Bonet Vitrells S.L. for offering me opportunities to collect the red glass samples and facilitating my close interaction with stained window glass. Thanks to Prof. Ian Freestone from the University College London for his support in obtaining the striated glass. Thanks to Vetraria Muñoz de Pablos S.L. and in particular, Pablo and Alfonso for providing one of the red glass pieces that were studied.

Next, I'd like to thank Prof. Judit Molera from the University of Vic, who assist me with the replication work of the yellow glazes, providing valuable suggestions, and extending a helping hand whenever needed. We also had a good time in BL04-MSPD of Alba synchrotron, and the numerous occasions of happiness we shared will always be memorised. Thanks to Prof. Nativitat Salvadó for her expertise and assistance with IR measurements. The moments spent with her were both enlightening and enjoyable. Thanks to Dr. Trifon Todorov Trifonov for his repeated help in SEM-FIB analysis, which proved to be invaluable in obtaining accurate results (Heavy metal is still alive!). Thanks to the Alba synchrotron staff include Dr. Oriol Vallcorba from BL04-MSPD, and Dr. Giulio Gorni from the BL22-CLÆSS for their highly professional and commendable in the field of micro-XRD and XAFS. Thanks to Dr. Marine Cotte and Dr. Hiram Castillo-Michel of ID21 in ESRF for their kind support and for providing an excellent opportunity for micro-XRF and XAFS measurement. Thanks to Prof. Maite Garcia Valles from the University of Barcelona for her generous assistance in lead glass replications. Thanks to Dr. Nadine Schibille and Dr. Bernard Gratuze from IRMAT of CNRS for their valuable support in LA-ICP-MS analysis. Thanks to Dr. Xavier Llovet from the University of Barcelona for the kind help in EMPA analysis. Thanks to Prof. Daniel Crespo for his invaluable help in programming the Fe K-edge pre-edge fitting, as well as for his unfailing kindness every time I met with him.

Thanks to Prof. Pere Bruna Escuer for his invaluable help in programming and Mössbauer analysis. Thanks to

Prof. Eloi Pineda Soler for the support of DSC analysis, as well as the well-organized gatherings that always create a positive and enriching environment. Thanks to my colleagues and friends, Chenyang Xie, Neda Shojaei, Francesc Albert Tortosa, Ruth Sadurni, David Loaeza, Lucía G. De la Cruz, Seyedeh Leila Panahi, Leandro Isidro, Martí Beltrán González, Dashuang Luo for their company and support throughout this journey. Your presence has made this experience truly special, and I am grateful for the opportunity to have met each one of you. Thanks to all my flatmates, Neda, Mariano, and Oscar for your inclusiveness, kindness, and understanding. In addition. I am profoundly grateful to MINECO (Spain) for their generous financial support of the project ‘Recuperando las Tecnologías Perdidas: impacto en la Historia y en la conservación del vidrio, la cerámica vidriada y la pintura’ (grant PID2019-105823RB-I00); and the Generalitat de Catalunya (grant 2017 SGR 0042, grant 2021 SGR 00343) for their financial support to this research. Thanks to the BAG HG-172: Structural analysis of historical materials, 2025. Thanks to the ALBA synchrotron for considering and approving our proposal (Proposal 2019093906). Furthermore, thanks to Agència de Gestió d'Ajuts Universitaris i de Recerca (AGAUR) and our university for providing me with the grant that allowed me to concentrate on my studies. Thanks to all the staff from the International Relations Bureau of UPC for their assistance with my contract, especially Begoña Martínez Prieto. A special thanks to the secretary of our department, Ana Maria Ortega. I would also like to express my gratitude to all the individuals who have helped me during my time in Barcelona. Thanks to my family for your unwavering love and encouragement. Your belief in me has been a constant source of motivation. Finally, thank myself. See you again.

Mingyue Yuan

2023/07/27

C1.1, Campus Diagonal-Besòs, UPC

Abstract

Coloured glazes and glasses have attracted human interest since antiquity for their aesthetic appeal and multiple functionalities. As indicators of technological progress, artistic expression, and social stratification in different historical periods, copper and iron have emerged as the predominant colourants in historic glazes and glasses, offering a remarkable spectrum of hues influenced by varying contents, ratios, and atmospheric conditions in their production. In order to explore the intricacies of copper red formation, to address the limited research on iron yellow in high-lead glazes, and to understand the interaction of both cations in glaze colour, we investigated four representative cases, high-lead imperial iron yellow glazes from the Ming (1368-1644) and Qing (1616-1912) dynasties, North Song (960-1127) dynasty copper and iron blue and red Jun ware glazes, late Tang (9th - 10th century) dynasty copper green and red Changsha ware glazes, and 13th to the 20th century European copper red window glasses. Using a complementary set of analytical techniques, including ultraviolet-visible-near infrared (UV-VIS-NIR) spectroscopy, optical microscopy (OM), scanning electron microscopy (SEM), electron microprobe analysis (EMPA), laser ablation inductively coupled plasma mass spectrometry (LA-ICP-MS), micro X-ray diffraction (μ -XRD) and X-ray absorption fine structure (XAFS), we investigated the optical properties, micro/nanostructures, glaze and glass compositions, valence state, and coordination structures. Our results revealed distinct variations in glaze and body composition for the high-lead yellow glazes of the Ming and Qing dynasties, while demonstrating the influence of factors such as glaze thickness, firing temperature, substrate composition, and firing atmosphere on glaze colour. The study of Jun ware glazes elucidated the glass nanostructure and the oxidation-reduction dynamics of iron and copper, explaining the sky-like appearance of the glazes. Similarly, our study of Changsha ware glazes revealed the role of phase separation and copper oxidation state in glaze opacity and colour, and the influence of sulphur in the formation of copper nanoparticles. Finally, our study of European red window glass identified three distinct technologies, highlighting the role of copper nanoparticles in the red colouring and the role of iron, sulphur and tin in copper reduction. In summary, this comprehensive investigation has improved our understanding of the colouring mechanisms and compositional differences in historic glazes and glasses, and provides valuable insights into ancient glassmaking technologies.

Key words: Historical glaze; Red window glass; Iron; Copper; Sulphur; Tin; XAFS; Micro-XRD

Resum

Els vidriats i els vidres de colors han captivat l'interès humà des de l'antiguitat, pel seu atractiu estètic i les seves diverses funcionalitats. Servint com a indicadors del progrés tecnològic, l'expressió artística i l'estratificació de la societat a través de diverses èpoques històriques, el coure i el ferro emergiren com a colorants predominants en vidriats i vidres històrics, oferint un notable espectre de matisos influïts per diferents continguts, proporcions i condicions atmosfèriques en la seva producció. Per explorar les complexitats de la formació del vermell de coure, abordar la investigació limitada sobre el groc de ferro en vidriats d'alt contingut de plom, així com entendre la interacció entre ambdós cations en el desenvolupament del color dels vidriats, s'ha investigat inclou quatre casos representatius: esmalts grocs de ferro amb alt contingut de plom de les dinasties Ming (1368-1644) i Qing (1616-1912), els vidriats blaus i vermells de coure i ferro Jun de la dinastia Song del Nord (960-1127), els vidriats verds i vermells de coure Changsha de la dinastia Tang tardana (segles IX-X) i els vidres de finestra vermells de coure Europeus d'entre els segles XIII al XX. Utilitzant un conjunt complementari de tècniques analítiques, incloent espectroscòpia ultraviolada-visible-infraroja propera (UV-VIS-NIR), microscòpia òptica (OM), microscòpia electrònica de rastreig (SEM), microsonda electrònica (EMPA), espectrometria de masses per plasma d'acoblament inductiu (LA-ICP-MS), micro difracció de raigs X (μ -XRD) i espectroscòpia d'absorció de raigs X (XAFS), hem aprofundit en les propietats òptiques, micro/nanoestructures, composicions del vidriat i vidre, estat de valència i coordinació dels cations. Hi ha diferències en la composició dels vidriats grocs de ferro amb alt contingut plom de les dinasties Ming i Qing, alhora que s'ha pogut demostrar la influència de factors com el gruix del vidriat, la temperatura de cocció, la composició del substrat i l'atmosfera de cocció en el color. L'estudi dels vidriats Jun ha demostrat la influència de la nanoestructura del vidriat i la dinàmica d'oxidació-reducció del ferro i el coure en l'aspecte dels vidriats. L'estudi dels vidriats Changsha ha revelat el paper de la nanoestructura del vidriat i de l'estat d'oxidació del coure en la l'opacitat i el color dels vidriats. Finalment, l'estudi del vidre vermell de finestra ha identificat l'existència de tres tecnologies de producció diferents, destacant el paper de les nanopartícules de coure en la coloració vermella i la importància del ferro, el sofre i l'estany en la reducció del coure. En resum, aquesta investigació exhaustiva millora la nostra comprensió dels mecanismes de coloració i les diferències de composició en els vidriats i vidres històrics, oferint informació valuosa sobre les tecnologies de fabricació.

Paraules clau: Esmalt històric; Vidre vermell; Ferro; coure; sofre; estany; XAFS; Micro-XRD

Resumen

Los vidriados y vidrios de colores han cautivado el interés humano desde la antigüedad, debido a su atractivo estético y diversas funcionalidades. Sirviendo como indicadores del progreso tecnológico, la expresión artística y la estratificación social a lo largo de diversas épocas históricas, el cobre y el hierro han surgido como colorantes predominantes en vidriados y vidrios históricos, ofreciendo un notable espectro de matices influenciados por diferentes contenidos, proporciones y condiciones atmosféricas durante la producción. Para explorar las complejidades de la formación del rojo cobre, abordar la investigación limitada sobre el amarillo de hierro en vidriados con alto contenido de plomo, así como entender la interacción entre los dos cationes en el desarrollo del color de los vidriados, llevamos a cabo una investigación enfocada que abarca cuatro casos representativos: vidriados de amarillo imperial con alto contenido de plomo de las dinastías Ming (1368-1644) y Qing (1616-1912), vidriados de cerámica Jun de color azul y rojo de cobre y hierro de la dinastía Song del Norte (960-1127), vidriados Changsha de color verde y rojo de cobre de finales de la dinastía Tang (siglos IX-X) y vidrios de ventana Europeos de color rojo cobre que abarcan desde el siglo XIII hasta el XX siglos. Empleando un conjunto integral de técnicas analíticas, que incluyen espectroscopia ultravioleta-visible-infrarrojo cercano (UV-VIS-NIR), microscopía óptica (OM), microscopía electrónica de barrido (SEM), análisis de microsonda electrónica (EMPA), ablación láser mediante espectrometría de masas con plasma acoplado inductivamente (LA-ICP-MS), microdifracción de rayos X (μ -XRD) y espectroscopia de absorción de rayos X (XAFS), profundizamos en las propiedades ópticas, micro/nanoestructuras, composiciones de vidrio y vidriados, estado de valencia, y coordinación de los cationes. Nuestros hallazgos revelaron distinta composición en los vidriados amarillos con alto contenido de plomo de las dinastías Ming y Qing, al tiempo que demostraron la influencia de factores como el espesor del vidriado, la temperatura de cocción, la composición del sustrato y la atmósfera de cocción en el color del vidriado. El estudio de los vidriado Jun relaciona la nanoestructura del vidriado y la dinámica de oxidación-reducción del hierro y el cobre en la apariencia de los vidriados. De manera similar, nuestra investigación de los vidriados de cerámica de Changsha reveló el papel de la nanoestructura del vidriado y el estado de oxidación del cobre en la opacidad y el color del vidriado. Finalmente, nuestra exploración del vidrio rojo de ventana identificó tres tecnologías distintas, determinando el papel de las nanopartículas de cobre en la coloración roja y la importancia del hierro, el azufre y el estaño en la reducción del cobre. En resumen, esta investigación mejora nuestra comprensión de los mecanismos de coloración y las diferencias de composición en los vidriados y vidrios históricos, y ofrece información valiosa sobre las tecnologías de fabricación de vidrio.

Palabras clave: Vidriado histórico; Vidrio de ventana rojo; Hierro; Cobre; Azufre; Estaño; XAFS; Micro-XRD

摘要

由于兼有观赏性和功能性，彩色釉和玻璃自古便引起人们的关注，釉和玻璃的颜色也成为判定不同历史时期技术发展、艺术表现和社会阶级的指标。在不同浓度、比例、烧成温度和气氛下，作为古代釉和玻璃的主要着色剂，铁和铜呈现出极其广泛的色彩区间。为了系统分析高铅铁黄釉，深入研究铜红的形成机理，同时探究铜铁两种离子对釉色的影响，我们选取四个典型案例进行研究，包括明清(1368-1912)高铅黄釉，北宋时期的钧窑蓝釉和红釉，晚唐长沙窑铜绿和铜红釉，以及13到20世纪欧洲教堂的铜红窗玻璃。通过使用一系列互补的分析技术，如紫外-可见-近红外分光光度计(UV-VIS-NIR)、光学显微镜(OM)、扫描电子显微镜(SEM)、电子探针分析(EMPA)、激光剥蚀电感耦合等离子体质谱(LA-ICP-MS)、微/纳束X射线衍射(μ -XRD)和X射线吸收精细结构光谱(XAFS)，我们研究了釉和玻璃的光学性能、微/纳米结构、成分，以及铜铁的价态和配位结构。研究结果揭示了明清两个不同朝代釉色和胎体成分的显著变化，同时证明了釉层厚度、烧成温度、基质成分和烧成气氛等因素对釉色的影响；对钧釉的研究阐明了釉的纳米结构以及铁铜的氧化还原反应对钧釉外观形成的影响。另外，我们对长沙窑釉料的研究揭示了分相和铜的不同价态对乳浊效果和颜色的影响，以及硫对铜纳米颗粒形成的关键作用。最后，我们对欧洲铜红窗玻璃的研究确定了三种不同的技术，强调了铜纳米颗粒在红色着色中的作用以及铁、硫和锡对铜的还原作用。总之，这项全面的研究提高了我们对古代釉料和玻璃的着色机制和成分差异的理解，并为古代玻璃及釉的制造技术提供了一定的借鉴。

关键词：古代釉；红色窗玻璃；铁；铜；硫；锡；X射线吸收精细结构(XAFS)；微/纳束X射线衍射(μ -XRD)

Contents

Chapter 1 Introduction	1
1.1 Glass or glaze?	1
1.2 The colours of glass and glaze and the role of copper and iron	3
1.3 The study of the iron and copper coloured glasses and glazes	5
1.4 The scope of this thesis	7
Chapter 2 Analytical Methods	13
2.1 Sample preparation	13
2.2 Optical Microscopy (OM)	13
2.3 Scanning Electron Microscopy (SEM)	14
2.4 Electron probe Microprobe (EMPA)	15
2.5 Laser Ablation ICP Mass Spectroscopy (LA-ICP-MS)	15
2.6 Ultraviolet-Visible-Near Infrared Spectroscopy (UV-Vis-NIR)	16
2.7 Micro-X-Ray Diffraction (μ -XRD)	17
2.8 X-Ray Fluorescence and X-Ray Absorption Spectroscopy (XANES and EXAFS)	18
2.8.1 XAS measurement parameters	19
<i>Fe and Cu K-edge acquired at Alba-CELL synchrotron</i>	19
<i>Fe, Cu, S K-edge and Sn L₃-edge acquired at ESRF synchrotron</i>	20
2.8.2 XAS analysis of iron	21
<i>The pre-edge fitting of the iron standards acquired at Alba synchrotron</i>	22
<i>The pre-edge fitting of the iron standards acquired at ESRF</i>	23
2.8.3 XAS analysis of copper	24
2.8.4 XAS analysis of sulphur	25
2.8.5 XAS analysis of tin	25
References	26
Chapter 3 Chinese yellow glazes	29
3.1 Introduction	29
3.1.1 Historical background of the yellow glazes	29
3.1.2 Oxidation state and coordination of iron in glazes and glasses	31
3.2 Objective	35
3.3 Materials	36
3.3.1 Historical materials	36

3.3.2 Replicated yellow glazes	40
3.4 Results	41
3.4.1 Historical materials.....	41
<i>Composition analysis of body</i>	42
<i>Composition of the transparent glazes</i>	44
<i>Composition of the yellow glazes</i>	46
<i>Composition of the blue pigment</i>	54
<i>Colour of the yellow glazes</i>	56
<i>Oxidation state of iron in the yellow glazes</i>	58
3.4.2 Replicated yellow materials	62
3.5 Discussion	69
3.5.1 The change in the composition of the body and transparent glaze, and differences in the glazing method between Ming and Qing.....	69
3.5.2 The firing conditions of the imperial yellow	71
3.5.3 The colour of the yellow glaze	72
3.6 Conclusions	72
References	74
Chapter 4 Jun ware glaze colours.....	81
4.1 Introduction.....	81
4.2 Objective	85
4.3 Materials and Methodology	86
4.3.1 Materials	86
4.3.2 XAS Methodology	88
4.4 XAS study and Discussion	88
4.5 Conclusions	98
References	99
Chapter 5 Changsha ware glaze colours.....	103
5.1 Introduction.....	103
5.2 Objective	109
5.3 Materials	109
5.4 Chemical and microstructural analysis	110
5.5 XAS study.....	121
5.6 Discussion	124
5.6.1 Colour and opacity of Changsha glazes	124
5.6.2 The red design	129

5.6.3 Underglaze or overglaze?	134
5.7 Conclusions	137
References	139
Chapter 6 Copper red stained glass	145
6.1 Introduction.....	145
6.2 Objective	149
6.3 Materials	149
6.4 Red glass-one case study of <i>striated</i> red glass in the 13th century	154
6.4.1 Results	154
6.4.2 Discussion	159
6.5 Red glass-from the 13 th to the 18 th century	161
6.5.1 XAS methods	161
6.5.2 Results	162
6.5.3 Discussion	172
6.6 Red glasses-from the 19 th to the 20 th century	173
6.6.1 Results	173
6.6.2 Discussion	179
6.7 Conclusions	181
References	184
Chapter 7 Conclusions.....	197

List of figures

Chapter 1

Figure 1.1. (A) Stained glass of Sainte-Chapelle, Paris, France; (B) Stained glass of Santa Maria de Mar. Photos took by the author.

Figure 1.2. Images of different glazes coloured by iron.

(A) Dish with dragon pattern, Kangxi period (1622-1722) of the Qing dynasty, the Palace Museum,

<https://www.dpm.org.cn/collection/ceramic/227258.html>

(B) Yellow wine cup, Yongzheng period (1723-1735) of the Qing dynasty, the Palace Museum,

<https://www.dpm.org.cn/collection/ceramic/226980.html>

(C) Celadon, Yuan dynasty (1271-1368), Longquan kiln, the Palace Museum. <https://www.dpm.org.cn/collection/ceramic/226753.html>

(D) Ru ware, Song dynasty (960-1279), the Palace Museum. <https://www.dpm.org.cn/collection/ceramic/227122>

(E) Jian ware, North Song dynasty (960-1127), Guanfu Museum, <http://www.guanfumuseum.org.cn/view.php?cid=100&sid=5>

Figure 1.3. Images of different glazes coloured by copper.

(A) Flower pattern Zun (the container for wine and used in sacrifice occasions), Hongwu period (1368-1398) of Ming dynasty, the Palace Museum, <https://www.dpm.org.cn/collection/ceramic/226807.html>;

(B) Red bowl, Xuande period (1426-1435) of the Ming dynasty, the Palace Museum,

<https://www.dpm.org.cn/collection/ceramic/227636.html>;

(C) Peony pattern bottle, Yuan dynasty (1260-1368), the Palace Museum, <https://www.dpm.org.cn/collection/ceramic/227555.html>;

(D) Green glaze, Liao dynasty (916-1125), the Palace Museum, <https://www.dpm.org.cn/collection/ceramic/226973.html>;

(E) The green glaze pot, Changsha ware, Tang dynasty (618-907), the Changsha Museum,

<https://www.csm.hn.cn/#/Collection/overview/detail/765?sid=C721>

Chapter 2

Figure 2.1. (A) Digital photography stage; (B) mould; (C) epoxy resin and epoxy hardener; (D) blocks mounted and polished.

Figure 2.2. Dark field reflection mode illumination, <https://www.olympus-ims.com/es/microscope/terms/feature14/>

Figure 2.3. (A) Bright filed (BF); (B) Dark filed (DF); (C) Polarized light (PL) of CS7 (CS7 was analysed in **Chapter 5**)

Figure 2.4. (A) An over view of the ISR 3100 Ulbricht integrating sphere incorporated within the Shimadzu 2700 instrument;

(B) double beam transmittance device;

(C) CIE 1931 (x,y) chromaticity diagram;

(D) The L^* value is represented on the center axis. The a^* and b^* axes (https://www.xrite.com/-/media/xrite/files/whitepaper_pdfs/110-001_a_guide_to_understanding_color_communication/110-001_understand_color_en.pdf)

Figure 2.5. (A) Thin section samples affixed onto glass slides for analysis;

(B) The cross-sectional view of CB3 (analysed in **Chapter 6**) in the beamline exhibits the analysed points of interest;

(C) MSPD BL04- μ -XRD setup

Figure 2.6. (A) JS24 (**Chapter 4**) affixed for XAS analysis in Alba-CELL synchrotron,

(B) BL22-CLÆSS beamline of the Alba-CELL synchrotron,

(C) ID21 beamline of ESRF;

(D) sample holder of ID21 beamline

Figure 2.7. (top) Fitted pre-edge peaks corresponding to the iron standards; and (bottom) variogram after Wilke et al (Wilke 2001), showing the fitted data corresponding to the iron standards.

Figure 2.8. (top) Fitted pre-edge peaks corresponding to the iron standards and (bottom) variogram after Wilke et al (Wilke 2001), showing the fitted data corresponding to the iron standards.

Chapter 3

Figure 3.1. (A) Tang sancai (713-741), Palace Museum, <https://www.dpm.org.cn/collection/sculpture/234681.html>;

(B) Glazed tile (Ming dynasty), Palace Museum, <https://www.dpm.org.cn/explore/building/236551.html>.

Figure 3.2. Absorbance of Fe ions. After (Bingham 2000).

Figure 3.3. The Ming samples.

Figure 3.4. The Qing samples.

Figure 3.5. Glazes fired in air after **Table 3.2**.

Figure 3.6. Replicated samples under different temperatures and atmosphere.

Figure 3.7. Dark field reflection optical microscope image of (A) ETH12A (Ming dynasty); (B) ETH6A (Qing dynasty).

Figure 3.8. (A) The content of R_xO_y (Wt%), the ratio of SiO_2/Al_2O_3 , (Fluxes in the glaze including Na_2O , K_2O , CaO and FeO are merged into R_xO_y); (B) and content of CaO , FeO , Na_2O , K_2O of the body in the different periods.

Figure 3.9. The comparison of the content of K_2O and Na_2O of the body.

Figure 3.10. Trace element of transparent glazes in the different periods measured by LA-ICP-MS.

Figure 3.11. PbO/SiO_2 ratio and FeO content (Wt%) of the different periods.

Figure 3.12. $CaO-Al_2O_3-Na_2O+K_2O$ triangular plot of the yellow glazes.

Figure 3.13. (A) Na_2O vs. K_2O content; and (B) Na_2O vs. Na_2O+K_2O for the Ming and Qing glazes.

Figure 3.14. (A) SiO_2 versus PbO and (B) Al_2O_3 versus PbO for the yellow glazes.

Figure 3.15. Comparison between the main elements present in the yellow glaze after subtracting PbO and Fe_2O_3 and the porcelain for the Qing samples.

Figure 3.16. Comparison between the main elements present in the yellow glaze after subtracting PbO and Fe_2O_3 and the transparent glaze for the Ming samples.

Figure 3.17. Profile composition analysis for the yellow glaze of (A) ETH12B (Zhengde) and (B) ETH3 (Kangxi).

Figure 3.18. Trace element of yellow glazes in the different periods measured by LA-ICP-MS.

Figure 3.19. SEM images in the white glaze of (A) ETH12A and (B) ETH15A of the Ming samples.

Figure 3.20. Interface SEM images of ETH12 (Zhengde), ETH13 (Jiajing) of the Ming dynasty; ETH3 (Kangxi), ETH5 (Xuantong) of the Qing dynasty and the micro-XRD analysis.

Figure 3.21. SEM images of ETH10 (Yongzheng) and ETH5 (Xuantong) blue pigment in white glaze and the micro-XRD analysis.

Figure 3.22. Trace elements comparison of ETH10A and ETH5B.

Figure 3.23. (A) Diffuse reflectance and (B) Absorbance of the yellow and white glazes of ETH2.

Figure 3.24. Colour coordinates from the historical yellow glazes.

Figure 3.25. Colour coordinates L^* and s^* vs. the thickness of the yellow glazes.

Figure 3.26. Fitted pre-edge peak ETH. (Top Left) Ming (Top Right) Kangxi and (Bottom Left) Yongzheng and Xuantong yellow glazes.

Figure 3.27. Variogram of ETH yellow glazes.

Figure 3.28. Colour coordinates L^* , s^* , a^* and b^* as a function of the Fe^{2+} content.

Figure 3.29. Colour parameters as a function of the thickness of the glaze.

Figure 3.30. Effect of the firing temperature.

(A) The colour is more yellow (h^* increases) with the firing temperature for the glazes with similar glaze thickness ($\approx 100 \mu m$).

(B) CaO content of the glazes vs. firing temperature and thickness of the glazes.

Figure 3.31. Variogram of the replicated glazes.

Figure 3.32. (A) a^* versus $A(Fe^{2+}/AF_{e_{tot}})$ showing that a larger a^* is related to a thicker glaze but there is no obvious relationship with the oxidation state of iron. (B) C versus dT . Considering only those glazes with similar thickness ($\approx 100 \mu m$), we can see that C increases with the firing temperature mainly for M(Y,T2), that is the one which incorporates more calcium in the glass due to the reaction with the porcelain.

Figure 3.33. Colour coordinates versus temperature. A (top) a^* and b^* ; B (bottom) L^* and s^* .

Figure 3.34. Fitted spectra of replicated sample fired under different atmospheres.

Figure 3.35. Variogram of samples fired under different atmospheres.

Figure 3.36. Centre Shift and Area of the pre-peak versus temperature and atmosphere.

Figure 3.37. (A) Area of the Fe²⁺ and Fe³⁺ pre-edge peaks; and (B) area of the Fe²⁺ peak over total area as a function of temperature and firing atmosphere.

Figure 3.38. The velocity flow diagram of flue gas in the kiln. (A) *hulu yao* (double-gourd kiln); (B) *zhen yao* (egg-shaped kiln). (Yan 2018)

Figure 3.39. PbO/SiO₂ ratio of replications under different temperatures.

Chapter 4

Figure 4.1. (A) The Classic Jun, North Song dynasty (960-1127), <https://www.dpm.org.cn/collection/ceramic/227953.html>; (B) The Classic Jun, Jin dynasty (1115-1234), <https://www.dpm.org.cn/collection/ceramic/227947.html>; (C) The numbered Jun (number ‘一’ is one in Chinese), Song dynasty (960-1275), <https://www.dpm.org.cn/collection/ceramic/227141.html>. This kind of furnishing objects is well decorated and has high quality, which was written the number from one to ten by Chinese character. The number indicates their size, with one being the largest and ten the smallest.

Figure 4.2. (A) Top view and (B) the side view of the kiln (Yan 2012)

Figure 4.3. (A) JS80F (The official Jun); (B) JS4F (The classic Jun) (Hou 2018)

Figure 4.4. Droplets scattering and absorption (Hou 2018).

Figure 4.5. Optical microscopy images of the (A) blue and (B) red glaze of JS27

Figure 4.6. Fitted pre-edge peaks corresponding to the Jun ware blue glazes.

Figure 4.7. Fitted pre-edge peaks corresponding to the brown glaze from JS78.

Figure 4.8. Fitted A(Fe²⁺/Fe) of the spectra vs. calcium content of the Jun ware blue glazes analysed.

Figure 4.9. X-Ray Fluorescence maps corresponding to calcium, iron and copper for JS24 (Top) blue glaze and (Bottom) red glaze. The intensities are the same for each element.

Figure 4.10. Fitted pre-edge peaks corresponding to the calcium rich and poor areas of the blue and red JS24 glazes.

Figure 4.11. (A) Surface appearance of the blue and red side from JS24. (B) Cross section, (C) nanostructure of the Ca-rich blue (left) and red (right) glazes, and (D) nanostructure of the Ca-poor blue. The white droplets are calcium rich in a darker silica rich matrix. Small precipitates of metal copper nanoparticles are present in the red glaze(C-right).

Figure 4.12. UV-Vis spectra from the Blue and Red sides of JS24. The large scattering contribution between 400 nm and 600 nm from the droplets structure and the broad absorption of Fe²⁺ (maximum at ≈ 1100 nm) extending to the red part of the visible spectra is also clearly seen. In the red side the Surface Plasmon Resonance Absorption peak corresponding to metal copper nanoparticles ($\lambda_p \approx 560$ nm) is clearly seen.

Figure 4.13. (A) Cu K-edge XANES spectra and (B) 1st derivative XANES spectra from the blue and red areas of JS24.

Figure 4.14. Cu K-edge experimental data (points) and curvefit (line) of BP1 (left) k³-weighted phase-uncorrected data. (right) R-space (FT magnitude and Imaginary component).

Figure 4.15. Linescan corresponding to a copper sulphide particle in the JS26 purple glaze.

Chapter 5

Figure 5.1. Typical Changsha bowls, Belitung Shipwreck, c. 830s, Asian Civilisations Museum, <https://www.nhb.gov.sg/acm/galleries/maritime-trade/tang-shipwreck>

Figure 5.2. the map of the part of Chinese province and some typical kilns (Wood 1999)

Figure 5.3. (A) Proto-porcelain, Warring States (475/403 B.C.E.-221 B.C.E), Keqiao District Museum, <https://www.ygwhmuseum.com/collection/treasuredetail?id=18>; (B) Celadon, East Han dynasty (25-220 C.E.), The Palace Museum, <https://www.dpm.org.cn/collection/ceramic/227092.html>; (C) Celadon, Three Kingdom Wu dynasty (222-280 C.E.), National Museum of China, https://www.chnmuseum.cn/zp/zpml/kgfjp/202112/t20211203_252538.shtml.

Figure 5.4. (A) Yue porcelain (Zhejiang province, the south), Tang dynasty (618-907), the Palace Museum. <https://www.dpm.org.cn/collection/ceramic/227521>; (B) Xing porcelain (Hubei province, the north), Tang dynasty (618-907), the Palace Museum. <https://www.dpm.org.cn/collection/ceramic/226955>

Figure 5.5. Typical splash decoration of Changsha ware. (A) Dish, Changsha ware, Tang dynasty (618-907), Hunan Museum website. <http://61.187.53.122/collection.aspx?id=1604&lang=zh-CN>; (B) Ewer, used as a wine vessel, Changsha ware, Tang dynasty (618-907), The Palace Museum, <https://en.dpm.org.cn/collections/collections/2009-10-19/1151.html>; (C) The handled ewer, used for wine or tea, Changsha ware, Tang dynasty (618-907), Hunan Museum website. <http://61.187.53.122/collection.aspx?id=2259&lang=en>.

Figure 5.6. (A) Bowl, Changsha ware, Tang dynasty (618-907), Hunan Museum, <https://de.hnmuseum.com/collection/collectionDetails.html?id=1002229327095398401&type=catalogueList#>; (B) Ewer, Changsha ware, Tang dynasty (618-907), the Palace Museum, <https://www.dpm.org.cn/collection/ceramic/227503.html>; (C) Ewer, Changsha ware, Tang dynasty (618-907), Changsha Museum, <https://www.csm.hn.cn/#/Collection/overview/detail/771?sid=C727>. (D) Ewer, Changsha ware, Tang dynasty (618-907), Changsha Museum. <https://www.csm.hn.cn/#/Collection/overview/detail/747?sid=C703>

Figure 5.7. (A) White and blue porcelain, Yuan dynasty (c. 1271-1368), The British Museum, https://www.britishmuseum.org/collection/object/A_1924-0114-1; (B) One example of the cross-section image of Xuande (1426-1435) imperial blue-and-white porcelain in backscattering mode. (Jiang 2019)

Figure 5.8. (A) CS2; (B) CS7; (C) CS8; (D) CS10; (E) CS28 sample and optical microscope darkfield image.

Figure 5.9. Trace elements of the glazes measured by LA-ICP-MS (Laser Ablation-Inductively Coupled Plasma Mass Spectrometry)

Figure 5.10. (A) OM image and line-scan through the white opaque glaze and white 'slip' of CS2, (B) SEM-BSD and OM image and line-scan through the iron-rich brown glaze over the colourless lime glaze of CS10, (C) OM image of a section of the red glaze and (D) micro-XRD patterns corresponding to different areas of CS28.

Figure 5.11. Glaze nanostructure of the opaque glazes showing the presence of spherical glass droplets (dark) and the glaze the matrix (light). W (white), G (green), T (turquoise). The line-scan shows that the droplets are richer in Si and poorer in Ca, Fe and Cu than the matrix.

Figure 5.12. (A) CS2W (white) glaze showing precipitates of fluorapatite. (B) CS2G (green) glaze showing precipitates of malayaite and cassiterite.

Figure 5.13. CS28 red decorated glaze (A) dark field OM image showing the red and colourless layers (B) magnification of the red area showing metallic copper nanoparticles. (C) SEM BSD image of a cross section of CS28 showing several crystalline precipitates, (D) magnification of the yellow framed area showing the presence of fluorapatite crystallites surrounded by metallic copper nanocrystallites and copper sulphide microcrystallites, (E) magnification of the red framed area showing the presence of anorthite crystals growing along the interface and metallic copper nanocrystallites.

Figure 5.14. SEM-BSD and line-scans of (A) copper sulphide (Cu₂S) microparticle, (B) copper sulphide with some copper-rich areas microparticle, (C) partly copper sulphide partly metallic copper nanoparticle, (D) metallic copper nanoparticle, (E) metallic copper surrounded by copper sulphide nanoparticle growing near a fluorapatite microcrystal.

Figure 5.15. UV-Vis-NIR spectra of (A) the opaque and (B) the transparent glazes. W: white, T: turquoise, G: green, BW: brown, R: red. The scattering glass droplet nanostructure, the Fe²⁺, Fe³⁺ and Cu²⁺ absorption bands and the Surface Plasmon Resonance (SPR) absorption of the Cu⁰ nanoparticles are shown.

Figure 5.16. (A) Cu K-edge and (B) Fe K-edge XAS data corresponding to the green glazes (CS2G and CS8G) and to the red glass and colourless transparent layers (CS28R, CS28T) and to the copper and iron standards; (C) S K-edge of some particles of the transparent glaze (particle 1) and the interface between transparent and red glaze (particle 2), and corresponding Cu₂S reference and Fe_{0.923}S and MgS after Fleet et al. (Fleet 2005) (D) Sn L3-edge corresponding to the green glazes and tin standards.

Figure 5.17. Cu K-edge EXAFS R-space (FT magnitude and imaginary part), data (points) and fit (line) of (A) red glaze of CS28 and (B) blue glaze of CS2. The data are k^3 -weighted and not phase-corrected.

Figure 5.18. Fe K-edge XAS pre-edge peak fitting. (A) Variogram showing the green glazes (CS2G and CS8G) (green dots) and measurements taken at different depths of the red glaze (CS28) (red dots) showing that iron is more oxidised near the surface and appears completely reduced in the red areas of the glaze. (B) Fitted pre-edge peak of the green glazes (CS2G and CS8G) and (C) of the red glaze at different depths (CS28TS, CS28T, CS28TR, CS28R). The peak at 7111.9 eV corresponds to Fe^{2+} and at 7113.5 to Fe^{3+} . (D) Centre Shift and Area of the pre-peak of CS28.

Figure 5.19. (A) Image of the decorated fragment studied (B) UV-Vis spectra of the green, red and colourless glaze (C) image of the red and green areas of the decoration, (D) OM image of the cross sections of the green and red areas and (E) chemical composition determined with XRF on the surface of the different colour areas according to Hou et al. (Hou 2022b).

Figure 5.20. From top to bottom, application of the copper pigment, the raw glaze mixture, after drying and after firing.

Figure 5.21. One example of the flower and bird painting, painter: Cui Bai(崔白), the North Song dynasty (960-1127), The Palace Museum, <https://www.dpm.org.cn/collection/paint/228138.html>.

Figure 5.22. Parts of the animal painting of Changsha ware (Changsha ware research group 1991, p122)

Figure 5.23. (A) This celadon was defined as the first underglaze celadon, Three-kingdom Wu dynasty (222-280), Six Dynasties Museum, <http://liuchao.njmuseumadmin.com/Collections/detail/id/16>; (B) Ou Kiln, the seventh year of Yonghe reign of the East Jin dynasty (351 CE), Wenzhou Museum, https://www.wzmuseum.cn/Art/Art_28/Art_28_3272.aspx; (C) Ou Kiln, South Dynasty (420-589), Wenzhou Museum, https://www.wzmuseum.cn/Art/Art_28/Art_28_3289.aspx; (D) Ou Kiln, Tang dynasty (618-907) Wenzhou Museum, https://www.wzmuseum.cn/Art/Art_28/Art_28_3280.aspx; (E) Qiong Kiln, Sichuan province, Tang dynasty (618-907), <https://www.dpm.org.cn/collection/ceramic/227102.htm;l> (F) Qiong Kiln, Tang dynasty, Yang 2013, Master thesis, page20. (G) Blue and white dish, probably Gongxian kilns, ca 830s, Belitung Shipwreck, c. 830s, Asian Civilisations Museum, <https://www.nhb.gov.sg/acm/galleries/maritime-trade/tang-shipwreck>.

Chapter 6

Figure 6.1. Red glass of sandwich type. (A) Fragment of Santa Eulalia window, cathedral of Barcelona, c. 1330. (B) transmission and reflection image and (C) dark field optical image of a cross section of CB1 from Sant Andreu & Sant Llorenç window, cathedral of Barcelona c. 1398-1408 by Nicoli de Maraye.

Figure 6.2. Red glasse of flashed types. (A) Stained glass window from Santa Maria del Mar made by the Campmajor workshop dated in 1790. Dark field reflection optical microscope image of (B) CB6.

Figure 6.3. Chemical composition of the red (r) and base (b) glasses from the 13th to the 20th analysed by Microprobe.

Figure 6.4. (A) Transmission optical image of the polished cross section of the red glass showing the analysed area. Magnified optical images of the analysed area in (B) transmitted light and (C) reflected light, dark field (DF) mode. The transmitted light image shows the red areas and the courless areas (white), while the the DF image shows the light scattered by the metallic nanoparticles on a dark background. Therefore, the transparent glass appears dark while the particles scatter light and appear white.

Figure 6.5. SEM-BSD image of one of the metallic copper nanoparticle layers. The particle sizes vary between 20 and 40 nm and form layers less than 1 μm thick

Figure 6.6. (A) Cu and Fe XRF line scan, (B) glass areas determined as a function of the copper and iron content and colour, (C) Dark field reflection optical image (D) transmission optical image, (E) Cu XRF map and (E) Fe XRF map. + and x correspond to the measured copper and iron points, respectively.

Figure 6.7. (A) Cu K-edge and (B) Fe K-edge absorption spectra corresponding to the four and five glass areas respectively, and reference compounds. Green: copper-rich colourless glass, red: copper rich red glass, pink: copper-poor reddish glass, grey: copper-poor colourless glass, blue: copper-free colourless substrate glass. The shift to a lower energy of the Fe K-edge (arrow) indicates that the iron is more reduced.

Figure 6.8. Cu K-edge experimental data (points) and curvefit (line) of red area (upper) k^3 -weighted phase-uncorrected data. (below) R-

space (FT magnitude and Imaginary component).

Figure 6.9. Variogram (Wilke 2001, Wilke 2005, Boubnov 2015), area (A) versus center shift (CE) showing the fitted standards (Fe_2O_3 and Fe_3O_4) and coloured glass areas.

Figure 6.10. (A) Copper speciation determined by fitting of the Cu K-edge EXAFS data and (B) fitted centroid and area from the Fe K-edge pre-peak for different areas of the glasses.

Figure 6.11. (A) Cu K-edge XANES of the model compounds, $^1\text{Cu(I)}$ -oxide, Low-S basaltic glass spectrum and $^2\text{Cu(I)}$ -sulphide, High-S basaltic glass spectrum after Lanzirotti (Lanzirotti 2019), Cu foil and Cu_2S (chalcocite); (B) S K-edge XANES, of the model compounds, 3 completely oxidised (black) and reduced (grey) basaltic glass after Jugo (Jugo 2010) and Cu_2S , chalcocite, (magenta) used to fit the red glasses.

Figure 6.12. (A) Sample PS15 (B) Optical transmission image of the cross section of PS15.

Figure 6.13. (A) SEM-BSD image of SC13 red glass showing the presence of a micrometric Cu_2S particle (B) Magnification of the red square from (A) showing the presence of small metallic copper nanoparticles. (C) magnification and chemical linescan of one of the Cu_2S particles showing the presence of Ag_2S precipitated at the edge and (D) magnification and linescan of the metallic copper nanoparticles. (E) Micro-XRD pattern taken from a cross section of the red glass.

Figure 6.14. (A) SEM-BSD image of Valls red glass showing the presence of many micrometric Cu_2S particles (B) Magnification of the red square from (A) showing the presence of small metallic copper nanoparticles. (C) magnification and (D) linescan of some large micrometric Cu_2S particles and (E) linescan of small nanometric metallic copper particles. (F) Micro-XRD pattern taken from a cross section of the red glass, tetragonal Cu_2S , chalcocite, ICDD pattern 01-72-1071.

Figure 6.15. (A) Copper K-edge EXAFS of the red glasses and copper sulphide particles from SC13 and Valls. (B) S K-edge XANES from SC13 transparent and red glasses and copper sulphide particles. Reference spectra corresponding to Cu_2S (magenta) and a completely oxidised (black) and reduced (grey) basaltic glass after Jugo (Jugo 2010).

Figure 6.16. Linear combination fitting Cu k-edge XANES data of the red glasses using metallic copper (Cu^0), Cu(I) -oxygen and Cu(I) -sulphide complexes after Lanzirotti (Lanzirotti 2019).

Figure 6.17. (A) Fe K-edge spectra corresponding to the transparent and red glasses from SC13, CB5, PS15 and Valls and to the standards. (B) Fe K-edge shift calculated using the Integral method.

Figure 6.18. (A) UV-Vis and NIR absorbance corresponding to Renaissance glasses containing Cu_2S precipitates. (B) CIE $L^*a^*b^*$ colour coordinates, a^* and b^* and fitted h^* line.

Figure 6.19. Secondary electrons FE-SEM images (TDM, Vic, CB7), micro-XRD patterns of the red glasses and line scan of a metallic copper nanoparticle of TDM.

Figure 6.20. UV-Vis absorption spectra taken in transmission mode showing the SPR extinction band at 560 nm characteristic of metallic copper nanoparticles (20 to 50 nm). The spectrum corresponding to TDM appears slightly red shifted due to the large particle size (50 to 150 nm)

Figure 6.21. (A) Cu K-edge spectra of SDC, CB7 and Cu standards; (B) Cu K-edge EXAFS (dots) and curve fitting (line) for SDC and CB7 red glasses in R-space (FT magnitude and imaginary component). Data are k^3 -weighted and not phase-corrected.

Figure 6.22. (A) Fe K-edge spectra of CB7 and SDC colourless substrate glasses and red glass layers (the red line and dots correspond to the red layer and the blue line and dots to the substrate transparent glass) and Fe standards. The edge shifts to higher energy as the iron becomes more oxidized; (B) pre-edge Center Shift (CE) of the glasses. The CE increases as the iron becomes more oxidized. The Fe^{3+} fraction has been calculated using the expression in A. Fiege et al (Fiege 2017).

Figure 6.23. Sn L_3 -edge spectra of SDC colourless substrate glass and red glass layer and Sn standards. Sn^{4+} predominates in the red glass layer while Sn^{2+} predominates in the colourless substrate glass

List of tables

Chapter 2

Table 2.1. Fitted parameters of the standards (first inflection of the edge at 7111.08 eV). In black the Fe³⁺ and Fe²⁺ peaks corresponding to the 1s → 3d electronic transitions and in grey those resulting from processes involving Fe 2nd neighbours (Wilke 2001).

Table 2.2. Fitted parameters of the standards (first inflection of the edge at 7111.08 eV). In black the Fe³⁺ and Fe²⁺ peaks corresponding to the 1s → 3d electronic transitions and in grey those resulting from processes involving Fe 2nd neighbours (Wilke 2001).

Chapter 3

Table 3.1. Historical sample details.

Table 3.2. Composition of the colourless (T1, T2) glaze and porcelain (P) and yellow Ming, M(Y) and Kangxi, K(Y) glazes.

Table 3.3. The body analysis of the Imperial samples.

Table 3.4. Transparent glaze composition of the Imperial samples. Microprobe data (major elements, wt%).

Table 3.5. LA-ICP-MS (trace elements; ppm) of the Transparent glazes of the Imperial sample.

Table 3.6. Microprobe data of the Imperial yellow glazes (major elements, wt%).

Table 3.7. LA-ICP-MS (trace elements; ppm) of the Yellow glazes.

Table 3.8. Blue pigment composition. Microprobe data (major elements, wt%).

Table 3.9. LA-ICP-MS (trace elements; ppm) of the blue mark. c: colourless b: blue.

Table 3.10. Calculated colour coordinates from the historical yellow glazes.

Table 3.11. Fitted parameters of the ETH yellow glazes. * fixed.

Table 3.12. Fitted parameters of the ETH yellow glazes. Centroid, total area and the area of the Fe²⁺ peak over the total area of the pre-edge peaks.

Table 3.13. Colour coordinates and chemical composition of the replicated glazes.

Table 3.14. Fitted pre-peak data of the replicated glazes.

Table 3.15. Colour parameters, thickness and glaze composition (measured by SEM-EDX (wt%)).

Table 3.16. Fitted parameters corresponding.

Chapter 4

Table 4.1. Sample information of Official and Classic Jun ware.

Table 4.2. Fitted pre-edge data corresponding the blue Jun ware glazes. fwhm, E₁, E₂, A₁, A₁ are the full width at half maximum, energy and area of the fitted peaks; C, A and A(Fe²⁺/Fe) are the centre shift, total area and Fe²⁺ peak area fraction.

Table 4.3. (Hou 2018) Chemical composition of the spherical droplets and of the matrix for JS4 determined by TEM-EDS. The index of refraction (n) and density (ρ) calculated from the chemical composition after (Priven 2003), and viscosity(η) after (Fluegel 2007).

Table 4.4. Fitted pre-edge peaks corresponding to the blue (B) and red (R) glazes in calcium rich (R) and poor (P) areas.

Table 4.5. Curvefit parameters^a for Cu K-edge EXAFS for JS24 glazes.

Chapter 5

Table 5.1. Major and minor element composition of the glazes determined by Microprobe (-bd: below detection limit).

Table 5.2. Trace elements of the glazes measured by LA-ICP-MS.

Table 5.3. Summary of the properties and microstructure of the glazes

Table 5.4. SEM-EDX data obtained on different areas of CS7, turquoise glaze, brown glaze interface,

white ceramic interface and body.

Table 5.5. Cu EXAFS fitting results of Changsha ware glazes.

Table 5.6. Fe K-edge fitting of the pre-edge peak of the Changsha ware glazes.

Table 5.7. Chemical composition of ceramics from different kilns of the Tang dynasty

Chapter 6

Table 6.1. Details on the red glass studied.

Table 6.2. Copper EXAFS fitted parameters of the *Striated* glass.

Table 6.3. Fitted centroid and area of the Fe K-edge pre-peak for the different glass areas.

^aFirst inflection of the metallic iron edge at 7111.08 eV. ^bIron speciation (Fiege 2017).

Table 6.4. Major and minor elements composition of the glasses. Microprobe analysis. bd: below detection limit.

*cover glass was missing

Table 6.5. Copper XANES speciation calculated using a linear combination of Cu(I)-oxide (Low-S basaltic glass) and Cu(I)-sulphide (High-S basaltic glass) after Lanzirrotti (Lanzirrotti 2019) and metallic Cu.

Table 6.6. Major, minor elements measured by Microprobe and trace elements measured by LA-ICP-MS. *CBCB was measured by LA-ICP-MS. T_w: the working temperature is the optimal temperature for blowing the glass has been calculated using the approximation given in Fluegel (Fluegel 2007).

Table 6.7. Fitted Cu K-edge EXAFS data of SDC and CB7 red glass layers

Table 6.8. Fitted pre-edge peak Center shift and Area of SDC and CB7 colourless substrate glasses and red glass layers, ϵ is the standard deviation of the fitted data. *Iron speciation calculated according to A. Fiege et al. 2017 (Fiege 2017).

Table 6.9. Chemical composition of the red glasses

Published papers:

Yuan MY, Hou JY, Gorni G, Crespo D, Li Y, Pradell T (2022), Jun ware glaze colours: An X-ray absorption spectroscopy study, *Journal of the European Ceramic Society*, 42(6): 3015–3022. <https://doi.org/10.1016/j.jeurceramsoc.2022.02.016>

Yuan MY, Bonet J, Cotte M, Schibille N, Gratuze B, Pradell T (2023). The role of sulphur in the early production of copper red stained glass. *Ceramics International*, 49(11), part B: 18602-18613. <https://doi.org/10.1016/j.ceramint.2023.02.236>

Yuan MY, Bonet J, Castillo-Michel H, Cotte M, Schibille N, Gratuze B, Pradell T (2023). The role of tin and iron in the production of Spanish copper red glass from the 19th to the 20th century. *Boletín de la Sociedad Española de Cerámica y Vidrio*. <https://doi.org/10.1016/j.bsecv.2023.07.005>

Chapter 1 Introduction

Chapter 1 Introduction

1.1 Glass or glaze?

Glasses are non-crystalline (or amorphous) solids formed from a melt by cooling to solid state (glass transition temperature) without crystallisation. Historical glasses are “silicate glasses” based on silicon dioxide (SiO_2). Silicate glasses are hard to produce due to their high melting temperature ($1723\text{ }^\circ\text{C}$ for pure silica). Also, they start to become rigid and, therefore, become difficult to work below a high temperature ($\sim 1185\text{ }^\circ\text{C}$). Therefore, other compounds, called fluxes, are added to silica to lower the melting temperature and reduce the viscosity of the melt. The most common fluxes are alkali oxides, sodium and potassium oxides (Na_2O , K_2O) and lead oxide (PbO), but also CaO . For instance, a congruent melt between silica and sodium silicate takes place at $793\text{ }^\circ\text{C}$ (74 wt% SiO_2), that of lead oxide and silica at $717\text{ }^\circ\text{C}$ (70 wt% PbO) and that of CaO and silica is obtained at $1473\text{ }^\circ\text{C}$ (63 wt% SiO_2).

A ceramic glaze is a thin glassy layer fused to the surface of a ceramic body through firing. The main difference between glaze and glass is that the glaze has a large surface to volume ratio, and that it interacts with the ceramic body and the atmosphere. While the glass chemical composition does not change significantly during firing, the chemical composition of the glaze changes during firing mainly due to the interaction with the ceramic and the volatilisation of some of the compounds. The interaction between the glaze and the ceramic body results in the interdiffusion of elements from the glaze into the body and from the body into the glaze. Consequently, glazes are not homogeneous, showing chemical composition gradients across the glaze thickness due to diffusion (Molera 2001). The interaction region (called interface) could be neat or filled with crystals formed by the reaction between the paste and the glaze depending on the temperature, single or double firing, and the composition of the paste and the glaze (Molera 1993, 2001; Tite 1998; Pradell 2010). Moreover, bubbles, raw material particles in the process of dissolution and other reaction compounds developed during the glaze production are also often present in the glaze. Due to their low melting temperatures, alkali-lime and lead glazes were commonly used in low fired ceramics (below 1100°C), while lime rich glazes were used in high fired ceramics, stoneware (between 1100 and 1200°C) and porcelain (above 1200°C).

The origins of glass production can be traced back to the second half of the 3rd millennium BC in Mesopotamia (modern Iraq and Syria) (Moorey 1994). Some of the earliest glass, made from plant ash and silica, was certainly intended to imitate semi-precious stones and was attributed apotropaic properties (Henderson 2013). Glass technology subsequently spread to regions such as Syria, Cyprus, Egypt and the Aegean. In classical antiquity, Greece witnessed significant advances in glass technology, followed by further developments during the Roman period. In its early stages, glass production probably remained relatively limited in scale, focusing primarily on the production of small objects.

Throughout the Middle Ages, a period of frequent warfare and strong religious influence, advances in glass-making technology remained relatively limited. However, religion played an important role in glass culture and art, giving rise to two distinct types: Byzantine glass, centred on Christianity, and Islamic glass,

influenced by Islamic culture. Research focusing on medieval Islamic and Byzantine glass from the 10th to 11th centuries indicates that the majority of these artefacts belong to the soda-lime glass category (Brill 1999). In particular, stained glass (**Figure 1.1**) gained prominence during this period, playing an important role in decorating the windows of churches.

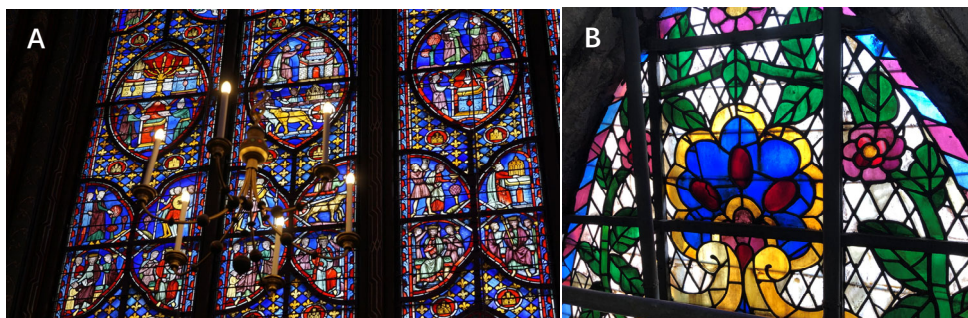


Figure 1.1. (A) Stained glass of Sainte-Chapelle, Paris, France; (B) Stained glass of Santa Maria de Mar. Photos taken by the author.

The composition of window glass has varied considerably over time (Schalm 2007). In Roman glass, the main constituents are sand and soda, resulting in what is known as soda-lime-silica glass, with the presence of lime accounting for approximately 8-10% of the composition. Around 900 AD, an alternative flux material was discovered - potassium-rich ash from the burning of forest wood or plants. In the 19th century, with the advent of the industrial age, synthetic soda ash became the preferred choice.

The evolution of glazes follows closely those of glass production. Glazes serve a dual purpose, contributing to both the aesthetics and functionality of ceramics by enhancing their appearance and rendering them waterproof for holding liquids and food. The earliest form of alkali-glazed objects, known as faience, originated in Egypt and the Middle East during the 4th millennium BC (Early Dynastic period) (Tite 1983). They were made from a mixture of sand, sodium salts (fluxing agents) and water. After compacting, drying and firing, the salts migrated to the surface with the water and formed a glaze during the firing process. The first glazed pottery was of the alkali-lime type, made from plant ash, and appeared in Mesopotamia in the middle of the 2nd millennium B.C. This tradition continued to flourish throughout the Middle East, covering regions from Syria to Iran, through the Roman, Byzantine, Parthian and Sassanid empires, and into the Islamic period (Hill 2004, Pace 2008). In the Roman Empire, high lead glazes were introduced in the 1st century BC (Walton 2004), and this practice continued in the Byzantine and Islamic worlds. Later in the Islamic world, high lead glazes evolved into lead-alkali glazes, as discussed in the context of tin opacification (Pradell 2019). In China, high-temperature lime glazes were dominant, with roots dating back to the Shang dynasty (1700-1027 BC). The most common flux materials used in these glazes were wood ash and limestone. However, low-temperature, high-lead glazes emerged later, during the Warring States period (475-221 BC) (Lang 2017), and reached their peak during the Han dynasty (202 BC-220 AD). This glazing tradition continued through the Tang (618-907) sancai, Song (960-1279) sancai, glazed tiles and imperial objects during the Yuan (1271-1368) and Ming (1368-1644) dynasties.

1.2 The colours of glass and glaze and the role of copper and iron

The colours of glass and glaze are obtained by the presence/addition of transition metals, fired under oxidising or reducing conditions. The colour given is due to the nature (iron, copper, manganese, cobalt), valence (Fe^{2+} , Fe^{3+} , Cu^{2+} , Cu^+ , Cu^0 , Co^{2+} , Mn^{3+} , etc), coordination number (four, five, six) and geometrical arrangement (tetrahedral, five-fold, octahedral) of the neighbouring atoms (Weyl 1951). The colour is caused by the absorption of light at specific light wavelengths by the metal ions.

Copper and iron are two of the earliest and most widely used colouring elements, renowned for producing an exquisite range of colours in ancient glazes and glasses. By meticulously controlling factors such as content, composition, atmosphere and firing, iron contributes to a range of colours including red, yellow, amber, green, blue, brown, black and even silver hues, making these elements indispensable for colouring in ancient glazes and glasses (**Figure 1.2**).

Similarly, copper and its oxides produce a fascinating range of colours in glaze and glass, from black, green and turquoise to brick red, cherry red, pink and purple (**Figure 1.3**).



Figure 1.2. Images of different glazes coloured by iron.

(A) Dish with dragon pattern, Kangxi period (1622-1722) of the Qing dynasty, the Palace Museum, <https://www.dpm.org.cn/collection/ceramic/227258.html>

(B) Yellow wine cup, Yongzheng period (1723-1735) of the Qing dynasty, the Palace Museum, <https://www.dpm.org.cn/collection/ceramic/226980.html>

(C) Celadon, Yuan dynasty (1271-1368), Longquan kiln, the Palace Museum. <https://www.dpm.org.cn/collection/ceramic/226753.html>

(D) Ru ware, Song dynasty (960-1279), the Palace Museum. <https://www.dpm.org.cn/collection/ceramic/227122>

(E) Jian ware, North Song dynasty (960-1127), Guanfu Museum, <http://www.guanfumuseum.org.cn/view.php?cid=100&sid=5>

The earth's crust is rich in iron, making up about 5% by weight of its composition, making it one of the most widely used metals. As a result, raw materials such as clay and ash naturally contain traces of iron. As a result, glazes and glasses from ancient times are often coloured due to the presence of iron in these materials. Since the industrial age, the technology of separation and purification has made it easier to

achieve colourlessness. Iron can be present in glazes and glasses as Fe^{2+} or Fe^{3+} , and in some cases also as crystalline iron oxide. Free Fe ions offer five available d-orbitals, with each orbital capable of accommodating no more than two electrons of opposite spin. The partially filled shell results in different energy states due to interactions between 3d electrons in the same sub-shell. Fe^{3+} has an electron structure of $[\text{Ar}]3d^5$, where the 3d sub-shell is half filled, while Fe^{2+} has the electron structure of $[\text{Ar}]3d^64s^2$. Normally Fe^{3+} gives a yellow colour, but the presence of reduced iron (ferrous) gives an absorption band in the near-infrared range, which usually gives a blue-green colour to the glaze or glass. Other intermediate colours depend on the balance of Fe^{2+} and Fe^{3+} . Both are normally present, the $\text{Fe}^{2+}/\text{Fe}^{3+}$ ratio being determined by the atmosphere and firing temperature; the higher the temperature, the higher the ratio.

Owing to its comparatively lower melting point, copper holds the distinction of being the earliest metal employed and smelted by humans in history. The utilization of copper as a pigment for coloration in glass appears to coincide with the emergence of the earliest glass vessels in the Near East around the sixteenth century BC (Vandiver 1982). In China, the use of copper to produce glazed wares dates back to the Western Zhou Dynasty (11th-8th century BC) (Hao 2014). In glaze and glass, copper appear in three forms, Cu^{2+} , Cu^+ and Cu^0 , sometimes a copper compound may also be formed if the content is high.

Under oxidising conditions, Cu^{2+} and Cu^+ are both present, and the high broad absorption of Cu^{2+} in the red with a large tail extending to the yellow, taken together with variations in the coordination and nature of the neighbouring atoms, produce a range of colours from turquoise to green. In contrast, firing under reducing conditions may result in the reduction of some of the copper to metallic copper, Cu^0 , which forms nanometric crystallites. Copper nanoparticles exhibit narrow absorption peaks in the visible range, known as Surface Plasmon Resonance (SPR), arising from the collective oscillation of free electrons at the surface of metal nanoparticles. In the case of Cu nanoparticles, SPR occurs around 570 nm, and provides a red to dark-red colour to the glass/glaze. It is worth noting that Cu nanoparticle size and shape both influence the colour, as the particle size decreases the SPR absorption of Cu nanoparticles shows a slight blue shift (Yeshchenko 2007). Additionally, a round shape tends to produce red hues, and an elongated shape results in blue colours (Farges 2006).



Figure 1.3. Images of different glazes coloured by copper.

- (A) Flower pattern Zun (the container for wine and used in sacrifice occasions), Hongwu period (1368-1398) of Ming dynasty, the Palace Museum, <https://www.dpm.org.cn/collection/ceramic/226807.html>;
- (B) Red bowl, Xuande period (1426-1435) of the Ming dynasty, the Palace Museum, <https://www.dpm.org.cn/collection/ceramic/227636.html>;
- (C) Peony pattern bottle, Yuan dynasty (1260-1368), the Palace Museum, <https://www.dpm.org.cn/collection/ceramic/227555.html>;
- (D) Green glaze, Liao dynasty (916-1125), the Palace Museum, <https://www.dpm.org.cn/collection/ceramic/226973.html>;
- (E) The green glaze pot, Changsha ware, Tang dynasty (618-907), the Changsha Museum, <https://www.csm.hn.cn/#/Collection/overview/detail/765?sid=C721>

One main difference between glass and glaze colour is that the interaction with the ceramic body is a source of introducing colouring elements into the glaze. Moreover, the colour of the ceramic bodies (greyish, reddish, creamy, etc.) may show through the transparent glaze and hinder the aesthetic purpose of the glaze. Therefore, although transparency is typically sought for glasses, this is not necessarily the case for glazes. Consequently, it is not uncommon to benefit from the presence of undissolved particles, crystallites formed during the firing, bubbles and glass nano-structures which increase the opacity of the glaze. This last type is mainly found in lime glazes in Chinese stoneware (i.e. celadons) and porcelain (Hou 2018, Li 2003).

1.3 The study of the iron and copper coloured glasses and glazes

Many studies have been carried out to investigate iron and copper coloured glazes and glass. High concentrations of iron oxide can cause the glass to turn black, especially when the Fe_2O_3 content exceeds 5 wt% (Ceglia 2014). It has also been found that Jian (Tenmoku) ware (Fujian Province, China. The feature can be seen in **Figure 1.2E**) contains a high Fe_2O_3 content of around 4-6 wt% and forms the iron oxide crystalline, which is the reason for the 'oil spot' feature (Li 2008). When iron oxide is added at high levels (around 8% or more), iron tends to show red tones in crystalline form at both high and low firing temperatures, although the red colouration in high temperature glazes appears more subdued compared to that in low temperature glazes.

Ancient glass typically had iron oxide levels (c. 0.5%) an order of magnitude higher than modern window glass, and the reduction of the relatively strong aqua-blue colour imparted by Fe^{2+} appears to have been a major concern of glassmakers (Rehren 2015). In silicate melt systems (see **Chapter 3.1** for more details), where both Fe^{2+} and Fe^{3+} coexist, the colour depends on the balance between Fe^{2+} and Fe^{3+} . It has been shown that the colour of celadon glazes can vary from pea green to sky green depending on the $\text{Fe}^{2+}/\text{Fe}^{3+}$ ratio. The role of iron in silicate glass matrices has also been studied, revealing its dual role as a network former and modifier (Nayak 2019). While in phosphate melts, iron can be completely reduced to Fe^{2+} under reduced atmospheres. In lead glazes, iron exhibits a wide range of bright colours, from yellow to brown (Yan 2022). However, lead glaze and glass systems have not been widely studied, and the influence on colour is also unknown.

Many factors will affect the colour. In alkali-silicate glass, where the absorption of Fe^{2+} shifts to higher wavelengths with increasing alkali ion radius. To achieve desirable hues in ancient glass, antimony and manganese were often added because of their oxidising properties (Janssens 2013, Arletti 2012, Bidegaray 2018). Titanium's role in celadon glazes is crucial and has been reported (Wood 2021), as it oxidises some Fe^{2+} ions to Fe^{3+} , transforming iron-blue glazes into green hues.

For copper-coloured glazes and glasses, it has been found that higher copper content contributes to the green colour. The quantification of Cu^+ and Cu^{2+} ions in the analysed samples showed that the colour saturation directly correlates with Cu^{2+} content in the glass when Cu^{2+} is the main chromophore ion (Silvestri 2012). The presence of high lead content favours the green colour instead of blue (Weyl 1951). In glasses with high copper and lead content, cuprite precipitation results in light red and orange hues (Drünert 2018).

From antiquity to the present day, achieving red colouration has been a challenging task, often reserved for objects of special symbolic significance and high status (Barber 2009), such as Celtic enamel, opaque red glass in the Roman period, monochrome red porcelain in China's Ming and Qing dynasties, and lustre ware, characterised by the presence of nanoparticles of copper and silver embedded in a glass matrix, represents another distinctive category. Various forms of copper have been reported to produce red glass and glazes, including metallic copper and the presence of cuprous oxide, resulting in lighter red to orange hues (Drünert 2018, Freestone 1992).

However, recent studies have pointed to metallic copper nanoparticles as the primary cause of bright red colouration in many copper-bearing vitreous materials (Li 2016, Moriyoshi 1992), such as copper ruby red and opaque red found in Roman glass, enamel, and Renaissance lustres. The production of translucent ("ruby") copper red was a challenge for early glass and ceramics makers, requiring the reduction of copper to metallic copper nanoparticles of a specific size (around 50nm) and volume fraction (0.02%-0.05%) (Pradell 2019, Li 2022).

By adding some reducing agents such as Fe (Barber 2009), Sn (Colomban 2010), or a uniform, slightly reducing atmosphere (Hou 2022, Dou 2017), metallic copper nanoparticles can be reduced. Studies indicate that the amount and type (SnO or SnO_2) of tin play a critical role in the development of the red colour. The

tin content must be more than twice the weight of copper (equivalent to 1/1 atoms). There is also some evidence that SnO can also prevent excessive growth of copper nanoparticles. Optimal heating temperatures are important; copper nuclei have been observed to form between 800°C and 1250°C, and can grow to colloidal size at around 650°C. Excessive growth results in muddy reds and blacks (Brown 1959), highlighting the importance of precise heating treatments (Bandiera 2020). The lower viscosity of the glaze melt facilitates the diffusion of iron and copper, thus increasing the degree of reduction of the copper red glaze. However, specific reduction details remain unclear, as the composition and technology evolve over time and the glass system is very complex.

1.4 The scope of this thesis

Many scholars have carried out extensive research to elucidate the underlying colouring mechanisms in both glass and glazes. Several studies have been carried out to investigate the colouring agents in different temporal and spatial contexts, and to distinguish between productions.

The low proportion of successful coloured glazes/glasses can be attributed to the difficulty of controlling the production parameters. Colour is influenced in a complex way by several factors, including glass composition and firing conditions, which in turn affect the valence state and coordination structure of the chromophores and thus the resulting colour. In addition, the thickness of the coloured glass/glaze layer and the composition and colour of the substrate also play a key role.

Iron and copper, as the most common transition elements, have been used extensively throughout history to colour glazed ceramics and glasses. The oxidation state and coordination of copper and/or iron in oxidised and reduced glazes and glasses, the interaction between the two chromophores and their role in the final colour of the glasses and glazes are the subject of debate.

Due to the richness of the cultural heritage, spanning thousands of years and its great diversity in different temporal and spatial contexts, many questions remain unanswered. For example, iron has often been described as necessary to obtain a red colour in copper glasses fired under reducing conditions, although its role is not yet clear. Indeed, the simultaneous presence of iron and copper in glasses and glazes raises questions about their individual contribution to colouration, and since a redox equilibrium between iron and copper species is eventually established as a function of firing temperature and atmosphere, it is not clear how this affects the final colour. Finally, the valence and coordination of iron in low-temperature, high-lead glazes and its role in colour has not yet been addressed.

A selection of glasses and glazes are examined to investigate oxidised iron in low temperature, high-lead glasses, iron and copper in reduced and oxidised high-temperature lime glazes, and reduced copper glasses. These include the high-lead, low-temperature, iron-coloured yellow glazes used by the royal family during the Ming and Qing dynasties in China (**Chapter 3**). We also examine the role of iron and copper in the colour of some of China's most famous reduced and oxidised high lime glazes; the Jun ware glazes are discussed in **Chapter 4** and the Changsha ware glazes in **Chapter 5**. Finally, we examine the technology of making of copper red window glass between the 13th and 20th centuries in **Chapter 6**.

Chapter 3 focuses on the rare and little-studied imperial yellow glazes of the Ming and Qing dynasties.

These glazes are characterised by a distinctive low-temperature high-lead composition and exhibit a remarkably pure yellow colour. The iron-coloured high-lead system has been little studied. While the yellow colour typically occurs in oxidising atmospheres, the role of glaze composition and thickness, firing temperature and atmospheres are investigated. Together with a selection of yellow glaze porcelains from the Ming and Qing dynasties, the study reveals differences among the different historical productions.

Chapter 4 explores the famous Jun ware, a renowned ceramic ware with origins dating back to the Song dynasty (960-1279) in China, which remains highly regarded in the present day. Jun ware is characterised by its captivating three-dimensional flowing patterns resulting from an heterogenous glass nanostructure, decorated with blue and red/purple hues resulting from a reducing firing. Many scholars have conducted extensive research on the subject and demonstrated that iron and copper are the primary colouring agents. However, the role of these elements in the development of the colour remains poorly understood and warrants further investigation.

Chapter 5 examines the distinctive characteristics of Changsha ware, a production that flourished in China during the mid to late Tang dynasty (766-907 C.E). As a renowned export production, it became famous for its distinctive decoration. In particular, the role of copper in the development of the green and turquoise colours is discussed. In addition, Changsha ware is considered to be the pioneer in the production of high lime red glazes in the history of Chinese ceramics. However, the mechanisms involved in the development of the copper-red designs remain a matter of debate. The development of opaque glazes has been observed in several of the Tang dynasty productions. Using the case of Changsha ware as an example, this chapter also examines the factors that contribute to the opacity and transparency.

Chapter 6 focuses on the study of the red glass, particularly red stained window glass. Copper red glass has generated much debate and research into the nature of the red colour and the technology of production. Despite the various studies that have been carried out on the subject, a systematic study of the materials and method of production over time has not yet been attempted. This chapter focuses on the study of red stained glass spanning from the 13th to the 20th centuries, covering the medieval and industrial periods. It seeks to understand the origin of the colour and how the materials and technology of production changed over time.

In summary, this study aims to elucidate the valence and speciation of Fe and Cu in glasses and glazes to gain valuable insights into their synthesis. Some long-standing questions, such as the mechanisms of colour development, the role of copper and iron as colourants and the methods of production would be addressed. We have to stress that the present availability of high-precision non-destructive micro-analytical techniques has been crucial to the success of this study.

Ancient technology is a rich heritage worthy of in-depth study. Although the ancient civilisations may not have had a full understanding of the scientific theories and mechanisms behind them, they were able to accomplish remarkable technological achievements. Scientific progress often comes from a wealth of experience, including the occasional setback. Therefore, exploring the field of ancient technology offers us invaluable learning opportunities.

References

- Arletti R, Quartieri S, Freestone IC (2012). A XANES study of chromophores in archaeological glass. *Appl. Phys.*, 111: 99–108. <https://doi.org/10.1007/s00339-012-7341-4>
- Barber DJ, Freestone IC, Moulding K M (2009). Ancient copper red glasses: investigation and analysis by microbeam techniques. In: Shortland, A., Freestone, I.C., Rehren, Th. (Eds.), *From Mine to Microscope - Advances in the Study of Ancient Technology*. Oxbow, Oxford (UK), p115–127.
- Bandiera M, Verità M, Lehuédé P, Vilarigues M (2020). The Technology of Copper-Based Red Glass Sectilia from the 2nd Century AD Lucius Verus Villa in Rome. *Miner.*, 10(10), 875. <https://doi.org/10.3390/min10100875>
- Brill RH (1999). *Chemical analysis of early glasses*. New York: The Corning Museum of Glass, Volume 2.
- Bidegaray AI, Ceglia A, Cicconi MR, Pham VT, et al (2018). An in-situ XANES investigation of the interactions between iron, manganese and antimony in silicate melts. *J. Non-Cryst. Solids*, 502: 227–235. <https://doi.org/10.1016/j.jnoncrysol.2018.09.015>
- Brown SF, Norton FH (1959). Constitution of Copper-Red Glazes. *J. Am. Ceram. Soc.*, 42 (11): 499-503.
- Ceglia A, Nuyts G, Cagno S et al (2014). A XANES study of chromophores: the case of black glass. *Anal. Methods*, 6: 2662–2671. <https://doi.org/10.1039/C3AY42029A>
- Colomban P (2010). The Use of Metal Nanoparticles to Produce Yellow, Red and Iridescent Colour, from Bronze Age to Present Times in Lustre Pottery and Glass: Solid State Chemistry, Spectroscopy and Nanostructure. *J. Nano Res.*, 8: 109-132. <https://doi.org/10.4028/www.scientific.net/JNanoR.8.109>
- Dou JH, Jin HT, Zhang ZH, Cui JF, Wang CQ (2017), Color change mechanisms of Yuanmingyuan glazed tiles (圆明园琉璃瓦表面釉层变色机理的研究), *Bull. Chinese Ceramic Soc. (硅酸盐学报)* 36(8): 2547–2552.
- Drünert F, Blanz M, Pollok K, Pan Z, Wondraczek L, Möncke D (2018). Copper-based opaque red glasses—understanding the colouring mechanism of copper nanoparticles in archaeological glass samples, *Opt. Mater.* 76: 375–381. <https://doi.org/10.1016/j.optmat.2017.12.054>
- Farges F, Etcheverry MP, Scheidegger A, Grolimund D (2006). Speciation and weathering of copper in “copper red ruby” medieval flashed glasses from the Tours cathedral (XIII century). *Appl. Geochem.*, 21(10): 1715-1731. <https://doi.org/10.1016/j.apgeochem.2006.07.008>
- Freestone IC, Barber DJ (1992), The development of the colour of sacrificial red glaze with special reference to a Qing dynasty saucer dish. *Chinese Copper Red Glaze* (percival David Foundation of Chinese Art Monograph), Eds. R.E.Scott, page 53–62. ISBN 10: 0728601877
- Hao WT, Yang YM, Zhu J, Gu Z, Xie YT, Zhang J, Wang LH (2014), XANES investigation of Chinese

- faience excavated from Peng State Cemetery site in Western Zhou Period (BC1046–BC771), *J. Electron Spectrosc.* 196: 133–135. <https://doi.org/10.1016/j.elspec.2013.11.011>
- Henderson J (2013). *Ancient Glass-An Interdisciplinary Exploration*. Cambridge University Press. ISBN 978-1-107-00673-7
- Hill DV, Speakman RJ, Glascock MD (2004). Chemical and mineralogical characterization of Sasanian and Early Islamic glazed ceramics from the Deh Luran Plain, southwestern Iran. *Archaeometry*, 46(4): 585–605. <https://doi.org/10.1111/j.1475-4754.2004.00175.x>
- Hou JY, Jia C, Zhang XG, Li H, Li G, Liu HW, Kang BQ, Lei Y (2022). The birth of copper-red glaze: Optical property and firing technology of the glaze from Changsha Kiln (8th–9th century), *J. Eur. Ceram. Soc.*, 42(3):1141-1148. <https://doi.org/10.1016/j.jeurceramsoc.2021.11.002>
- Hou JY, Pradell T, Li Y, Miao JM (2018), Jun ware glazes: Chemistry, nanostructure and optical properties, *J. Eur. Ceram. Soc.*, 38: 4290-4302. <https://doi.org/10.1016/j.jeurceramsoc.2018.05.010>.
- Janssens K (2013). *Modern methods for analysing archaeological and historical glass*. John Wiley & Sons, Ltd, Chichester, West Sussex, United Kingdom. ISBN:9781118314234 DOI:10.1002/9781118314234
- Lang, JF, Cui JF (2017). A study of style and producing area of the glazed pottery lei liquid vessels unearthed from a Qi tomb of the Warring States period in Linzi city (临淄战国齐墓出土釉陶器的风格与产地—兼论我国铅釉陶的起源问题). *Huaxia Archaeology (华夏考古)*, 2: 95–101.
- Li YQ, Yang YM, Zhu J, Zhang XG, Jiang S, Zhang ZX, Yao ZQ, Solbrekken G (2016). Colour-generating mechanism of copper-red porcelain from Changsha Kiln (A.D. 7th–10th century), China. *Ceram. Int.*, 42(7): 8495–8500. <http://dx.doi.org/10.1016/j.ceramint.2016.02.072>
- Li WD, Li JZ, Wu J, Guo JK (2003). Study on the phase-separated opaque glaze in ancient China from Qionglai kiln. *Ceram. Int.*, 29 (8): 933-937. [https://doi.org/10.1016/S0272-8842\(03\)00048-8](https://doi.org/10.1016/S0272-8842(03)00048-8)
- Li WD, Luo HJ, Li JN, Li JZ, Guo JK (2008), Studies on the microstructure of the black-glazed bowl sherds excavated from the Jian kiln site of ancient China. *Ceram. Int.*, 34(6): 1473–1480. <https://doi.org/10.1016/j.ceramint.2007.04.004>
- Li G, Lei Y (2022), The computational simulation of the reflection spectra of copper red glaze. *AIP Advances* 12(9): 095319. <https://doi.org/10.1063/5.0095570>.
- Moriyoshi Y (1992), The microstructure of sacrificial red glaze. *Chinese Copper Red Glaze (percival David Foundation of Chinese Art Monograph)*, Eds. R.E.Scott, page 63–75. ISBN 10: 0728601877
- Molera J, Pradell T, Salvadó N, Vendrell-Saz M (2001). Interactions between Clay Bodies and Lead Glazes. *J. Am. Ceram. Soc.*, 84(5): 1120–1128. <https://doi.org/10.1111/j.1151-2916.2001.tb00799.x>
- Molera J, Pradell T, Martinez-Manent S, Vendrell-Saz M (1993). The growth of sanidine crystals in the lead

of glazes of Hispano-Moresque pottery. *Appl. Clay Sci.*, 7: 483-491. [https://doi.org/10.1016/0169-1317\(93\)90017-U](https://doi.org/10.1016/0169-1317(93)90017-U)

Moorey PRS (1994). *Ancient Mesopotamian materials and industries: the archaeological evidence*. Oxford University Press. ISBN 10: 0198149212

Nayak MT, Desa JAE, Reddy VR, Nayak C, Bhattacharyya D, Jha SN (2019). Structures of silicate glasses with varying sodium and fixed iron contents. *J. Non-Cryst. Solids*, 509: 42–47. <https://doi.org/10.1016/j.jnoncrysol.2019.01.009>

Pace M, Bianco Prevot A, Mirti P, Venco Ricciardi RV (2008). The technology of production of Sasanian glazed pottery from Veh Ardasir (central Iraq), *Archaeometry*, 50(4): 591-605. <https://doi.org/10.1111/j.1475-4754.2007.00369.x>

Pradell T, Molera J, Salvadó N, Labrador A (2010). Synchrotron radiation micro-XRD in the study of glaze technology. *Appl. Phys. A*, 99: 407–417. <https://doi.org/10.1007/s00339-010-5639-7>

Pradell T (2019). Lustre and Nanostructures-Ancient Technologies Revisited. In: Dillmann, P., Bellot-Gurlet, L., Nenner, I. (eds) *Nanoscience and Cultural Heritage*. Atlantis Press, Paris. https://doi.org/10.2991/978-94-6239-198-7_1

Pradell T, Molera J (2020). Ceramic technology. How to characterise ceramic glazes. *Archaeol. Anthropol. Sci.*, 12: 189. <https://doi.org/10.1007/s12520-020-01136-9>

Rehren T, Freestone IC (2015). Ancient glass: from kaleidoscope to crystal ball. *J. Archaeol. Sci.*, 56: 233-241. <http://dx.doi.org/10.1016/j.jas.2015.02.021>

Schalm O, Janssens K, Wouters H, Caluwé D (2007). Composition of 12–18th century window glass in Belgium: Non-figurative windows in secular buildings and stained-glass windows in religious buildings. *Spectrochim. Acta. Part B*, 62(6-7): 663–668. <https://doi.org/10.1016/j.sab.2007.03.006>

Silvestri A, Tonietto S, D’Acapito F, Molin G (2012). The role of copper on colour of palaeo-Christian glass mosaic tesserae: An XAS study. *J. Cult. Herit.*, 13: 137–144. <https://doi.org/10.1016/j.culher.2011.08.002>

Tite MS, Freestone IC, Bimson M (1983). Egyptian faience: An investigation of the methods of production. *Archaeometry*, 25 (1): 17-27. <https://doi.org/10.1111/j.1475-4754.1983.tb00658.x>

Tite MS, Freestone IC, Mason R, Molera J, Vendrell-Saz M, Wood N (1998) Lead Glazes in Antiquity—Methods of Production and Reasons for Use. *Archaeometry*, 40(2): 241-260. <https://doi.org/10.1111/j.1475-4754.1998.tb00836.x>

Vandiver PB (1982) Technological change in Egyptian faience. In: Olin JS, Franklin AD (eds) *Archaeological ceramics*. Smithsonian Institution Press, Washington DC, pp 167–179

Walton MS (2004). *A Materials Chemistry Investigation of Archaeological Lead Glazes*. Doctoral Thesis,

University of Oxford.

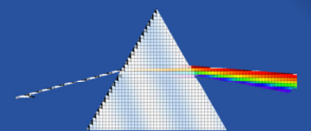
Weyl WA (1951). Coloured Glasses. Reprint by Society of Glass Technology, Sheffield, 2016.

Wood N (2021), Nought-point-two per cent titanium dioxide: A key to Song ceramics? *J. Archaeol. Sci. Rep.*, 35: 102727. <https://doi.org/10.1016/j.jasrep.2020.102727>.

Yan LT, Zhou Y, Ma B, Sun HY, Li L, Feng XQ (2022). The coordination structure and optical property of iron ions in the traditional lead glazes. *J. Mol. Struct.*, 1257: 132593. <https://doi.org/10.1016/j.molstruc.2022.132593>

Yeshchenko OA, Dmitruk IM, Dmytruk AM, Alexeenko AA (2007). Influence of annealing conditions on size and optical properties of copper nanoparticles embedded in silica matrix. *Mater. Sci. Eng. B*, 137(1-3):247-254. <https://doi.org/10.1016/j.mseb.2006.11.030>

Chapter 2 Analytical Methods



Chapter 2 Analytical Methods

2.1 Sample preparation

The glazed wares and glass fragments were sampled using a diamond tool and the sampling positions were carefully described and documented using digital photography. Cross-sections of the samples were embedded in epoxy resin and polished with diamond pastes down to 1 μm grade.

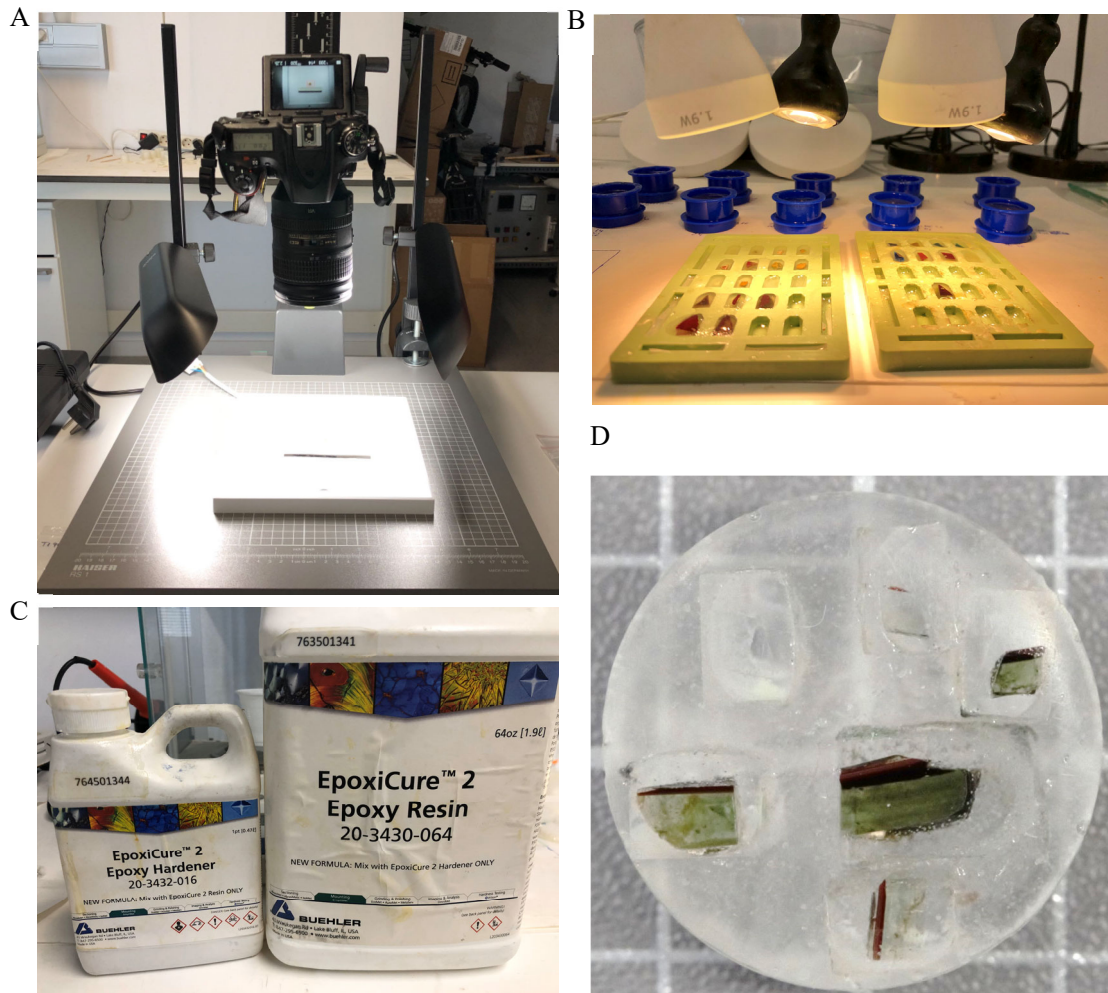


Figure 2.1. (A) Digital photography stage; (B) mould; (C) epoxy resin and epoxy hardener; (D) blocks mounted and polished.

2.2 Optical Microscopy (OM)

The polished sections were examined under reflected light (Bright, Polarised light and Dark field) using a Nikon Eclipse LV100D optical microscope equipped with an Infinity 1.3C camera. Bright field (BF) microscopy, the simplest of all the illumination techniques, has gained popularity because of its simplicity. The sample is illuminated and observed from above by a white beam and all the light reflected from the sample surface is collected. For transparent samples it is also possible to work with transmitted light. Dark field (DF) is an illumination technique used to enhance the contrast and contours. It works by masking the direct beam which is not collected by the objective lens, so that only the light scattered by the sample

surface is thus collected. The result is a characteristic visual effect of a dark, almost black background against which bright objects appear prominently. The light scattered by the specimen surface shows the true colour of the surface.

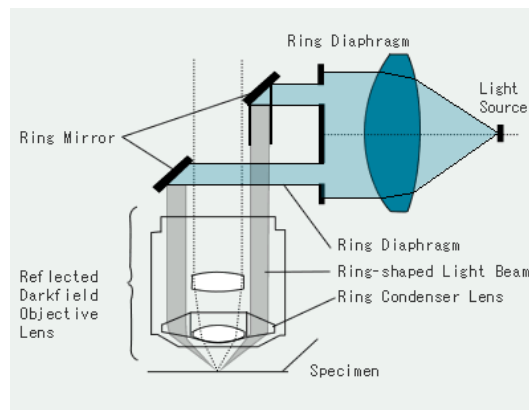


Figure 2.2. Dark field reflection mode illumination, <https://www.olympus-ims.com/es/microscope/terms/feature14/>

Polarized light microscopy offers valuable insights into the absorption colour and optical path boundaries between crystalline planes with varying refractive indices, akin to the capabilities of brightfield illumination. However, what sets this technique apart is its ability to discern between isotropic and anisotropic substances. By leveraging polarized light, microscopy examinations of anisotropic materials yield significantly higher-quality images compared to conventional light microscopy methods.

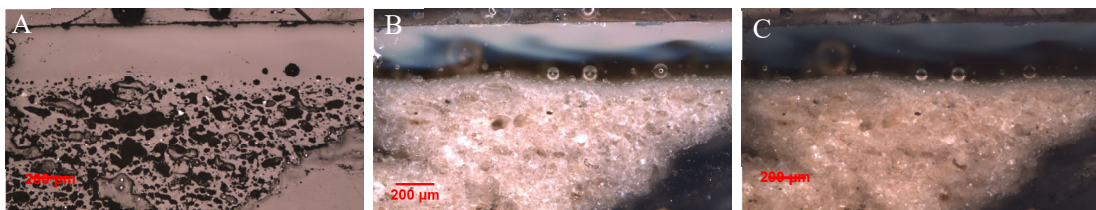


Figure 2.3. (A) Bright filed (BF); (B) Dark filed (DF); (C) Polarized light (PL) of CS7 (CS7 was analysed in **Chapter 5**)

2.3 Scanning Electron Microscopy (SEM)

The scanning electron microscope (SEM) stands as a highly versatile instrument in the field of microstructure analysis, enabling comprehensive investigations into morphology and chemical composition characterizations. With its advanced capabilities, the SEM offers a wide range of applications for precise examination and analysis.

The cross sections were coated with a carbon layer ($\approx 20 \mu\text{m}$ thick) and were examined in a crossbeam workstation (Zeiss Neon 40) equipped with scanning electron microscopy (SEM) GEMINI (Shottky FE) column (high brightness $\approx 10^8 \text{ Acm}^{-2}\text{rad}^{-2}$, small electron source size 15-20 nm and low energy spread 0.7-1 eV) with secondary (SE) Backscattered (BSE) and In-lens (IE) electron detectors and an energy-dispersive X-ray spectrometer detector (EDS) (Ultim EDS Detector, Oxford Instruments. Aztec Oxford Instruments). The equipment operated between 2 and 20 kV accelerating voltage, 20 nA current with typical 1.1 nm lateral resolution. BSE images of the nanostructures were obtained at 20 kV acceleration voltage. A

Focus Ion Beam (FIB, Ga ions, acceleration voltage 30 kV) was used to polish the surface and to obtain high resolution SE images (5 kV) of the nanoparticles when they were too small to be observed directly on the mechanically polished cross section.

2.4 Electron probe Microprobe (EMPA)

Electron probe microanalysis (EMPA) is a non-destructive analytical technique widely employed for the determination of local composition in solid samples (Reed 1993). The electron microprobe system consists of an electron column and several X-ray spectrometers, including several wavelength-dispersive (WDS) and energy-dispersive (EDS) spectrometers. The EDS spectrometer utilizes a solid-state x-ray detector, typically a crystal semiconductor such as Si or Ge, which allows x-rays to be discriminated on the bases of their energy. The wavelength-dispersive (WDS) spectrometer has a monocrystal that selects the X-rays emitted by the sample with a certain energy range, giving a higher energy resolution for quantitative analysis (typically ten times higher) (Llovet 2021).

The composition of ceramics, glazes and glasses has been quantitatively analysed by electron microprobe analysis (EMPA) using a JEOL JXA-8230 EMP (JEOL Ltd, Akishima, Tokyo, Japan) with 5 WDS spectrometers from the Scientific and Technological Centres of the Universitat de Barcelona.

In **Chapter 3**, the body composition of the Chinese yellow porcelain was determined using the EDS spectrometer with the following measurement conditions: 20KV acceleration voltage, 1 nA beam current, 300µm beam diameter, 60 s counting time (peak and background are measured simultaneously), XPP method (Pouchou and Pichoir) correction, the oxygen content was calculated by stoichiometry. Calibration was performed using wollastonite (Si and Ca), albite (Na), corundum (Al), Fe₂O₃ (Fe), and orthoclase (K) as standards.

The composition of transparent and yellow glazes in **Chapter 3**, Changsha ware glazes in **Chapter 5** and red glasses in **Chapter 6** were quantified using five WDS spectrometers, with a probe current of 15 nA. Mineral and glass standards were used for calibration.

2.5 Laser Ablation ICP Mass Spectroscopy (LA-ICP-MS)

Laser Ablation Inductively Coupled Plasma Mass Spectrometry (LA-ICP-MS) was used for the chemical analysis, including minor and trace components, of the glazes and glasses, allowing the study of micrometric regions while simultaneously providing elemental information. LA-ICP-MS has the advantage of being able to examine micrometric areas while achieving a wide analytical range.

Samples were analysed by LA-ICP-MS in the IRAMAT-CEB at the CNRS, Orléans (France), using a Resonetics M50E excimer laser (ArF, 193 nm) equipped with an S155 ablation cell and a Thermo Fisher Scientific ELEMENT XR mass spectrometer system. Ablations were typically performed with an energy of 5 mJ, a pulse frequency of 10 Hz in spot mode and a beam diameter of 100 µm for the base glass. The glasses and glazes were typically analysed along the surface due to insufficient thickness with a beam diameter of 50 µm, occasionally reduced to 25 µm when signal saturation occurred due to high

concentrations of transition metals. A pre-ablation time of either 10 s or 20 s, depending on the thickness of the sample was followed by 30 s of signal acquisition, resulting in 10 mass scans. The ablated material is transported to the plasma torch by an argon/helium flow at a rate of approximately a l/min for Ar and 0.65 l/min for He. Ion signals are recorded in counts-per-second for 58 isotopes (from Li to U). Standard Reference Material (NIST SRM610) and Corning glasses B, C, and D and APL1 (in-house standard glass) were used for external calibration, while ^{28}Si was used as an internal standard. Quantitative concentrations were calculated using procedures described by Gratuze (Gratuze 2001) with high precision and accuracy are reflected in the repeatability of the Corning A and NIST SRM612 reference glasses.

2.6 Ultraviolet-Visible-Near Infrared Spectroscopy (UV-Vis-NIR)

Ultra-Violet and Visible (UV-Vis) diffuse reflectance measurements were obtained from the surface of the glazes using a double beam spectrophotometer (Shimadzu 2700) equipped with an ISR 3100 Ulbricht integrating sphere (spot size of 3mm x 1mm and 1nm resolution, D65 standard illumination source, barium sulphate provided a white standard).

Ultraviolet-Visible (UV-Vis) diffuse absorption measurements of the glass were obtained in transmission mode using a double beam spectrophotometer (Shimadzu 2700), recorded between 200 nm and 800 nm, and NIR transmittance measurements using a double beam spectrophotometer (Shimadzu 3600) recorded between 800 nm and 3000 nm with a spot size of 8 mm x 1 mm.

The colour coordinates ($L^*a^*b^*$) are calculated from the Diffuse Reflectance UV-Vis spectra defined by the International Commission on Illumination (CIE) in 1976 (<http://cie.co.at/>). L^* corresponds to the lightness and a^* and b^* the colour coordinates. The lightness value, L^* , varies between black at $L^* = 0$, and white at $L^* = 100$, while $a^* = 0$ and $b^* = 0$ correspond to neutral. The a^* axis represents the green-red component, where green is negative and red is positive. The b^* axis represents the blue-yellow component, with blue in the negative direction and yellow in the positive direction. The scaling and limits of the a^* and b^* axes vary between ± 100 . The $L^*a^*b^*$ values are calculated relative to CIE standard illuminant D65, using BaSO_4 as the white standard. From them the chroma c^* , $c^* = \sqrt{a^{*2} + b^{*2}}$; the hue h^* , $h^*(^\circ) = \tan^{-1}(b^*/a^*)$ and the colour saturation s^* , $s^* = \sqrt{L^{*2} + c^{*2}}$ are defined (**Fig. 2.4**).

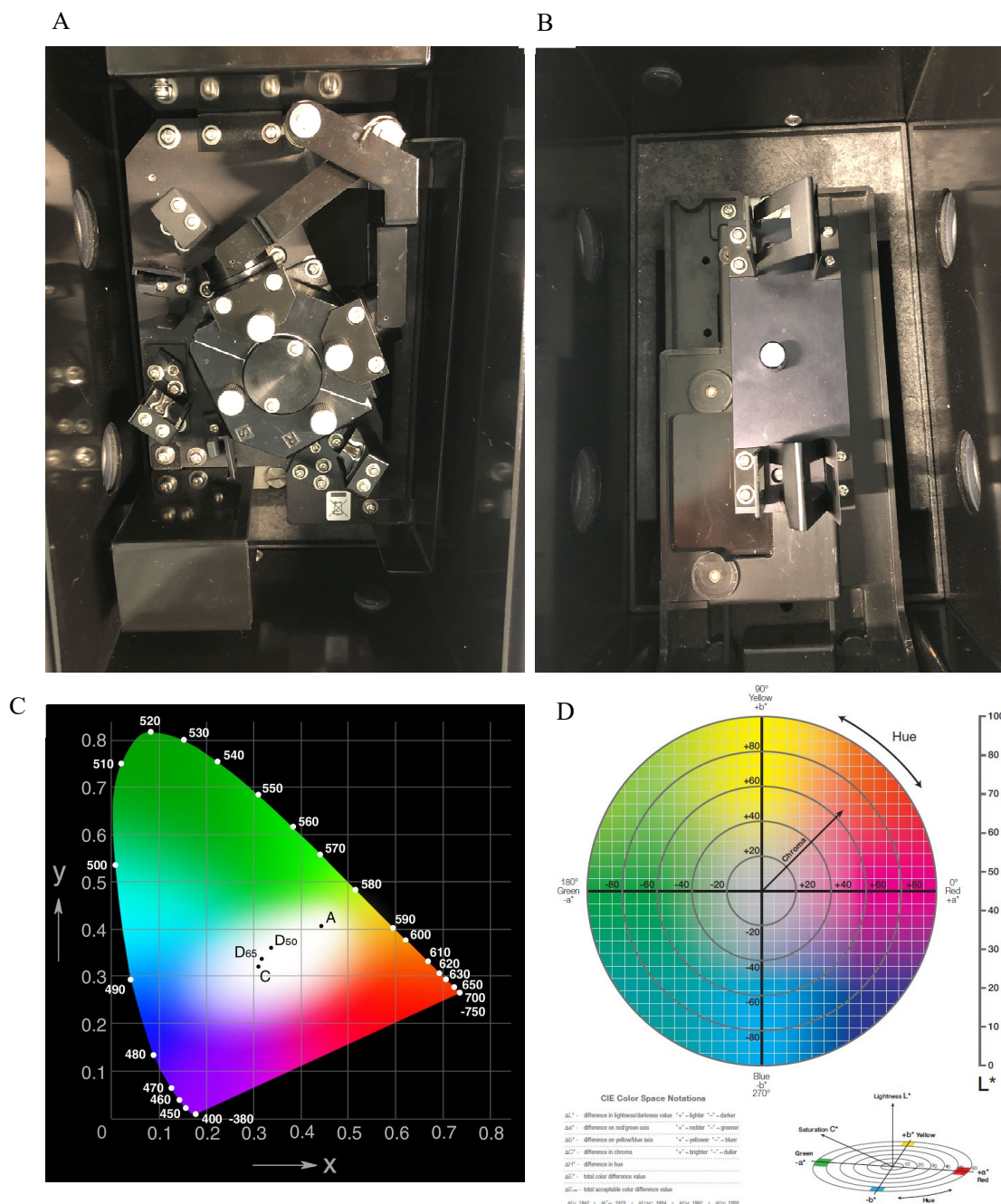


Figure 2.4. (A) An over view of the ISR 3100 Ulbricht integrating sphere incorporated within the Shimadzu 2700 instrument; (B) double beam transmittance device; (C) CIE 1931 (x,y) chromaticity diagram; (D) The L^* value is represented on the center axis. The a^* and b^* axes (https://www.xrite.com/-/media/xrite/files/whitepaper_pdfs/110-001_a_guide_to_understanding_color_communication/110-001_understand_color_en.pdf)

2.7 Micro-X-Ray Diffraction (μ -XRD)

The micro-XRD patterns were obtained from thin cross sections (approximately 200 μm) cut from small fragments of the samples included in epoxy resin using a low speed diamond saw. The synchrotron micro-XRD patterns were collected at the Materials Science and Powder Diffraction beamline (MSPD BL04) (Fauth 2013), at the ALBA Synchrotron Light (Cerdanyola, Spain) in transmission geometry, using a wavelength of 0.4246 \AA (29.2 keV), a spot size of 20 \times 20 μm^2 spot size, and a CCD camera, SX165

detector (Rayonix, L.L.C., Evanston, IL). However, a small angular rotation ($\pm 5^\circ$) was applied to avoid intense spots. The 2D images were integrated using the d2Dplot program (Vallcorba 2019). The XRD data were identified using the Powder Diffraction File Database (PDF) of the International Centre for Diffraction Data (ICS) (ICDD).

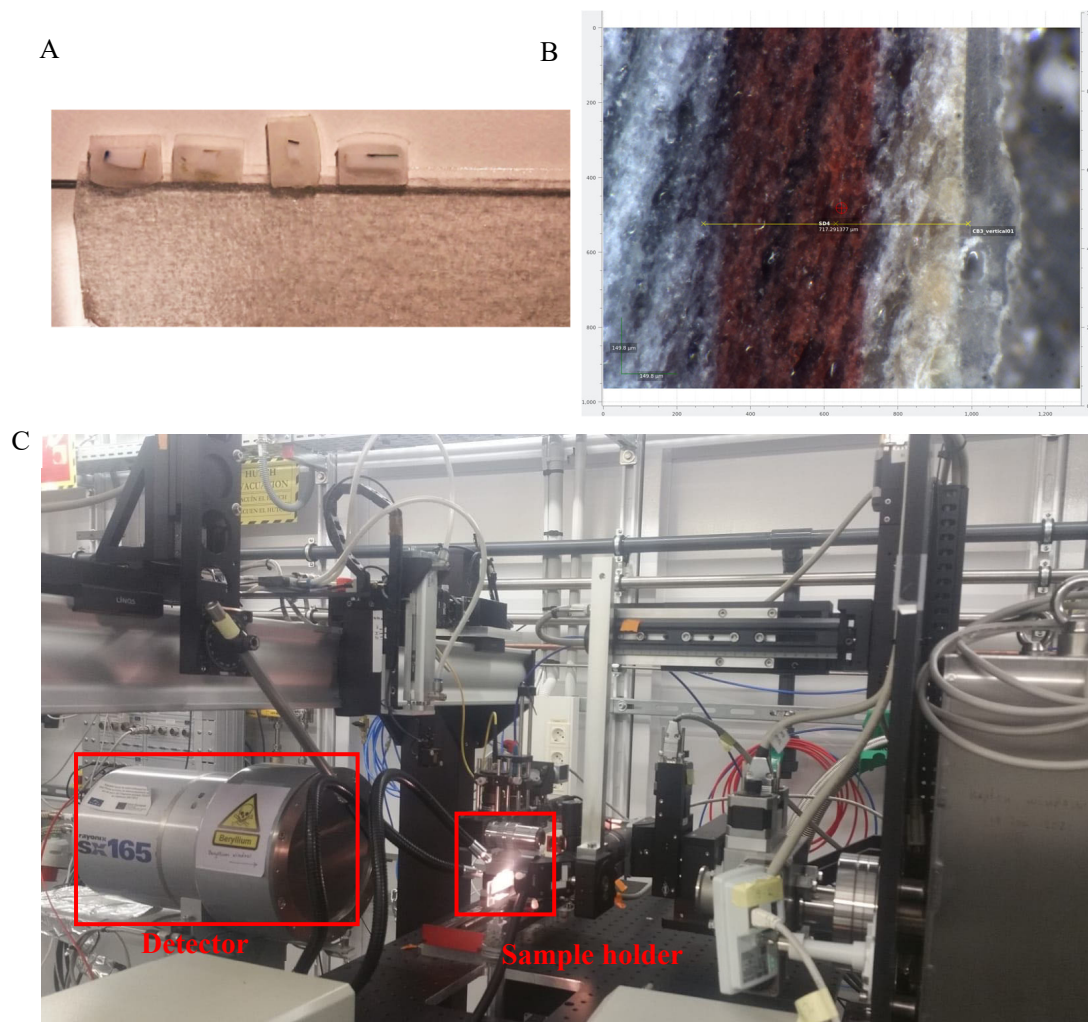


Figure 2.5. (A) Thin section samples affixed onto glass slides for analysis; (B) The cross-sectional view of CB3 (analysed in Chapter 6) in the beamline exhibits the analysed points of interest; (C) MSPD BL04- μ -XRD setup

2.8 X-Ray Fluorescence and X-Ray Absorption Spectroscopy (XANES and EXAFS)

X-ray Fluorescence (XRF) occurs when an electron in the inner shell of an atom is removed by the incident X-ray photons (X-ray beam), an electron from a higher energy level shell of the atom ‘falls’ into the lower energy vacant inner shell with the subsequent release of an X-ray photon (called secondary or characteristic) is emitted carrying the excess energy. (Diamond synchrotron website)

From the total number and energy of the secondary photons, it is possible to determine the elemental composition of the sample at the point where the X-ray beam interacts with the sample. By using calibrated standards, XRF can be quantitative.

The study of the shape and structure of the X-rays absorption peak gives information on valence state and

coordination of the atom probed. The X-ray absorption peak has two regions of interest: the X-ray absorption near-edge structure (XANES) and the extended X-ray absorption fine structure (EXAFS).

XANES refers to the absorption fine structure close to an absorption edge, about the 10 eV below the absorption edge and 20 eV above the edge. This technique provides information on the electronic structure of the unoccupied levels. Within the XANES regime, the spectral features primarily arise from multiple scattering events with many atoms, representing higher-order atomic correlation functions. Consequently, this spectral region gives also information on the local coordination of the probed atom.

The EXAFS regime spans from approximately 50-1000 eV above the absorption edge and is primarily governed by single scattering phenomena. Within this regime, valuable information such as coordination numbers and distances between the absorbing atom and its surrounding atoms within a range of 5 Å can be derived.

The X-ray absorption spectroscopy (XAS) studies were carried out at two synchrotron facilities, the BL22-CLÆSS beamline at Alba in Barcelona and the ID21 beamline at the ESRF in Grenoble. The BL22-CLÆSS beamline of the Alba-CELLS synchrotron offers an excellent and consistent signal quality, despite a relatively large beam size (500 μm x 300 μm full beam and 200 μm x 100 μm focused beam). Considering the size of the areas of interest and the thickness of the glaze layers, the Fe K-edge XAS spectra of the Chinese yellow glazes in **Chapter 3** and the Fe and Cu K-edge XAS spectra of the Jun ware glaze coloured areas in **Chapter 4**, were acquired at the BL22-CLÆSS beamline of the Alba-CELL synchrotron (Simonelli 2016) directly from the glaze surface.

However, considering the internal position and shallow thickness of the glass layers and the presence of micron-sized particles, the μXAFS data for the Fe, Cu, S K-edge, and Sn L₃-edge of the Changsha ware glazes in **Chapter 5** and of the copper red stained glass samples in **Chapter 6** were obtained from cross-sections of the glass and glazes at the ID21 beamline, ESRF (Cotte 2017, Sole 2007).

2.8.1 XAS measurement parameters

Fe and Cu K-edge acquired at Alba-CELL synchrotron

The energy was selected with a Si (111) monochromator with energy resolution better than the width of the corresponding K α lines. Harmonic rejection was obtained by choosing proper angle and coating of a vertical collimating and vertical focusing mirror. The spot size was adjusted to be around 500 (H) x 300 (V) μm². Fe K-edge absorption spectra were collected in fluorescence mode (45° detection angle) from the glazes and the fluorescent signal collected by a silicon drift detector (SDD). Additionally, Fe K-edge absorption spectra from several iron standards (Fe foil, Fe₂O₃, FeOOH, Fe₃O₄, and FeO) were collected in transmission mode using two ionization chambers to detect the incident and transmitted intensity. All spectra were calibrated to the first inflection point in a simultaneously measured Fe foil. Data treatment and normalisation was performed using the Athena software (Ravel 2005).

Additionally, submillimetric glaze features of **Chapter 4** Jun ware glazes were also measured by using a smaller beam size, 200(H) x 100(V) μm². In order to select the areas, X-ray Fluorescence maps from the

JS24 blue and red glazes were previously recorded. Then, both Fe K-edge and Cu K-edge absorption spectra were obtained from the selected areas. The energy scans at Fe K-edge were performed from 7005 to 7708 eV and at Cu K-edge from 8870 to 9575 eV.

Fe, Cu, S K-edge and Sn L₃-edge acquired at ESRF synchrotron

X-rays were produced with an undulator, and their energy was set using a Si (111) double crystal monochromator. For the analysis of glass samples, the beam was focused to $0.3 \times 0.9 \mu\text{m}^2$ (v×h) using a Kirkpatrick Baez mirror system. The samples were mounted vertically, at an angle of 62° with respect to the incident beam. X-rays was detected using a single energy-dispersive silicon drift detector (SGX, 80mm^2) at 28° of the sample surface. XRF maps were first acquired at 9.5 keV, over 2D regions in order to locate elements (especially Cu, Fe and S) and identify regions of interest.

XRF batch fitting was done using Python scripts and the PyMca software (Sole 2007). From these maps, points of interest were selected on which XANES spectra were acquired, in XRF mode, at the Cu, Fe and S K-edge. To avoid beam damage, the acquisition time was set at 0.1 s, each spectrum was collected only once on each point, and several spectra from different points were then averaged, to reduce the cumulated dose, the XRF detector was placed as closed as possible to the sample and the flux was reduced using titanium and aluminium foils of various thicknesses and the scans were collected in "continuous" mode. The spectra are deadtime corrected and corrected by the beam intensity, measured continuously with a photodiode upstream the sample. Given the need to measure the cross-section and account for the presence of multiple layers of glass, particularly in the case of *striated* glass (**Chapter 6.4**), it is crucial to consider an important parameter: lateral resolution. The lateral resolution is determined by the depth to which X-rays can penetrate the glass.

For the 9.65 keV X-ray used to obtain the XRF map, the penetration depth in the glass is $80 \mu\text{m}$, but taking into account the geometry of the system, the actual penetration is $d = 80 \mu\text{m} \cdot \cos(62^\circ) \cdot \sin(62^\circ) = 33 \mu\text{m}$. If the glass was not perfectly perpendicular, say the beam was tilted by 10° , the lateral resolution would be $x = d \cdot \sin(10^\circ) = 6 \mu\text{m}$. Therefore, we will measure an area of 6×33 (v x h) and it will not be possible to resolve thinner layers.

For Fe K-edge XANES, the energy was scanned from 7.1 to 7.35keV and for Cu K-edge μEXAFS from 8.95 to 9.5keV, with steps of 0.5eV. The monochromator was calibrated using the first inflection point of the copper, iron and tin metal foils (maximum of the first derivative at 8979 eV for Cu foil, 7112 eV for Fe foil and 3929 eV for Sn foil) using Athena software (Ravel 2005). Spectra of reference powders (Cu_2S , CuO , Cu_2O , Fe_2O_3 , Fe_3O_4 , SnO and SnO_2) were acquired with an unfocussed beam ($0.3 \times 0.3\text{mm}^2$), in transmission mode. Powders were spread on a piece of tape and covered with an ultralene foil. As the energy scanned for iron is lower than for the XRF mappings the penetration depth ($d = 23 \mu\text{m}$) and consequently the lateral resolution is smaller ($x = 4 \mu\text{m}$).

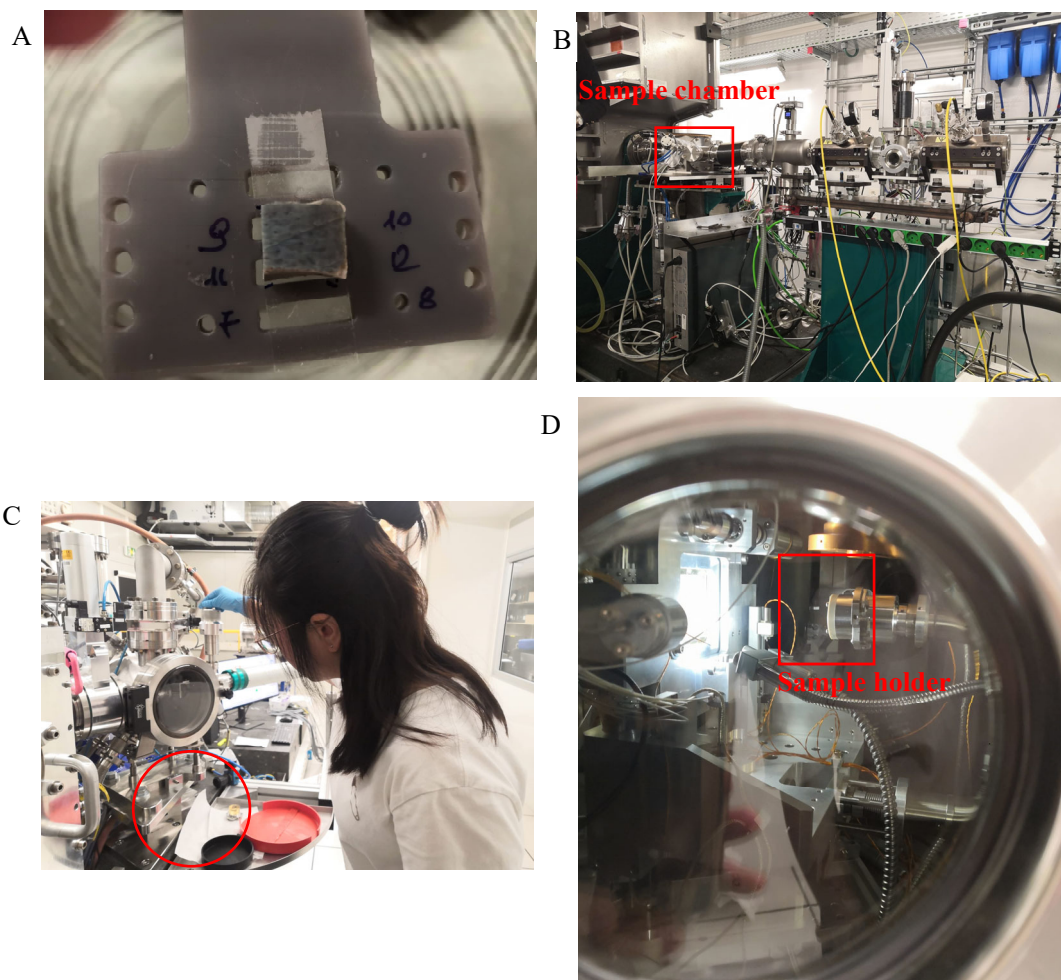


Figure 2.6. (A) JS24 (Chapter 4) affixed for XAS analysis in Alba-CELL synchrotron, (B) BL22-CLÆSS beamline of the Alba-CELL synchrotron, (C) ID21 beamline of ESRF; (D) sample holder of ID21 beamline

2.8.2 XAS analysis of iron

The pre-edge feature of the Fe K-edge absorption has a double peak, one related to Fe^{3+} (7113.5 eV) and the other to Fe^{2+} (7111.9 eV) which is particularly sensitive to the valence state and local geometry. The pre-peak area and the average peak position is known to shift to higher energy as the ratio of ferric to ferrous iron increases; and a variogram where the average peak positions (centroids) are plotted against total integrated area can be drawn (Wilke 2001) giving an estimation of the different species and their coordination state. The centroid energy of the pre-edge (the energy position at which half of the total area is integrated) can be related to the average iron oxidation state in glass and is determined using Eq: Centroid (eV) = $(E_1A_1 + E_2A_2)/(A_1 + A_2)$ (Bidegaray 2018) The area of the pre-peak is larger for tetrahedral coordination and smaller for octahedral coordination. In fact, in glasses, iron is expected to be in distorted sites of both coordinations, and also in the intermediate five-fold coordination.

Furthermore, a quantification of the Fe^{2+}/Fe ratio can be obtained provided that an empirical calibration is available for reference materials of known oxidation state. In glasses, where both Fe^{3+} and Fe^{2+} are present and the coordination geometry is poorly constrained, a glass-based calibration is preferred to crystalline materials (Wilke 2005, Farges 2004, Knipping 2015, Alderman 2017). The coordination of the iron species

in the glass and using the expression given in (Fiege 2017), the oxidation state of iron may be estimated. The pre-edge region of the normalized X-ray absorption near-edge structure (XANES) spectra was analyzed developing a python code based on procedures described in literature (Wilke 2001, Wilke 2005, Boubnov 2015). The absorption edge onset was modelled by fitting the energy regions below and above the pre-edge feature with an inclined arctangent function (Boubnov 2015), then the peaks were fitted using a Voigt profile which is the convolution of the Lorentzian peak related to the lifetime broadening of the $1s \rightarrow 3d$ electronic transition (with typical $\text{FWHM} \approx 1\text{eV}$) (Farges 2004) with a Gaussian contribution from the experimental set-up. In our code, an exact Voigt profile has been used instead of the analytical pseudo-Voigt profile. Profile fitting was performed by using the Trust Region Reflective algorithm, as implemented in the `scipy.optimize` standard python library (Jones 2001). The region fitted was selected between 7100 eV and 7118 eV to 7124 eV depending on the edge position.

The pre-edge fitting of the iron standards acquired at Alba synchrotron

Considering the number of variables involved, imposing some restriction to the number of experimental parameters is advisable. For this reason, the Full Width at Half Maximum (FWHM) and Gaussian fraction were constrained to be shared by all peaks. Moreover, the Gaussian contribution dominates the peak profile of the pre-edge spectrum ($\text{XG} > 0.9$) measured in standard resolution (Boubnov 2015). For this reason, we decided to fix the gaussian contribution to 1. Nevertheless, the results obtained did not vary substantially fixing a lower Gaussian contribution or even leaving it as a free parameter of the fit. The corresponding fitted data is shown in **Table 2.1** and the variogram in **Figure 2.7**. The values obtained are in good agreement with those obtained by other authors (Wilke 2001, Boubnov 2015).

Table 2.1. Fitted parameters of the standards (first inflection of the edge at 7111.08 eV). In black the Fe^{3+} and Fe^{2+} peaks corresponding to the $1s \rightarrow 3d$ electronic transitions and in grey those resulting from processes involving Fe 2nd neighbours (Wilke 2001).

	FWHM (eV)	E_1	A_1	E_2	A_2	E_3	A_3	E_4	A_4	E_5	A_5
$\alpha\text{-Fe}_2\text{O}_3$	1.29 (3)	7114.11 (3)	0.063 (2)	7112.70 (2)	0.044 (3)	7115.6 (1)	0.049 (2)	7116.8 (1)	0.027 (1)	7118.1 (1)	0.012 (1)
Fe_3O_4	1.57 (5)	7113.29 (3)	0.132 (1)	7111.57 (9)	0.015 (2)	7115.0 (1)	0.041 (2)				
FeO	1.50 (4)	7113.34 (3)	0.027 (1)	7111.78 (5)	0.02 (3)						
FeOOH	1.93 (3)	7113.55 (2)	0.143 (3)			7115.8 (2)	0.040 (5)	7117 (1)	0.027 (6)		

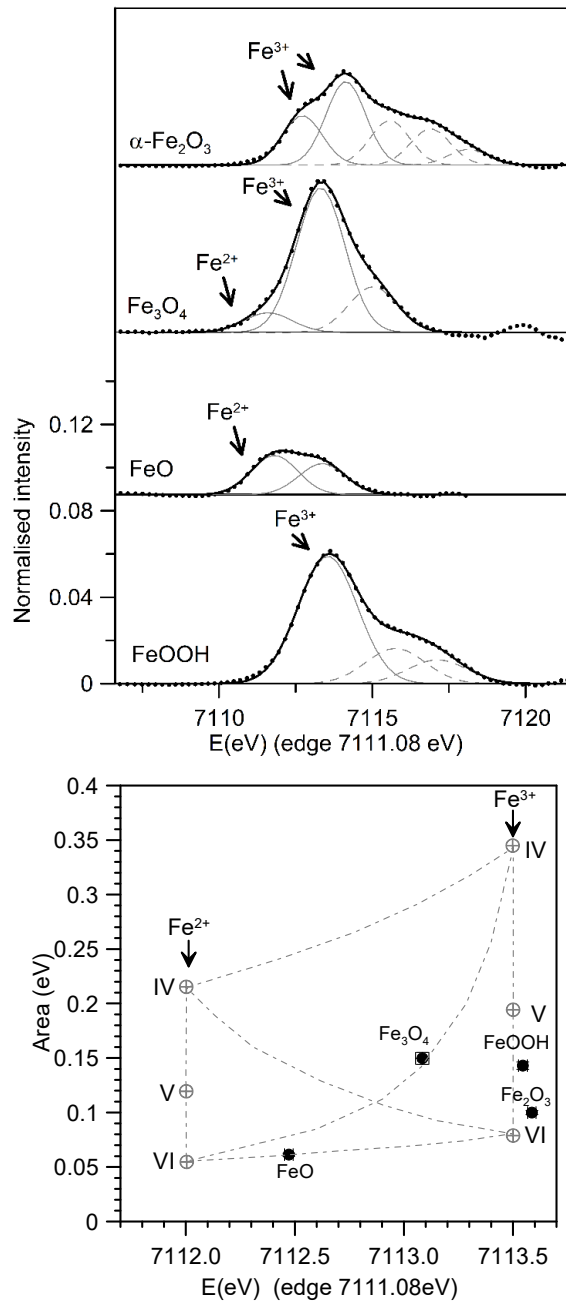


Figure 2.7. (top) Fitted pre-edge peaks corresponding to the iron standards; and (bottom) variogram after Wilke et al (Wilke 2001), showing the fitted data corresponding to the iron standards.

The pre-edge fitting of the iron standards acquired at ESRF

The Full Width at Half Maximum (FWHM) and Gaussian fraction were constrained to be shared by all peaks, and the gaussian contribution was fixed to 1. Considering that the data has standard resolution ($\Delta E=0.5$ eV), it was advisable to incorporate some extra restrictions, only two peaks were fitted and the FWHM was fixed to 2.1 eV. The corresponding fitted data is shown in **Table 2.2** and variogram in **Figure 2.8**. The values obtained are in good agreement with those obtained by other authors (Wilke 2001, Boubnov 2015).

Table 2.2. Fitted parameters of the standards (first inflection of the edge at 7111.08 eV). In black the Fe^{3+} and Fe^{2+} peaks corresponding to the $1s \rightarrow 3d$ electronic transitions and in grey those resulting from processes involving Fe 2nd neighbours (Wilke 2001).

	E_1	A_1	E_2	A_2
$\alpha\text{-Fe}_2\text{O}_3$	7113.6 (2)	0.12 (1)	7116.0 (4)	0.05 (1)
Fe_3O_4	7113.0 (1)	0.13 (2)	7114.6 (4)	0.05 (2)

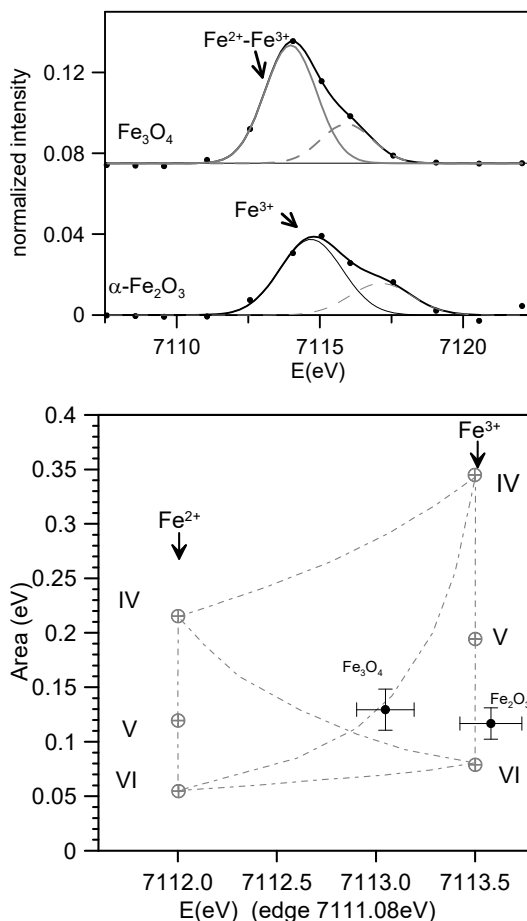


Figure 2.8. (top) Fitted pre-edge peaks corresponding to the iron standards and (bottom) variogram after Wilke et al (Wilke 2001), showing the fitted data corresponding to the iron standards.

2.8.3 XAS analysis of copper

The copper speciation was obtained from the analyses of the Cu K-edge XAS spectra. Copper is either dissolved in the glaze and glass in the form Cu^+ and Cu^{2+} , or precipitated as Cu^0 nanoparticles. In fact, a redox equilibrium between them is known to happen depending on the composition of the glass and the presence of other transition metal ions is expected. EXAFS fitting was carried out with Artemis software. The spectrum is a linear combination of model compounds each weighted by each compound fraction with Artemis software (Ravel 2005). Nevertheless, the lack of any longer-range order consistent with copper ions dissolved in the glass produces smooth EXAFS oscillations, making it difficult to fit more than the first shell. The first Cu-O and Cu-Cu shells were fitted taking as model compounds those of Cu_2O , CuO

and metal Cu, each weighted by a compound fraction. The spectrum as a linear combination of model compounds each weighted by each compound fraction and the sum set equal to 1 (Calvin 2013).

Linear combination fitting of some model compounds was also conducted using Athena software (Ravel 2005), and comprehensive details can be found in **Chapter 6.5.1**.

2.8.4 XAS analysis of sulphur

XANES spectroscopy is the ideal non-destructive technique for characterizing and quantifying S species in compositionally complex natural materials such as silicate glasses. S K-edge XANES allows non-destructive investigation of the coordination chemistry and oxidation state of sulphur species ranging from sulphide, S^{2-} to sulphate, S^{6+} . Sulphur species have a characteristic spectral feature representing the s→p and d-hybridization photoelectron transitions. On the contrary, the information that EXAFS can provide is limited because the oscillatory structure decays rapidly to a line past the edge (Fleet 2005). As reviewed in Fleet (Fleet 2005), the behavior of sulphur in melts, minerals and fluids is complicated, with speciation changing primarily as a function of composition and fugacity of O and S. S^{2-} or S^{6+} are generally agreed to dominate in silicate glasses rarely showing intermediate oxidation states (Backnaes 2008 and Jugo 2010) as the presence of sulphites is commonly attributed to beam damage. Oxidised glasses show a sharp K-edge feature with respect to the sodium thiosulphate at about 2483.0 eV corresponding to S^{6+} while reduced glasses have a broad band at 2476.9 eV corresponding to S^{2-} . In our red glasses from **Chapter 6**, sulphur is present dissolved both in the transparent base and in the red glass where it was also present forming copper sulphide particles.

The monochromator was calibrated using the first feature of sodium thiosulphate ($Na_2S_2O_3 \cdot 5H_2O$) (2472 eV) using Athena software (Ravel 2005). Spectra of some reference powders (Cu_2S) spread on a piece of tape and covered with an ultralene foil were also acquired with an unfocussed beam ($0.3 \times 0.3 mm^2$) in transmission mode.

2.8.5 XAS analysis of tin

Tin speciation was obtained from the analysis of the Sn L-edge spectra to avoid the rather high energy required to collect the K-edge information (26.2 keV) and an obscure s-p transition (Masai 2018). Moreover, the Sn $L_{3,2}$ -edge has been selected considering the low fluorescence yield of the L_1 and L_2 -edges. The absorption features of Sn L-edge absorption spectra of SnO, and SnO₂ have been assigned to corresponding electronic structures (Liu 2004). The $L_{3,2}$ -edge white line corresponds to the transition from filled $2p_{3/2}$, $2p_{1/2}$ Sn states to empty $5d_{5/2}$, $5d_{3/2}$ Sn orbitals and the two fine structures appearing before the $L_{3,2}$ white lines were assigned to the $2p_{3/2} \rightarrow 5s_{1/2}$ transitions due to the s-p hybridization. The Sn L-edge spectra corresponding to Sn^{2+} and Sn^{4+} in glass are similar to those of crystalline SnO and SnO₂, but show smoother and broader absorption peaks (Masai 2018).

References

- Alderman OLG, Lazareva L, Wilding MC, Benmore CJ, Heald SM, Johnson CE et al. (2017), Local structural variation with oxygen fugacity in $\text{Fe}_2\text{SiO}_{4+x}$ fayalitic iron silicate melts, *Geochim. Cosmochim. Acta*, 203: 15–36. <https://doi.org/10.1016/j.gca.2016.12.038>
- Backnaes L, Stelling J, Behrens H, Goettlicher J, Mangold S, Verheijen O, Beerkens RGC, Deubener J (2008), Dissolution mechanisms of tetravalent sulphur in silicate melts: Evidences from sulphur K edge XANES studies on glasses. *J. Amer. Ceram. Soc.* 91(3): 721-727. <https://doi.org/full/10.1111/j.1551-2916.2007.02044.x>
- Bidegaray AI, Ceglia A, Cicconi MR, Pham VT, et al (2018). An in-situ XANES investigation of the interactions between iron, manganese and antimony in silicate melts. *J. Non-Cryst. Solids*, 502: 227–235. <https://doi.org/10.1016/j.jnoncrysol.2018.09.015>
- Boubnov A, Lichtenberg H, Mangold S, Grunwaldt JD (2015), Identification of the iron oxidation state and coordination geometry in iron oxide- and zeolite-based catalysts using pre-edge XAS analysis, *J. Synchrontron Radiat.* 22: 410–426. <https://doi.org/10.1107/S1600577514025880>
- Calvin S (2013), *XAFS for Everyone*, 1st ed., CRC Press, pp. 342-343. ISBN-10: 1439878633.
- Cotte M, Pouyet E, Salomé M, Rivard C, Nolf WD, Castillo-Michel H, Fabris T et al (2017), The ID21 X-ray and infrared microscopy beamline at the ESRF: status and recent applications to artistic materials. *J. Anal. At. Spectrom.* 32: 477-493. <https://doi.org/10.1039/C6JA00356G>
- Diamond synchrotron website, <https://www.diamond.ac.uk/Instruments/Techniques/Imaging/XRF.html>
- Farges F, Lefrère Y, Rossano S, Berthereau A, Calas G, Brown Jr. GE (2004), The effect of redox state on the local structural environment of iron in silicate glasses: a combined XAFS spectroscopy, molecular dynamics, and bond valence study, *J. Non-Cryst. Solids*, 344(3): 176–188. <https://doi.org/10.1016/j.jnoncrysol.2004.07.050>
- Fauth F, Peral I, Popescu C, Knapp M (2013), The new material science powder diffraction beamline at ALBA synchrotron, *Powder Diffr.* 28(S2): S360–S370. <https://doi.org/10.1017/S0885715613000900>
- Fiege A, Ruprecht P, Simon AC, Bell AS, Göttlicher J, Newville M, Lanzirotti T, Moore G (2017), Calibration of Fe XANES for high precision determination of Fe oxidation state in glasses: Comparison of new and existing results obtained at different synchrotron radiation sources, *Am. Mineral.* 102: 369–380. <https://doi.org/10.2138/am-2017-E102410>
- Fleet ME, Liu XY, Harmer SL and King PL (2005), Sulfur K- edge XANES spectroscopy: chemical state and content of sulfur in silicate glasses. *Can. Mineral.* 43: 1605-1618. <https://doi.org/10.2113/gscanmin.43.5.1605>

- Gratuze B, Blet-Lemarquand J, Barrandon JN (2001), Mass Spectrometry with laser sampling: A new tool to characterize Archaeological materials, *J. Radioanal. Nucl. Chem.* 247: 645–656.
<https://doi.org/10.1023/A:1010623703423>
- ICCD. web site of the International Centre for Diffraction Data. <https://www.icdd.com/>
- Jones E, Oliphant T, Peterson P and others (2001), SciPy: Open Source Scientific Tools for Python. Curve_fit. https://docs.scipy.org/doc/scipy/reference/generated/scipy.optimize.curve_fit.html
- Jugo PJ, Wilke M, Botcharnikov RE (2010), Sulfur K-edge XANES analysis of natural and synthetic basaltic glasses: Implications for S speciation and S content as function of oxygen fugacity, *Geochim. Cosmochim. Acta*, 74(20): 5926-5938. <https://doi.org/10.1016/j.gca.2010.07.022>
- Knipping JL, Behrens H, Wilke M, Goettlicher J, Stabile P (2015), Effect of oxygen fugacity on the coordination and oxidation state of iron in alkali bearing silicate melts, *Chem. Geol.* 411 C:143–154. <https://doi.org/10.1016/j.chemgeo.2015.07.004>
- Liu ZL, Handa K, Kaibuchi K, Tanaka Y, Kawai J (2004), Comparison of the Sn L edge X-ray absorption spectra and the corresponding electronic structure in Sn, SnO, and SnO₂. *J. Electron Spectrosc. Relat. Phenom.* 135: 155–158. <https://doi.org/10.1016/j.elspec.2004.03.002>
- Llovet X, Moy A, Pinard PT, Fournelle JH (2021). Electron probe microanalysis: A review of recent developments and applications in materials science and engineering. *Prog. Mater. Sci.*, 116: 100673. <https://doi.org/10.1016/j.pmatsci.2020.100673>
- Masai H, Ina T, Okumura S, Mibu K(2018), Validity of Valence Estimation of Dopants in Glasses using XANES Analysis, *Sci Rep.* 8: 415. <https://doi.org/10.1038/s41598-017-18847-0>
- Ravel B and M. Newville (2005), ATHENA, ARTEMIS, HEPHAESTUS: Data Analysis for X-Ray Absorption Spectroscopy Using IFEFFIT, *J. Synchrotron Radiat.* 12(4): 537-541. <https://doi.org/10.1107/S0909049505012719>
- Simonelli L, Marini C, Olszewski W, Ávila Pérez M, Ramanan N, Guilera G, Cuartero V & Klementiev K (2016), CLÆSS: The hard X-ray absorption beamline of the ALBA CELLS synchrotron, *Cogent Phys.* 3 1231987. <https://doi.org/10.1080/23311940.2016.1231987>
- Sole VA, Papillon P, Cotte M, Walter P, Susini J (2007), A multiplatform code for the analysis of energy-dispersive X-ray fluorescence spectra. *J. Spectrochim. Acta B: At. Spectrosc.* 62(1): 63-68. <https://doi.org/10.1016/j.sab.2006.12.002>
- Reed SJB (1993). *Electron Microprobe Analysis*, Cambridge Univ. Press, Cambridge.
- Vallcorba O and Rius J (2019), d2Dplot: 2D X-ray diffraction data processing and analysis for through-the-substrate microdiffraction, *J. Appl. Cryst.* 52: 478-484. <https://doi.org/10.1107/S160057671900219X>

Wilke M, Farges F, Petit PM, Brown GE, Martin F (2001), Oxidation state and coordination of Fe in minerals: An Fe K-XANES spectroscopic study, *Am. Mineral.* 86(5): 714-730. <https://doi.org/10.2138/am-2001-5-612>

Wilke M, Partzsch GM, Bernhardt R, Lattard D (2005), Determination of the iron oxidation state in basaltic glasses using XANES at the K-edge, *Chem. Geol.* 220: 143-161. <https://doi.org/10.1016/j.chemgeo.2005.03.004>

Chapter 3 Chinese yellow glazes

明清黄釉



Chapter 3 Chinese yellow glazes

3.1 Introduction

3.1.1 Historical background of the yellow glazes

Among the range of coloured glazes employed, yellow has a distinct historical precedence and bears considerable symbolic significance in China. Its usage dates back to the earlier periods and holds a paramount position in Chinese culture. This significance can be traced to "The Book of Changes" (周易 Zhou Yi), an ancient Chinese divination text, which has documented the association of yellow with good fortune since the West Zhou dynasty (11th-8th B.C.E). In alignment with the Chinese five elements theory, yellow is attributed to the element 'Earth', which holds a central position and commands the other four cardinal directions (represented by Gold, Wood, Water, and Fire, corresponding to West, East, North, and South, respectively). Notably, the phonetic representation of 'Yellow' in the Chinese language coincides with the phonetic rendering of 'Emperor' (皇 Huang). Hence, the colour yellow epitomizes both imperial and supreme authority, symbolizing the fundamental embodiment of royalty and hierarchical structure within Chinese feudal society.

Two distinct categories of Chinese yellow glaze can be identified: high-temperature lime glaze and low-temperature lead glaze. Iron is employed as the colorant in both cases. Unlike high lime glaze, which primarily incorporates minerals and wood ashes, lead glaze relies on the refined by-product of smelting. Consequently, the advent of low-temperature lead glaze in China occurred subsequent to the emergence of high-temperature lime glaze. Its origins can be traced back to the Warring States period (475-221 B.C.E) (Lang 2017), and it reached its zenith during the Han Dynasty (202 B.C.E-220 C.E).

High lead glazes offer numerous advantages compared to other compound glazes. They exhibit easier preparation and superior compatibility with the thermos-mechanical properties of the ceramic body. Moreover, high lead glazes possess higher density and refractive index, along with lower viscosity. Consequently, these glazes demonstrate enhanced resistance to cracking and chipping (Tite 1998), resulting in glaze finishes of superior quality characterized by transparency, brightness, and a smooth, uniform surface. During the Tang Dynasty, in addition to Tang sancai (**Figure 3.1A**), lead glaze found application in architectural objects, with a broader range of colours including blue, yellow, red, and white (**Figure 3.1B**). Subsequently, the development of lead glazes continued, leading to the emergence of Song (960-1279) Sancai (tri-colour) and glazed tiles during the Yuan (1271-1368) and Ming (1368-1644) dynasties.



Figure 3.1. (A) Tang sancai (713-741), Palace Museum, <https://www.dpm.org.cn/collection/sculpture/234681.html>; (B) Glazed tile (Ming dynasty), Palace Museum, <https://www.dpm.org.cn/explore/building/236551.html>.

During the Ming Dynasty, the imperial court imposed stringent regulations regarding the usage of coloured glazes, particularly emphasizing the exclusive utilization of high lead yellow glazes in specific contexts. These occasions primarily encompassed ceremonial events held at the Temple of Earth and daily use within the imperial family. In order to fulfill the court's porcelain requirements and facilitate internal and external rewards and exchanges, the establishment of the Imperial kiln was set in Jingdezhen. The precise establishment date of the kiln is a subject of debate, with two viewpoints positing either c. 1369 or 1402. The primary objective of this endeavor was to establish a monopoly over the production of coloured glazes. Prior to the Ming dynasty, low-temperature glazes were predominantly applied to pottery bodies, resulting in weak adhesion of the glaze and yielding hues primarily ranging from yellow-brown to dark yellow. In the early Ming dynasty, the colour shifted towards orange, reflecting technological limitations at the time. However, during the Yongle era (1403-1424) and subsequent periods, high lead glazes began to be applied to porcelains, enabling the emergence of vibrant and brilliant yellow tones. Notably, the yellow glaze during the Xuande era (1426-1435) and Chenghua era (1465-1487) demonstrated exceptional delicacy and garnered the highest acclaim. Additionally, yellow glaze porcelain, referred to as "Jiao Huang" glaze (浇黄釉) in Chinese, acquired its name because the glaze was poured (Jiao) directly onto white-glazed porcelain or biscuit ware.

During the Qing dynasty, the use of yellow glaze became strictly regulated based on social status, eventually being prohibited for commoners. Following the decline of the Qing dynasty, the quality of yellow-glazed products witnessed a decline after the Qianlong era (1735-1796), and the Imperial kiln was temporarily halted and abandoned. However, through the marriage of Emperor Tongzhi (1856-1875), the Imperial kiln

was revived for the production of numerous sets of high-quality porcelain. The production of Imperial yellow at Jingdezhen concluded with China's last Manchu ruler, Pu Yi (1906-1967), who reigned as the Xuantong emperor from 1909 to 1912.

Extensive research has been conducted in the field of archaeometry regarding the high lead glaze, which has found widespread usage globally. Studies have encompassed various artifacts such as Tang Sancai ceramics, Han pottery, lead-glaze tiles, Islamic lead-glaze pottery, Roman lead glaze, as well as regional pottery types. Scholars like Cui et al. (Cui 2010) and Shen et al. (Shen 2019) have conducted analyses on ancient Tang Sancai ceramic compositions and lead isotope ratios, aiming to discern kiln production techniques and trace trading routes. Furthermore, investigations by scholars including Ting et al. (Ting 2019), Schibille et al. (Schibille 2020), Özçatal et al. (Özçatal 2014), and Holmqvist et al. (Holmqvist 2020) have provided valuable insights into the development of techniques, exchange activities, and cultural aspects through the analysis of Islamic lead glazes and regional lead-glazed potteries. Efforts have also been dedicated to exploring the composition and degradation mechanisms of lead glazes, as demonstrated by the works of Yin et al. (Yin 2020) and Zhang et al. (Zhang 1980). Additionally, scholars have engaged in discussions regarding the production of lead glazes, exploring the vitreous coating achieved through the application of glazing components onto unfired clay bodies or fired biscuit ware. This involves the use of a mixture of lead compounds and silica-rich materials, or solely the use of lead compounds. Contributions in this area have been made by researchers such as Gulmini et al. (Gulmini 2006) and Molera et al. (Molera 2001). In order to comprehend glaze structure, iron oxidation states, and coordination states, scholars like Yan et al. (Yan 2022) have conducted analyses on Tang Sancai lead glazes. Their findings suggest that iron ions in Sancai lead glazes primarily exhibit a tetrahedral coordination structure, characterized by isolated $[\text{Fe}^{3+}\text{O}_4]$ units, and the d-d absorption band of Fe^{3+} emerges as a key factor influencing the appearance of glaze colouration.

The examination of Imperial Yellow has predominantly focused on its historical significance, artistic appreciation, and its presence in the auction market, often lacking a scientific approach. However, in his master's thesis completed in 2007, Wu (Wu 2007) undertook a comprehensive and systematic analysis of low-temperature yellow lead glazes employed during the Ming and Qing dynasties. According to Wu, the yellow glaze was achieved through a secondary firing process conducted under an oxidation atmosphere at a temperature of approximately 760°C. The resulting yellow coloration was determined by the Fe_2O_3 content and the specific firing conditions. Furthermore, Zhang et al. (Zhang 1980) proposed that iron was incorporated into the high lead glazes in the form of ochre during the Ming and Qing dynasties.

3.1.2 Oxidation state and coordination of iron in glazes and glasses

Considerable knowledge has been acquired regarding the oxidation state of iron in alkali and alkali-earth glasses, and how this related to the colour of the glasses. The perception of colour in glasses is attributed to the selective absorption of specific wavelengths of visible light. Even at low levels of dopants or impurities, glasses can exhibit intense and broad charge transfer transitions from ligands (e.g., oxygen or

fluorine ions) to the metal ion ($L \rightarrow M$), resulting in strong absorption in the short-wavelength ultraviolet range (Möncke 2014; Fenstermacher 1980). The introduction of iron oxides into glasses and glazes establishes an equilibrium between ferric ion, Fe^{3+} , and ferrous ion, Fe^{2+} , in various coordination environments. Both Fe^{2+} and Fe^{3+} ions exhibit highly intense ultraviolet charge transfer bands (at approximately 208 nm and 263 nm, respectively), which are sufficiently influential to affect the visible range. Consequently, even trace amounts of iron impart a yellowish colour to the glass. In the visible range (see **Figure 3.2**), Fe^{3+} also demonstrates several absorption bands between approximately 370 nm and 500 nm, occurring in both tetrahedral and octahedral coordination, although V-fold coordination has also been proposed (Stoch 2014). Additional bands at 570 nm and 670 nm are attributed to the clustering of Fe^{2+} and Fe^{3+} ions, resulting in inter-valence charge transfer (IVCT) interactions. Furthermore, octahedrally coordinated Fe^{2+} ions exhibit two highly intense near-infrared (NIR) bands at 950 nm and 1330 nm, while tetrahedrally coordinated Fe^{2+} ions display two absorption bands in the infrared (IR) at 2000 nm and 2860 nm. The absorbance of Fe^{2+} ions in the near-infrared region is particularly significant, to the extent that even a small quantity can have a notable impact.

The ionic radius of Fe^{3+} , approximately 64pm, is very close to the boundary between IV- and VI-coordination, which occurs at around 60pm based on geometrical constraints. On the other hand, Fe^{2+} has an ionic radius of 74pm and this is further away from the dividing line between IV- and VI- coordination making it more likely to occur in octahedral VI-coordinated sites. It is worth noting that both trigonal bipyramid and square pyramid coordination ($CN=5$) are feasible arrangements (Burns 1993), the possibility of V-coordinated Fe-ions in glass has also been explored (Farges 2004, Rossano 1999). Consequently, it is well established that mixed coordination is expected in glasses (Uchino 2000, Hannoyer 1992, Fenstermacher 1980), although the tetrahedral coordination dominates for Fe^{3+} (Wong 1976) while for Fe^{2+} is the octahedral coordination as a network modifier (Mysen 1985, Hannoyer 1992).

Furthermore, it is notable that Fe^{3+} ions exhibit collective behaviour. In general, within alkali-alkali-earth glasses, the presence of Fe^{3+} imparts a yellow hue to the glazes, while the presence of Fe^{2+} imparts a blue coloration. However, it is crucial to acknowledge that the oxidation state and coordination of iron in a glass depend on the glass composition and the firing parameters, including temperature and atmosphere. Even under oxidizing conditions, both Fe^{2+} and Fe^{3+} coexist in the glass matrix. There is a possibility for Fe^{3+} to dissociate into Fe^{2+} and oxygen, although this phenomenon becomes significant only at very high temperatures (exceeding 1100°C) and extended firing durations.

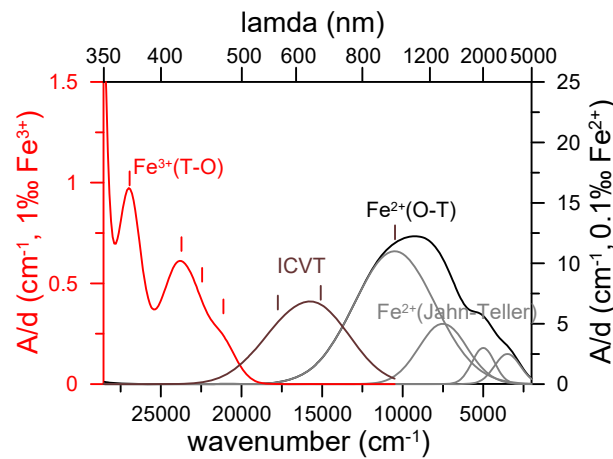


Figure 3.2. Absorbance of Fe ions. After (Bingham 2000).

The influence of oxygen fugacity on iron oxidation and the attainment of the yellow coloration has been observed (Wood 1999, Bingham 2000). Glazes fired in air and nitrogen predominantly exhibit Fe^{3+} state, whereas those fired under reducing atmospheres primarily consist of Fe^{2+} with a small amount of Fe^{3+} (Wakamatsu 1987). The partial pressure of oxygen, $P_{(\text{O}_2)}$, also exerts a significant influence on the redox state. Thermodynamically, higher temperatures tend to promote iron reduction (Schreiber 1986). The addition of network modifier cations, such as calcium, sodium, and potassium, leads to an increase in the $\text{Fe}^{3+}/\text{Fe}^{2+}$ ratio, with the influence of network modifier cations on the ferric/ferrous ratio following the order $\text{Ca} < \text{Na} < \text{K}$ (Borisov 2017). Redox reactions are also strongly affected by glass basicity. The oxidised Fe^{3+} state is favoured as the optical basicity of the glass increases. (Duffy 1993) The impact of viscosity on redox is argued to be minimal compared to the effect of chemical composition (Densem 1938). The study done by Bingham (Bingham 2000) shows that the $\text{Fe}^{2+}/\sum\text{Fe}$ redox ratio is unaffected by iron content but is inversely proportional to the ratio of alkali/alkaline earth ionic radii. The coordination of Fe^{2+} and Fe^{3+} ions is influenced by Fe_2O_3 content, and this accompanied clustering. Increasing Fe_2O_3 content results in an increase in the tetrahedral/octahedral ratio, particularly for Fe^{3+} ions compared to Fe^{2+} ions (Bingham 2000). In soda-lime-silicate glasses, Fe^{3+} is in both tetrahedral and octahedral coordination, and the proportion of octahedral Fe^{3+} decreases with increasing amounts of Fe^{3+} in glasses containing the same total iron. (Hannoyer 1992)

In conclusion, under oxidising conditions

- Fe^{2+} can be as high as 30% of the total iron for alkali and alkali-earth glasses containing trace amounts of iron. Increasing Fe content of the glasses the Fe^{2+} content is reduced. Above 3-4 mol% Fe_2O_3 in the glass the Fe^{2+} is reduced to 8% of the total iron.

- Increasing the alkali content of the glasses, the colour changes from yellowish-green to brown, although more than 90% of the iron is present as Fe^{3+} . This colour shift is associated to the red shift of the glass UV edge. This should be related to a change in the Fe^{3+} bond from tetrahedral to octahedral coordination.

- The presence of Fe^{3+} in the glass may be increased adding some elements such as Mn^{4+} , As^{5+} and Sb^{5+} and also Na_2SO_4 which act as oxidising agents to iron.

-The most convincing structural hypothesis is that only alkali cations stabilize tetrahedral Fe^{3+} ions, and their ability to do so increases linearly with increasing ionic radius or oxide basicity and with decreasing cation field strength. The ability of alkaline earth cations to inhibit or oppose this also varies linearly in the same way. (Bingham 2007)

- Fe^{3+} ions exist mainly in tetrahedral sites and the Fe^{3+} -O distance is approximately 1.89 Å. The octahedral Fe^{3+} -O distance is approximately 2.18 Å.

-The Jahn-Teller effect causes broadening and asymmetry of absorption bands, due to distortions of coordination polyhedral from regular symmetry.

Limited studies have been conducted on the structure and optical properties of lead silicate glasses. Lead oxide (PbO) possesses distinctive characteristics that profoundly influence glass structure, attributed to the high polarizability and relatively low field strengths of Pb cations compared to conventional glass formers like SiO_2 (Rao 2012). Various spectroscopic techniques, including NMR, EXAFS, FTIR, and Raman spectroscopy, have been employed in numerous studies (Fayon 1999, Dupree 1987), revealing two distinct roles of lead. At lower concentrations of lead oxide, lead functions as a modifier which is similar to alkali or alkaline earth elements, while at higher concentrations, it acts as a network former. In cases of high Pb^{2+} content, polarization-induced electron cloud distortion causes positional movement of eight oxygen ions, with four approaching Pb^{2+} . Consequently, Pb^{2+} exhibits characteristics resembling a IV-coordinated ion, forming $[\text{PbO}_4]$ square pyramids, while VI-coordinated Pb^{2+} ions give rise to $[\text{PbO}_3]$ pyramids within the glass network. It also has been reported (Rybicki 2001) that the dominance of PbO_4 groups persists irrespective of PbO concentration, and the coexistence of PbO_4 groups and PbO_3 pyramids is possible at low concentrations, indicating the presence of two types of Pb-O bonds. The first type is covalent and associated with network-forming behavior, while the second type is ionic and associated with network-modifying behavior. In other words, the Pb-O bond is believed to be predominantly ionic at lower PbO content and gradually shift towards covalent bonding at higher PbO concentrations (Khalil 2010).

Efforts to characterize the molecular structure of lead silicate glass have been actively pursued, but this subject remains contentious, particularly when lead content exceeds 70% by weight, leading to discontinuity within the silicate structural network (Rybicki 2001, Fayon 1999). In heavy lead glasses, transition metals exhibit more vibrant colours compared to ordinary lead-free glasses, owing to the influence of the PbO bond within the glass structure (Weyl 1951). Even trace amounts of iron can impart colour to lead glasses. As the temperature rises in heavy lead glasses, the glass colour tends to become browner due to the thermal dissociation of lead silicate into unbonded lead oxide (Hampton 1946). Moreover, due to their high vapor pressure, lead compounds are prone to volatilization, leading to firing temperatures not exceeding approximately 800-1000°C, which also impacts the iron oxidation state, glass structure, so influences coloration. In the early studies of lead glass, the yellow coloration was attributed to impurities from Fe^{3+} or SiO_2 microcrystals (Cohen 1973). Hampton (Hampton 1946) and Stroud (Stroud 1971) successfully prepared colourless lead glasses using high-purity reagents in thoria and high-purity ceramic crucibles, respectively. Baiocchi's experiments (Baiocchi 1981) demonstrated that the Fe^{3+} ion

spectrum could be explained in terms of double coordination of Fe^{3+} ions as FeO_4 and FeO_6 centres in lead silicate glasses with a composition of 37.9 mol% PbO , 0.3 mol% PbO_2 , and 61.8 mol% SiO_2 , incorporating all first-row transition metals under air at 1200°C , similar to the silicate melt system. Iron-doped lead silicate glasses also exhibit absorption related to the Fe^{2+} ion content, indicating Fe^{2+} - Fe^{3+} interaction involving charge transfer through O^{2-} ions (Ookawa 1997). The content of Fe and Pb has also been studied, confirming their effect on the width of the D-d band (Yan 2022). However, the study of single-doped iron colorants in lead silicate melts is scarce and requires further detailed investigation.

In addition to glasses, the coloration of glazes also involves the presence or addition of transition metals. However, the interaction between the glaze and the ceramic body modifies the composition of the glaze and can introduce colouring elements such as iron, manganese or titanium cations. Moreover, the inherent colour of ceramic bodies, such as greyish, reddish, or creamy tones, can manifest through transparent glazes, potentially compromising the desired aesthetic effect of the glaze (Pradell 2020). Therefore, it is crucial to consider various factors that contribute to the yellow coloration of glazes. Mössbauer spectroscopy is a highly effective analytical technique for determining the oxidation state of iron. However, its application to glazes is impeded by the significant absorption of lead content, rendering it impractical. UV-VIS-NIR spectroscopy and X-ray Absorption Fine Structure (XAFS) spectroscopy, on the other hand, offer powerful methods for investigating the optical properties of glazes and exploring the atomic-scale microstructure near iron ions. Consequently, these analytical techniques offer valuable insights into the technological aspects underlying the production methods employed for ancient high lead yellow glazes.

3.2 Objective

Ancient imperial yellow high lead glazes and some replicas are subjected to a comprehensive investigation using optical absorption spectroscopy (UV-VIS-NIR), Scanning Electron Microscopy - Energy Dispersive X-ray spectroscopy (SEM-EDX), and X-ray absorption fine structure (XAFS). The primary objective is to explore the various factors influencing the colouration of these glazes and differences in the manufacturing (materials, firing temperature, atmosphere) and of the glazes from different periods. The analysed ancient imperial yellow samples, originating from the 16th to the 20th century and associated with the Chinese imperial family, encompass fragments from different dynasties, thereby representing diverse manufacturing processes. By evaluating colour coordinates within the CIE Lab colour space, glaze composition, iron redox ratios, and coordination geometry, we establish correlations with the atmospheric conditions, glaze layer thickness, firing temperatures, and structural characteristics, elucidating the changes in the materials and methods of production.

In addition, some replicas of the Ming and Qing samples were made to investigate some of unsolved inquiries regarding iron in high lead glazes:

- 1- Do yellow high lead glazes contain Fe^{2+} ? Does its presence affect the colour of the glaze?
- 2- Little is known about iron in lead glasses. Is there a change in the coordination of Fe^{2+} and Fe^{3+} in a high lead glass?

- 3- How the firing temperature affect the oxidation state of iron in a high lead glass?
- 4- How the oxygen deficient atmosphere affects the oxidation state of iron in a high lead glass?
- 5- The presence of a transparent glaze or a porcelain background modifies the composition of the lead glazes. How this influences the colour of the yellow glazes?
- 6- Which is the effect of the thickness of the glaze in its colour?

3.3 Materials

3.3.1 Historical materials

The fragments of monochrome-glazed porcelain are supported by School of Archaeology of University of Oxford, comprises specimens with provenance tracing back to the imperial family of ancient China.

These bowls and dishes were collected by the late Professor Edward Hall (1924-2001) physicist, inventor, and founding-director of the RLAHA from 1955 until his retirement in 1989. Professor Hall had a private collection of Chinese monochrome-glazed porcelains, a large part of which were sold at Christie's in 2004.

The bowls are in a broken state (mostly large pieces) after the shelf on which they were displayed in Professor Hall's office in Keble Road collapsed sometimes in the late 1970s. (Confirmed by Prof. Mark Pollard.) Professor Hall gave the bowls, together with a few other Chinese monochromes and polychrome glazed porcelain sherds from the same accident, to the RLAHA for study (confirmed by Prof. Mark Pollard). Over the years body-analyses of the bowls have been used in many RLAHA papers: eg. Wood 1983(Wood 1983); Hatcher, Tregear and Wood 1985 (Hatcher 1985); Pollard and Wood 1986 (Pollard 1986) and Hall and Pollard 1986 (Hall 1986); Wood 2021(Wood 2021), as well as in Wen Rui's DPhil (Wen 2012). thesis on variations in Chinese cobalt-blue ceramic pigments.

These fragments span from the Zhengde period (1506-1521) in the Ming dynasty to the Xuanton period (1909-1912) in the Qing dynasty. Ten imperial yellow glazes were studied and the details are listed in **Table 3.1, Figure 3.3 and Figure 3.4.**

Table 3.1. Historical sample details.

Dynasty	Period	Object	Description	Sample No.	Part
Ming	Zhengde (1506-1521)	ETH12	dish	ETH12A	rim
				ETH12B	foot
		ETH15	dish	ETH15A	rim
				ETH15B	foot
	Jiajing (1522-1566)	ETH13	dish	ETH13A	foot
				ETH13B	rim
Qing	Kangxi (1662-1722)	ETH1	bowl	ETH1B	foot
				ETH2	foot
				ETH3	foot
				ETH4B	foot
				ETH4C	rim
	Yongzheng (1723-1735)	ETH10	dish	ETH10A	base
				ETH10B	base
	Xuantong (1909-1912)	ETH5	bowl	ETH5A	rim
				ETH5B	base
		ETH6	bowl	ETH6A	rim
				ETH6B	foot

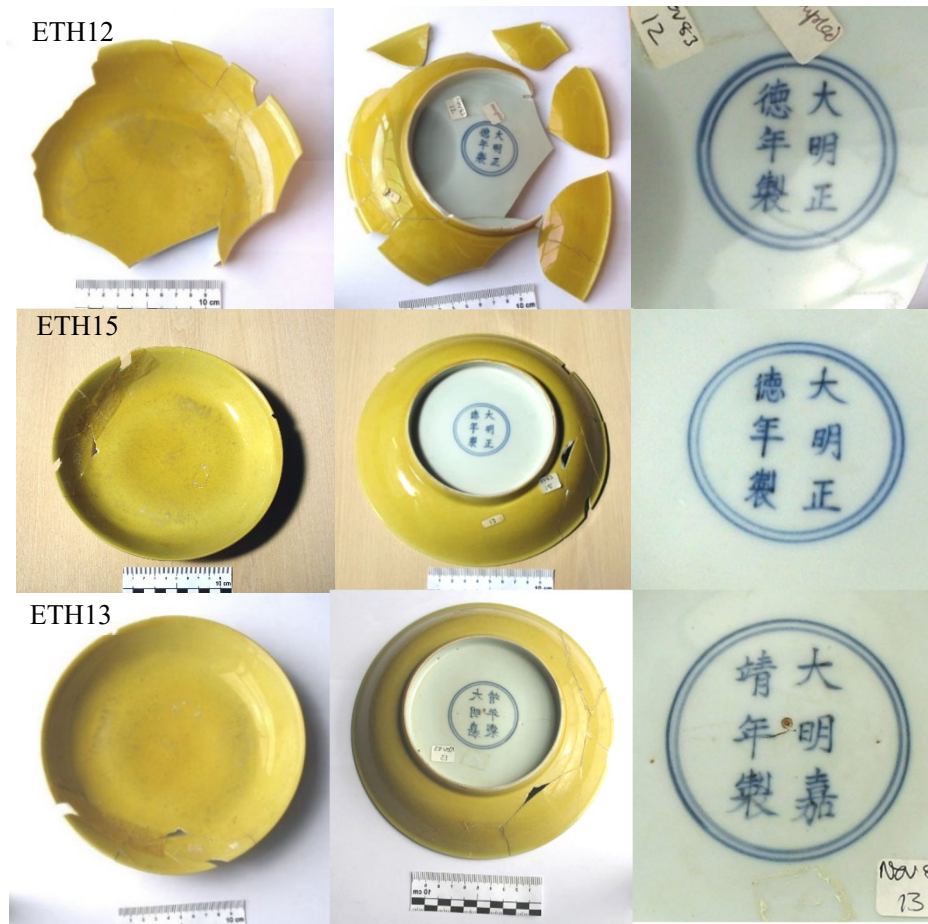


Figure 3.3. The Ming samples.

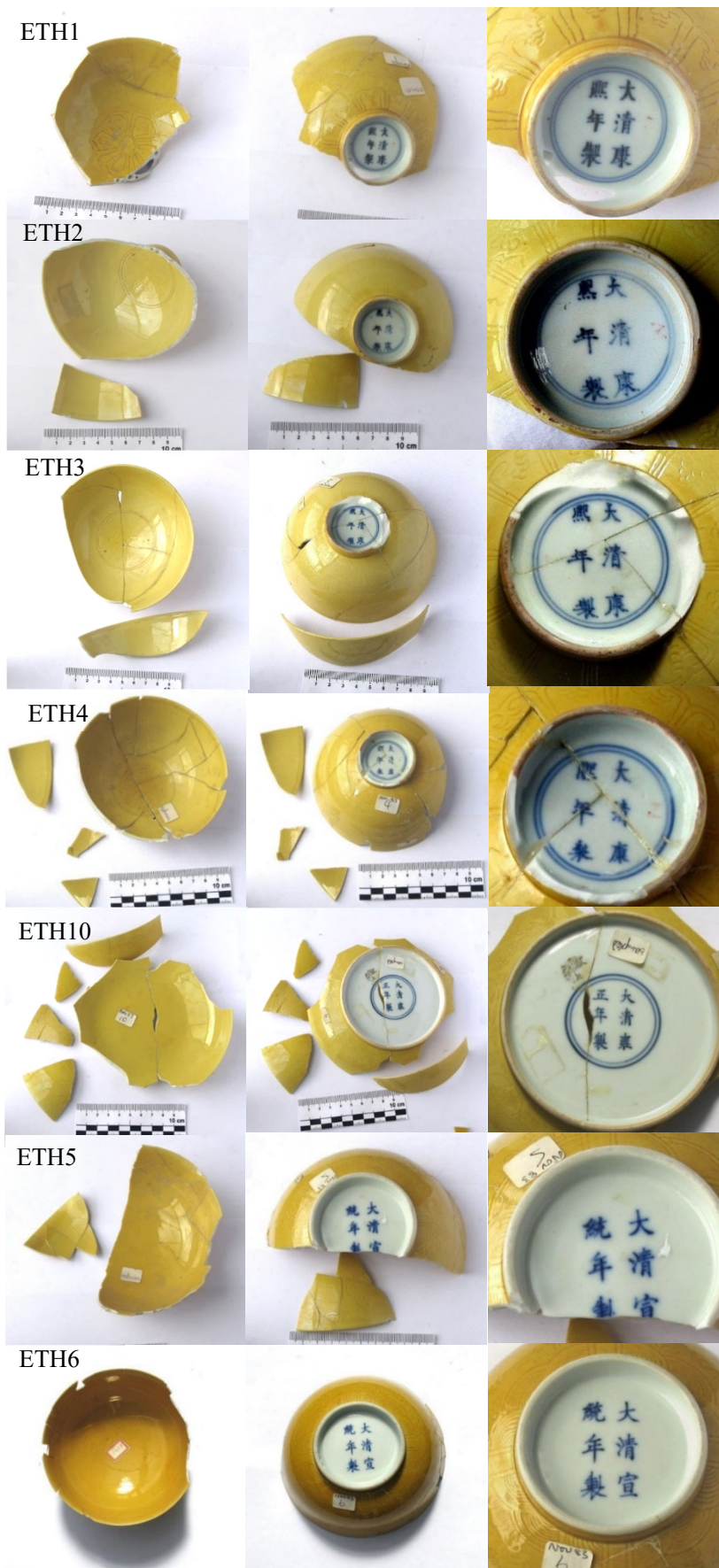


Figure 3.4. The Qing samples.

3.3.2 Replicated yellow glazes

Yellow glazes were synthesized using two distinct techniques observed in historical porcelain production: direct application of glaze onto the porcelain surface, and application of glaze over a transparent glaze layer. For the Ming-like yellow glazes, a high lead glaze composition (70% PbO, 30% SiO₂) was employed, with the addition of 4% Fe₂O₃ (referred to as M(Y)). This glaze was applied over two selected transparent glaze compositions: one with a high CaO content (designated as T1), and the other with a low CaO content (designated as T2). The Kangxi-like yellow glazes, on the other hand, were directly applied onto the porcelain surface (designated as P), utilizing a high lead glaze with 3% K₂O, 4% Al₂O₃, and 4% Fe₂O₃ (referred to as K(Y)). The specific compositions of the glazes and the Kangxi porcelain are presented in **Table 3.2**.

Table 3.2. Composition of the colourless (T1, T2) glaze and porcelain (P) and yellow Ming, M(Y) and Kangxi, K(Y) glazes.

		K ₂ O	Na ₂ O	CaO	Al ₂ O ₃	SiO ₂	PbO	Fe ₂ O ₃
Colourless glaze	T1	0	6	4	16	74		
	T2	0	5	18	14	63		
ground Porcelain body	P	3	2	1	26	68		
	M(Y)					29	67	4
yellow glaze	K(Y)	3	0	0	4	26	64	3

Yellow glazes were experimentally applied onto porcelain plaquettes using varying thicknesses achieved by applying multiple layers of the raw glaze. Furthermore, the glazes were fired at different temperatures ranging from 900°C to 1100°C. It was observed that at firing temperatures of 900°C and 950°C, the glazes exhibited scattered crimson-coloured spots indicative of undissolved Fe₂O₃. However, as the firing temperature increased, the glazes displayed a homogeneous appearance without any noticeable colour variations or undissolved particles.

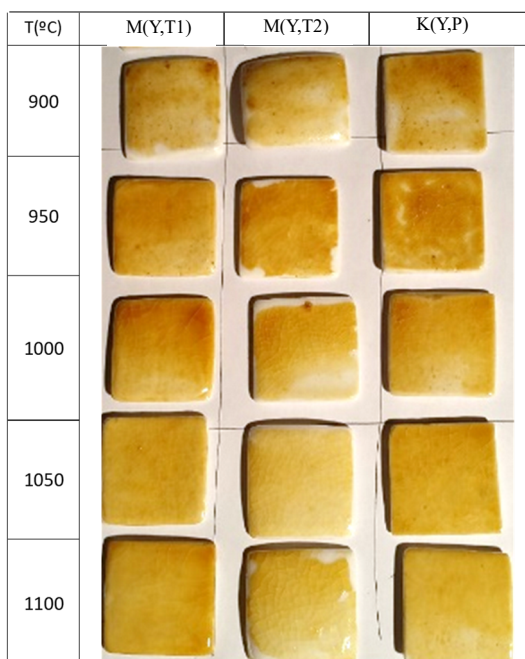


Figure 3.5. Glazes fired in air after **Table 3.2**.

To investigate the impact of firing atmosphere and temperature on the iron oxidation state and resultant colour in glass, a series of glass samples were prepared at varying firing temperatures (950-1000-1100°C) using an alumina crucible. Due to the unfavourable outcome associated with highly reducing conditions, wherein lead tends to be reduced to the metallic state and volatilize, only two gases, air and nitrogen (N₂), were employed. The glass composition consisted of a mixture of quartz (SiO₂) and lead oxide (PbO) in a ratio that approximated a near eutectic composition of 70%PbO and 30%SiO₂. Additionally, 3%FeO was added to the raw mixture. The prepared mixtures were subjected to firing in an alumina crucible under a gas flow rate of 50 ml/min, utilizing either dry air or N₂. The heating process involved a rate of 20K/min from room temperature (RT) to 400°C, followed by a rate of 5K/min from 400°C to the designated maximum temperature (950 °C /1000 °C /1100 °C), which was maintained for a duration of 1 hour. Subsequently, the glasses were gradually cooled to 400°C at a cooling rate of 10K/min, followed by further cooling from 400°C to RT at a rate of 20K/min.

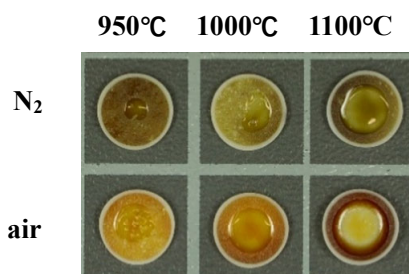


Figure 3.6. Replicated samples under different temperatures and atmosphere.

3.4 Results

3.4.1 Historical materials

Some interesting differences are found between the early Ming dynasty porcelains and later Qing dynasty porcelains. The Ming yellow glazes are applied over a transparent glaze which in its turn is applied over the porcelain; on the contrary the Qing yellow glazes were applied directly over the porcelain (**Figure 3.7**). The bases of bowls and dishes were in both cases glazed with a transparent glaze over the reign mark painted in blue as shown in **Figure 3.3** and **Figure 3.4**.

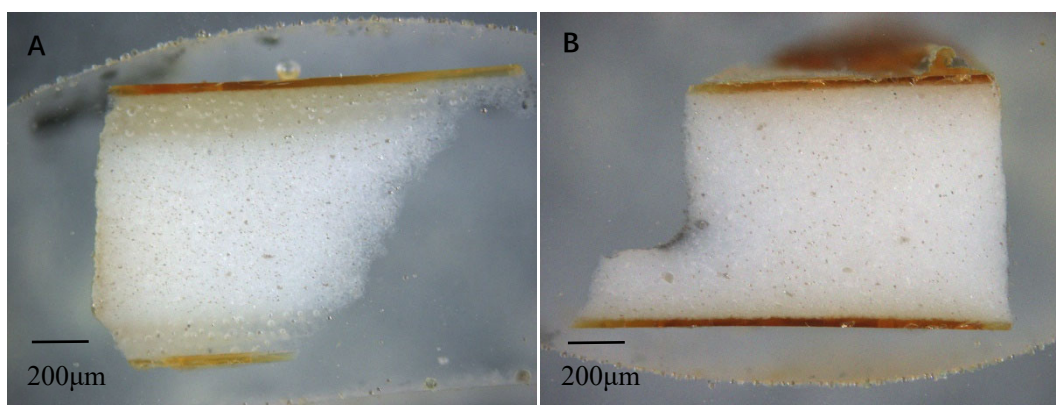


Figure 3.7. Dark field reflection optical microscope image of (A) ETH12A (Ming dynasty); (B) ETH6A (Qing dynasty).

Composition analysis of body

The total varied between 98-99% (indicative of the high vitrification of the bodies), and the total amount is normalized to 100wt% given in **Table 3.3**.

Table 3.3. The body analysis of the Imperial samples.

dynasty	mark	sample	fragment	Na ₂ O	Al ₂ O ₃	SiO ₂	K ₂ O	CaO	FeO	SiO ₂ /Al ₂ O ₃	
Ming	Zhengde (1506-1521)	dish	ETH12A	rim	1.20	17.07	77.73	2.94	0.19	0.88	4.6
			ETH12B	foot	0.81	12.91	82.44	2.65	0.35	0.84	6.4
		dish	ETH15A	rim	0.84	16.80	78.80	2.77	0.15	0.64	4.7
			ETH15B	foot	0.90	19.39	75.14	3.60	0.00	0.97	3.9
	Jiajing (1522-1566)	dish	ETH13B	rim	1.42	19.64	75.05	3.05	0.12	0.72	3.8
			ETH13A	foot	1.54	20.91	72.87	3.61	0.17	0.89	3.5
Kangxi (1662-1722)	bowl	ETH1B	foot	1.97	25.88	67.61	2.99	0.52	1.03	2.6	
		ETH2B	foot	1.44	23.08	71.56	2.91	0.15	0.86	3.1	
	bowl	ETH3	foot	1.57	25.53	68.90	3.00	0.15	0.85	2.7	
	bowl	ETH4C	rim	1.93	28.73	65.42	2.74	0.30	0.87	2.3	
		ETH4B	foot	1.51	26.61	68.29	2.45	0.27	0.87	2.6	
	Qing (1723-1735)	Yongzheng (1723-1735)	dish	ETH10A	Base/inside	1.51	25.99	68.19	3.33	0.52	0.46
Xuantong (1909-1912)			bowl	ETH5A	rim	2.45	22.68	70.41	3.32	0.19	0.95
			ETH5B	Base/inside	2.14	22.57	70.80	3.46	0.21	0.81	3.1
		bowl	ETH6A	rim	2.24	24.43	68.42	3.63	0.16	1.13	2.8
			ETH6B	foot	2.10	24.57	69.03	3.28	0.06	0.96	2.8

Table 3.3 provides insights into the composition of major and minor elements, such as Na, Al, Si, K, Ca, and Fe, present in the porcelain body. These findings reveal notable variations across different dynasties. Specifically, the imperial samples from the Ming dynasty exhibited SiO₂ content ranging from 72wt% to 83wt%, Al₂O₃ content between 12% and 21%, and a SiO₂/Al₂O₃ ratio spanning from 3.5 to 6.4. In contrast, the Qing dynasty samples displayed SiO₂ content ranging from 65% to 72%, Al₂O₃ content between 22% and 29%, and a SiO₂/Al₂O₃ ratio ranging from 2.2 to 3.2.

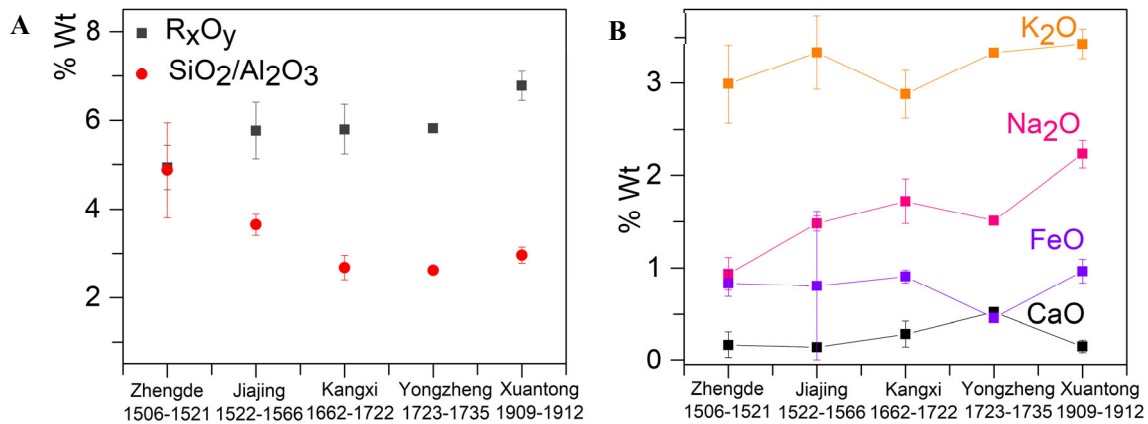


Figure 3.8. (A) The content of R_xO_y (Wt%), the ratio of SiO₂/Al₂O₃, (Fluxes in the glaze including Na₂O, K₂O, CaO and FeO are merged into R_xO_y.); (B) and content of CaO, FeO, Na₂O, K₂O of the body in the different periods.

Figure 3.8A displays a decreasing trend in the $\text{SiO}_2/\text{Al}_2\text{O}_3$ ratio over time, while the fluxes in the bodies exhibit opposite changes. **Figure 3.8B** reveals the addition of different fluxes, with the CaO content below 0.6%. Interestingly, CaO content increases from the Ming dynasty to the Qing dynasty but decreases again in the Xuanton era (1909-1912). This suggests the possibility of either reduced amounts of calcareous materials being added or the presence of CaO associated with major clay ingredients rather than being separately added. Among the fluxes, K_2O exhibits the highest content, averaging around 3%, which remains consistent. Additionally, the Na_2O content in the Ming dynasty is lower than in the Qing dynasty. The FeO content of all samples remains below 1.2wt%, with no significant changes from the Ming to Qing dynasties, except for the Yongzheng era, indicating careful selection of raw materials.

Previous studies have indicated that the $\text{SiO}_2/\text{Al}_2\text{O}_3$ ratio in raw materials can be influenced by source variations, formulation changes, or washing processes (Yin 2011). Moreover, the degree of weathering of porcelain clay can also contribute to variations in SiO_2 and Al_2O_3 contents, suggesting that the depth of porcelain clay extraction has an impact on the $\text{SiO}_2/\text{Al}_2\text{O}_3$ ratio in the ceramic body. The incorporation of porcelain stone as a raw material marks a significant innovation in Chinese porcelain production. Porcelain stone, primarily composed of quartz and sericite, is abundant in the southern regions of China and has played a vital role in the creation of distinct highly siliceous southern Chinese wares (Guo 1987). Investigations conducted on porcelain stone in Jingdezhen have revealed a $\text{SiO}_2/\text{Al}_2\text{O}_3$ ratio ranging from 4.2 to 5 (Wood 2021), surpassing the ratio observed in most imperial samples depicted in **Figure 3.8A**. Scholarly works propose that since the Yuan dynasty (1271-1368 AD), a combination of porcelain stone and kaolin has been utilized in the production of the porcelain body (Guo 1987). The $\text{SiO}_2/\text{Al}_2\text{O}_3$ wt% concentration ratio of pure kaolinite is 1.2:1 (Tite 2012). By comparing our data, it becomes evident that the porcelain bodies consist of a blend of kaolinite and porcelain stone. Our findings strongly support the hypothesis that the increased incorporation of kaolin in the Qing porcelain bodies, as previously classified by N. Wood (Wood 2021), enables them to withstand higher firing temperatures compared to Ming porcelains. Furthermore, the increased addition of kaolin in the Qing samples is accompanied by a corresponding rise in the use of flux agents. In contrast, the Ming porcelains predominantly employed micaceous flux agents, with comparatively lower content of albite (Wood 2021).

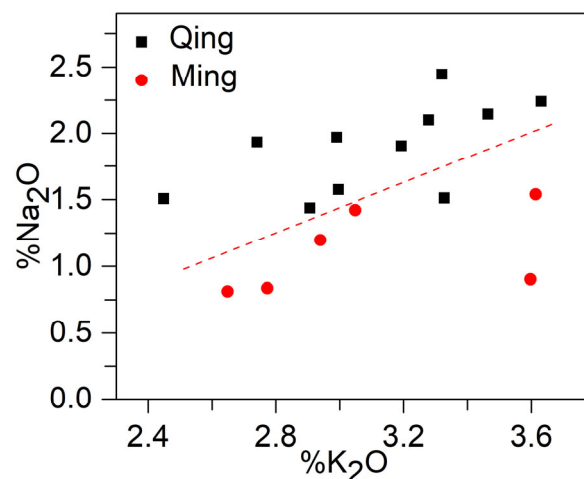


Figure 3.9. The comparison of the content of K_2O and Na_2O of the body.

The K₂O and Na₂O contents show a positive correlation (**Figure 3.9**), suggesting a common origin from the raw materials used. Generally speaking, micaceous rocks are the main source of potassium, while albite-rich rocks are the main source of sodium.

Composition of the transparent glazes

Table 3.4 shows the major chemical composition of the transparent glazes measured by Microprobe.

Table 3.4. Transparent glaze composition of the Imperial samples. Microprobe data (major elements, wt%).

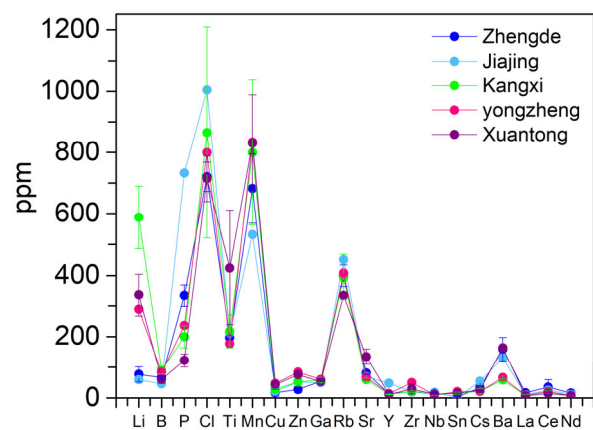
dynasty	mark	sample	fragment	Na ₂ O	MgO	Al ₂ O ₃	SiO ₂	K ₂ O	CaO	MnO	FeO	PbO	
Ming	Zhengde (1506-1521)	dish	ETH12A	rim	2.94	0.25	16.70	69.31	4.85	4.29	0.10	0.89	0.01
			ETH12B	foot	2.07	0.28	15.84	71.19	4.86	4.10	0.08	1.04	0.04
		dish	ETH15A	rim	2.40	0.23	14.39	73.80	5.64	1.98	0.12	0.98	0.03
			ETH15B	foot	1.73	0.38	15.04	71.31	5.86	3.91	0.12	1.17	0.01
	(1522-1566)	Jiajing	ETH13B	rim	3.11	0.19	17.62	69.00	4.74	3.97	0.07	0.93	0.04
		dish	ETH13A	foot	2.41	0.47	15.84	70.06	4.99	3.97	0.12	1.70	0.06
Qing	Kangxi (1662-1722)	bowl	ETH1B	foot	2.85	0.28	14.89	71.43	3.59	5.79	0.10	0.82	0.07
		bowl	ETH2B	foot	2.57	0.31	16.17	71.65	3.85	3.78	0.15	1.28	0.02
		bowl	ETH3	foot	2.42	0.31	16.52	69.75	3.01	6.70	0.13	0.91	0.01
		bowl	ETH4B	foot	2.23	0.31	13.05	74.46	3.59	5.43	0.09	0.66	0.01
	Yongzheng (1723-1735)	dish	ETH10A	Base/inside	1.72	0.46	14.86	71.33	3.88	6.32	0.16	1.04	0.03
(1909-1912)	Xuantong	bowl	ETH5B	Base/inside	2.72	0.36	16.50	71.20	3.96	3.67	0.19	1.11	0.02
		bowl	ETH6B	foot	2.56	0.28	19.82	66.73	2.79	6.96	0.10	0.62	0.00

The transparent lime glazes exhibit remarkable similarity, with SiO₂/Al₂O₃ ratios ranging from 3.1% to 5.7%, and combined CaO+Na₂O+K₂O content between 10.0% and 13.7% with MgO content below 0.5% and about 0.1% of MnO. The maturing temperature (defined as log(v(Pa·s)) = 3) of the transparent glazes considering a composition, 72% SiO₂, 16% Al₂O₃, 3% Na₂O, 4% K₂O, 4% CaO, 1% FeO, is 1342°C. (Fluegel 2007).

The trace element analysis was conducted using LA-ICP-MS, and the corresponding data is presented in **Table 3.5** and **Figure 3.10**. The presence of impurities in significant quantities is likely attributed to the utilization of natural raw materials. Notably, the Qing samples demonstrate elevated Li content and decreased P content compared to the Ming samples.

Table 3.5. LA-ICP-MS (trace elements; ppm) of the Transparent glazes of the Imperial sample.

dynasty	mark	sample	fragment	Li	B	P	Cl	Ti	Mn	Cu	Zn	Ga	Rb	Sr	Y	Zr	Nb	Sn	Cs	Ba	La	Ce	Nd
Ming		ETH12A	rim	51	64	306	723	202	577	5	23	54	419	86	9	20	16	4	38	142	9	17	8
	Zhengde	ETH12B	foot	60	66	308	728	201	592	14	32	60	353	79	17	24	16	5	28	142	12	23	11
	(1506-1521)	ETH15A	rim	96	64	383	657	193	791	18	16	41	432	84	13	20	17	2	38	135	15	30	14
		ETH15B	foot	100	71	339	774	189	768	32	39	61	395	77	16	19	16	5	31	216	30	71	31
	Jiajing (1522-1566)	ETH13B	rim	59	46	733	1004	211	532	21	52	49	451	69	48	19	18	2	54	130	11	25	13
Qing		ETH1B	foot	454	86	168	701	144	623	31	63	54	341	54	13	18	9	17	16	58	8	18	7
	Kangxi	ETH2B	foot	694	77	181	1363	209	1061	25	67	65	491	59	13	20	9	19	33	61	9	19	8
	(1662-1722)	ETH3	foot	625	102	195	809	258	939	31	43	66	413	66	11	23	12	17	21	61	12	25	9
		ETH4B	foot	578	94	252	588	257	577	25	38	48	333	58	11	22	12	11	18	53	7	16	6
	Yongzheng (1723-1735)	ETH10	Base/outside	289	83	236	800	177	834	47	84	60	408	67	14	50	10	20	21	66	9	21	8
	Xuantong (1909-1912)	ETH5B	Base/outside	287	69	137	767	293	942	39	70	59	333	152	16	41	12	15	26	165	6	13	6
	ETH6B	foot	384	51	107	661	556	719	47	81	47	335	117	7	18	13	16	26	162	7	16	8	

**Figure 3.10.** Trace element of transparent glazes in the different periods measured by LA-ICP-MS.

Composition of the yellow glazes

Table 3.6 shows the major chemical composition of the yellow glazes measured by Microprobe.

Table 3.6. Microprobe data of the Imperial yellow glazes (major elements, wt%).

dynasty	mark	sample	fragment	Thickness (μm)	Na ₂ O	Al ₂ O ₃	SiO ₂	K ₂ O	CaO	FeO	PbO		
Ming	Zhengde	dish	ETH12A	rim	90	0.42	2.43	34.1	0.45	0.53	3.28	58.6	
			ETH12B	foot	81	0.28	2.05	34.4	0.49	0.58	3.58	58.4	
	1506-1521	dish	ETH15A	rim	51	0.56	3.75	39.0	0.85	1.08	4.23	50.1	
			ETH15B	foot	23	0.45	5.06	43.0	1.28	1.1	3.73	45.0	
	1522-1566	Jiajing	dish	ETH13B	rim	54	0.92	7.90	48.3	1.62	1.59	3.10	36.2
				ETH13A	foot	36	0.72	4.24	43.6	1.01	1.41	3.73	44.9
Qing	Kangxi	bowl	ETH1A	rim	58	0.29	2.96	31.5	0.26	0.09	2.97	61.8	
			ETH1B	foot	181	0.27	1.98	34.0	0.25	0.15	4.06	59.1	
	1662-1722	bowl	ETH2B	foot	62	0.28	3.42	34.1	0.32	0.12	3.51	58.0	
			ETH3	foot	44	0.29	2.77	39.3	0.44	0.11	3.79	53.0	
		bowl	ETH4C	rim	44	0.32	4.50	33.9	0.32	0.2	2.65	57.9	
			ETH4B	foot	57	0.25	3.69	30.5	0.25	0.1	2.34	62.7	
	Yongzheng	dish	ETH10A	Base/inside	56	0.21	2.92	27.6	0.25	0.11	2.51	66.2	
	1723-1735		ETH5A	rim	76	0.70	5.88	29.8	0.44	0.09	2.21	60.7	
	Xuantong	bowl	ETH5B	Base/inside	62	0.57	5.27	27.2	0.38	0.09	2.03	64.2	
			ETH6A	rim	56	0.61	5.98	30.6	0.52	0.09	2.06	59.9	
1909-1912	bowl	ETH6B	foot	38	0.57	5.96	32.4	0.5	0.09	3.37	56.8		

The yellow glazes are essentially a high lead glaze to which about 3% of FeO has been added to impart the yellow colour.

One interesting aspect is the thickness of the glazes which has been measured accurately and we have observed:

- Ming dynasty: the yellow glaze of the **foot is thinner** than those of the rim. They are dishes
- Kangxi dynasty: the yellow glaze of the **foot is thicker** than those of the rim. They are bowls
- Yongzheng dynasty: we only had a fragment of the base (inside yellow glaze, outside white glaze). A dish.
- Xuantong dynasty: the yellow glaze of the **foot is thinner** than those of the rim. They are bowls

The observed variations in the glaze composition may be attributed to factors such as the positioning of the objects (upward or downward) and the specific glazing techniques employed during the drying and firing stages in the kiln. Three distinct glazing methods, namely pouring, blowing and painting, were utilized for the application of the coloured glazes (Zhang 1980).

Figure 3.11 illustrates several intriguing disparities in the glaze compositions. Notably, the PbO/SiO₂ ratio exhibits an increasing trend from the Ming to the Qing periods, whereas the FeO content experiences a slight decrease. The upward shift in PbO content implies a lower maturing temperature of the glaze. Ming

yellow glazes with PbO/SiO_2 between 1 and 1.5 (between $50\%\text{SiO}_2+50\%\text{PbO}$ and $40\%\text{SiO}_2+60\%\text{PbO}$) have maturing temperature (defined as $\log(v(\text{Pa}\cdot\text{s}) = 3)$) of 1092°C and 973°C while Kangshi, Yongzheng and Xuanton with $\text{PbO}/\text{SiO}_2 \approx 2$ ($33\%\text{SiO}_2+66\%\text{PbO}$) have a melting temperature of 885°C (Fluegel 2007).

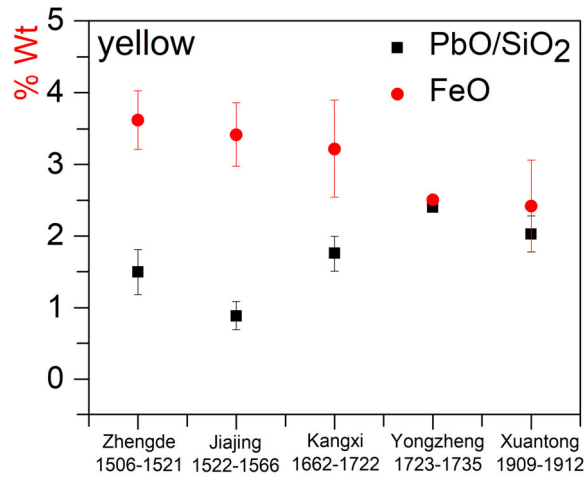


Figure 3.11. PbO/SiO_2 ratio and FeO content (Wt%) of the different periods.

The existence of additional elements beyond the primary glaze raw materials (PbO , SiO_2 , and FeO) is depicted in the triangular representation illustrated in Figure 3.12. A notable distinction emerges in terms of the Ming glazes having a higher CaO content and a lower Al_2O_3 content, while the Qing glazes exhibit higher Al_2O_3 levels. These disparities primarily stem from the incorporation of elements originating from the porcelain in the case of Qing glazes, and from the transparent glaze in the case of Ming glazes. The occurrence of inter-diffusion between the glazes and glaze-porcelain composite relies on the specific firing duration and temperature.

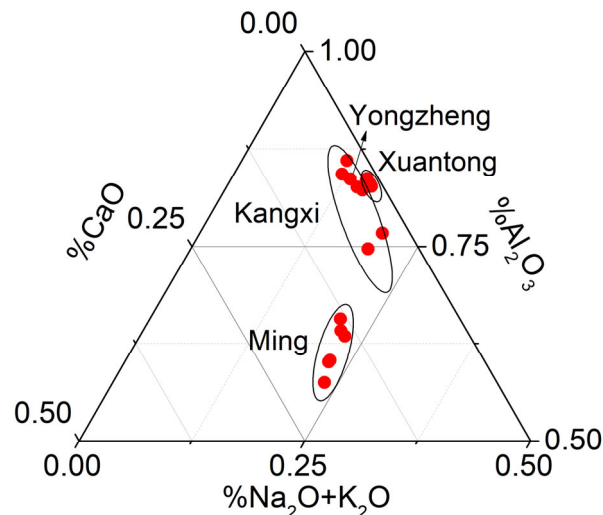


Figure 3.12. $\text{CaO}-\text{Al}_2\text{O}_3-\text{Na}_2\text{O}+\text{K}_2\text{O}$ triangular plot of the yellow glazes.

Divergent Na_2O and K_2O compositions can also be observed, as depicted in Figure 3.13, highlighting distinct correlations between these two elements within both Qing and Ming glazes. They are related to the

differences in the CaO, Na₂O, and K₂O contents on the porcelain bodies for the Qing samples and of the transparent glaze for the Ming samples as shown in **Figure 3.15** and **Figure 3.16**.

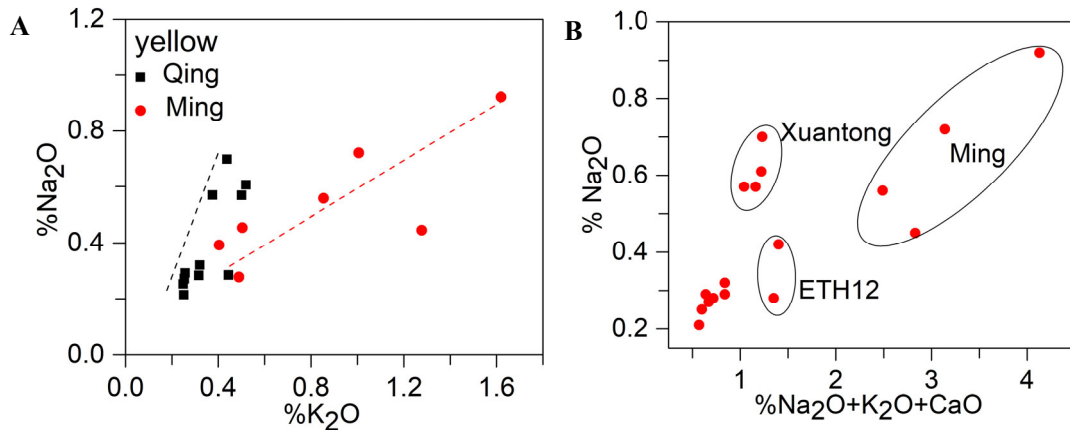


Figure 3.13. (A) Na₂O vs. K₂O content; and (B) Na₂O vs. Na₂O+K₂O for the Ming and Qing glazes.

As demonstrated in **Figure 3.14**, a distinctive inverse correlation between PbO and SiO₂ is observed, a pattern commonly associated with the incorporation of elements from the interfacial region (i.e., porcelain for the Qing or transparent glaze for the Ming). Additionally, a greater quantity of Al₂O₃ is incorporated into the Ming and Xuantong yellow glazes. The lower PbO, higher SiO₂, and increased Al₂O₃ content within the Ming yellow glazes collectively signify more elevated melting temperatures.

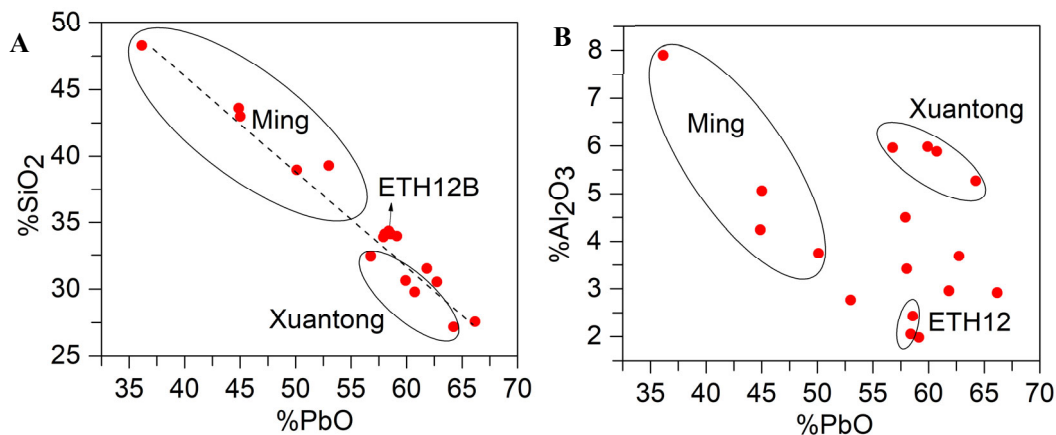


Figure 3.14. (A) SiO₂ versus PbO and (B) Al₂O₃ versus PbO for the yellow glazes.

By comparing the composition of the Qing yellow glazes with that of the porcelain, after subtracting the lead and iron content, it becomes possible to identify the presence of elements derived from the porcelain in the glaze. **Figure 3.15** exhibits correlations between SiO₂, Na₂O, K₂O, CaO, and Al₂O₃. The data clearly indicates that SiO₂ is intentionally added to the glaze, while Na₂O, K₂O, and Al₂O₃ are incorporated from the porcelain. However, the yellow glaze exhibits a higher CaO content than expected from the dissolution of porcelain body in the yellow glaze, and maybe associated to the addition of some lime ashes.

Similar observations are made for the Ming yellow glazes, as depicted in **Figure 3.16**. SiO_2 is introduced to the yellow glaze, while Na_2O , K_2O , Al_2O_3 , and to a large extent CaO , are incorporated from the transparent glaze.

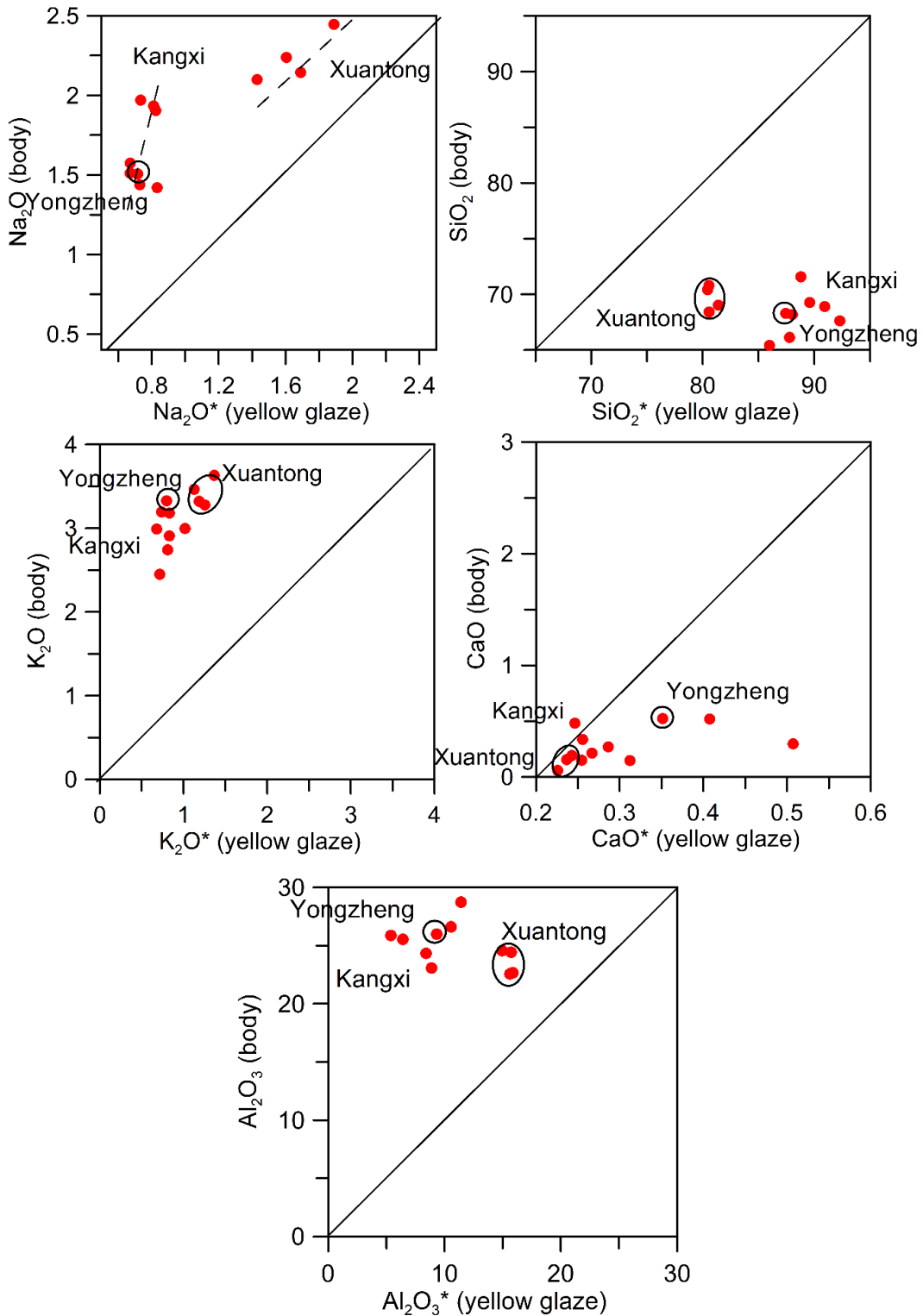


Figure 3.15. Comparison between the main elements present in the yellow glaze after subtracting PbO and Fe_2O_3 and the porcelain for the Qing samples.

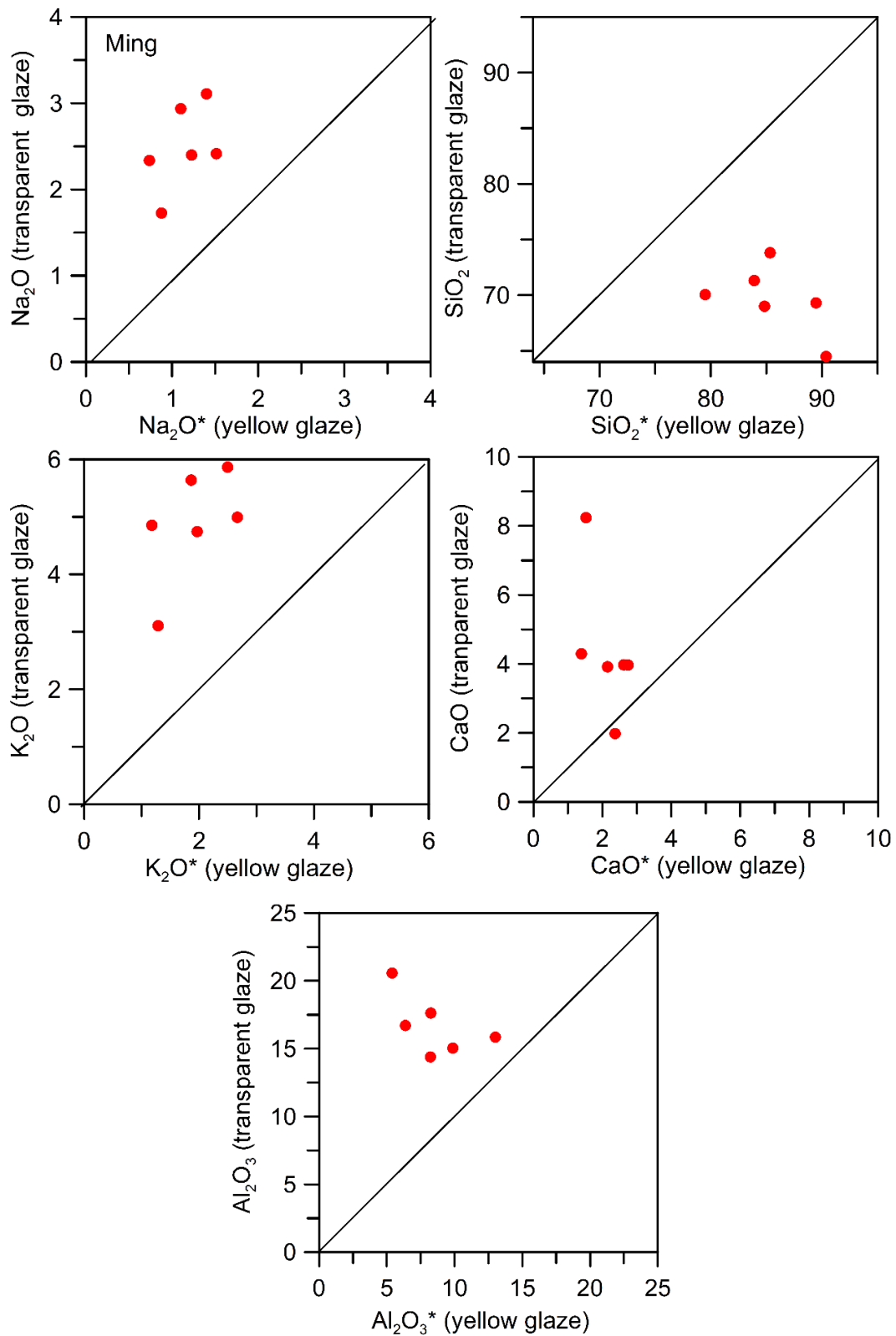


Figure 3.16. Comparison between the main elements present in the yellow glaze after subtracting PbO and Fe₂O₃ and the transparent glaze for the Ming samples.

The diffusion of elements from the underlying porcelain or transparent glaze into the yellow glazes can be observed by analysing the chemical composition across the glaze using Microprobe (EMPA). **Figure 3.17**

presents elemental profiles obtained from cross sections of a Zhengde and a Kangxi yellow glaze, providing visual evidence of this diffusion process.

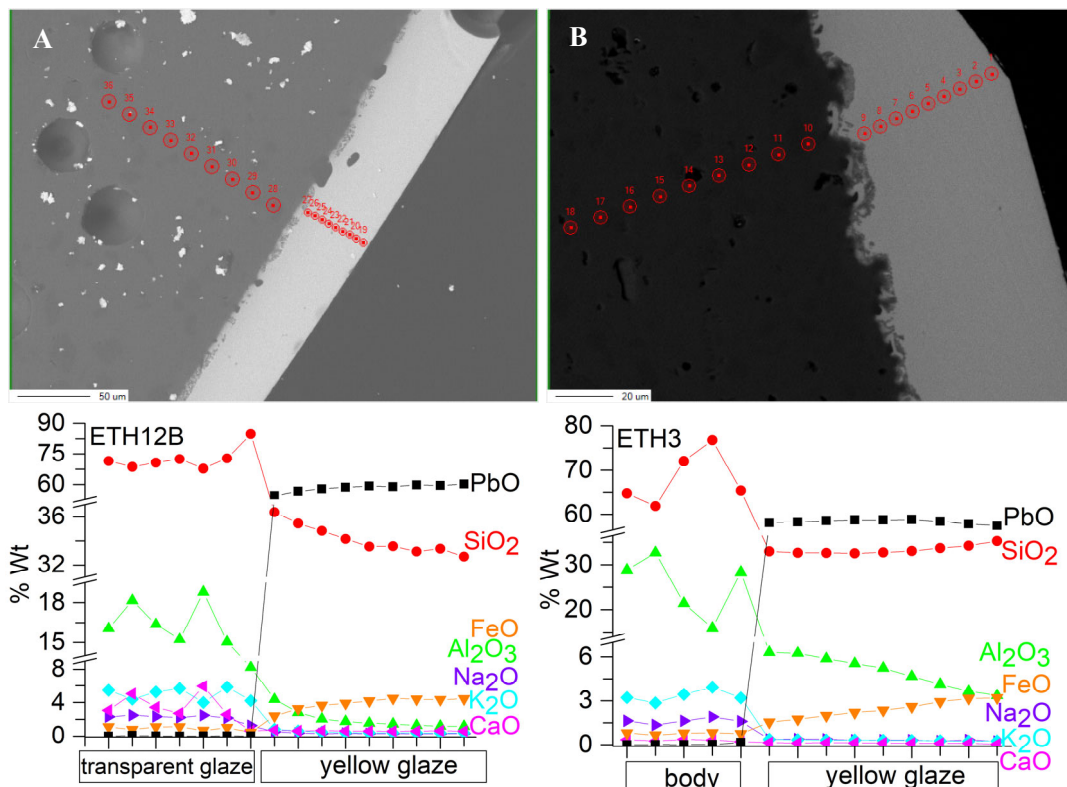
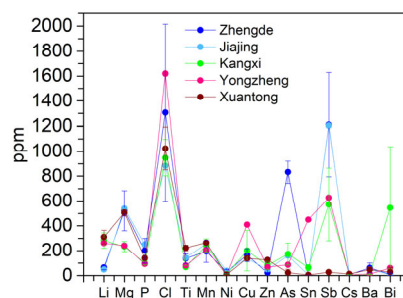


Figure 3.17. Profile composition analysis for the yellow glaze of (A) ETH12B (Zhengde) and (B) ETH3 (Kangxi).

The trace elements present in the yellow glazes were quantified using laser ablation inductively coupled plasma mass spectrometry (LA-ICP-MS) and are presented in **Table 3.7**. A notable difference between the Ming and Qing glazes is the low lithium (Li) content observed in the Ming glazes, consistent with the findings in the transparent glazes. The higher phosphorus (P) content in the Ming yellow glazes may be attributed to its presence in the underlying transparent glazes, particularly in association with calcium (Ca). The presence of antimony (Sb) and arsenic (As) as impurities associated with the source of lead is evident, with significantly higher concentrations (hundreds or even thousands of ppm) compared to the transparent glazes, except for the Xuantong yellow glazes, which exhibit lower levels (around ten ppm). Bismuth (Bi) concentrations are also higher in the Kangxi glazes, reaching a few hundred ppm compared to tens of ppm. Chlorine (Cl) content, on the other hand, is slightly elevated (thousands of ppm) compared to the transparent glazes.

Table 3.7. LA-ICP-MS (trace elements; ppm) of the Yellow glazes.

dynasty	mark	sample	fragment	thickness	Li	Mg	P	Cl	Ti	Mn	Ni	Cu	Zn	As	Sn	Sb	Cs	Ba	Bi	
Ming	Zhengde 1506-1521	dish	ETH12A	rim	90	48	350	129	1112	98	114	16	97	20	706	2	773	4	29	6
			ETH12B	foot	81	51	421	129	2328	128	125	39	163	27	857	6	953	2	27	6
		dish	ETH15A	rim	51	79	672	341	688	191	252	23	175	18	916	2	1455	13	106	20
			ETH15B	foot	23	80	646	202	1101	132	287	48	224	22	850	2	1661	10	83	5
	Jiajing 1522-1566	dish	ETH13B	rim	54	49	539	250	884	144	255	38	137	48	160	5	1205	12	48	7
Qing	Kangxi 1662-1722	bowl	ETH1A	rim	58	215	200	86	1010	65	164	9	287	69	79	31	256	6	10	547
			ETH1B	foot	181	214	284	92	765	65	312	19	0	129	79	55	378	4	6	1515
		bowl	ETH2B	foot	62	358	282	119	850	82	267	7	314	77	233	84	827	8	10	201
			ETH3	foot	44	254	221	107	1193	82	274	7	381	110	299	98	1019	8	9	249
	bowl	ETH4C	rim	44	306	182	90	917	55	202	5	219	70	202	68	531	6	10	433	
		ETH4B	foot	57	343	231	111	955	54	228	10	0	35	150	45	422	9	13	328	
	Yongzheng 1723-1735	dish	ETH10	Base/inside	56	261	241	93	1620	81	207	7	408	68	86	449	627	6	12	60
	Xuantong 1909-1912	bowl	ETH5A	rim	76	347	501	155	1034	219	267	6	148	128	8	4	25	14	50	6
ETH5B			Base/inside	62	337	481	122	846	200	268	4	118	131	5	2	26	12	44	9	
bowl		ETH6A	rim	56	248	534	144	1188	247	260	11	149	119	55	8	30	12	48	69	

**Figure 3.18.** Trace element of yellow glazes in the different periods measured by LA-ICP-MS.

In contrast to glass, the appearance and opacity of the glaze are influenced by factors such as the colour of the underlying porcelain body, undissolved particles, crystallites formed during firing, and the presence of bubbles. To investigate these aspects, techniques such as scanning electron microscopy (SEM) and micro-X-ray diffraction (micro-XRD) are employed to examine the crystallites and particles present within the glazes. **Figure 3.19** demonstrates the presence of undissolved calcium phosphate particles in the transparent glazes dating back to the Ming dynasty, contributing to their visual characteristics and opacity.

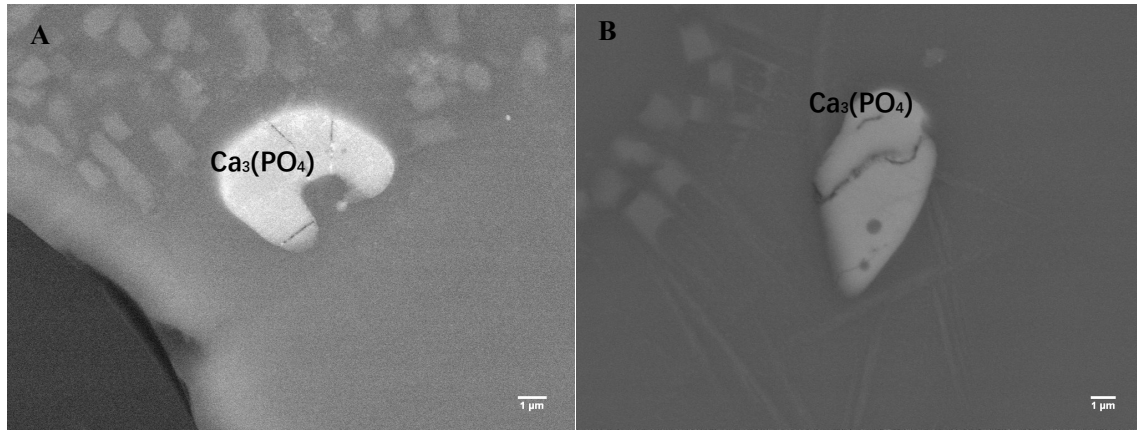


Figure 3.19. SEM images in the white glaze of (A) ETH12A and (B) ETH15A of the Ming samples.

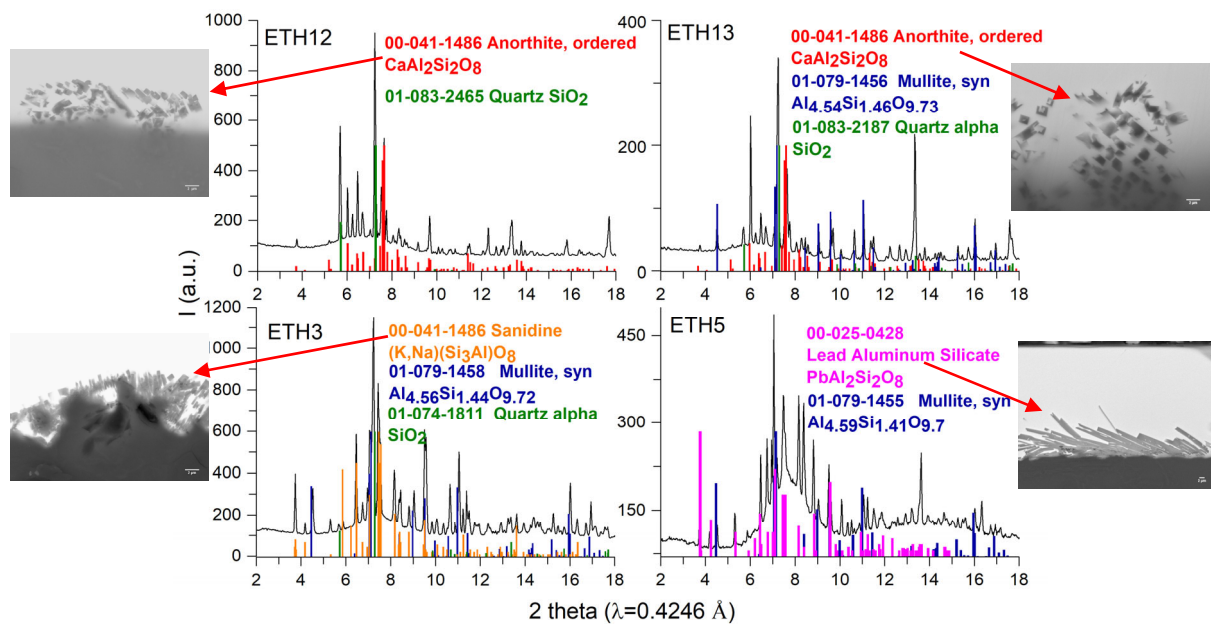


Figure 3.20. Interface SEM images of ETH12 (Zhengde), ETH13 (Jiajing) of the Ming dynasty; ETH3(Kangxi), ETH5 (Xuantong) of the Qing dynasty and the micro-XRD analysis.

Figure 3.20 illustrates the crystal formations occurring at the interface between the porcelain and both the Ming transparent glazes and the Qing yellow glazes. In all cases, feldspars are observed to form. Specifically, the Ming transparent glazes exhibit the presence of anorthite (calcium rich feldspars), while the Qing yellow glazes display lead-potassium and lead feldspars with sanidine structure.

Furthermore, it is important to note that each of the Imperial samples has been meticulously inscribed with the specific reign on the underside, providing valuable historical information. Additionally, the cobalt blue

calligraphy present on the samples has undergone comprehensive examination, including composition and crystallite analyses, in order to gain a deeper understanding of its characteristics and origins.

Composition of the blue pigment

Table 3.8 shows the major chemical composition of the two blue pigments that could be sampled measured by Microprobe.

Table 3.8. Blue pigment composition. Microprobe data (major elements, wt%).

mark	sample		Na ₂ O	MgO	Al ₂ O ₃	SiO ₂	K ₂ O	CaO	MnO	FeO	CoO
Yongzheng 1723-1735	ETH10A	colourless	1.68	0.45	14.5	69.7	3.79	6.18	0.15	1.02	-
		blue	1.29	0.66	36.5	41.6	0.37	12.9	1.88	1.52	4.16
Xuantong 1909-1912	ETH5B	colourless	2.63	0.35	16.0	68.9	3.83	3.55	0.18	1.07	-
		blue	1.73	0.47	35.4	44.4	0.43	12.7	1.07	1.19	4.09

The pigment contains a higher amount of Al₂O₃, CaO, CoO and MnO and lower amount of SiO₂, K₂O and Na₂O than the transparent glaze above.

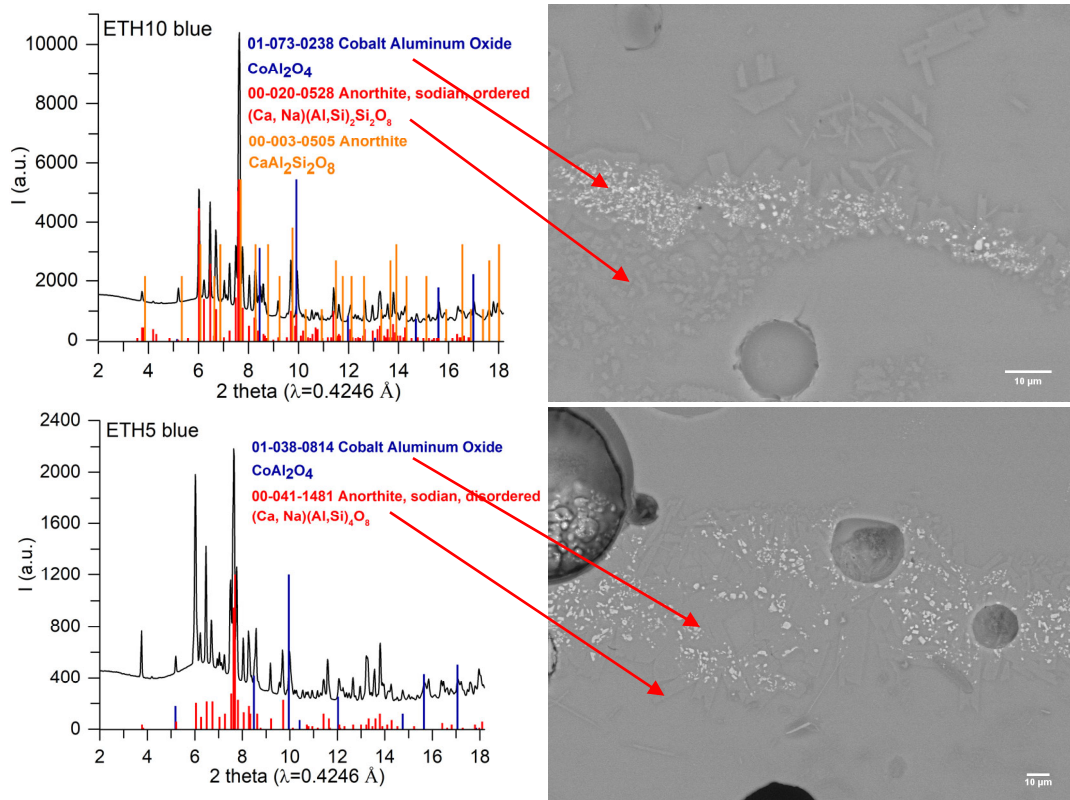
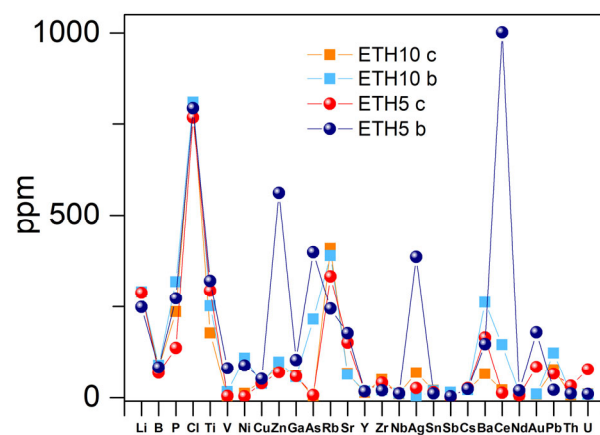


Figure 3.21. SEM images of ETH10 (Yongzheng) and ETH5 (Xuantong) blue pigment in white glaze and the micro-XRD analysis.

Figure 3.21 shows the cobalt pigment attached on the surface of anorthite, and the micro-XRD patterns obtained from the blue area determine the presence of CoAl₂O₄. This cobalt aluminate which incorporates also some Mn is formed during the firing.

Table 3.9. LA-ICP-MS (trace elements; ppm) of the blue mark. c: colourless b: blue.

mark	sample	Li	B	P	Cl	Ti	V	Ni	Cu	Zn	Ga	As	Rb	Sr	Y	Zr	Nb	Ag	Sn	Sb	Cs	Ba	Ce	Nd	Au	Pb	Th	U	
Yongzheng 1723-1735	ETH10A	c	289	83	236	800	177	2	11	47	84	60	1	408	67	14	50	10	69	20	6	21	66	21	8	8	78	7	9
		b	290	90	318	809	251	16	109	38	98	57	215	389	64	17	21	12	1	19	15	21	262	146	13	10	123	11	8
Xuandong 1909-1912	ETH5B	c	287	69	137	767	293	4	3	39	70	59	7	333	152	16	41	12	26	15	2	26	165	13	6	85	66	33	79
		b	249	83	273	793	321	81	89	52	562	104	399	244	177	17	19	11	386	11	3	24	147	1002	19	180	21	11	10

**Figure 3.22.** Trace elements comparison of ETH10A and ETH5B.

The trace element from the transparent glaze and blue pigment were measured by LA-ICP-MS and are show in **Table 3.9** and **Figure 3.22**.

The blue pigment of Yongzheng period (ETH10) shows a higher Zn, As, Ag, Ce and Au content compared to the Xuandong period (ETH5), but the Rb, Ba and Pb content are the opposite.

Colour of the yellow glazes

The UV-Vis-NIR analysis of the historical yellow and transparent glazes yielded distinct spectra, exemplified in **Figure 3.23**. In the case of the yellow glazes, a characteristic increase in reflectance is observed within the 400-430 nm range. This optical behaviour can be attributed to the presence of Fe^{3+} ions in tetrahedral coordination within the glaze matrix. However, it is noteworthy that the nature of the glass, particularly a high lead content, also influences this phenomenon. High lead glasses have a high refraction index and a shifted UV absorption edge towards longer wavelengths. Furthermore, a decrease in reflectance is evident in the near-infrared (NIR) region, reaching a minimum around 1100 nm. This observation can be associated with the presence of Fe^{2+} ions in octahedral coordination within the glass structure. The concentration of Fe^{2+} ions in the glazes is influenced by factors such as the atmospheric conditions during firing, sintering temperature, and the presence of traces of transition metal elements such as antimony or manganese. It noteworthy that the Sb content in the Ming dynasty is higher than that in Qing dynasty although both are in the ppm level. The transparent glazes, on the other hand, are characterized by their alkali-lime composition and negligible iron content. Their UV absorption edge occurs at approximately 300 nm. They also show the presence of a decrease in the reflectance at around 1100 nm, which we could relate to the presence of Fe^{2+} in octahedral coordination, although less intense.

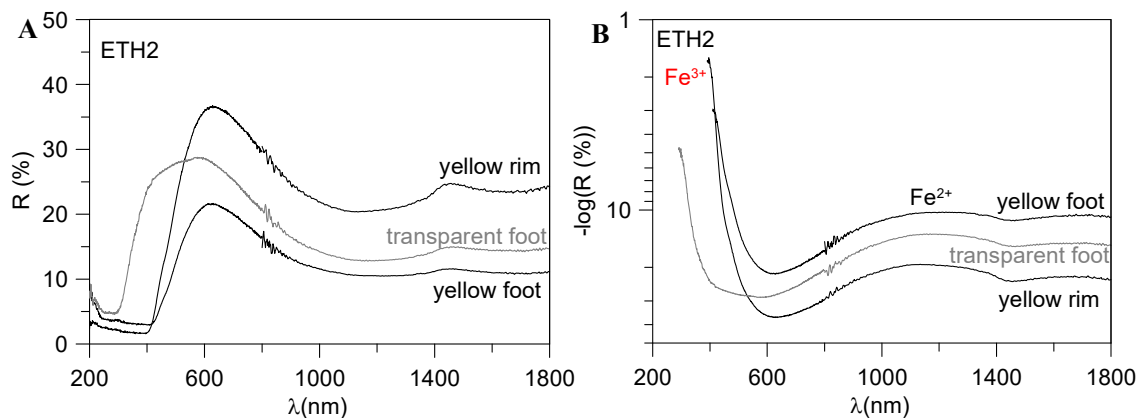


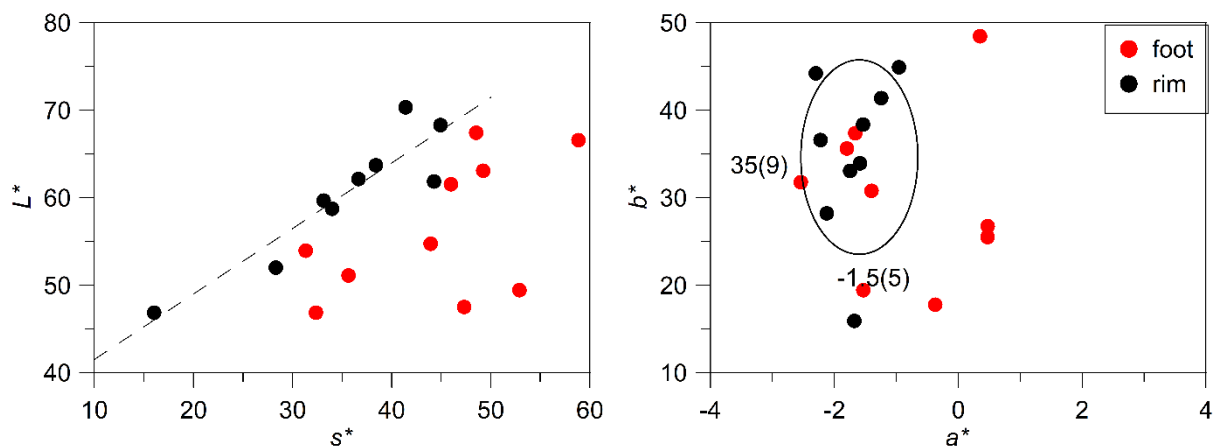
Figure 3.23. (A) Diffuse reflectance and (B) Absorbance of the yellow and white glazes of ETH2.

The colour coordinates calculated from the Reflectance spectra are shown in **Table 3.10** and in **Figure 3.24**. We can see that the yellow glazes located at the foot of the objects show a larger variability, this could be related to the geometry, thinner or thicker glazes, position in the kiln, etc.

Table 3.10. Calculated colour coordinates from the historical yellow glazes.

dynasty	mark	sample	fragment	Thickness (μm)	λ_d	L^*	a^*	b^*	c^*	h^*	s^*	
Ming	Zhengde (1506-1521)	ETH12A	rim	90	575	61.9	-2.3	44.3	44.3	92.9	58.2	
		ETH12B	foot	81	577	47.5	0.5	25.5	25.5	88.9	47.4	
	Jiajing (1522-1566)	ETH15A	rim	51	575	52.0	-2.1	28.3	28.3	94.2	47.8	
		ETH15B	foot	23	575	51.1	-1.5	19.5	19.5	94.4	35.7	
	Qing dynasty	Kangxi (1662-1722)	ETH13B	rim	54	574	46.9	-1.6	16.0	16.1	96.0	32.4
			ETH13A	foot	36	573	64.7	-3.9	26.1	26.3	98.5	37.7
Yongzheng (1723-1735)		ETH1A	rim	58	577	68.3	-0.9	45.0	45.0	91.2	55.0	
		ETH1B	foot	181	576	54.8	0.5	26.8	26.8	88.9	44.0	
		ETH2B	foot	62	575	49.5	-1.4	30.8	30.9	92.5	52.9	
		ETH3	foot	44	575	63.1	-1.8	35.7	35.7	92.8	49.3	
Xuantong (1909-1912)		ETH4C	rim	44	575	63.7	-1.5	38.4	38.4	92.2	51.7	
		ETH4B	foot	57	575	67.4	-1.6	37.4	37.5	92.5	48.6	
		ETH10A	Base/inside	56	575	61.6	-2.5	31.8	31.9	94.5	46.0	
		ETH5A	rim	76	576	70.3	-1.2	41.4	41.4	91.7	50.8	
Xuantong (1909-1912)	ETH5B	Base/inside	62	576	66.6	0.4	48.5	48.5	89.5	58.9		
	ETH6A	rim	56	575	59.7	-1.7	33.1	33.2	92.9	48.6		
		ETH6B	foot	38	576	53.9	-0.3	17.8	17.8	91.1	31.4	

Figure 3.24 shows that the glazes have a high b^* colour coordinate (yellow) and slightly negative a^* (slightly greenish) and that the lightness (L^*) shows a good positive correlation with the saturation (s^*). The colour of the glazes is nearly a pure yellow with colour coordinates $L^* \sim 60\%$, $a^* \sim -1.5$, $b^* \sim 35$, $h^* \sim 93^\circ$, $s^* \sim 49\%$.

**Figure 3.24.** Colour coordinates from the historical yellow glazes.

As it would be expected the Lightness, L^* , and colour saturation, s^* , increase with the thickness of the glaze. However, only very slightly. In fact, the glazes are very thin, typical thickness varies between 50 and 75 μm .

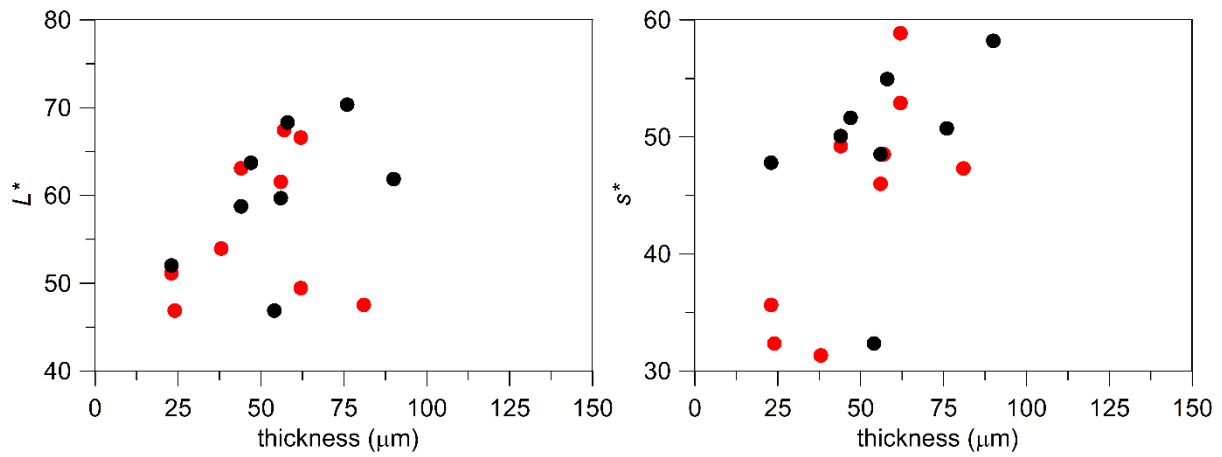


Figure 3.25. Colour coordinates L^* and s^* vs. the thickness of the yellow glazes.

Oxidation state of iron in the yellow glazes

The pre-edge feature of the Fe K-edge absorption is particularly sensitive to the valence state and local geometry. The pre-peak area and the average peak position is known to shift to higher energy as the ratio of ferric to ferrous iron increases; and a variogram where the average peak positions (centroids) are plotted against total integrated area can be drawn (Wilke 2001) giving an estimation of the different species and their coordination state (More details can be seen in **Chapter 2**). Different peaks can be fitted for Fe^{2+} and Fe^{3+} . Although the area of the peaks is related to the amount of each specie, a calibration is necessary, which normally is obtained using glasses of a similar composition of known oxidation state. However, there are lack of studies about the calibration of iron species in a high lead near eutectic glass, so the Fe^{2+} and Fe^{3+} proportion are not calibrated in this study.

The fitted data is shown in **Table 3.11** and **Figure 3.26**.

Table 3.11. Fitted parameters of the ETH yellow glazes. * fixed.

dynasty	period	date	Sample	FWHM	E_1 (eV)	A_1 (eV)	E_2 (eV)	A_2 (eV)
Ming	Zhengde	1506-1521	ETH12	1.71 (2)	7113.54 (1)	0.214 (3)	7111.5 (1)	0.023 (2)
	Jiajing	1522-1566	ETH13	1.83 (3)	7113.55 (1)	0.229 (4)	7111.4 (2)	0.019 (3)
Kangxi	1662-1722	ETH1B	1.84 (5)	7113.55 (3)	0.232 (8)	7111.6 (3)	0.020 (6)	
		ETH2	1.76 (2)	7113.57 (1)	0.201 (3)	7111.6 (1)	0.019 (6)	
		ETH3A	1.87 (5)	7113.54 (3)	0.225 (8)	7111.7 (3)	0.023 (6)	
		ETH4A	1.71 (2)	7113.52 (1)	0.202 (2)	7111.6 (3)	0.018 (2)	
Qing	Yongzheng	1723-1735	ETH10	1.88 (5)	7113.53 (2)	0.214 (7)	7111.4 (3)	0.020 (4)
	Xuanton	1909-1912	ETH5A	2.00 (4)	7113.61 (2)	0.205 (4)	7112.0 *	0.035 (5)
			ETH6A	1.72 (2)	7113.43 (1)	0.208 (3)	7111.5 (1)	0.021 (2)

The fitting results, as shown in **Table 3.11**, reveal that iron species in the glazes primarily exist as Fe^{3+} , with a minor contribution attributed to Fe^{2+} . It is possible to represent the data in a variogram (Wilke 2005) where the centroid, calculated as the weighted average position is plotted versus the total area of the fitted pre-peak spectra, as shown in **Figure 3.27**. Previous investigations have established that the centroid

position is sensitive to the oxidation state of iron, while the total area reflects its coordination environment. The dashed lines within the plot indicate the relative variation in both Fe^{3+} to Fe^{2+} ratio and coordination states. However, as depicted in the variogram, the contribution of Fe^{2+} to the pre-peak is consistently smaller than that of Fe^{3+} , particularly in the IV-fold and V-fold coordination, where it becomes exceedingly minute. Consequently, the detectability and sensitivity towards Fe^{2+} are diminished. (Vercamer 2016)

To visualize the position of the ETH samples within the variogram, **Figure 3.27** provides an overview. Notably, all the glazes examined primarily exhibit V-fold coordination. Regarding glass compositions, it is commonly observed that iron tends to be present as V-fold coordination; however, a certain level of debate persists regarding the interpretation of the data. Some researchers accept the predominant presence of iron in V-fold coordination, while others propose the existence of a mixture of various coordination sites.

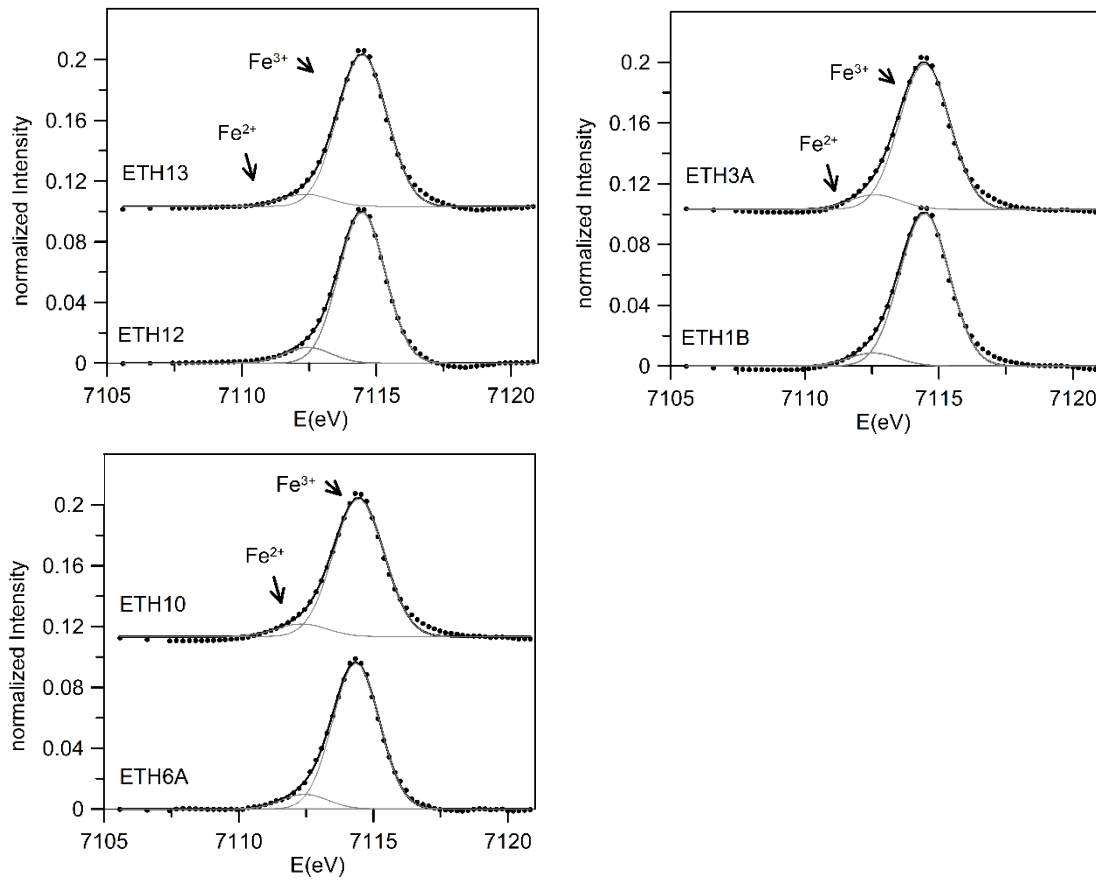
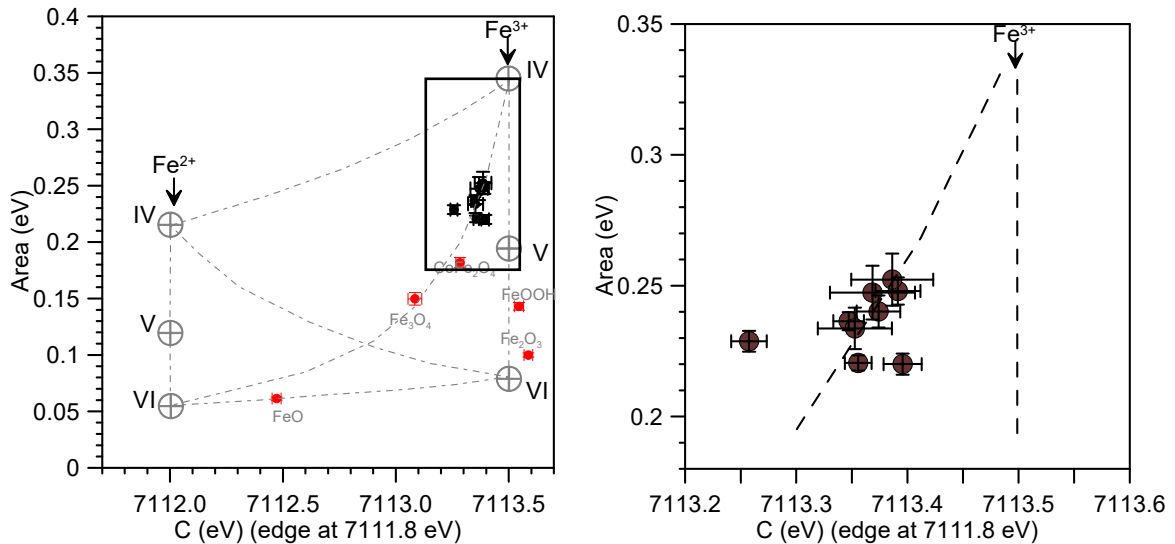


Figure 3.26. Fitted pre-edge peak ETH. (Top Left) Ming (Top Right) Kangxi and (Bottom Left) Yongzheng and Xuantong yellow glazes.

Table 3.12. Fitted parameters of the ETH yellow glazes. Centroid, total area and the area of the Fe^{2+} peak over the total area of the pre-edge peaks.

	period	Sample	C(E)	A(eV)	$A(\text{Fe}^{2+}/\text{Fe}_{\text{tot}})$ x100
Zhengde	1506-1521	ETH12	7113.35 (1)	0.236 (3)	9.5 (1)
		ETH13	7113.39 (2)	0.248 (5)	7.5 (2)
Kangxi	1662-1722	ETH1B	7113.39 (4)	0.25 (1)	7.9 (3)
		ETH2	7113.40 (2)	0.220 (3)	8.7 (2)
		ETH3A	7114.36 (1)	0.25 (1)	9.1 (4)
		ETH4A	7113.35 (3)	0.220 (3)	8.4 (1)
Yongzheng	1723-1735	ETH10	7113.35 (3)	0.234 (8)	8.4 (1)
Xuantong	1909-1912	ETH5A	7113.37 (2)	0.240 (6)	14.6 (4)
		ETH6A	7113.26 (2)	0.229 (4)	9.2 (2)

**Figure 3.27.** Variogram of ETH yellow glazes.

The changes in the area or in the centre shift among samples are very small. Nevertheless, the area ratio between Fe^{2+} and Fe^{3+} is more sensible. A discernible correlation between the colour coordinates of the yellow glazes and the oxidation state of iron within the glaze matrix can be observed. As depicted in **Figure 3.28**, an elevation in the fraction of reduced iron ($A(\text{Fe}^{2+})/A(\text{Fe})$) corresponds to an increase in the values of L^* , s^* , and b^* , while a^* exhibits a decrease. This trend signifies a heightened saturation of colour, characterized by a more prominent yellow component and a diminished red/green contribution, concurrently accompanied by an augmented Reflectance of the glaze. Hence, it is evident that the reddish hue imparted by Fe^{3+} is partially counterbalanced by the presence of Fe^{2+} .

The increase in lightness (L^*), which signifies the degree of light reflection, can be attributed to the decrease in the Fe^{3+} content that absorbs visible light, coupled with an increase in Fe^{2+} content, which primarily absorbs light in the Near Infrared (NIR) region. Notably, the calculation of lightness (L^*) solely considers

the visible light spectrum, ranging between 360 nm and 780 nm. This indicates the use of a slightly oxygen-depleted atmosphere, which varies slightly between the samples.

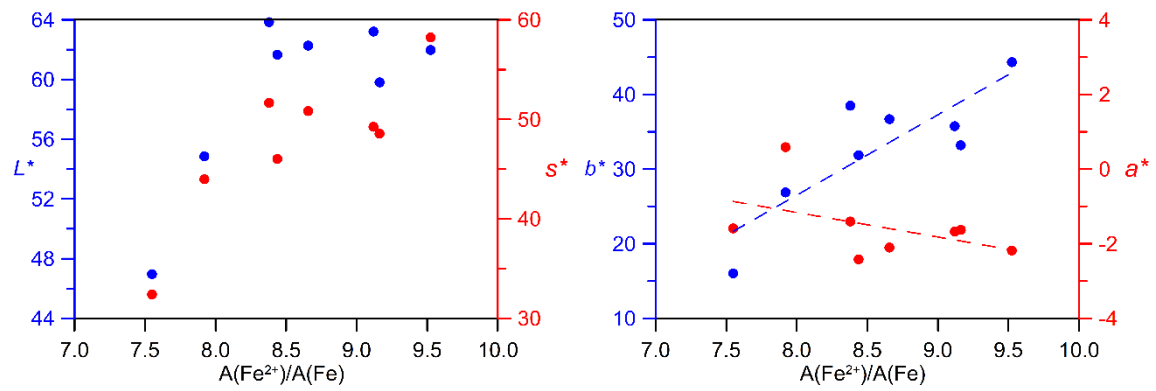


Figure 3.28. Colour coordinates L^* , s^* , a^* and b^* as a function of the Fe^{2+} content.

3.4.2 Replicated yellow materials

Yellow glazes were prepared using two distinct procedures documented in historical porcelain production: direct application of the glaze onto the porcelain and application of the glaze over a transparent glaze layer. Further details regarding these procedures can be found in the **Chapter 3.3.2 Replication materials** section.

The primary finding of this study reveals that when the glazing process is conducted under atmospheric air conditions, the resulting glazes exhibit a yellow-golden hue, **Figure 3.5**. Notably, the thickness of the glaze layer emerges as a crucial factor influencing the coloration, as demonstrated in **Figure 3.29**. Increasing in the thickness of the glaze results in a decrease in the lightness L^* and an increase in the colour saturation s^* , indicating a decrease in the contribution of the white substrate. The increase in the colour saturation is also associated with a 30% and 50% increase in the colour variables, a^* and b^* , respectively, when the thickness is increased between 100 μm to 200 μm . However, a^* , which is very small (-4), shifts from negative to positive (+8), from green to red. Consequently, the hue, h^* , decreases from yellow to yellow-reddish.

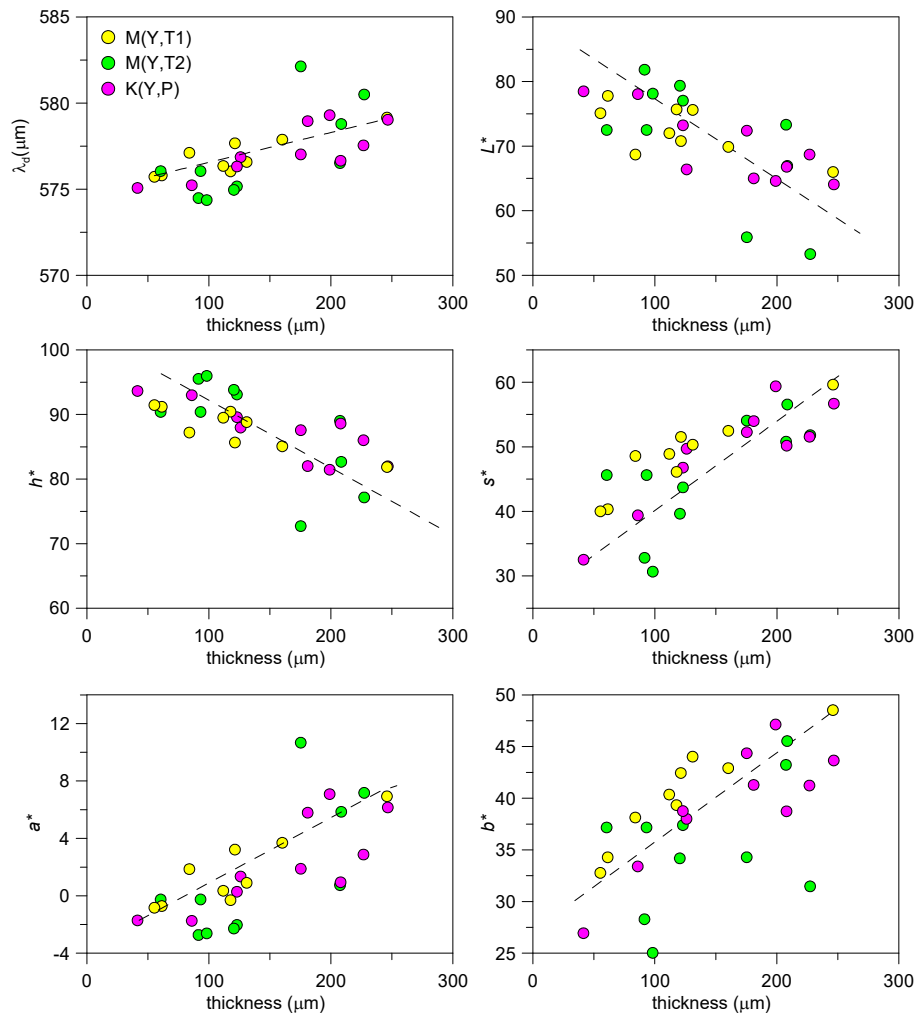


Figure 3.29. Colour parameters as a function of the thickness of the glaze.

Table 3.13. Colour coordinates and chemical composition of the replicated glazes.

	Temp. (°C)	Thick. (µm)	<i>L</i> *	<i>a</i> *	<i>b</i> *	<i>c</i> *	<i>h</i> *	<i>s</i> *	Na ₂ O	Al ₂ O ₃	SiO ₂	K ₂ O	CaO	FeO	PbO	
M(Y,T1)	900	84	83.9	1.2	45.2	45.3	88.5	47.5	0.6	1.3	33.1		0.7	2.6	61.7	
		121	57.5	1.1	20.9	20.9	87.1	34.1	0.7	3.2	34.6		1.1	2.0	58.4	
	950	61	79.5	-0.8	30.1	30.2	91.6	35.5	0.6	1.8	36.3		1.3	3.8	56.2	
		160	79.5	3.2	55.8	55.9	86.8	57.5	0.6	2.4	38.9		1.0	2.3	54.8	
	1000	55	87.5	-1.0	41.5	41.5	91.3	42.8	1.1	3.2	41.2		1.5	2.0	51.0	
		346	58.0	20.2	71.4	74.2	74.2	78.8	0.2	0.4	31.0		0.4	3.6	64.3	
	1050	118	82.1	1.5	56.8	56.8	88.5	56.9	0.2	0.3	29.7		0.4	2.6	66.9	
		131	85.3	-0.6	47.1	47.2	90.7	48.4	0.2	0.4	29.9		0.3	2.7	66.5	
	1100	119	79.3	0.1	49.1	49.1	89.9	52.7	0.4	1.0	34.4		1.1	2.8	60.3	
		246	74.8	6.9	52.8	53.3	82.5	58.0	0.4	1.1	33.9		0.6	2.4	61.6	
	M(Y,T2)	900	61	73.6	1.9	42.2	42.3	87.5	49.8	0.4	1.2	31.2		2.7	3.5	60.9
			175	59.2	10.4	27.4	29.3	69.3	44.4	0.6	0.6	33.4		2.0	2.5	60.9
950		93	79.9	2.4	51.6	51.7	87.4	54.3	0.8	3.0	44.4		7.3	2.9	41.7	
		227	68.8	13.0	47.1	48.8	74.5	57.9	0.9	3.5	41.4		6.1	2.2	45.8	
1000		123	88.3	-2.9	39.7	39.8	94.2	41.1	1.8	8.2	48.8		7.6	0.9	32.6	
		209	62.8	7.9	45.2	45.9	80.1	59.0	0.1	0.1	29.9		0.6	2.7	66.6	
1050		92	90.3	-3.7	32.0	32.2	96.5	33.6	0.2	0.2	30.3		1.0	3.0	65.3	
		121	82.4	-2.8	31.3	31.4	95.2	35.6	0.4	1.0	33.2		1.7	2.4	61.3	
1100		98	85.1	-3.4	26.4	26.6	97.3	29.8	0.9	2.5	41.0		6.0	2.4	47.2	
		208	45.6	0.0	20.2	20.2	89.9	40.4	0.7	2.9	37.5		3.9	2.2	52.7	
K(P)		900	42	82.8	-2.2	28.8	28.9	94.4	33.0	0.7	3.8	30.9	0.3	0.4	2.1	61.8
			181	68.5	5.0	34.7	35.0	81.8	45.6	0.7	2.9	31.4	0.5	0.4	2.0	62.3
	950	126	74.0	2.0	51.4	51.5	87.8	57.1	0.8	6.7	36.9	0.7	0.6	2.0	52.3	
		265	69.6	3.2	60.2	60.3	86.9	65.4	0.9	7.3	42.1	0.9	0.5	1.8	46.5	
	1000	50	80.9	1.1	46.4	46.4	88.6	49.8	0.8	5.2	35.6	0.4	0.4	1.8	55.8	
		199	58.2	3.9	29.6	29.9	82.5	45.7	0.5	2.7	28.3	0.4	0.2	2.1	65.8	
	1050	208	74.6	1.5	43.6	43.6	88.1	50.5	0.5	2.1	30.1	0.7	0.2	2.1	64.4	
		247	68.4	10.6	64.8	65.6	80.7	69.2	0.6	3.2	30.9	0.5	0.3	1.9	62.5	
	1100	86	88.9	-2.0	39.7	39.7	92.8	40.8	0.8	5.3	36.2	0.8	0.4	1.7	54.9	
		160	76.0	1.4	41.9	41.9	88.0	48.3	0.6	3.2	31.5	0.5	0.3	1.9	62.0	

On the other hand, when considering glazes of comparable thickness, the colour is influenced by both the firing temperature and the composition of the glaze, specifically the CaO content, as depicted in **Figure 3.30**. As the temperature rises, the glaze exhibits a more pronounced yellow hue (indicated by an increase in *h**), primarily attributed to a reduction in the red contribution (positive *a**). This effect is particularly pronounced in the replicated samples M (Y, T2), characterized by higher calcium content due to interactions with the underlying calcium-rich transparent glaze.

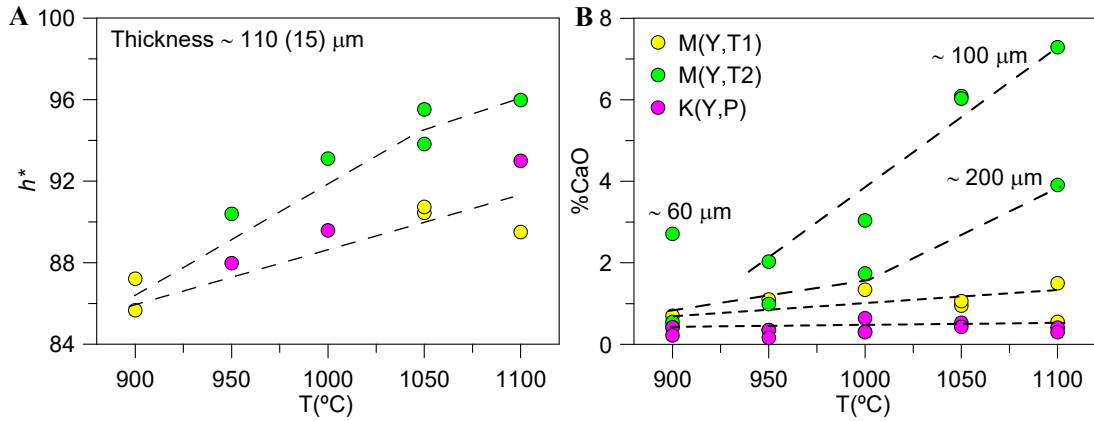


Figure 3.30. Effect of the firing temperature. (A) The colour is more yellow (h^* increases) with the firing temperature for the glazes with similar glaze thickness ($\approx 100 \mu\text{m}$). (B) CaO content of the glazes vs. firing temperature and thickness of the glazes.

The influence of oxidation state on glaze coloration is investigated through the analysis of the Fe K-pre-edge. In the replicated glazes, iron predominantly exists as Fe^{3+} , although notable variations are observed in the fitted parameters (**Table 3.14**). **Figure 3.31**, shows how the fitted data follow the Fe^{3+} (IV) - Fe^{2+} (VI) line in the variogram. However, it is important to note that the error bars are relatively large due to the comparatively smaller size of the Fe^{2+} peak in relation to the Fe^{3+} peak.

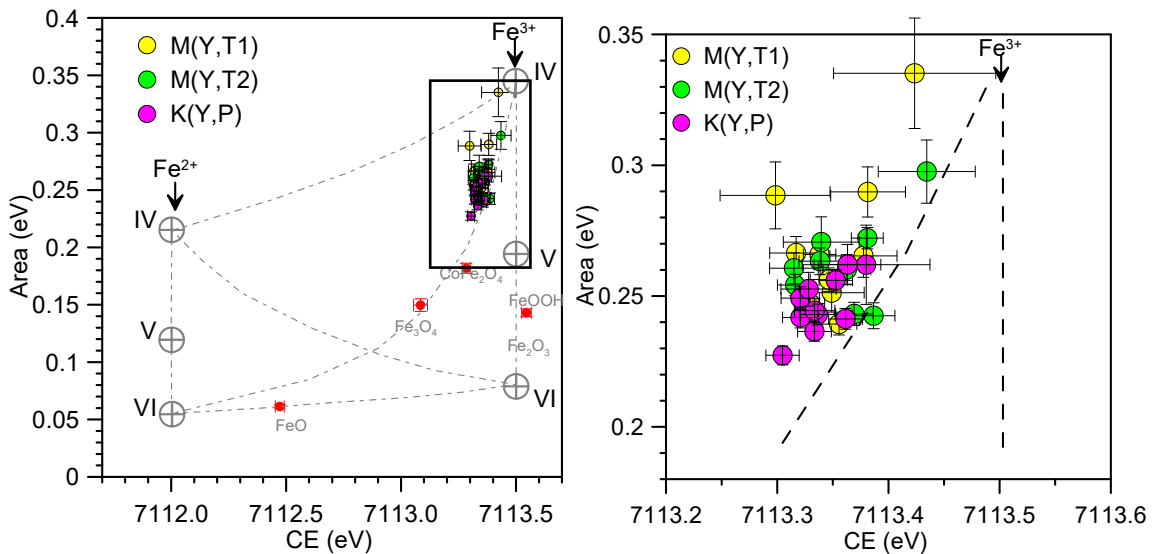


Figure 3.31. Variogram of the replicated glazes.

Table 3.14. Fitted pre-peak data of the replicated glazes.

	Temp. (°C)	Thick. (µm)	FWHM (eV)	E ₁ (eV)	A ₁ (eV)	E ₂ (eV)	A ₂ (eV)	C (eV)	A (eV)	A(Fe ²⁺)/A _{tot} X100	
M(Y,T1)	900	84	1.69(2)	7113.52(1)	0.219(3)	7111.7(1)	0.021(2)	7113.52(2)	0.239(4)	8.7(2)	
		121	1.82(4)	7113.55(2)	0.243(7)	7111.5(3)	0.022(5)	7113.55(3)	0.265(8)	8.3(5)	
	950	61	1.67(2)	7113.51(1)	0.224(3)	7111.6(1)	0.023(2)	7113.51(1)	0.247(4)	9.5(2)	
		160	1.81(4)	7113.52(2)	0.230(6)	7111.5(3)	0.021(4)	7113.52(3)	0.251(7)	8.4(4)	
	1000	55	2.2(1)	7113.60(5)	0.31(2)	7111.2(7)	0.02(1)	7113.60(7)	0.34(2)	7(1)	
		346	1.75(2)	7113.53(1)	0.233(4)	7111.5(1)	0.023(2)	7113.53(2)	0.256(4)	9.1(2)	
	1050	118	1.90(5)	7113.57(3)	0.265(8)	7111.4(3)	0.025(5)	7113.57(3)	0.29(1)	8.7(5)	
		131	1.82(4)	7113.52(2)	0.241(5)	7111.4(2)	0.025(3)	7113.52(2)	0.266(6)	9.6(3)	
	1100	119	1.71(2)	7113.53(1)	0.241(3)	7111.4(1)	0.025(2)	7113.53(1)	0.266(4)	9.3(2)	
		246	2.10(8)	7113.53(4)	0.26(1)	7110.9(4)	0.025(7)	7113.53(5)	0.29(1)	8.8(7)	
	M(Y,T2)	900	61	1.74(3)	7113.55(1)	0.222(4)	7111.6(2)	0.021(3)	7113.55(2)	0.242(5)	8.6(3)
			175	1.70(2)	7113.51(1)	0.210(3)	7111.4(1)	0.020(2)	7113.51(1)	0.230(3)	8.7(2)
950		93	1.70(2)	7113.54(1)	0.222(4)	7111.6(1)	0.021(2)	7113.54(2)	0.243(4)	8.6(2)	
		227	1.84(5)	7113.52(3)	0.245(8)	7111.6(3)	0.025(6)	7113.52(3)	0.27(1)	9.3(6)	
1000		123	1.77(3)	7113.54(1)	0.241(4)	7111.2(2)	0.023(3)	7113.54(2)	0.263(5)	8.7(3)	
		209	1.78(2)	7113.51(1)	0.232(3)	7111.3(1)	0.023(2)	7113.51(2)	0.254(4)	8.9(2)	
1050		92	1.76(3)	7113.53(2)	0.236(5)	7111.2(2)	0.024(3)	7113.53(3)	0.261(6)	9.3(3)	
		121	1.79(3)	7113.56(2)	0.237(5)	7111.4(2)	0.023(3)	7113.56(1)	0.260(6)	8.7(3)	
1100		98	2.03(6)	7113.59(3)	0.28(1)	7111.3(5)	0.020(6)	7113.59(3)	0.30(1)	6.8(6)	
		208	1.71(2)	7113.56(1)	0.250(3)	7111.4(1)	0.022(2)	7113.56(7)	0.272(4)	8.3(2)	
K(P)		900	42	1.7	7113.5(2)		7111.1(5)	0.03(1)	7113.54(2)	0.241(4)	9.2(2)
			181	1.82(2)	7113.52(1)	0.24(1)	7111.5(3)	0.018(9)	7113.52(3)	0.26(2)	6.8(9)
	950	126	1.67(2)	7113.52(1)	0.215(3)	7111.4(2)	0.022(2)	7113.52(2)	0.236(4)	9.2(2)	
		265	1.81(2)	7113.51(1)	0.206(3)	7111.4(1)	0.021(2)	7113.49(1)	0.227(4)	9.4(2)	
	1000	50	2.23(2)	7113.54(1)	0.222(3)	7111.5(5)	0.020(2)	7113.52(5)	0.243(4)	8.4(2)	
		199	1.75(7)	7113.52(4)	0.223(4)	7111.5(2)	0.022(2)	7113.52(2)	0.244(5)	9.0(2)	
	1050	208	1.90(2)	7113.49(1)	0.220(3)	7111.5(1)	0.022(2)	7113.51(1)	0.242(4)	8.9(2)	
		247	1.82(3)	7113.52(1)	0.226(4)	7111.4(2)	0.023(2)	7113.52(2)	0.249(4)	9.2(2)	
	1100	86	1.71(3)	7113.52(1)	0.233(3)	7111.4(3)	0.023(2)	7113.54(3)	0.256(4)	9.1(2)	
		160	2.10(5)	7113.55(2)	0.241(7)	7111.2(2)	0.021(4)	7113.55(2)	0.262(8)	7.9(4)	

As can be seen in **Figure 3.32**, it is evident that there is an increase in the Fe³⁺ content (larger Centre Shift) with the firing temperature, especially for the M(Y,T2) replicas, indicating that the iron is more oxidised and corresponding to the incorporation of more calcium in the glaze due to the reaction with a calcium-rich glaze substrate. The Centre Shift corresponding to the replica yellow glazes is slightly greater than that of the historical glazes, in good agreement with the use of more oxidising conditions for the replications than for the historic glazes. This is quite reasonable considering that although the historic glazes were also fired

under oxidising conditions, we used an electric kiln, whereas the historic glazes were fired in a wood-feed kiln.

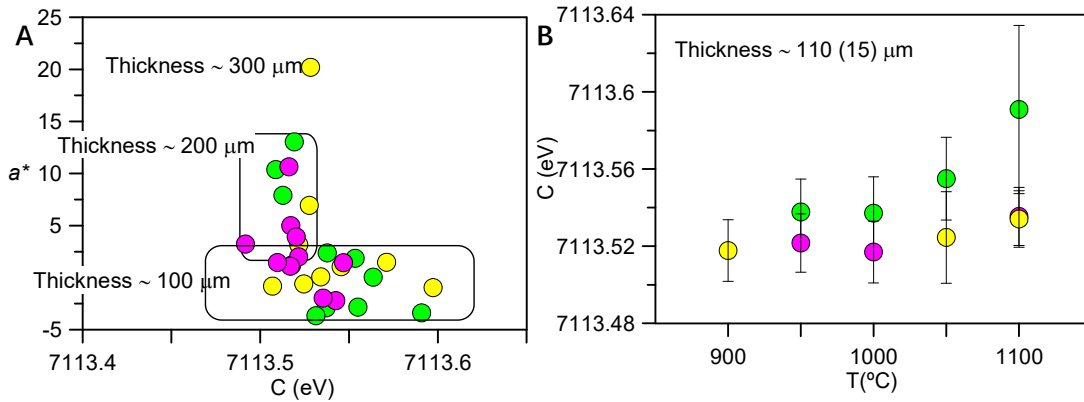


Figure 3.32. (A) a^* versus $A(\text{Fe}^{2+}/A\text{Fe}_{\text{tot}})$ showing that a larger a^* is related to a thicker glaze but there is no obvious relationship with the oxidation state of iron. (B) C versus T . Considering only those glazes with similar thickness ($\approx 100 \mu\text{m}$), we can see that C increases with the firing temperature mainly for M(Y,T2), that is the one which incorporates more calcium in the glass due to the reaction with the porcelain.

In order to evaluate the effect of the firing atmosphere and temperature on the oxidation state of the iron in the glaze, and consequently, in the colour, glasses were produced in the absence of oxygen, in a pure N_2 atmosphere flow, at different firing temperatures (950-1000-1100 $^{\circ}\text{C}$) in an alumina crucible to avoid substrate interaction as much as possible. (See the **Chapter 3.3.2 Replication materials** section for details)

The colour of the glazes obtained, **Figure 3.6**, was yellow for those fired in air, and green for those fired in N_2 . The viscosity of the melt decreased increasing the firing temperature and this affected the thickness of the glasses obtained. The thickness, composition and colour coordinates of the glazes obtained is shown in **Table 3.15**.

Table 3.15. Colour parameters, thickness and glaze composition (measured by SEM-EDX (wt%)).

	T ($^{\circ}\text{C}$)	Thick. (μm)	L^*	a^*	b^*	c^*	h^*	s^*	Al_2O_3	SiO_2	FeO	PbO
air	950	128	52.1	4.3	23.5	23.9	79.7	41.7	1.0	26.9	3.2	68.8
	1000	49	56.3	2.0	25.1	25.2	85.5	40.9	4.3	24.5	3.4	67.9
	1100	181	55.9	2.0	24.3	24.4	85.4	40.0	6.7	22.4	3.4	67.5
N_2	950	132	50.0	1.2	20.1	20.2	86.5	37.4	1.7	26.6	2.9	68.9
	1000	184	49.2	1.0	18.4	18.4	86.9	35.0	3.5	29.3	2.9	64.3
	1100	135	45.7	1.3	16.1	16.2	85.3	33.4	7.8	26.9	2.7	62.6

The glazes are quite thick, between 100 and 180 μm . As a result of the reaction between the glass and the alumina crucible, an increase in the Al_2O_3 content is observed (from 1% to 7.8%) when the temperature is

increased from 950°C to 1100°C. Glazes fired in N₂ show a greater decrease in the PbO content, due to the lead volatilisation. Consequently, it can be observed that there is an important change between the colour coordinates at 950°C for the glazes air-fired glasses, a^* , b^* and s^* decrease and L^* increases in **Figure 3.33**. The change is less pronounced for the glazes fired in a N₂ atmosphere. In all the cases, the colour coordinates have lower values for the glazes fired in N₂ than in air. The colour coordinates are small positive a^* and large b^* with smaller a^* , b^* and L^* and larger h^* for the glazes fired in N₂ atmosphere.

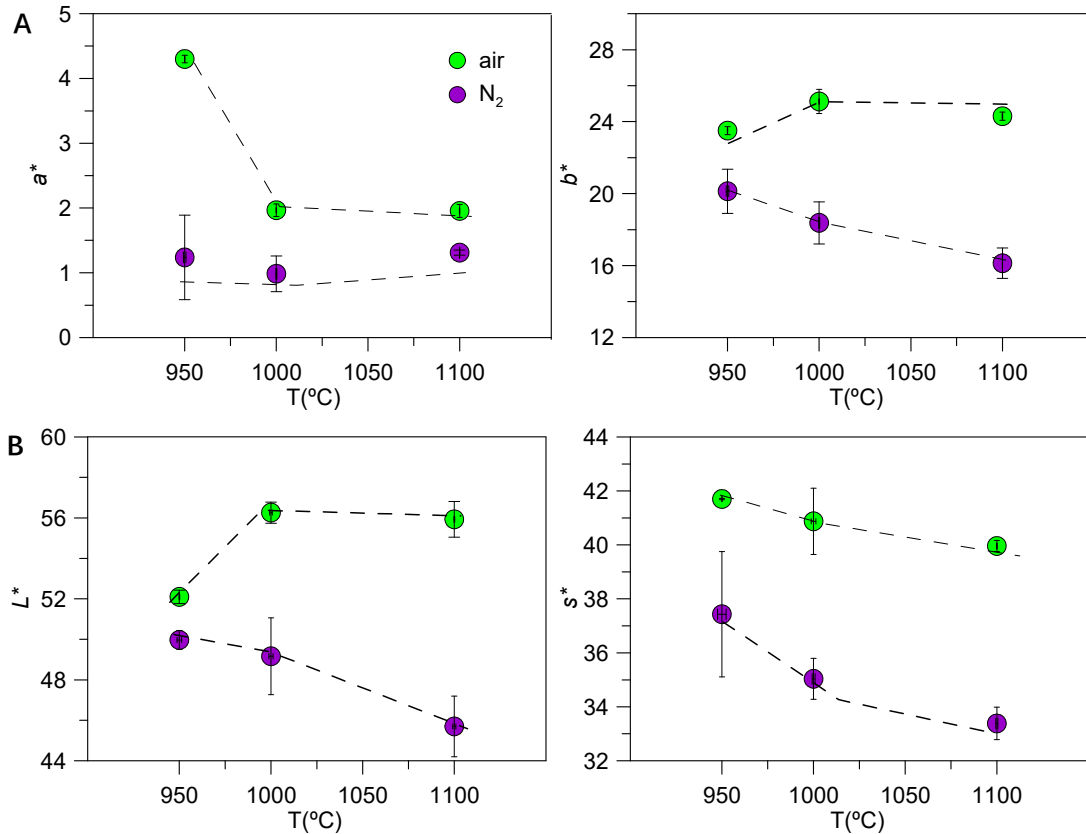


Figure 3.33. Colour coordinates versus temperature. **A** (top) a^* and b^* ; **B** (bottom) L^* and s^* .

With respect to the iron oxidation state, the Fe-K α XAS fit of the pre-peak is shown in **Table 3.16** and **Figure 3.34**. The variogram is shown in **Figure 3.35**, and the centre shift and total area are shown in **Figure 3.36**. The glazes fired in air appear more oxidised and show small differences between the glazes fired at different temperatures. The decrease of the total area at higher temperature, indicates a tendency towards a fivefold coordination.

Table 3.16. Fitted parameters corresponding.

	T (°C)	E ₁ (eV)	A ₁ (eV)	E ₂ (eV)	A ₂ (eV)	C (eV)	A (eV)	A(Fe ²⁺)/A _{tot} x100
air	950	7113.57(1)	0.229(3)	7111.8(1)	0.017(1)	7113.44(1)	0.245(3)	6.9(1)
	1000	7113.53(1)	0.214(3)	7111.8(1)	0.015(1)	7113.41(1)	0.229(3)	6.5(1)
	1100	7113.53(2)	0.208(5)	7111.9(2)	0.016(2)	7113.42(2)	0.224(5)	7.0(2)
N ₂	950	7113.58(1)	0.209(4)	7111.7(1)	0.028(1)	7113.36(1)	0.236(4)	11.7(2)
	1000	7113.58(1)	0.193(3)	7111.9(1)	0.028(1)	7113.36(1)	0.221(3)	12.5(2)
	1100	7113.54(1)	0.166(3)	7111.8(1)	0.030(1)	7113.27(1)	0.196(3)	15.2(2)

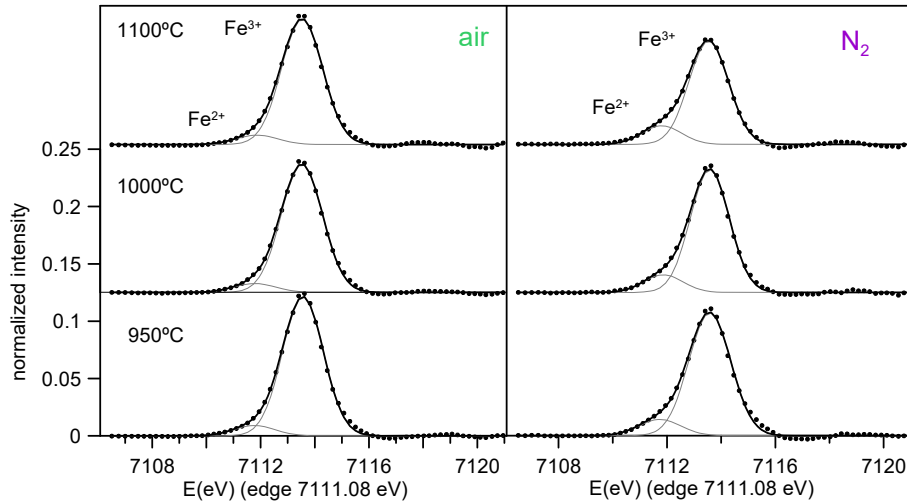


Figure 3.34. Fitted spectra sample fired under different atmospheres.

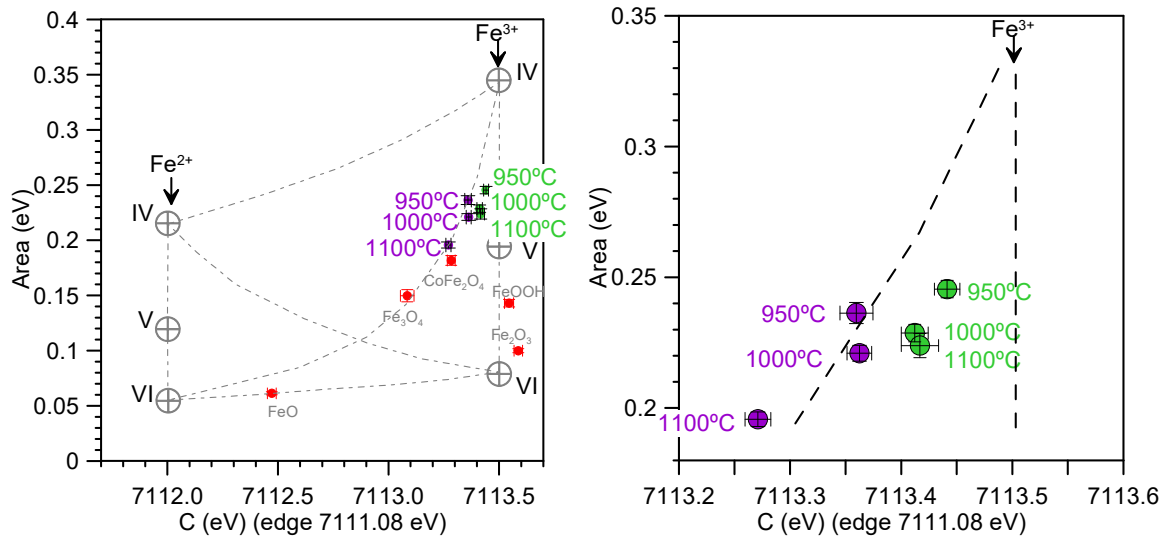


Figure 3.35. Variogram of samples fired under different atmospheres.

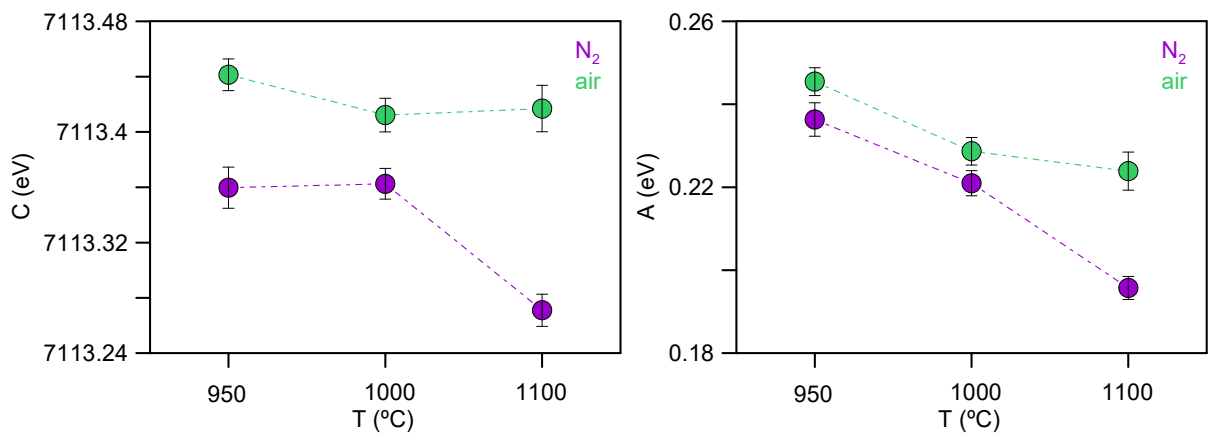


Figure 3.36. Centre Shift and Area of the pre-peak versus temperature and atmosphere.

The main Fe^{3+} peak shows mainly a fivefold coordination and a minor Fe^{2+} peak representing about 7% of the total spectral area for the glazes fired in an air atmosphere, **Figure 3.37**. On the contrary the Fe^{2+} species

fired in both air and N₂ show a sixfold coordination arrangement. The area of the Fe²⁺ peak is more important for the glasses fired in N₂ and increases with the firing temperature (from 11% to 15% of the total area).

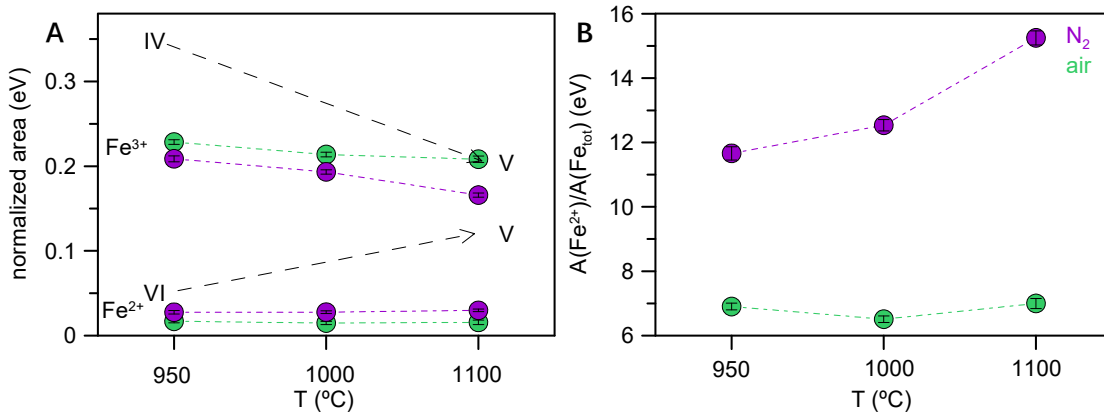


Figure 3.37. (A) Area of the Fe²⁺ and Fe³⁺ pre-edge peaks; and (B) area of the Fe²⁺ peak over total area as a function of temperature and firing atmosphere.

3.5 Discussion

3.5.1 The change in the composition of the body and transparent glaze, and differences in the glazing method between Ming and Qing

Analysis of both ceramic body and glaze composition reveals significant variations in raw material selection and glazing techniques employed during the Ming and Qing dynasties. In a recent study by Nigel (Wood 2021), the author contributes valuable insights suggesting that the increase in kaolin content in the ceramic body composition in the early 17th century reflects a remarkable display of ingenuity, possibly driven by initial raw material scarcity. In particular, there was a transition from the predominant use of *hulu yao* (double-gourd kiln) in the Yuan and Ming dynasties to the adoption of the *zhen yao* (egg-shape) kiln during the Qing dynasty. This transition required a higher proportion of kaolin in the porcelain to accommodate the temperature range of 1180-1350°C (Yuan 2023).

Estimates by Zhou and Li (Zhou 1960) of the firing temperatures for representative siliceous Ming porcelains indicate a range of 1200±20°C, whereas for aluminous Qing bodies the range is around 1300±20°C, indicating a significant increase in the maturation temperature. This increased firing temperature resulted in improved density and strength, associated with the higher levels of mullite and glass at the expense of quartz. Consequently, the increased density and structural integrity resulted in improved translucency and increased thermal shock resistance (Wood 2021).

Despite the relative ease of temperature and atmosphere control in the *hulu yao* (double-gourd kiln) during the Yuan and Ming dynasties, the limited capacity and wide temperature range posed a challenge to production. As a result, the *zhen yao* (egg-shape) kiln became the dominant type during the Qing dynasty, largely due to its ability to address overcome these limitations. To illustrate this point, a simulation of the flue gas velocity flow diagram in both *hulu yao* and *zhen yao* by Yan et al (Yan 2018) is presented (**Figure 3.38**). The simulation clearly shows that the *zhen yao* (egg-shaped kiln) provides greater control over the

atmosphere and temperature, thereby improving the quality through precise regulation of air supply and chimney pumping.

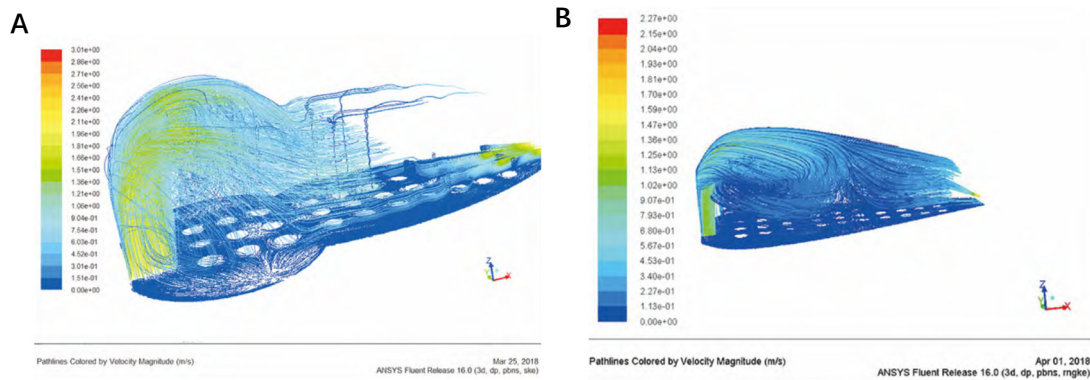


Figure 3.38. The velocity flow diagram of flue gas in the kiln. (A) *hulu yao* (double-gourd kiln); (B) *zhen yao* (egg-shaped kiln). (Yan 2018)

The composition differences observed in the yellow glazes have significant implications for the selection of raw materials and the inter-diffusion processes occurring between the glaze and the ceramic body. These variations also play a crucial role in the long-term stability and preservation of lead glazes in ancient ceramics, with particular emphasis on the presence of aluminium (Al) due to the diffusion from the body. The reactions and diffusion processes that take place from the body to the glaze are critical in determining the overall quality and stability of lead-rich glazes (Molera 2001). In this regard, despite the absence of a transparent lime glaze layer between the body and the yellow glaze in the Qing samples, the higher concentration of Al in the body and its diffusion into the glaze matrix contribute to a strong bond and enhanced stability of the yellow glaze network, thus ensuring the maintenance of high-quality characteristics.

It is therefore possible that the absence of an underlying transparent lime glaze in the Qing yellow glazes is a result of the increase in the Al_2O_3 content of the porcelain body. This change during the Yuan-Ming dynasties only affects the yellow glazed imperial porcelains and not the glazed tiles. However, advances in atmospheric and temperature control together with improved selection and refinement of raw materials, made it possible to achieve a pure yellow colour even when the glaze was applied directly to the porcelain body.

The analysis did not reveal any significant variations in the colour parameters between the imperial yellow glazes. However, there were notable differences in the thickness of the rim and foot in different object types. Ming samples, especially dishes, had thinner feet compared to Kangxi bowls, which had thicker feet. As no supporting pins were found in any of the objects, and while the rim was fully glazed, the edge of the foot remained unglazed. Consequently, the yellow glazes were fired with the foot providing support rather than being inverted.

3.5.2 The firing conditions of the imperial yellow

Iron occurs predominantly as Fe^{3+} in fivefold coordination in all the imperial yellow glazes, while the presence of Fe^{2+} is minimal. Fe^{2+} , as evidenced by the broad absorption observed around 1100nm, which is found in yellow glazes and transparent lime glazes, may contribute to their slightly greenish appearance.

The imperial yellow hue, characterised by an almost pure yellow colour, is based on the application of a thin glaze layer of approximately 50 μm in thickness. The variation in the colour coordinates observed in the foot of the objects can be attributed to the different thicknesses of the glaze layer. No significant differences in thickness are observed between the Ming and Qing samples. The lightness and oxidation state of the historic samples are intermediate between the replicas fired in air and those in an oxygen-free atmosphere. A comparative analysis of the replicated yellow glazes shows that the historical glazes were fired under oxidising conditions, but slightly more reducing than the electric kiln used in our replication experiments. It is worth noting that the presence of a lime glaze substrate, as observed in the Ming glazes, can contribute to enhancing the yellow colour of the glazes, although both thickness and firing temperature are more important. Furthermore, the presence of transparent yellow glaze results in a higher calcium content, which also favours the oxidation of iron. This suggests that the Ming yellow glazes may have been fired under a more reducing atmosphere than the Qing samples.

Both the yellow and transparent glazes are very homogeneous, with no undissolved particles found except for the presence of feldspars at the interface. The refractive index of anorthite (1.573-1.590) (Kuryaeva 2007) found in the Ming glazes is slightly higher than that of sanidine (1.524-1.534) present in the Qing glazes (Laurell Lyne 2013). This difference may contribute to a higher gloss appearance, although it is not expected to have a significant impact on the overall appearance.

The presence of large crystallites at the interface suggests a prolonged cooling process. The $\%(\text{PbO}/\text{SiO}_2)$ ratio of replica glazes of comparable thickness (approximately 100 μm) is shown in **Figure 3.39**. When compared with those of the historical yellow glazes (**Figure 3.11**), the ratios for the Ming and Qing yellow glazes are approximately 1 to 1.5 and 2 to 2.5 respectively. These ratios correspond to firing temperatures above 1000°C for the Ming glazes and below 1000°C for the Qing glazes. It is important to note, however, that this is an approximation, as we have not taken into account firing and cooling rates, nor the slightly reducing atmosphere used in the historical samples.

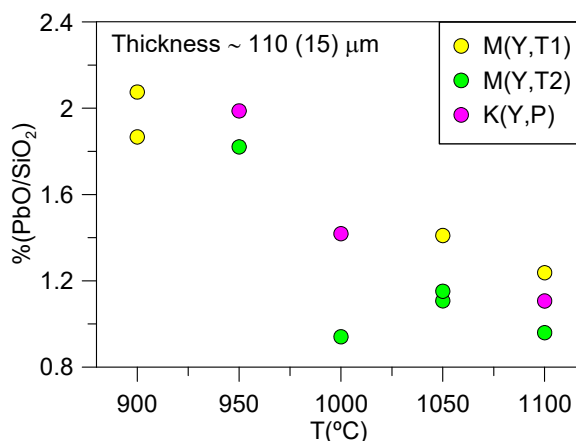


Figure 3.39. PbO/SiO₂ ratio of replications under different temperatures.

3.5.3 The colour of the yellow glaze

The yellow glazes of the Qing dynasty show a slight decrease in iron content compared to the Ming dynasty. However, within a specific range of iron additions, no significant variations are observed in the oxidation state and coordination state of iron. This suggests that factors other than iron content play a more significant role in determining the colouration of the glazes.

The findings derived from the replicated samples indicate that several factors play a significant role in determining the ultimate colour of the yellow glaze, including the glaze thickness, firing temperature, substrate composition, and firing atmosphere. Importantly, these factors are interconnected, as variations in firing temperature and glaze thickness impact the interdiffusion between the glaze and substrate, consequently influencing the glaze composition. Among the various elements, calcium demonstrates a particularly pronounced effect on enhancing the yellow hue. Furthermore, the presence of elevated levels of CaO has been shown to facilitate the oxidation of iron, a phenomenon previously documented by Yuan et al. (Yuan 2022). A higher firing temperature also increases the yellow colour (an elevation in the hue, h^* value). Thickness reduces the lightness and increases the colour saturation due to the reduced contribution of the underlying substrate. It also increases the a^* and b^* colour coordinates, but increasing a^* from negative to positive changes the hue from yellow-greenish to yellow-reddish. Therefore, thin glazes are required to avoid a reddish shift in colour. A small amount of Fe^{2+} is present in all the cases, which contributes to increased lightness and saturation. However, it also results in a shift towards more greenish tones and less prominent red hues and indicates a positive impact on the yellow coloration.

Regarding the atmosphere during the firing, Fe^{3+} is mainly present in fivefold coordination both in air and in oxygen-free firing atmospheres. In air, the Fe^{3+} shifts towards fivefold coordination as the temperature increases. The use of an oxygen-free atmosphere leads to an increase in the Fe^{2+} contribution in six-fold coordination, as a result of which we observe a decrease in the colour coordinates, a^* and b^* , as well as in the colour saturation, s^* and lightness, L^* , which are more important at higher firing temperatures.

3.6 Conclusions

Several changes have been noted between the Ming and Qing imperial yellow porcelains: changes in the composition of the porcelain, which have been attributed to the initial shortage of raw materials, and which resulted in an increase in the firing temperature of the porcelain (from 1200 °C to 1300 °C). Changes in kiln design, from the *hulu yao* (double-gourd kiln) to the *zhen yao* (egg-shaped kiln), which allowed for greater control of temperature and atmosphere and finally, changes in the glazing technique, from applying the yellow glaze over a transparent lime glaze in the Ming dynasty to direct glazing directly into the porcelain in the Qing dynasty.

The study of glazes of controlled composition applied over different substrates and fired under controlled conditions showed that the final colour of the yellow glaze is influenced by four interrelated parameters: glaze thickness, firing temperature, substrate composition, and firing atmosphere. The interdiffusion

between the glaze and substrate, influenced by the firing temperature and glaze thickness, has a direct effect on glaze composition and colour. A thin glaze layer and oxidizing conditions are required to achieve the yellow colour. All the historical yellow glazes are very thin, typical thickness about 50 μm . The presence of calcium has a more pronounced effect on enhancing the yellow colour compared to other elements. The presence of a high-lime transparent glaze beneath the yellow glaze in the Ming glazes increases the calcium content of the yellow glazes compared to the Qing glazes.

Higher firing temperatures also contribute to a deeper yellow colour. The experiments showed that typical firing temperatures of the yellow glazes must have been around 1000°C. However, the firing and cooling times of historical glazes are far longer than those used in the glazes obtained in the laboratory.

The primary form of iron in the glazes is Fe^{3+} with fivefold coordination. Fe^{2+} is also determined even in the glazes fired in air. The relative Fe^{2+} content increases with increasing the firing temperature. The colour of the yellow glaze shifts from yellow-gold in air-fired samples to yellow-green in air-free-fired samples, with lower b^* and L^* values that decrease with increasing the firing temperature. All the results show that the historic glazes were fired under oxidising conditions but slightly more reducing than the electric kiln we used in the replications. The presence of a small amount of Fe^{2+} has a positive effect on the brightness by increasing transparency.

References

- Baiocchi E, Montenero A, Bettinelli M, Sotgiu A (1981). Optical and magnetic properties of first-row transition metal ions in lead-silicate glass. *J. Non-Cryst. Solids*, 46 (2): 203-215.
[https://doi.org/10.1016/0022-3093\(81\)90161-7](https://doi.org/10.1016/0022-3093(81)90161-7)
- Bingham PA (2000). *The Environment of Iron in Silicate Glasses*. University of Sheffield. Doctoral Thesis.
- Bingham PA, Parker JM, Searle TM, Smith I (2007). Local structure and medium range ordering of tetrahedrally coordinated Fe³⁺ ions in alkali–alkaline earth–silica glasses. *J. Non-Cryst. Solids*, 353 (24-25): 2479-2494. <https://doi.org/10.1016/j.jnoncrysol.2007.03.017>
- Borisov A, Behrens H, Holtz F (2017). Effects of strong network modifiers on Fe³⁺/Fe²⁺ in silicate melts: an experimental study. *Contrib Mineral Petrol*, 172:34. <https://doi.org/10.1007/s00410-017-1337-1>
- Burns RG (1993). *Mineralogical Applications of Crystal Field Theory*, 2nd Ed., Cambridge Univ. Press.
<https://doi.org/10.1017/CBO9780511524899>
- Cohen BM, Uhlmann DR, Shaw RR (1973). Optical and electrical properties of lead silicate glasses. *J. Non-Cryst. Solids*, 12 (2): 177-188. [https://doi.org/10.1016/0022-3093\(73\)90067-7](https://doi.org/10.1016/0022-3093(73)90067-7)
- Cui JF, Lei Y, Jin ZB, Huang BL and Wu XH (2010). Lead isotope analysis of tang sancai pottery glazes from gongyi kiln, henan province and huangbao kiln, shaanxi province. *Archaeometry*, 52(4): 597–604.
- Densem NE, Turner WES, *J. Soc. Glass Tech.*, 1938, 22: 372. <https://doi.org/10.1111/j.1475-4754.2009.00495.x>
- Duffy JA (1993), A review of optical basicity and its applications to oxidic systems. *Geochim. Cosmochim. Acta*, 57 (16): 3961-3970. [https://doi.org/10.1016/0016-7037\(93\)90346-X](https://doi.org/10.1016/0016-7037(93)90346-X)
- Dupree R, Ford N, Holland D (1987), An examination of the ²⁹Si environment in the PbO-SiO₂ system by magic angle spinning nuclear magnetic resonance. *Phys. Chem. Glasses* 28(2): 78-84.
- Farges F, Lefrère Y, Rossano S, Berthereau A, Calas G, E. Brown Jr. G (2004). The effect of redox state on the local structural environment of iron in silicate glasses: a combined XAFS spectroscopy, molecular dynamics, and bond valence study. *J. Non-Cryst. Solids*, 344(3): 176-188.
<https://doi.org/10.1016/j.jnoncrysol.2004.07.050>
- Fayon F, Bessada C, Douy A, Massiot D (1999). Chemical bonding of lead in glasses through isotropic vs anisotropic correlation: PASS shifted echo. *J. Magn. Reson.*, 137(1): 116-21.
<https://doi.org/10.1006/jmre.1998.1641>
- Fenstermacher JE (1980). Optical absorption due to tetrahedral and octahedral ferric iron in silicate glasses. *J. Non-Cryst. Solids*, 38-39, part1: 239-244. [https://doi.org/10.1016/0022-3093\(80\)90425-1](https://doi.org/10.1016/0022-3093(80)90425-1)

- Fluegel A (2007), Glass viscosity calculation based on a global statistical modeling approach, *Eur. J. Glass Sci. Technol. A* 48 (1): 13–31. <https://glassproperties.com/viscosity/>
- Gulmini M, Appolonia L, Framarin P, Mirti P (2006). Compositional and technological features of glazed pottery from Aosta Valley (Italy): a SEM–EDS investigation. *Anal Bioanal Chem*, 386: 1815–1822. <https://doi.org/10.1007/s00216-006-0806-6>
- Guo YY (1987). Raw materials for making porcelain and the characteristics of porcelain wares in the north and south China in ancient times. *Archaeometry*, 29 (1): 3–19.
- Hannoyer B, Lenglet M, Durr J, Cortes R (1992), Spectroscopic evidence of octahedral iron (III) in soda-lime silicate glasses. *J. Non-Cryst. Solids*, 151(3): 209-216. [https://doi.org/10.1016/0022-3093\(92\)90031-E](https://doi.org/10.1016/0022-3093(92)90031-E)
- Hampton WM (1946). Colour of Heavy Lead Silicate Glass. *Nature*, 158; 582. <https://doi.org/10.1038/158582a0>
- Hatcher H, Tregear M, Wood N (1985), Ceramic Changes at Jingdezhen in the 17th CAD. The 2nd International Conference on Ancient Chinese Pottery and Porcelain - Its Scientific and Technical Insights (Abstracts), China Academic Publishers, Beijing, 69-70.
- Hall E, Pollard AM (1986). Analysis of Chinese Monochrome Glazes by X-Ray Fluorescence Spectrometry. Scientific insights on ancient Chinese pottery and porcelain. In: Shanghai Institute of Ceramics. Science Press, Peking, pp. 382–386.
- Holmqvist E, Heinonen T, Väisänen R, Pihlman A, Koivisto A, Russow E (2020). Ceramic fabrics and lead glazes of late medieval redware pots in the Helsinki, Turku and Tallinn regions (ED-XRF, SEM-EDS). *J. Archaeol. Sci. Rep.* , 34:102627. <https://doi.org/10.1016/j.jasrep.2020.102627>
- Khalil EMA, El-Batal FH, Hamdy YM, Zidan HM, Aziz MS, Abdelghany AM (2010). UV-Visible and IR Spectroscopic Studies of Gamma Irradiated Transition Metal Doped Lead Silicate Glasses. *Silicon*, 2:49–60. <https://doi.org/10.1007/s12633-009-9029-8>
- Kuryaeva R, Kirkinskii VA, Surkov N (2007). Refractive Index of CaAl₂Si₂O₈ Glass and Crystalline Anorthite at Pressures up to 5.0 Gpa. *Geochem. Int.* , 45(3): 308-311. <https://doi.org/10.1134/S001670290703010X>
- Lang JF, Cui JF (2017). A study of style and producing area of the glazed pottery lei liquid vessels unearthed from a Qi tomb of the Warring States period in Linzi city (临淄战国齐墓出土釉陶器的风格与产地—兼论我国铅釉陶的起源问题). *Huaxia Archaeology (华夏考古)*, 2: 95–101.
- Laurell Lyne Å, Redelius P, Collin M, Birgisson B (2013). Characterization of stripping properties of stone material in asphalt. *Mater. Struct.* , 46: 47–61. <https://doi.org/10.1617/s11527-012-9882-6>

- Molera J, Pradell T, Salvadó N, Vendrell-Saz M (2001). Interactions between Clay Bodies and Lead Glazes. *J. Am. Ceram. Soc.*, 84(5): 1120–1128. <https://doi.org/10.1111/j.1151-2916.2001.tb00799.x>
- Möncke D, Papageorgiou M, Winterstein-Beckmann A, Zacharias N (2014). Roman glasses coloured by dissolved transition metal ions: redox reactions, optical spectroscopy and ligand field theory. *J. Archaeol. Sci.*, 46: 23-36. <http://dx.doi.org/10.1016/j.jas.2014.03.007>
- Mysen BO, Carmichael ISE, Virgo D (1985), A comparison of iron redox ratios in silicate glasses determined by wet-chemical and ^{57}Fe Mössbauer resonant absorption methods. *Contrib. Min. Petrol.*, 90: 101-106. <https://doi.org/10.1007/BF00378253>
- Ookawa M, Sakurai T, Mogi S, Yokokawa T (1997). Optical Spectroscopic Study Lead Silicate Glasses Doped Heavily with Iron Oxide. *Materials Transactions JIM*, 38(3): 220-225. <https://doi.org/10.2320/matertrans1989.38.220>
- Özçatal M, Yaygingöl M, İssi A, Kara A, et al (2014). Characterization of lead glazed potteries from Smyrna (Izmir/Turkey) using multiple analytical techniques; Part I: Glaze and engobe. *Ceram. Int.*, 40(1): 2143–2151. <https://doi.org/10.1016/j.ceramint.2013.09.014>
- Pollard M, Wood N (1986), The development of Chinese porcelain technology at Jingdezhen. *Proceedings of the 24th International Symposium on Archaeometry*. Smithsonian Institution Press. Washington, 105-116.
- Pradell T, Molera J (2020). Ceramic technology. How to characterise ceramic glazes. *Archaeol. Anthropol. Sci.*, 12,189. <https://doi.org/10.1007/s12520-020-01136-9>
- Rao TGVM, Rupesh Kumar A, Hanumantha Rao B, Veeraiah N, Rami Reddy M (2012). Optical absorption, ESR, FT-IR spectral studies of iron ions in lead oxyfluoro silicate glasses. *J. Mol. Struct.*, 1021: 7–12. <https://doi.org/10.1016/j.molstruc.2012.04.026>
- Rossano S, Balan E, Morin G, Bauer JP, Calas G, Brouder C (1999). ^{57}Fe Mössbauer spectroscopy of tektites. *Phys. Chem. Miner*, 26: 530–538. <https://doi.org/10.1007/s002690050216>
- Rybicki J, Rybicka A, Witkowska A, Bergmanski G, Di Cicco A, Minicucci M, and Mancini G (2001). The structure of lead-silicate glasses: molecular dynamics and EXAFS studies. *J. Phys. Condens. Matter*, 13, 9781–9797. DOI 10.1088/0953-8984/21/39/395502
- Schreiber HD, Kozak SJ, Merkel RC, Balazs, Jones Jr PW (1986), Redox equilibria and kinetics of iron in a borosilicate glass-forming melt. *J. Non-Cryst. Solids*, 84 (1): 186-195.
- Schibille N, De Juan Ares J, Teresa Casal García M, Guerrot C (2020). Ex novo development of lead glassmaking in early Umayyad Spain. *PNAS*, 117(28): 16243–16249. <https://doi.org/10.1073/pnas.200344011>

- Shen JY, Henderson J, Evans J, Chenery S, Zhao FY (2019). A study of the glazing techniques and provenances of Tang sancai glazes using elemental and lead isotope analyses. *Archaeometry* 61(2): 358–373. <https://doi.org/10.1111/arcm.12436>
- Stroud JS (1971), Optical Absorption and Color Caused by Selected Cations in High-Density, Lead Silicate Glass. *J. Am. Ceram. Soc.* 54 (8): 401-406. <https://doi.org/10.1111/j.1151-2916.1971.tb12331.x>
- Stoch P, Szczerba W, Bodnar W, Ciecinska M, Stoch A, Burkel E (2014). Structural properties of iron-phosphate glasses: spectroscopic studies and ab initio simulations. *Phys. Chem.Chem.Phys.*, 16: 19917-19927. <https://doi.org/10.1039/C4CP03113J>
- Ting C, Lichtenberger A, Raja R (2019). The technology and production of glazed ceramics from Middle Islamic Jerash, Jordan. *Archaeometry* 61(6): 1296–1312. <https://doi.org/10.1111/arcm.12489>
- Tite MS, Freestone IC, Mason R, Molera J, Vendrell-Saz M, Wood N (1998). Lead Glazes in Antiquity—Methods of Production and Reasons for Use. *Archaeometry* 40(2): 241-260. <https://doi.org/10.1111/j.1475-4754.1998.tb00836.x>
- Tite MS, Freestone IC, Wood N (2012). An investigation into the relationship between the raw materials used in the production of Chinese porcelain and stoneware bodies and the resulting microstructures. *Archaeometry*, 54(1): 37–55. <https://doi.org/10.1111/j.1475-4754.2011.00614.x>
- Uchino T, Nakaguchi K, Nagashima Y, Kondo T (2000). Prediction of optical properties of commercial soda–lime–silicate glasses containing iron. *J. Non-Cryst. Solids*, 261 (1-3), 72–78. [https://doi.org/10.1016/S0022-3093\(99\)00617-1](https://doi.org/10.1016/S0022-3093(99)00617-1)
- Vercamer V (2016). Spectroscopic and Structural Properties of Iron in Silicate Glasses. Université Pierre et Marie Curie. Doctoral Thesis.
- Wakamatsu M, Takeuchi N, Ishida S (1987). Effect of furnace atmosphere on color of iron glaze. *J. Non-Cryst. Solids*, 95-96, part 2: 733-740. [https://doi.org/10.1016/S0022-3093\(87\)80675-0](https://doi.org/10.1016/S0022-3093(87)80675-0)
- Weyl WA, 1951. *Coloured Glasses*. Reprint by Society of Glass Technology, Sheffield, 2016.
- Wen R (2012). The cobalt blue pigment used on Islamic ceramics and Chinese blue-and-white porcelains. University of Oxford. Doctoral thesis. ISNI: 0000 0003 7912 7938.
- Wilke M, Farges F, Petit P, Jr. Brown GE, Martin F (2001), Oxidation state and coordination of Fe in minerals: An Fe K-XANES spectroscopic study, *Am. Mineral.* 86(5): 714-730. <https://doi.org/10.2138/am-2001-5-612>.
- Wilke M, Partzsch GM, Bernhardt R, Lattard D (2005), Determination of the iron oxidation state in basaltic glasses using XANES at the K-edge, *Chem. Geol.* 220: 143-161. <https://doi.org/10.1016/j.chemgeo.2005.03.004>.

- Wong J, Austin AC, *Glass Structure by Spectroscopy*, Marcel Dekker, New York, 1976, p589. ISBN-10: 0824764684
- Wood N (1999), *Chinese Glazes: Their Origins, Chemistry and Recreation*, A&C Black, London, UK, 1999.
- Wood, N, 1983. Provenance and technical studies of Far Eastern ceramics. In: Kamei Meitoku (Ed.), *Trade Ceramics Studies 3*. Japan Society for the Study of Oriental Trade Ceramics, Kamakura City, pp. 119–144.
- Wood N (2021). An AAS study of Chinese imperial yellow porcelain bodies and their place in the history of Jingdezhen's porcelain development. *Advances in Archaeomaterials*, 2(1): 49–65.
<https://doi.org/10.1016/j.aia.2021.09.002>
- Wu JM (2007). *The Preliminary Study of Jingdezhen's Traditional Low Temperature Yellow-glaze*. Master thesis. Jingdezhen Ceramic University.
- Yan LT, Zhou Y, Ma B, Sun HY, Li L, Feng XQ (2022). The coordination structure and optical property of iron ions in the traditional lead glazes. *J. Mol. Struct.*, 1257: 132593.
<https://doi.org/10.1016/j.molstruc.2022.132593>
- Yan XH, Li CT, Feng Q, Lu L (2018). Study on the Relationship between the Structure of Gourd Kiln and Jingdezhen Kiln(葫芦窑与景德镇窑结构关系的研究). *China Ceramics (中国陶瓷)*: 54(8): 57-64.
DOI:10.16521/j.cnki.issn.1001-9642.2018.08.011
- Yin XS, Huang TJ, Gong H (2020). Chemical evolution of lead in ancient artifacts-A case study of early Chinese lead-silicate glaze. *J. Eur. Ceram. Soc.*, 40(5): 2222-2228.
<https://doi.org/10.1016/j.jeurceramsoc.2020.01.002>
- Yin M, Rehren T, Zheng JM (2011), The earliest high-fired glazed ceramics in China: the composition of the proto-porcelain from Zhejiang during the Shang and Zhou periods (c. 1700-221 BC), *J. Archaeol. Sci.* 38: 2352–2365. <http://dx.doi.org/10.1016/j.jas.2011.04.014>
- Yuan MY, Hou JY, Gorni G, Crespo D, Li Y, Pradell T (2022), Jun ware glaze colours: An X-ray absorption spectroscopy study, *J. Eur. Ceram. Soc.* 42(6): 3015–3022.
<https://doi.org/10.1016/j.jeurceramsoc.2022.02.016>
- Yuan Q, Wu JM (2023), Interior Spatial Distribution of Temperature in Jingdezhen Kilns Based on Experimental Archaeology (基于实验考古的景德镇窑内部温度空间分布研究), *China Ceramic Industry (中国陶瓷工业)*, 30(3): 14-17. DOI: 10.13958/j.cnki.ztcg.2023.03.003

Zhang FK, Zhang ZG (1980). Low-temperature coloured glazed of successive dynasties in ancient China. *Journal of the Chinese Ceramic Society (硅酸盐学报)*, 8(1): 9-19. DOI:10.14062/j.issn.0454-5648.1980.01.002

Zhou R, Li JZ (1960). Research on the porcelain body, glaze and firing technology of Jingdezhen in the past. (景德镇历代瓷器胎、釉和烧制工艺的研究), *Silicate (硅酸盐)* 2: 49-62.

Chapter 4 Jun ware glaze colours

钧窑



Chapter 4 Jun ware glaze colours

4.1 Introduction

Jun ware is a high-fired grey stoneware with a subtle pale bluish and red or purple lime glaze, created in the end of the North Song dynasty (960-1127) in the first quarter of the 12th century (Tichane 1978, Wood 1999, Wood 2013) and which continued to be produced during the Jin (1115-1234), Yuan (1271-1368), early Ming (1368-1435) dynasties in the vicinity of ancient Yuzhou (Henan province, central plains) of China.

Unlike other translucent glazes, Jun ware glazes are distinguished by their medium gloss and depth, which attracts much admiration and attention. Jun ware can be divided into Classic Jun (including monochrome and red splashed Jun) and Official Jun (also known as numbered Jun) (**Figure 4.1**). While there is little debate about the continuous production of Classic Jun, the dating of Official Jun remains a subject of considerable debate, with some scholars placing it in the early Ming dynasty (Li 2007), while others argue for its existence in the Jin (1115-1234) or Yuan (1271-1368) dynasties (Miao 2016). The distinguishing feature of Classic Jun is in its opalescent light blue glaze decorated with purple/red splashes (**Figure 4.1A, B**), while Official Jun is characterised by a purple/red glaze either mixed or applied over a darker blue glaze (**Figure 4.1C, D**). On closer inspection, the blue glaze reveals submillimetre areas of varying colour and opacity; the combination of dark blue transparent areas and light blue opaque areas, gives to the glaze a three-dimensional resemblance to a cloudy sky. Similarly, the red glaze combines translucent purple areas with light red opaque areas.

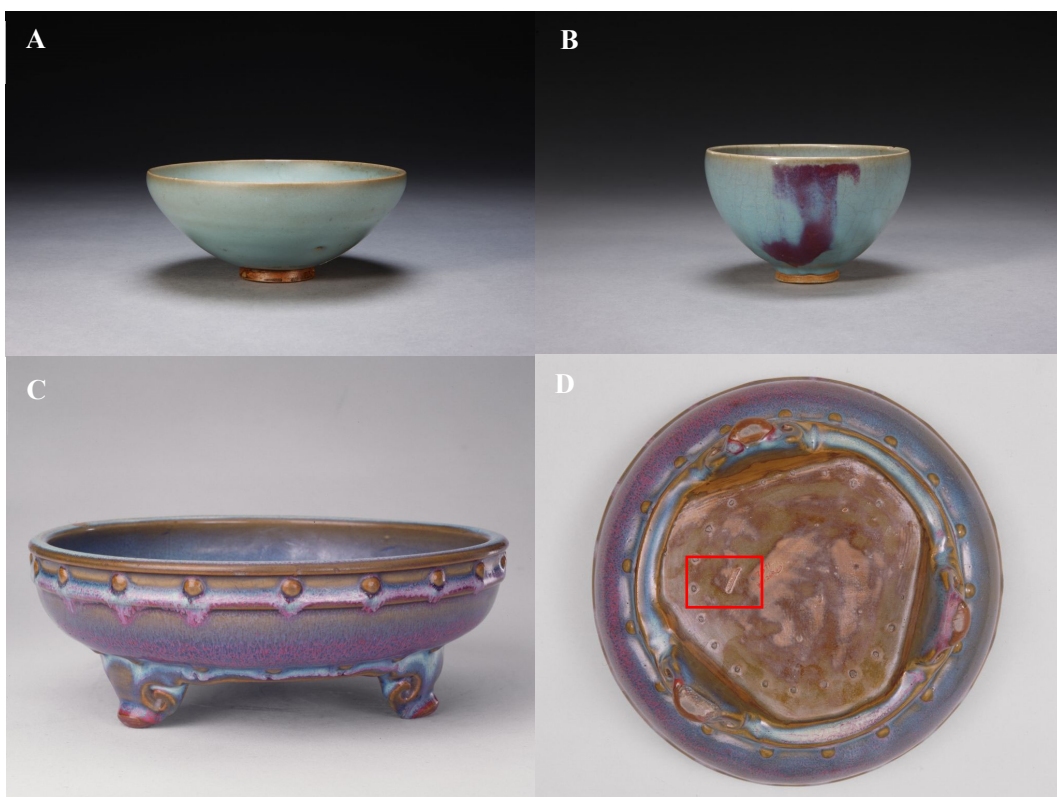


Figure 4.1. (A) The Classic Jun, North Song dynasty (960-1127), <https://www.dpm.org.cn/collection/ceramic/227953.html>; (B) The Classic Jun, Jin dynasty (1115-1234), <https://www.dpm.org.cn/collection/ceramic/227947.html>; (C, D) The numbered Jun (number ‘一’ is one in Chinese), Song dynasty (960-1275), <https://www.dpm.org.cn/collection/ceramic/227141.html>. This kind of furnishing objects is

well decorated and has high quality, which was written the number from one to ten by Chinese character. The number indicates their size, with one being the largest and ten the smallest.

Furthermore, the use of copper glaze and pigments in Jun ware represents a significant advance in the field of ancient Chinese porcelain. Jun ware stands out as a pioneering example of the successful application of red glaze application in the history of Chinese porcelain. The introduction of reds and purples was achieved by incorporating copper into the glazes, either in the form of brush strokes (**Figure 4.1b**) or as a surface layer (**Figure 4.1c**). Based on the knowledge and documented experience of potters, the glaze composition is thought to include a combination of finely ground alkali stone, iron ore, copper ore, animal bone, shell, and white agate (Gao 2014a). The presence of brass stone and malachite has also been suggested as potential constituents (Gao, 2014b).

In addition to the composition of the body and glaze, and the technique used to apply the glaze, the firing process plays a crucial role in determining the visual characteristics of the glaze, as the colour of metallic ions or oxides within the glaze is dependent on their oxidation state during firing. The achievement of high temperatures and the implementation of a slow cooling process are also essential factors influencing the aesthetic appearance of the glaze, as they contribute to the formation of bubbles, crystals, and phase separation (Wood 1999). The Mantou kiln, named for its resemblance to the shape of a steamed bun (馒头, the staple food of the central and northern regions of China), is recognised as the archetypal and earliest kiln associated with Jun ware, which was prevalent in northern China since the Warring States period (475/403-221 B.C.E) to the late Ming dynasty (1368-1644 AD) (Cooper 2020). Excavations of Song dynasty Jun ware kilns provide insight into the firing process employed. Initially, firing takes place in an oxidising atmosphere, followed by the addition of more wood to maintain a full and enclosed space within the kiln. This phase ensures incomplete combustion of the wood, generating sufficient smoke to maintain a reduced atmosphere for sufficient period of time. Once the temperature has reached a uniform and sufficiently high level, the wood is quickly removed, and the kiln door is opened to begin the cooling process. This final stage takes place in a neutral (weakly reducing) atmosphere. **Figure 4.2** shows a detailed top view and side view of the Mantou kiln to illustrate its features. The kiln, which is built into the ground, has excellent heat retention properties, allowing for a gradual cooling process that prevents damage to the objects even when the kiln door is opened abruptly.

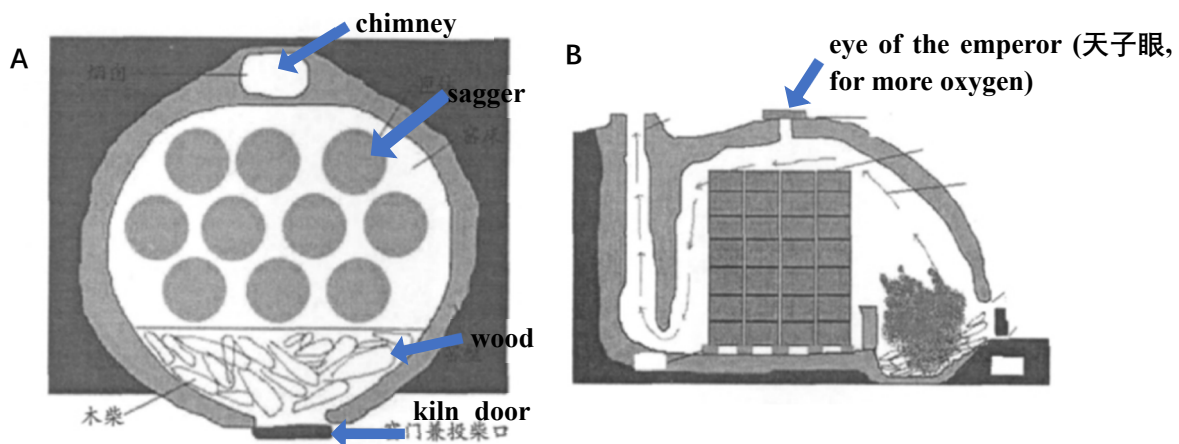


Figure 4.2. (A) Top view and (B) the side view of the kiln (Yan 2012)

Observation of Jun ware blue glazes reveals a distinctive appearance reminiscent of the sky, characterised by the presence of transparent blue and whitish-opaque submillimetre regions (**Figure 4.5** and **Figure 4.11**). Extensive research has shown that the nanostructure and the presence of metal ions, particularly Fe ions, play a significant role in producing this visual effect. The opacity of the glazes results from the scattering of light within the glass nanostructure (Hou 2018), which occurs as a result of a liquid-liquid phase separation occurring in a lime glaze at firing temperatures of around 1200°C, facilitated by a high SiO₂:Al₂O₃ ratio over 7:1 (Hou 2018, Kingery 1983a, Kingery 1983b, Chen 1983, Vandiver 2016). Two glass nanostructures are found, a lime-rich (also enriched in Fe, Mg, P and Ti) droplet-like and a silica-rich (also enriched in K and Na) matrix (Hou 2018, Chiang 1983) (**Figure 4.3**), similar to that found in basaltic systems (Hou 2018, Roedder 1977, Roedder 1992, Philpotts 1982). Recent investigations into the nanostructure of Jun glazes (Hou 2018) have further shown that the presence of different nanostructures (worms and interconnected areas, mainly observed in Official Jun glazes, and spherical droplets, mainly observed in Classic Jun glazes) correlates with variations in the K₂O/Na₂O content of the glazes (**Figure 4.3**), while higher concentrations of CaO and P₂O₅ contribute to a greater volume fraction of larger lime-rich droplets, either isolated or interconnected. The different index of refraction of the two glass components give rise to Mie scattering, whereby light travels through the glaze until it is scattered in the nanostructure (via multiple scattering processes) or is absorbed by the metal ions present in the glaze. Ultimately, the back-scattered light reaches the surface of the glaze, and a higher volume fraction of droplets contributes to an increase in total diffuse reflectance, resulting in increased lightness and opacity (Hou 2018). Distinct submillimetre regions of the glaze exhibit variations in their calcium content, leading to the formation of larger and more numerous droplets in calcium-rich areas (resulting in greater opacity), whereas smaller and fewer droplets are observed in calcium-poor areas (resulting in greater transparency). Consequently, the final visual characteristics of the glazes, including their colour (ranging from dark to light blue) and pearlescent translucency, result from the interplay between these submillimetre calcium-rich and calcium-poor regions. The blue colour of the glazes, which is attributed to Fe²⁺ ions dissolved in the glaze which show a broad and prominent absorption band in the near infrared (NIR) region around 1100 nm, extending into the red part of the spectrum (Weyl 1951, Ehrt 2001). A previous study using Mössbauer spectroscopy showed that iron primarily exists as Fe²⁺ in both the dark blue glazes and the light blue glazes, with no significant differences between them. Therefore, the previous explanation provided does not seem to be entirely satisfactory. However, we know that iron is more concentrated in the calcium-rich droplets than in the calcium poor matrix, regrettably the oxidation state of iron in the calcium-rich and calcium-poor areas of the glaze remains unknown.

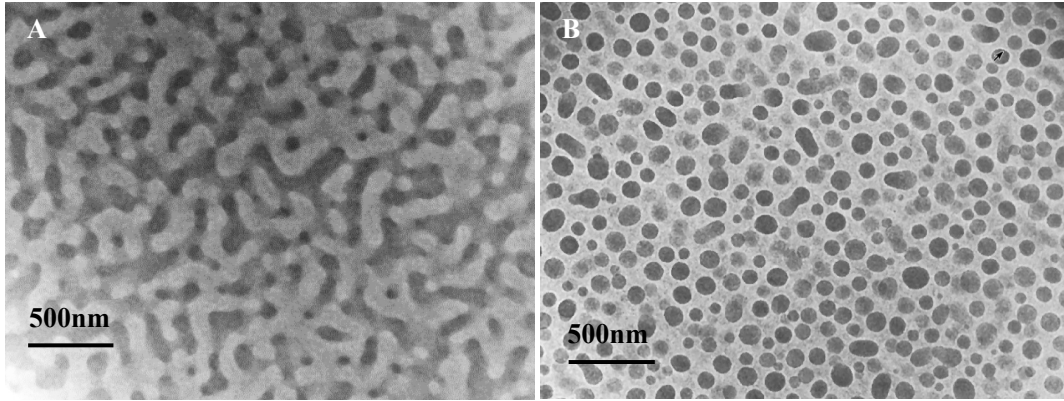


Figure 4.3. (A) JS80F (The official Jun); (B) JS4F (The classic Jun) (Hou 2018)

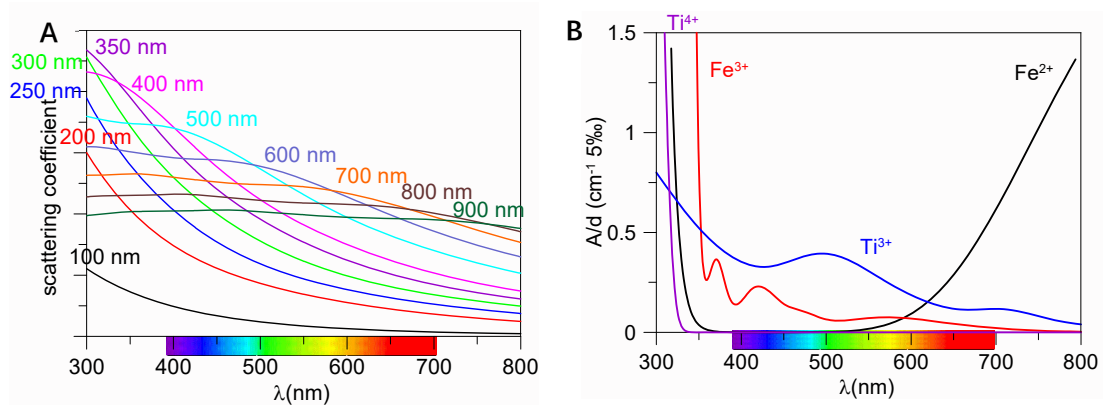


Figure 4.4. Droplets scattering and absorption (Hou 2018).

Titanium is another important component of Jun ware glazes. Traces of titanium dioxide occur naturally in crustal rocks, including the granitic rock used as one of the raw materials in Jun ware production (Wood 1999). The interaction between the glaze and the stoneware ceramic results in chemical interdiffusion, leading to the formation of a dark olive-brown glaze layer at the interface, which is richer in aluminium oxide (Al_2O_3) and does not exhibit a glass nanostructure (**Figure 4.5**) (Wood 2013, Hou 2018, Vandiver 2016, Chiang 1983). This thin layer under the glaze acts as a dark background over which the scattering and absorption of light in the glazes is not affected by the stoneware. The brown colour is attributed to the incorporation of Ti^{4+} from the stoneware with the concomitant oxidation of Fe^{2+} to Fe^{3+} and reduction of Ti^{4+} to Ti^{3+} (**Figure 4.4**) (Kim 2001, Jeon 2014). Indeed, in good agreement with this, a recent investigation using Mössbauer spectroscopy has shown that the brown glaze is more oxidised than the blue glaze in Jun ware (Hou 2018). Furthermore, recent research has shown that the titanium content in blue Jun ware glazes ($>0.2\%$ TiO_2) is high enough to cause a colour shift from blue to green due to the increase in Fe^{3+} resulting from the reduction of Ti^{4+} . This is the main reason why celadons (lime glazes) usually show green rather than bluish colours (Wood 2021). This apparent discrepancy has been resolved considering that titanium also tends to be incorporated into the lime-rich droplets which would leave fewer titanium ions in the transparent blue areas of the glaze, which have fewer and smaller lime-rich droplets.

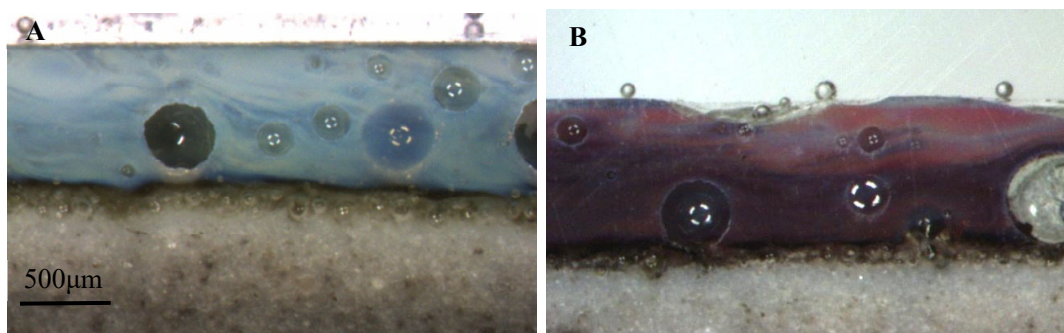


Figure 4.5. Optical microscopy images of the (A) blue and (B) red glaze of JS27

The coloration of the blue, red, and brown glazes in Official Jun has primarily been associated with the oxidation states or form of the chromophore species, whether they exist as particles or ions dissolved in the glaze matrix. A study conducted by Chen et al. (Chen 1988) demonstrated that copper can originate from various sources such as copper ore, copper smelting slag, or even impure copper scraps. Previous studies have reported the presence of cubic cuprite crystals (Chen 1983) and big metallic copper particles (2-350 μm) (Chen 1988) while copper sulphide particles have also been described, particularly in the dark blue and purplish-blue glazes (Chen 1983). This might indicate that the colouring mechanism of Jun ware glaze cannot be ascribed solely to a single factor. Recent investigations have demonstrated the presence of copper metal nanoparticles in both red and purple glazes (Hou 2018) (**Figure 4.11**). These copper nanoparticles exhibit a Surface Plasmon Resonance (SPR) extinction peak at 560 nm (Kreibig 1995), which absorbs yellow light and gives the glaze a red hue. Iron and copper ions may coexist in the glazes as different species, Cu^{2+} , Cu^+ , Cu^0 , Fe^{2+} and Fe^{3+} which will eventually reach an equilibrium depending on the firing temperature and atmosphere. However, the specific species present in different coloured areas of the glazes remain to be investigated.

The remarkable visual properties of Jun glazes are attributed to their distinct optical properties, which involve both the scattering of light in the nanostructure and the absorption of light by metal ions. While a previous study has investigated the influence of the nanostructure on the optical properties (Hou 2018), the oxidation state of iron in the glazes remains incompletely understood. This knowledge gap is partly due to the complex layered structure of the glazes, with higher calcium content near the surface, lower calcium content near the ceramic interface, and the formation of a droplet-free olive-brown glaze layer at the interface. In addition, the presence of a glass nanostructure further complicates the analysis. Some glazes were analysed by Mössbauer spectroscopy, which showed that the brown glaze was more oxidised than the blue glaze (Hou 2018), but no difference in the oxidation state of iron was found between the light blue and dark blue glazes. As the oxidation state of iron within the lime-rich and silica-rich nanostructures could not be determined, the specific role of these structures in determining the colour and appearance of the glazes remains unknown.

4.2 Objective

A previous study has already explained the opalescent nature of the Jun glazes and provided insights into the general valence state of the iron contributing to the blue and brown colours using Mössbauer spectroscopy. The



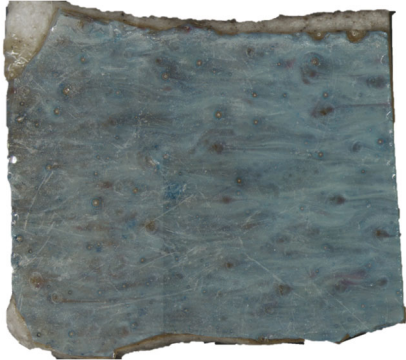

results indicate that iron is more reduced in blue glazes and more oxidised in brown glazes. However, there was no difference in the oxidation state of iron was found between the light blue and dark blue glazes. As the oxidation state of iron within the lime-rich and silica-rich nanostructures could not be determined, the specific role of these structures in determining the colour and appearance of the glazes remains unknown. To investigate this further, we propose to use synchrotron light X-ray absorption spectroscopy, which provides information on the oxidation state and local short-range order information of specific elements (Fe and Cu) and allows the analysis of micro-areas. The focus of this chapter is to investigate the oxidation state of iron and copper in calcium-rich and calcium-poor regions of Jun ware glazes, as well as the formation of metallic copper nanoparticles and their influence on the colour and appearance of the glazes. The data obtained will be supplemented by chemical analyses of the glazes and spectroscopic studies conducted in the ultraviolet and visible range.

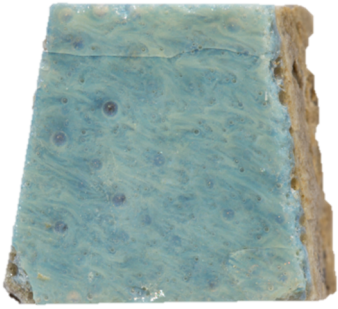

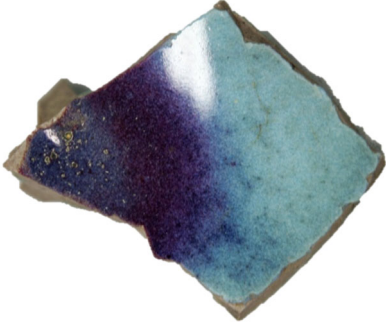
4.3 Materials and Methodology

4.3.1 Materials

A selection of Jun ware samples belonging to the collection of the Palace Museum in Beijing. They were excavated at Yuzhou (Henan). Five shards from the excavation of the Juntai kiln (JS24, JS26, JS27, JS77 and JS78) (Zhao 1975) and one sample (JS4) from the excavation of the Liujiamen kiln. The blue glazes from JS24, JS26, JS27, JS77 and JS4, the brown glaze from JS78 and the red glaze from JS24 were analysed (**Table 4.1**). The Juntai kiln, recognized as the official Jun kiln, occupies a prominent role within the kilns associated with the court. Notably, the Liujiamen kiln, situated about 20 km west of Juntai, possesses an extensive operational legacy and exemplifies exceptional quality, epitomizing the defining attributes of Classic Jun ware (Beijing University 2003). It serves as an exemplary illustration of a classic Jun kiln.

Table 4.1. Sample information of Official and Classic Jun ware.

Brown glaze	<p>JS78</p> 	
Red glaze	<p>JS24</p> 	
Blue glaze	<p>JS24</p> 	Juntai kiln (Official Jun kiln)
	<p>JS26</p> 	
	<p>JS27</p>	

		
JS77		
JS4		Liujiamen kiln (Classic Jun kiln)

4.3.2 XAS Methodology

Details can be seen in **Chapter 2 Analytical Methods**.

Considering that Jun glazes have a double silica-rich/lime-rich glass nanostructure, the use of a similar glass for the calibration is preferable. Nevertheless, it is important to note that the X-ray absorption spectroscopy (XAS) analysis conducted on the sample surface may yield valence states that are more oxidized than the actual state. In our study, the comparative analysis of different areas provides sufficient evidence to elucidate the observed phenomenon, thus no calibration in this investigation.

4.4 XAS study and Discussion

The Fe K-edge pre-edge fitted peaks from the blue glazes (JS24, JS26, JS27, JS77 and JS4) and the brown glaze (JS78) are shown in **Figure 4.6** and **Figure 4.7** respectively and the corresponding parameters, Fe^{3+} and Fe^{2+} peak positions and areas (E1, E2, A1 and A2), the centroid (C) and total area (A) and relative data of the Fe^{2+} peak ($A(\text{Fe}^{2+}/\text{Fe})$) obtained are shown in **Table 2.1 (chapter 2)** and the variogram in **Figure 2.7 (chapter 2)**.

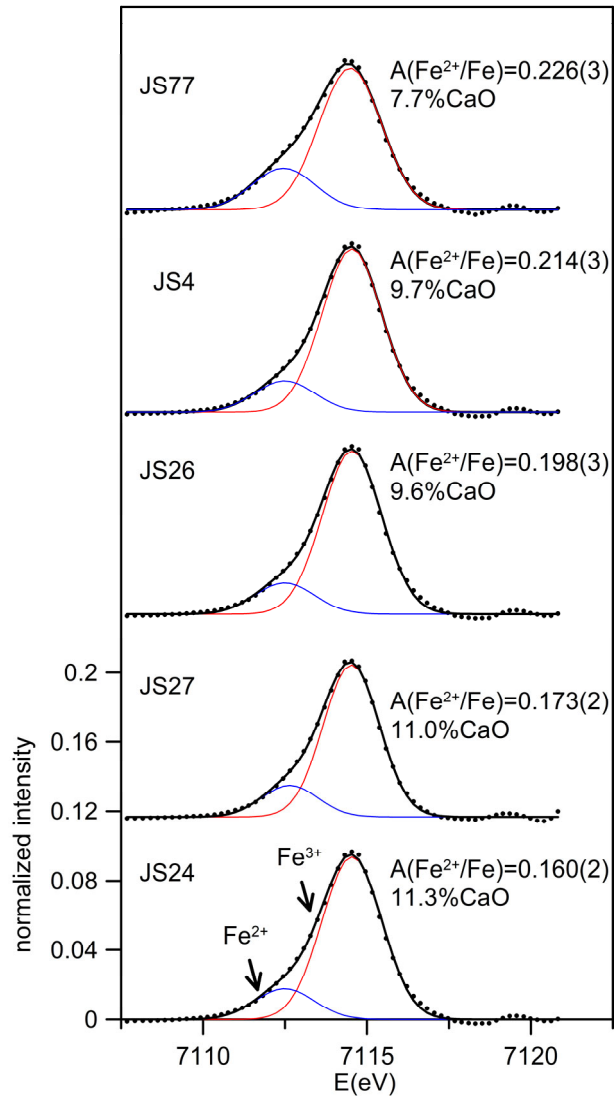


Figure 4.6. Fitted pre-edge peaks corresponding to the Jun ware blue glazes.

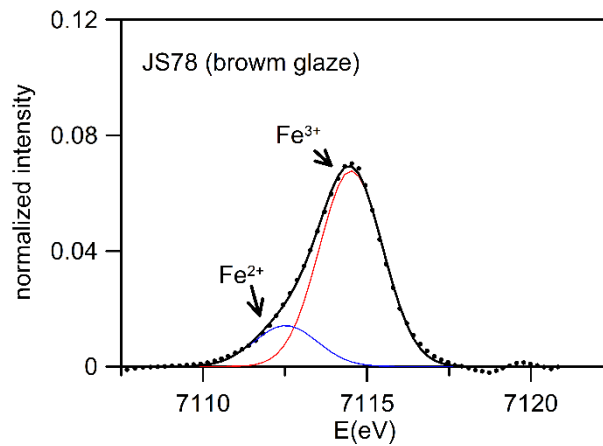


Figure 4.7. Fitted pre-edge peaks corresponding to the brown glaze from JS78.

Table 4.2. Fitted pre-edge data corresponding the blue Jun ware glazes. fwhm, E_1 , E_2 , A_1 , A_2 are the full width at half maximum, energy and area of the fitted peaks; C, A and $A(\text{Fe}^{2+}/\text{Fe})$ are the centre shift, total area and Fe^{2+} peak area fraction.

sample	fwhm (eV)	Fe^{3+}		Fe^{2+}		C (eV)	A (eV)	$A(\text{Fe}^{2+}/\text{Fe})$
		E_1 (eV)	A_1 (eV)	E_2 (eV)	A_2 (eV)			
JS24	1.82 (3)	7113.62 (1)	0.18 (1)	7111.57 (5)	0.044 (3)	7113.29 (2)	0.255 (4)	0.160 (2)
JS26	1.61 (2)	7113.62 (1)	0.25 (1)	7111.76 (5)	0.053 (3)	7113.25 (1)	0.243 (4)	0.198 (2)
JS27	1.71 (2)	7113.60 (1)	0.15 (1)	7111.72 (5)	0.054 (3)	7113.28 (1)	0.228 (3)	0.173 (2)
JS4	1.80 (2)	7113.60 (1)	0.22 (1)	7111.69 (6)	0.050 (3)	7113.19 (1)	0.245 (4)	0.214 (2)
JS77	1.90 (2)	7113.57 (2)	0.26 (1)	7111.53 (6)	0.043 (2)	7113.11 (2)	0.251 (5)	0.226 (3)
JS78	1.80 (3)	7113.59 (1)	0.32 (1)	7111.52 (5)	0.063 (3)	7113.33 (2)	0.237 (4)	0.125 (2)

The data corresponding to the blue glazes show a relatively good correlation with the average calcium content of the glazes as is shown in **Figure 4.6**. The iron in calcium rich glazes appear more oxidized than the calcium poorer glazes (**Figure 4.8**).

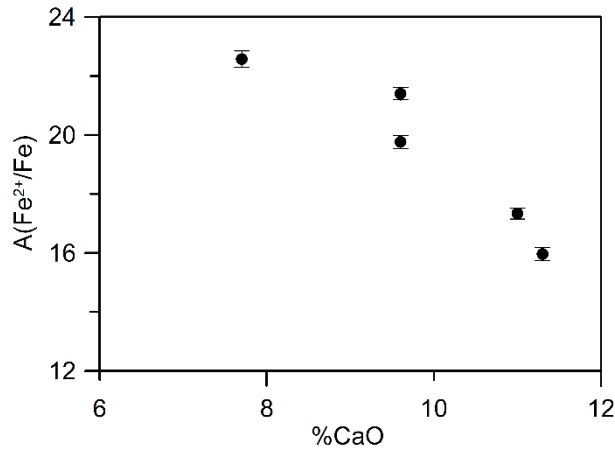


Figure 4.8. Fitted $A(\text{Fe}^{2+}/\text{Fe})$ of the spectra vs. calcium content of the Jun ware blue glazes analysed.

However, the heterogeneous submillimetre lime rich and poor structures shown by the glazes are large enough to affect the data obtained. For this reason, a smaller beam size was selected and an X-ray Fluorescence map was obtained from the blue glaze of JS24. **Figure 4.9** shows the corresponding fluorescence maps of Fe and Ca which show a good correlation. Generally speaking, the calcium rich areas are also iron rich while calcium poor areas are iron poor. In fact, in a previous study, lime rich droplets were found to be also iron rich while the silica rich (and lime poor) were also iron poor (**Table 4.3**). Therefore, the X-ray Fluorescence data showing that iron is concentrated in the calcium rich areas of the glaze confirms that the lime rich droplets are also iron richer.

Table 4.3. (Hou 2018) Chemical composition of the spherical droplets and of the matrix for JS4 determined by TEM-EDS. The index of refraction (n) and density (ρ) calculated from the chemical composition after (Priven 2003), and viscosity(η) after (Fluegel 2007).

	Na ₂ O	MgO	Al ₂ O ₃	SiO ₂	P ₂ O ₅	K ₂ O	CaO	TiO ₂	FeO	n (IOR)	ρ (g/cm ³) RT	ρ (g/cm ³) 1400°C	Log(η (Pa·s) (1250°C)
matrix	1.4	0.9	9.3	74.4	0.2	3.9	8.9	0.2	0.8	1.503	2.729	2.322	3.1
droplets	0.2	3.7	8.2	59.7	1.1	1.0	23.1	0.5	2.4	1.545	2.443	2.538	1.9

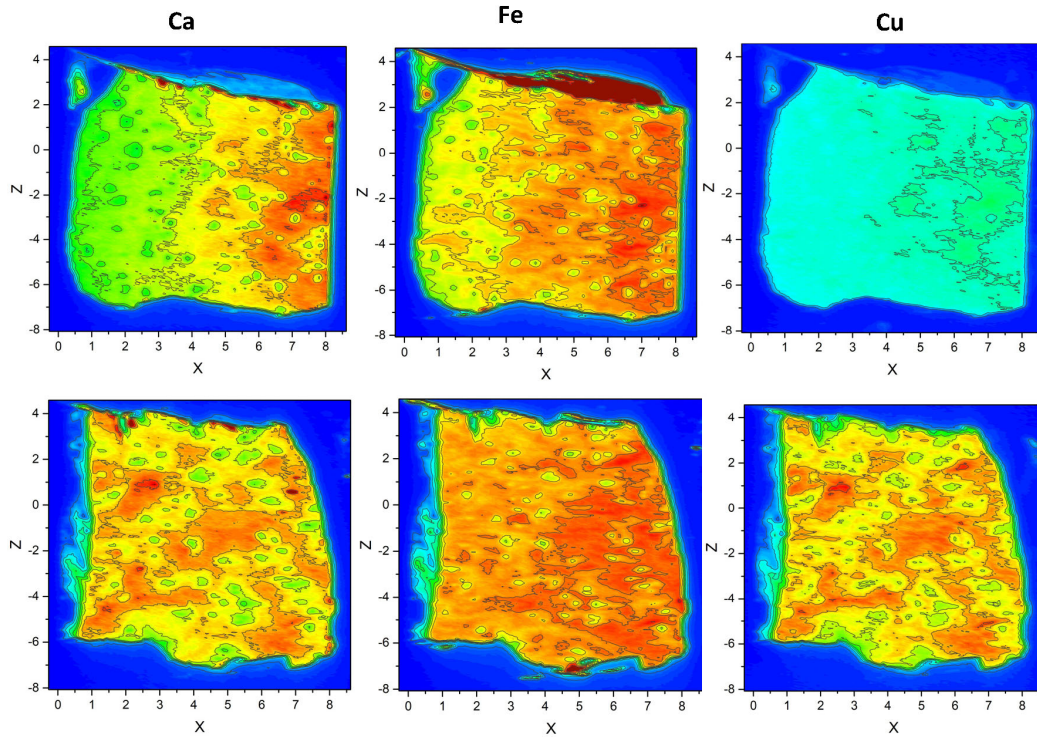


Figure 4.9. X-Ray Fluorescence maps corresponding to calcium, iron and copper for JS24 (Top) blue glaze and (Bottom) red glaze. The intensities are the same for each element.

Moreover, the pre-edge fitted data is shown in **Table 4.4** and the spectra corresponding to a calcium rich and a calcium poor area in **Figure 4.10**. The data shows that iron appears also more oxidized in the calcium rich areas suggesting that lime rich droplets incorporate more Fe^{3+} than the silica rich droplets.

Table 4.4. Fitted pre-edge peaks corresponding to the blue (B) and red (R) glazes in calcium rich (R) and poor (P) areas.

JS24	fwhm	Fe^{3+}		Fe^{2+}		C	A	$A(\text{Fe}^{2+}/\text{Fe})$		
		$E_1(\text{eV})$	$A_1(\text{eV})$	$E_2(\text{eV})$	$A_2(\text{eV})$					
Blue	Ca-rich	BR1	1.79 (2)	7113.52 (1)	0.200 (3)	7111.53 (8)	0.028 (2)	7113.28 (1)	0.228 (3)	0.121 (2)
		BR2	1.77 (2)	7113.52 (1)	0.198 (2)	7111.52 (8)	0.026 (1)	7113.29 (1)	0.224 (3)	0.115 (1)
	Ca-poor	BP1	1.71 (3)	7113.51 (1)	0.158 (3)	7111.62 (6)	0.041 (2)	7113.12 (2)	0.199 (4)	0.206 (2)
		BP2	1.77 (3)	7113.51 (2)	0.167 (3)	7111.54 (7)	0.038 (2)	7113.15 (2)	0.205 (4)	0.185 (2)
Red	Ca-rich	RR1	1.79 (2)	7113.52 (1)	0.200 (2)	7111.53 (7)	0.024 (1)	7113.31 (1)	0.224 (3)	0.106 (1)
		RR2	1.78 (1)	7113.54 (1)	0.202 (2)	7111.48 (7)	0.023 (1)	7113.33 (1)	0.225 (2)	0.100 (1)
	Ca-poor	RP1	1.76 (2)	7113.53 (1)	0.195 (3)	7111.53 (6)	0.029 (1)	7113.27 (1)	0.224 (2)	0.128 (1)
		RP2	1.77 (2)	7113.53 (1)	0.179 (3)	7111.58 (7)	0.036 (2)	7113.20 (2)	0.215 (4)	0.167 (2)

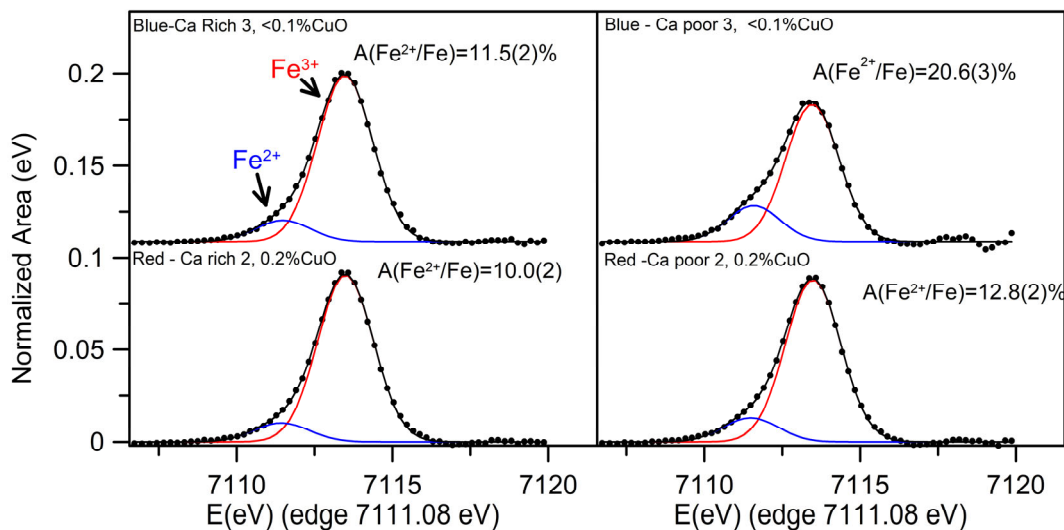


Figure 4.10. Fitted pre-edge peaks corresponding to the calcium rich and poor areas of the blue and red JS24 glazes.

Figure 4.11 shows a SEM image of the glass nanostructure developed in the blue glaze from JS24. Calcium richer areas have more and larger droplets than calcium poorer areas. This side of JS24 contains some copper but below 0.1% CuO even in the richest areas. Previous analyses of the droplets and the matrix of the glaze (**Table 4.3**) have shown that the glass droplets are enriched in Ca, Mg, Fe, P and Ti (about 3 times those of the matrix) while the matrix is enriched in Si, Na and K. A simultaneous oxidation of Fe^{2+} into Fe^{3+} and reduction of Ti^{4+} into Ti^{3+} which has been observed at the glaze in contact with the ceramic, suggests that the higher concentration of titanium in the calcium rich droplets may also be responsible of the greater oxidation of iron in the calcium rich areas.

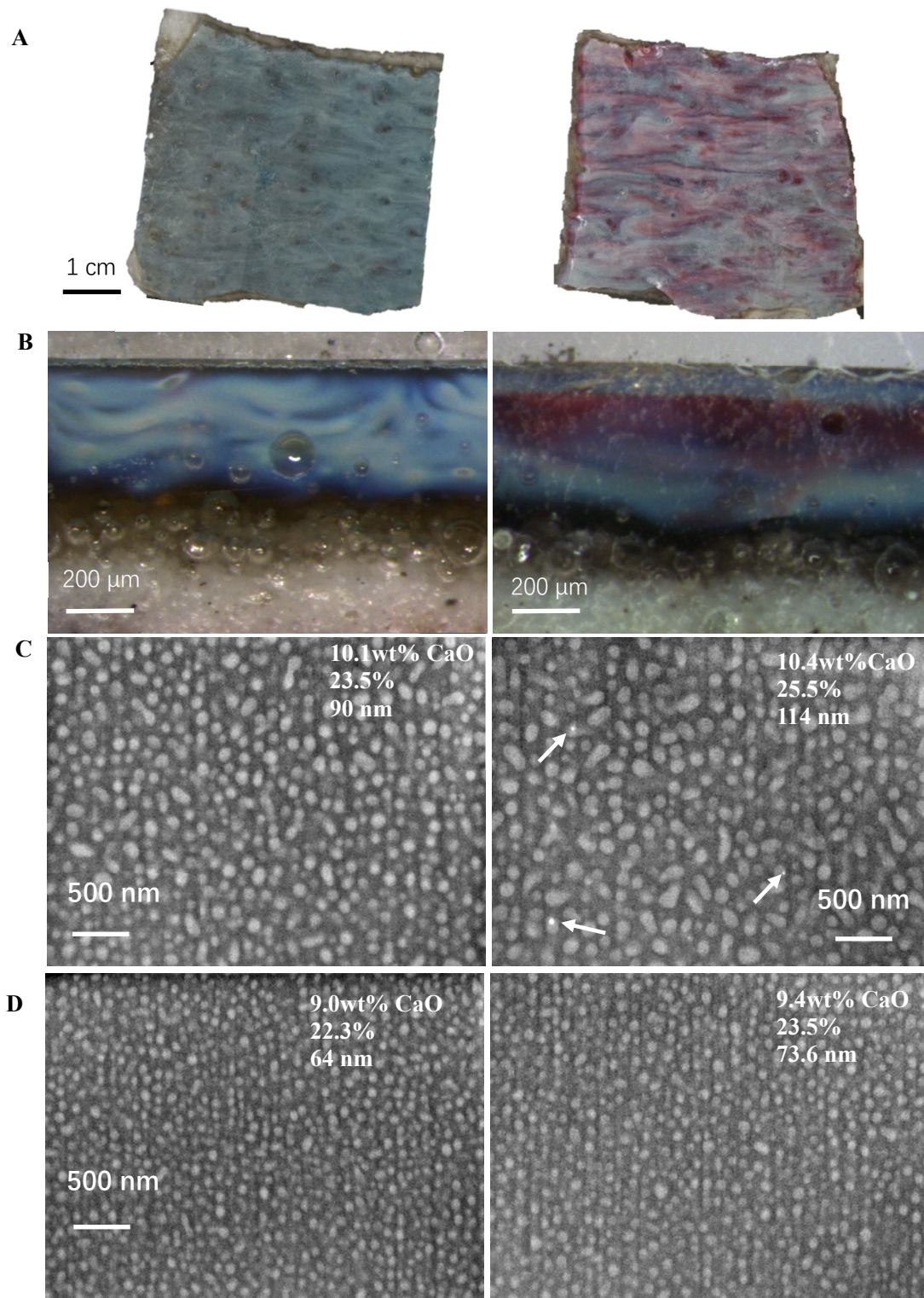


Figure 4.11. (A) Surface appearance of the blue and red side from JS24. (B) Cross section, (C) nanostructure of the Ca-rich blue (left) and red (right) glazes, and (D) nanostructure of the Ca-poor blue. The white droplets are calcium rich in a darker silica rich matrix. Small precipitates of metal copper nanoparticles are present in the red glaze(C-right).

Both calcium rich and poor areas of the red glaze were also measured and the fitted parameters and spectra are also shown in **Table 4.4** and **Figure 4.10** respectively. The copper content in this side is 0.2%CuO, which is associated with the presence of 0.3%SnO₂ and 0.2% PbO which indicates the reuse of bronze. We

can see that the iron in the calcium rich and poor areas of the red glaze is more oxidized (10-11% $A(\text{Fe}^{2+}/\text{Fe})$ and 13-17% $A(\text{Fe}^{2+}/\text{Fe})$) than the corresponding calcium rich and poor areas of the blue glaze (11-12% $A(\text{Fe}^{2+}/\text{Fe})$ and 19-21% $A(\text{Fe}^{2+}/\text{Fe})$). **Figure 4.11** shows the nanostructure developed in the calcium-rich areas of the JS24 red glaze. Although the nanostructure is the same, a few copper nanoparticles, absent in the blue area, are found in the red area. The copper particles are formed at the interface between the droplets and the matrix.

UV-Vis data was also obtained from the blue and the red sides of JS24. Besides the small copper content present in the red side (0.2 %CuO) and the scarcity and small size of the copper nanoparticles, the Surface Plasmon Resonance (SPR) absorption is an important contribution to the scattering contribution of the glass nanostructure and Fe^{2+} absorption characteristic of the blue glaze (**Figure 4.12**).

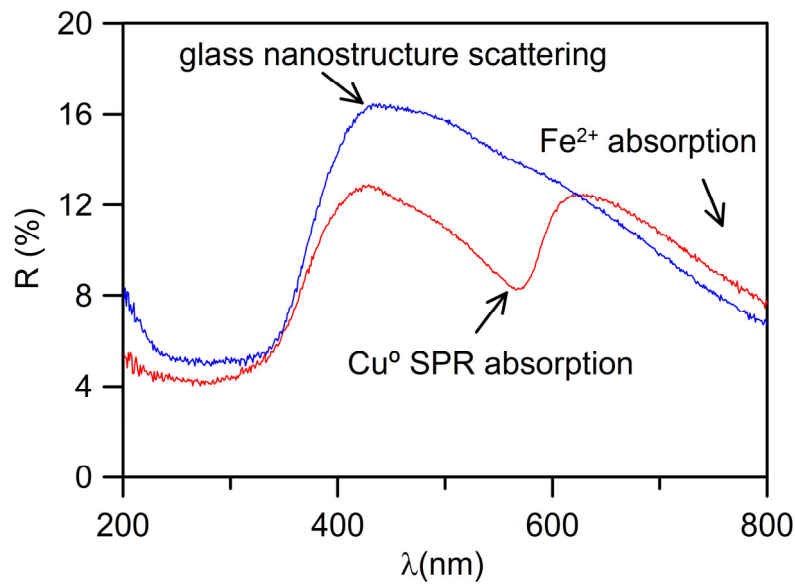


Figure 4.12. UV-Vis spectra from the Blue and Red sides of JS24. The large scattering contribution between 400 nm and 600 nm from the droplets structure and the broad absorption of Fe^{2+} (maximum at ≈ 1100 nm) extending to the red part of the visible spectra is also clearly seen. In the red side the Surface Plasmon Resonance Absorption peak corresponding to metal copper nanoparticles ($\lambda_p \approx 560$ nm) is clearly seen.

The position of the absorption XANES edge shifts characteristically with oxidation state (8982.3 eV for Cu^0 , 8983.8 eV for cuprite, Cu^+ and 8986.9 eV for tenorite, Cu^{2+}). From the XANES spectrum (**Figure 4.13**) it is quite evident that Cu is present mainly as Cu^+ due to the absence of a $1s \rightarrow 3d$ transition and the intense feature at 8983 eV.

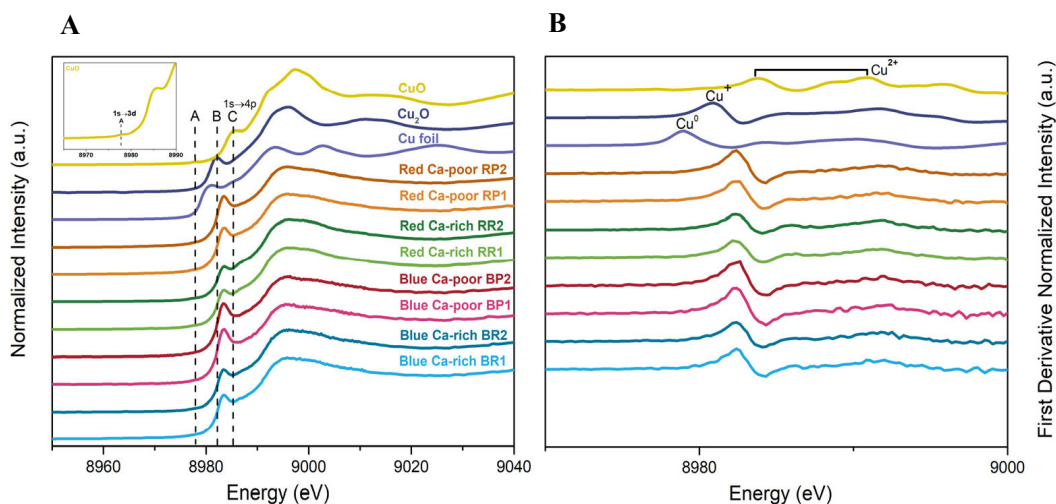


Figure 4.13. (A) Cu K-edge XANES spectra and (B) 1st derivative XANES spectra from the blue and red areas of JS24.

The copper K-edge and the 1st derivative XANES spectra from copper standards and the blue and red areas of JS24 are shown in **Figure 4.13**. Copper K-edge XANES spectra of both Cu²⁺ and Cu⁺ contain features characteristic of the oxidation state and speciation (Berry 2006). The pre-edge feature which corresponds to dipole-forbidden electronic transitions from core 1s levels to the first empty 3d states (but hybridized by 2p orbitals of the O ligands). For Cu⁰ and Cu⁺ in Cu₂O, there is no empty 3d initial states, so the pre-edge is the signature of Cu²⁺. Due to only one empty 3d orbital to accept the excited 1s electron, the feature has an extremely weak intensity.

Figure 4.13 shows no pre-edge features characteristic of metallic copper (Cu⁰), Cu⁺ in cuprite or Cu²⁺ in tenorite. The feature located near 8982 eV is attributed to the 1s→4p electric dipole transition and is often considered a signature of Cu⁺ (Maurizio 2000). Actually, this transition is intense and sharp in cuprite (Cu₂O), in which the copper atoms are located in a linear geometry (2-coordinated by oxygens) (Restori 1986). The edge shift between Cu⁺ and Cu²⁺ is typically large (>5 eV) and derives from an intense Cu⁺ pre-edge feature (1s → 4p) that merges with, and is usually referred to as, the absorption edge (Fulton 2000). Features comprising the edge are often more easily identified in the derivative spectra, shown also in **Figure 4.13**, in which inflections appear as peaks. The energy positions of the feature discriminate between Cu⁺ and Cu²⁺. In general, **Figure 4.13** shows the expected shift of absorption edge to higher energy with increasing oxidation state and differences in the edge shape.

EXAFS data was fitted to determine the distances, coordination number, and neighbour atoms. The signal corresponding to the Cu-Cu bond length could not be fitted, probably because of the few particles present, their small size and their large surface/volume ratio. The copper atoms at the particles surface have other atoms than copper as near neighbours, this reduces even further their contribution to the EXAFS spectra. The k³ weight k-space and R-space experiment data (points) and the corresponding fits (solid lines) of a calcium poor area from the blue glaze (BP1) are shown in **Figure 4.14**. Full results of the fitting of the spectra are given in **Table 4.5** together with the crystallographic information corresponding to cuprite (ID:

mp-361; DOI: 10.17188/1207131) and tenorite (code COD: 9014580). The R factor gives the misfit and it is used as an estimator for the goodness of the fitting.

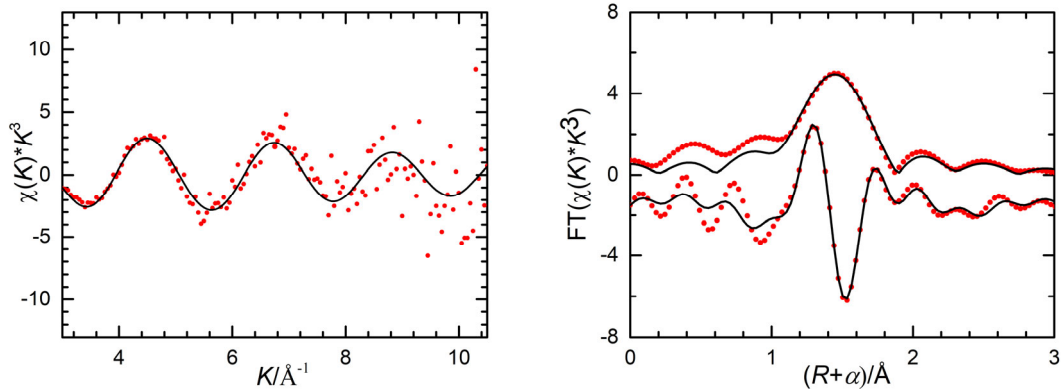


Figure 4.14. Cu K-edge experimental data (points) and curvefit (line) of BP1 (left) k^3 -weighted phase-uncorrected data. (right) R-space (FT magnitude and Imaginary component).

Table 4.5. Curvefit parameters^a for Cu K-edge EXAFS for JS24 glazes.

JS24	Path	N ^b	R/ Å	$\sigma^{2(c)}/ \text{Å}^2$	R ^d factor (%)	Cu ⁺ /(Cu ⁺ +Cu ²⁺)	
Ca-rich	BR1	Cu-O1	2.0	1.84(1)	0.003(2)	0.6%	0.7(1)
		Cu-O2	4.0	1.94(1)	0.003(2)		
Blue	BR2	Cu-O1	2.0	1.84(2)	0.003(3)	2.1%	0.7(2)
		Cu-O2	4.0	1.94(2)	0.003(3)		
Ca-poor	BP1	Cu-O1	2.0	1.87(1)	0.002(1)	0.2%	0.89(6)
		Cu-O2	4.0	1.97(1)	0.002(1)		
	BP2	Cu-O1	2.0	1.86(1)	0.002(1)	0.5%	0.87(9)
		Cu-O2	4.0	1.96(1)	0.002(1)		
Ca-rich	RR1	Cu-O1	2.0	1.84(1)	0.003(1)	0.2%	0.65(8)
		Cu-O2	4.0	1.94(1)	0.003(1)		
Red	RR2	Cu-O1	2.0	1.83(1)	0.004(1)	0.3%	0.6(1)
		Cu-O2	4.0	1.93(1)	0.004(1)		
Ca-poor	RP1	Cu-O1	2.0	1.85(1)	0.003(1)	0.9%	0.8(1)
		Cu-O2	4.0	1.95(1)	0.003(1)		
	RP2	Cu-O1	2.0	1.86(1)	0.003(1)	0.2%	0.84(7)
		Cu-O2	4.0	1.96(1)	0.003(1)		

^a S_0^2 was obtained from the analysis of Cu foil and fixed to 0.81. Data ranges: $3.0 \leq k \leq 10.5 \text{ Å}^{-1}$, $1.0 \leq R \leq 2.3 \text{ Å}$. ^b These coordination numbers were constrained as $N(\text{Cu-O1}) = 2$ and $N(\text{Cu-O2}) = 4$ based on the crystal structure of Cu_2O and CuO . ^c The Debye-Waller factors were constrained as $\sigma^2(\text{Cu-O1}) = \sigma^2(\text{Cu-O2})$ to decrease variable parameters. ^d R factor is the goodness of fit parameter

The data indicates that copper is mainly present as Cu^+ and Cu^{2+} appearing more oxidised in the calcium rich areas, $\text{Cu}^+ / (\text{Cu}^+ + \text{Cu}^{2+}) \approx 0.6-0.7$, than in the calcium poor areas, $\text{Cu}^+ / (\text{Cu}^+ + \text{Cu}^{2+}) \approx 0.8-0.9$. The ratio in the red and the blue glazes is essentially the same. We know that in the red side we also have copper

nanoparticles. However, the copper nanoparticles are so few and their size so small that it has been not possible to identify the corresponding back-scattering paths in the EXAFS signal.

Copper is dissolved in a glaze as Cu^+ and Cu^{2+} , the relative ratio of both depends on the composition of the glass and on the firing atmosphere. The composition of both, the blue and the red side is equivalent in the calcium rich and calcium poor areas and the firing atmosphere was the same. Consequently, the reduction of copper to the metallic state and precipitation of copper metal nanoparticles can only be related to simultaneous oxidation of the other transition metal ions present, iron and titanium. The reduction of copper from Cu^+ to Cu^0 is obtained by the simultaneous oxidation of Fe^{2+} to Fe^{3+} . In fact, iron appears more oxidised in the red glaze (13-17% $A(\text{Fe}^{2+}/\text{Fe})$ in the calcium rich areas and 10-11% $A(\text{Fe}^{2+}/\text{Fe})$ in the calcium poor areas) than in the blue side (19-21% $A(\text{Fe}^{2+}/\text{Fe})$ in the calcium rich areas and 11-12% $A(\text{Fe}^{2+}/\text{Fe})$ in the calcium poor areas).

The presence of copper sulphide particles has been also detected in the red and purple glazes (**Figure 4.15**). Due to the high immiscibility of sulphur in silicate glasses and the fact that copper is a highly chalcophilic element, the precipitation of copper sulphide is expected at high temperature in a reducing atmosphere. It is possible that the decomposition of copper sulphides added to the precipitation of metallic copper nanoparticles, although the role of iron in the equilibrium of species present is more important as our data has demonstrated.

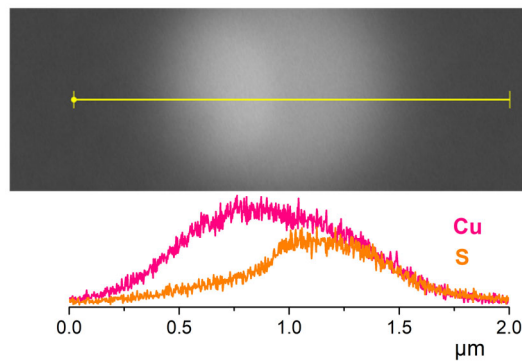


Figure 4.15. Linescan corresponding to a copper sulphide particle in the JS26 purple glaze.

The sky-like appearance shown by the blue Jun ware glazes is due to the combination of transparent-blue and whitish-opaque submillimetre areas. Moreover, the presence of a larger size/high volume fraction of droplets in the calcium rich areas is therefore responsible for their opacity, the presence of smaller droplets in the calcium poor areas for a transparent glaze. Now we have demonstrated that iron is more reduced in the calcium poor transparent areas than in the calcium rich opaque areas (19-21% $A(\text{Fe}^{2+}/\text{Fe})$ instead of 11-12% $A(\text{Fe}^{2+}/\text{Fe})$). This indicates also that iron is more oxidised in the lime-rich droplets than in the silica-rich matrix where it appears mainly as Fe^{2+} . Therefore, the dark blue colour of the calcium poor areas of the glaze is due to the high Fe^{2+} content. The iron speciation is therefore directly related to the calcium content of the glazes, as higher calcium contents will result in a greater number of larger droplets in which Fe^{3+} concentrates, yet Official Jun glazes show a layered glaze structure with variable calcium contents, whereas Classic Jun glazes are thick and homogeneous. In fact, the final appearance of the glaze depends

on the layered structure, with some layers appearing dark blue transparent and others creamy opaque. The overall oxidation state of iron may be similar throughout the glaze, but the layered structure produces a different appearance.

Titanium is concentrated in the lime-rich droplets where iron is mainly oxidised, they are responsible for the high white-yellowish scattered light. However, the colour of the glaze is dominated by the iron present in the transparent calcium areas which are also titanium poor and where iron is mainly Fe^{2+} . This is the reason why Jun ware glazes are blue and not green although they contain above 0.2% TiO_2 .

The high absorbance associated to the Surface Plasmon Resonance at $\lambda \approx 560$ nm of copper metal nanoparticles is responsible for the red and violet colour to the white/yellowish and blue areas of the glaze respectively even if very few nanoparticles are present.

4.5 Conclusions

A glass nanostructure is developed in Jun ware glazes due to the high $\text{SiO}_2:\text{Al}_2\text{O}_3$ ratio (above 7:1), which, when fired at temperatures of about 1200°C , undergoes a liquid-liquid phase separation. A double glass nanostructure, lime-rich (enriched also in Fe, Mg, P and Ti) droplets in a silica-rich matrix (enriched also in K and Na) is developed. A XAS study has demonstrated that iron is more oxidised in the calcium rich areas than in the calcium poor areas of the glaze, $\approx 11\text{-}12\%$ $\text{A}(\text{Fe}^{2+}/\text{Fe})$ and $\approx 19\text{-}21\%$ $\text{A}(\text{Fe}^{2+}/\text{Fe})$ respectively, implying that iron is predominantly oxidised in the lime-rich droplets and reduced in the silica-rich matrix.

Consequently, the sky-like appearance shown by the blue Jun ware glazes is due to the combination of the light absorption in the transparent-dark-blue Fe^{2+} rich and titanium poor areas and light scattering in the white-yellowish Fe^{3+} rich areas.

Copper was also added to the glazes to imprint red/violet colours. Besides the formation of small copper nanoparticles, copper appears mainly as Cu^+ and Cu^{2+} in the glaze, the ratio between both is known to depend on the composition of the glaze and atmosphere. Iron is more oxidised in the red glaze where copper metal nanoparticles are present than in the blue glaze where they are absent. This effect is more pronounced in the calcium poor areas (containing more Fe^{2+}) than in the calcium rich areas (containing more Fe^{3+}). The results obtained point out to the simultaneous reduction of copper from Cu^+ to Cu^0 and oxidation of iron from Fe^{2+} to Fe^{3+} .

References

- Berry AJ, Hack AC, Mavrogenes JA, Newville M, Sutton SR (2006), A XANES study of Cu speciation in high-temperature brines using synthetic fluid inclusions, *Am. Mineral.* 91 1773–1782. <https://doi.org/10.2138/am.2006.1940>
- Beijing University, The Centre for Archaeological Studies & The Cultural Relics and Archaeology Research Institute of Henan Province (2003), Excavation of a Jun Kiln at Liujiamen, Yuzhou, Henan. *Cultural Relics (文物)*, 11: 26-52.
- Chen XQ, Huang RF, Chen SP, Song XY, Zhou XL (1983). On the Interlayer, Opalescence and coloration of Jun (Chun) ware in the Song and Yuan dynasties. *Journal of the Chinese Ceramic Society(硅酸盐学报)*, 11(2): 1298-140.
- Chen XQ, Huang RF, Chen SP (1988). Metallic Copper in the Jun glaze of Liu Jia Gou. *Journal of the Chinese Ceramic Society(硅酸盐学报)*, 16(3): 233-237.
- Chiang YM, Kingery WD (1983), Spinodal Decomposition in a K₂O-Al₂O₃-CaO-SiO₂ glass, *Commun. Am. Ceram. Soc.* 66(9) c171-c172. <https://doi.org/10.1111/j.1151-2916.1983.tb10632.x>
- Cooper L, Costello S, Eremin K, Moy M, King K, Walton M, Pouyet E, Shortland A, Dussubieux L (2020): Numbered Jun Ware—a technical study. *J. Am. Inst. Conserv.*, 60(4):255-268. <https://doi.org/10.1080/01971360.2020.1748971>
- Ehrt D, Leister M, Matthai A (2001), Polyvalent elements iron, tin and titanium in silicate, phosphate and fluoride glasses and melts, *Phys. Chem. Glasses* 42(3) 231-239.
- Fluegel A (2007), Glass viscosity calculation based on a global statistical modelling approach, *Eur. J. Glass Sci. Technol. A* 48 (1) 3013–3031.
- Fulton JL, Hoffmann MM, Darab JG (2000), An X-ray absorption fine structure study of copper(I) chloride coordination structure in water up to 325 °C, *Chem. Phys. Lett.* 330 300–308. [https://doi.org/10.1016/S0009-2614\(00\)01110-6](https://doi.org/10.1016/S0009-2614(00)01110-6)
- Gao YH (2014a), A preliminary study on the production process of Jun porcelain in the late Northern Song Dynasty (北宋后期钧瓷生产工艺初探), *Ceramics Science & Art.* DOI:10.13212/j.cnki.csa.2014.09.008.
- Gao GC (2014b), Research on firing temperature of Jun ware oven(烘炉钧瓷烧成技艺研究), *Ceramics Science & Art.* DOI:10.13212/j.cnki.csa.2014.09.010
- Hou JY, Pradell T, Li Y, Miao JM (2018), Jun ware glazes: Chemistry, nanostructure and optical properties, *J. Eur. Ceram. Soc.* 38: 4290-4302. <https://doi.org/10.1016/j.jeurceramsoc.2018.05.010>
- Jeon AY, No HG, Kim US, Cho WS, Kang GI (2014), Mössbauer Spectroscopic and Chromaticity Analysis

on the Colourative Mechanism of Ancient Goryeo Celadon from GangJin and Buan, *Archaeometry*, 56(3): 392-405. <https://doi.org/10.1111/arcm.12032>

Kim JY, No HG, Jeon AY, Kim US, Pee JH, Cho WS, Kim KJ, Kim CM, Kim CS (2001), Mössbauer spectroscopic and chromaticity analysis on colorative mechanism of celadon glaze, *Ceram. Int.* 37: 3389-3395. <https://doi.org/10.1016/j.ceramint.2011.05.141>

Kingery WD, Vandiver PB (1983a), Song Dynasty Jun (Chün) Ware Glazes, *Am. Ceram. Soc. Bull.* 62(11): 1269-1274, 1279.

Kingery WD, Vandiver PB, Huang IW, Chiang YM (1983b), Liquid-liquid immiscibility and phase separation in the quaternary systems $K_2O-Al_2O_3-CaO-SiO_2$ and $Na_2O-Al_2O_3-CaO-SiO_2$, *J. Non-Cryst. Solids*, 54: 163-171. [https://doi.org/10.1016/0022-3093\(83\)90090-X](https://doi.org/10.1016/0022-3093(83)90090-X)

Kreibig U, Vollmer M (1995), Optical properties of metal cluster, Springer series 25, Springer, Berlin, Germany.

Li BP (2007), Numbered Jun wares: controversies and new kiln site discoveries, *Trans. Orient. Ceram. Soc.* 71: 65–77.

Maurizio C, d'Acapito F, Benfatto M, Mobilio S, Cattaruzza E, Gonella F (2000), Local coordination geometry around Cu and Cu ions in silicate glasses: an X-ray absorption near edge structure investigation, *Eur. Phys. J. B*, 14: 211–216. <https://doi.org/10.1007/s100510050122>

Miao JM, Xia JD, Wang GY, J. Hou JY, Guo PY, Han ZH (2016), T.L. Dating, Research on Song Dynasty Jun ware The Palace Museum, Beijing, China, Proceedings of International Symposium on Science and Technology of Five Great Wares of the Song Dynasty, 220–230.

Philpotts AR (1982), Compositions of immiscible liquids in volcanic rocks, *Contrib. Mineral. Petrol.* 80 201-218. <https://doi.org/10.1007/BF00371350> Priven AI, Mazurin OV (2003), Comparison of methods used for the calculation of density, refractive index and thermal expansion of oxide glasses, *Glass Technol.* 44(4) 156–166.

Restori R, Schwarzenbach D (1986), Charge Density in Cuprite, Cu_2O , *Acta Cryst.* B42: 201-208. <https://doi.org/10.1107/S0108768186098336> Roedder E (1992), Fluid inclusion evidence for immiscibility in magmatic differentiation, *Geochim. Cosmochim. Acta.* 56: 5-20. [https://doi.org/10.1016/0016-7037\(92\)90113-W](https://doi.org/10.1016/0016-7037(92)90113-W)

Tichane R (1978), Those Celadon Blues, Institute for Glaze Research, New York State, US.

Vandiver PB (2016), Variability of Song Dynasty Green Glaze Technology Using Microstructure, Microcomposition and Thermal History to Compare Yaozhou, Jun, Ru, Yue, Longquan, Guan, and Korean Koryo Dynasty Materials and Practices, The Palace Museum. Beijing, China, Proceedings of International Symposium on Science and Technology of Five Great Wares of the Song Dynasty: 391-432.

Weyl WA (1951), *Coloured Glasses*. Sheffield: Society of Glass Technology, UK, 1951.

Wood N (1999), *Chinese Glazes: Their Origins, Chemistry and Recreation*, A&C Black, London, UK.

Wood N (2013), *Some mysteries of Jun ware manufacture*, Junyao. Eskenazi, pp.17–28 London, UK.

Wood N (2021), Nought-point-two per cent titanium dioxide: A key to Song ceramics? *J. Archaeol. Sci. Rep* 35: 102727. <https://doi.org/10.1016/j.jasrep.2020.102727>

Yan F, Wang SH (2012), Effects of Traditional Kiln Structure and Loading Technology on Jun Ware's Appearance(窑炉结构与装烧工艺对钧釉外观特征的影响), *Journal of Ceramics(陶瓷学报)*, 33(3) :376-379.

Zhao QY (1975), The excavation of Juntai Kiln, Yuzhou, Henan Province, *J. Cult. Relics(文物)* 6: 57-64. 10.13619/j.cnki.cn11-1532/k.1975.06.006

Chapter 5 Changsha ware glaze colours

长沙窑



Chapter 5 Changsha ware glaze colours

5.1 Introduction

The Changsha kiln is a well-known export kiln that flourished in the late Tang Dynasty (9th–10th century) in China, located near Shizhu Lake, Tongguan Town, Wangcheng (now Wangcheng District), Changsha, Hunan Province. Extensive archaeological research demonstrates the extensive trade of Changsha ware over 20 countries along the Maritime Silk Road (Changsha ware research group 1991). Changsha ware was essentially a high-lime glazed stoneware fired at around 1110-1200°C (Zhang 1985), resulting in a porous body structure with relatively high imperfections compared to contemporary production. The artistic significance of Changsha ware in Chinese ceramic history is remarkable due to its opalescent glaze and vibrant colours, as well as, the incorporation of exotic Central Asian-style decoration (**Figure 5.1**).



Figure 5.1. Typical Changsha bowls, Belitung Shipwreck, c. 830s, Asian Civilisations Museum, <https://www.nhb.gov.sg/acm/galleries/maritime-trade/tang-shipwreck>

Changsha, a city located in the south of China (**Figure 5.2**), is geographically separated from the northern region by the Qinling-Huai River line, and has significant cultural and geological differences with northern region which impact in the ceramic composition. Typically, ceramics originating from southern China are made from igneous rocky materials (Wood 1999). As a result, ceramics from the southern region have higher levels of Si and K, and lower levels of Al than those of the northern region. The city has a well-developed water system, anchored by its largest river, the Xiang Jiang, which joins to the central section of the Yangtze (Yangzi) River. Moreover, Changsha also benefits from abundant clay and firewood resources, which facilitate large-scale ceramic production and efficient transportation.

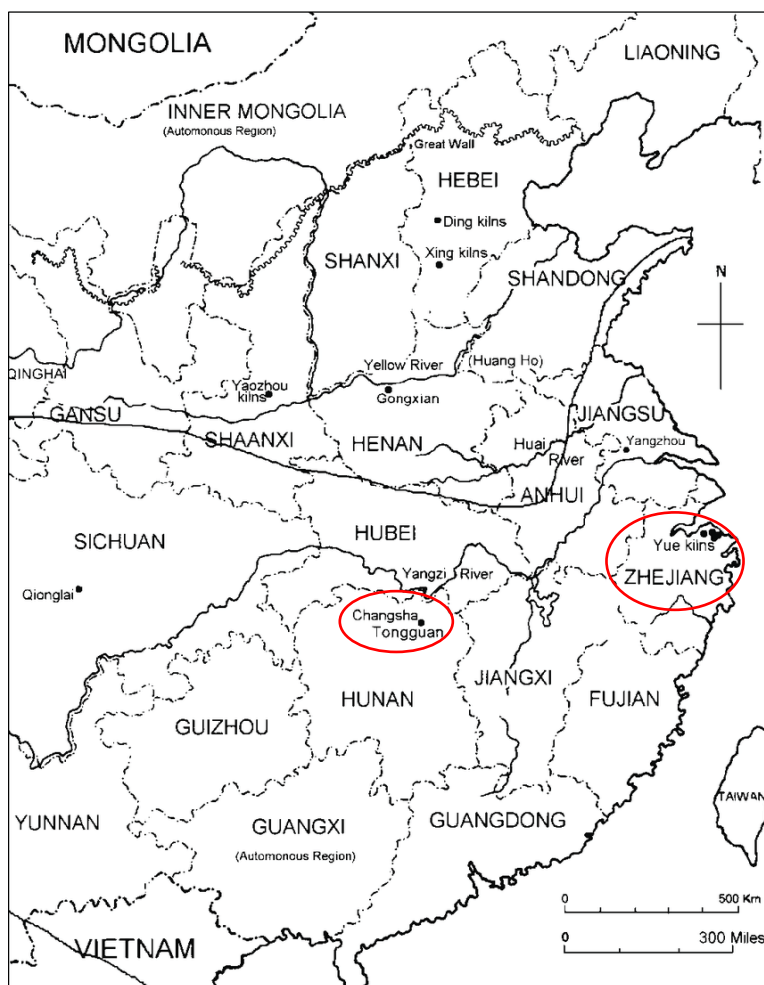


Figure 5.2. the map of the part of Chinese province and some typical kilns (Wood 1999)

The emergence of high lime glazes in the south marked a significant milestone in the production and development of Chinese porcelain which requires a firing temperature above 1300 °C. The use of high-fired lime-rich glazes requiring firing temperatures above 1200°C can be traced back to the Shang dynasty (1700 -1027 B.C.E) in Zhejiang province (Figure 5.2). These glazes typically exhibit a composition with approximately 60-65 wt% silica, around 15 wt% alumina, and 15-20 wt% lime and magnesia, and total alkali oxide content below 5 wt% (Rehren 2012). This early production of proto-porcelain, also known as stoneware, occurred during the Shang (1700-1027 B.C.E) and Zhou (1027-221 B.C.E) dynasties (Figure 5.3A). The presence of iron impurities imparts a yellow-green or bluish-grey hue to Shang-Zhou proto-porcelain (~13th B.C.E -8th B.C.E) (Yin 2011). It is remarkable, that even during the Shang and Zhou periods (1700-221 B.C.E) the potters were able to achieve sufficiently high temperatures (Yin 2011). Subsequently, in the Eastern Han dynasty (25-220 C.E.) (Figure 5.3B), firing techniques underwent significant advances, and a major leap from proto-porcelain to porcelain. In particular, the Zhejiang province (Figure 5.2) became a major center of Chinese porcelain production during this early period. However, it was not until the Three Kingdoms period (220-280 C.E.) that the Yue kilns in Zhejiang province began to show distinct glaze characteristics, primarily featuring a light cyan colour reflecting improved control over reducing atmospheres (Figure 5.3C) (Chinese Ceramics History 1982). Due to its geographical

location along the middle of the Yangtze River, Changsha high fired ceramics developed later than in the Zhejiang province, probably beginning during the Wu dynasty of the Three Kingdoms period (222-280 C.E.). The quality of ceramics produced in Changsha was inferior to those of the Zhejiang province, mainly due to the raw materials containing higher levels of Al and lower levels of Fe than those in Zhejiang, and resulting in unsintered bodies and vitrified glazes.



Figure 5.3. (A) Proto-porcelain, Warring States (475/403 B.C.E.-221 B.C.E), Keqiao District Museum, <https://www.ygwhmuseum.com/collection/treasuredetail?id=18>; (B) Celadon, East Han dynasty (25-220 C.E.), The Palace Museum, <https://www.dpm.org.cn/collection/ceramic/227092.html>; (C) Celadon, Three Kingdom Wu dynasty (222-280 C.E.), National Museum of China, https://www.chnmuseum.cn/zp/zpml/kgfjp/202112/t20211203_252538.shtml.

Unlike other well-known kilns, there is a notable absence of specific references to Changsha ware in the ancient literature, possibly due to problems of nomenclature. The term ‘Changsha’ refers to the city itself, while the term ‘Changsha kiln’ is used by archaeologists and some scholars to refer specifically to the kiln at Wazhaping, Tongguan town, Changsha. Despite its proximity of about 10 km to the Yuezhou kiln (also located in Changsha and documented in the famous Tang dynasty book ‘The Classic of Tea’), the name ‘Changsha kiln’ was adopted because of its distinct decorative features. However, the appearance of Changsha ware was not an abrupt event, but rather an evolutionary process. Archaeological excavations conducted in 2016 revealed the presence of typical products of the Yuezhou kiln in the underlying layers of Changsha ware (Zheng 2019). Consequently, Changsha ware can be perceived as either inheriting the traditions of the Yuezhou kiln or representing its later development. Furthermore, the An Lushan rebellion (755-763 C.E.) during the mid-Tang dynasty disrupted ceramic production, prompted migration of many potters from the north to the south, and subsequently introduced new creative approaches in the production of Changsha ware.

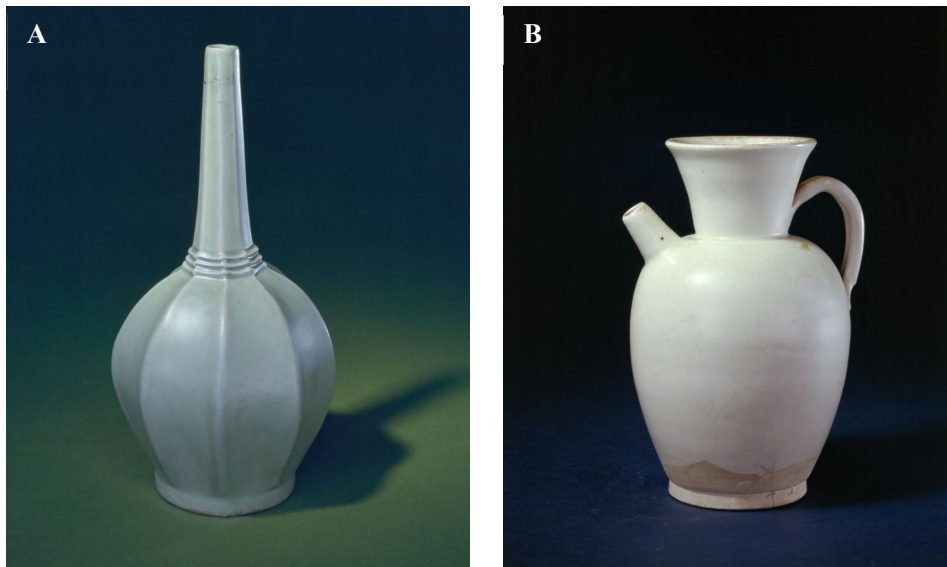


Figure 5.4. (A) Yue porcelain (Zhejiang province, the south), Tang dynasty (618-907), the Palace Museum. <https://www.dpm.org.cn/collection/ceramic/227521>; (B) Xing porcelain (Hubei province, the north), Tang dynasty (618-907), the Palace Museum. <https://www.dpm.org.cn/collection/ceramic/226955>

Archaeological excavations have shown that Changsha kiln, which initially involved the production of transparent lime glazes subsequently evolved into the firing of both transparent and opaque lime polychrome glazes (Ye 2011, Changsha ware research group 1991). During this period, the ceramic production in China displayed contrasting colours, with cyan glazes being prevalent in the southern regions and white glazes in the northern regions, as illustrated in **Figure 5.4**. In this context, the emergence of polychrome Changsha ware during the same period is a notable artistic development that defies the conventional single-market aesthetic. The polychrome glazes can be divided into two distinct categories. The first category (**Figure 5.5**) consists of coarse polychrome decorations applied over the glaze, featuring shades of green, green-turquoise, brown, and red against a background of either white opaque or yellowish transparent glaze. These decorations are mainly in the form of large area splash designs.



Figure 5.5. Typical splash decoration of Changsha ware. (A) Dish, Changsha ware, Tang dynasty (618-907), Hunan Museum website. <http://61.187.53.122/collection.aspx?id=1604&lang=zh-CN>; (B) Ewer, used as a wine vessel, Changsha ware, Tang dynasty (618-907), The Palace Museum, <https://en.dpm.org.cn/collections/collections/2009-10-19/1151.html>; (C) The handled ewer, used for wine or tea, Changsha ware, Tang dynasty (618-907), Hunan Museum website. <http://61.187.53.122/collection.aspx?id=2259&lang=en>.

Another variation of polychrome glazes (**Figure 5.6**) is the combination of different transparent glazes of several colours, such as green and brown, red and green, or brown and turquoise which are used for intricate drawings or poetic inscriptions, usually applied underglaze.



Figure 5.6. (A) Bowl, Changsha ware, Tang dynasty (618-907), Hunan Museum, <https://de.hnmuseum.com/collection/collectionDetails.html?id=1002229327095398401&type=catalogueList#>; (B) Ewer, Changsha ware, Tang dynasty (618-907), the Palace Museum, <https://www.dpm.org.cn/collection/ceramic/227503.html>; (C) Ewer, Changsha ware, Tang dynasty (618-907), Changsha Museum, <https://www.csm.hn.cn/#/Collection/overview/detail/771?sid=C727>. (D) Ewer, Changsha ware, Tang dynasty (618-907), Changsha Museum, <https://www.csm.hn.cn/#/Collection/overview/detail/747?sid=C703>

The introduction of opaque glaze and of red decorations occurred during the Tang dynasty. The opacity of the ceramics is a consequence of the light scattering by the glass nanostructure due to the separation of two immiscible liquids at high temperature (about 1200°C), which resulted from the high ratio of SiO₂ to Al₂O₃ (about 7:1) in a lime rich glaze (Hou 2018, Kingery 1983, Chen 1989, Yuan 2022). The presence of glass droplets within the glaze produce a milky appearance, reminiscent of the translucency of jade. The opacity in Changsha ware followed the productions of Huai'an kiln (Fujian province), Wuzhou kiln (Zhejiang province), and Tang Jun ware (Henan province) all of them in the Tang dynasty (c.7th-10th century) (Chen 1991). The white opalescent appearance of the glazes may be linked to the cultural significance of jade in Chinese tradition, often serving as a metaphor for personal virtue and spirit. Alternatively, it may have been influenced by the aesthetic preference for white glaze in northern regions, which often mimicked the appearance of silver objects, or even catered to the preferences of foreign markets (Hou 2022c). An study on the origins of Changsha glaze technology suggested that it represented an integration of glaze techniques from both southern and northern China. The addition of quartz (SiO₂) to the traditional transparent lime glaze formula of southern China may have enabled the development of opaque glazes. It has been postulated that this exchange of porcelain technology between the southern and northern regions occurred during the An Lushan rebellion (Hou 2022a).

The presence of metallic copper nanoparticles, particularly in the appropriate size range (below 50 nm), and at lower volume fractions (between 0.02% and 0.05%), is responsible for the striking ruby red colour observed in glazes and glasses (Weyl 1951, Ishida 1987, Pradell 2019, Li 2022). Due to their rarity, red pigments have significant cultural value in different societies and are often reserved for high status. The Jun red coloured glazes from the Song Dynasty (960-1279) was traditionally recognised as the earliest manifestation of high-temperature red glaze in China. However, excavations of the Changsha kiln from the

mid to late Tang dynasty (766-907) revealed the existence of red painted glaze, red splashed glaze, and even red monochrome objects. These findings challenge previous assumptions and require a deeper understanding of the development of red glaze in ancient Chinese ceramics. Scientific investigations focusing on the Changsha copper red glazes or paints have consistently found the presence of copper nanoparticles (Li 2016). However, the question of whether the production of these red ceramics was an occasional occurrence or whether the potters of the late Tang dynasty (9th century C.E.) had already mastered the technique remains controversial.

Copper, which can occur in the forms of Cu^0 , Cu(I) , and Cu(II) , typically exists as Cu(I) and Cu(II) in a silicate melt due to the limited solubility of metallic copper. The absorption spectrum of Cu(II) has a broad absorption band with a peak around 830 nm, giving the glaze a green to turquoise colour. Cu(I) is colourless, but the presence of Cu_2O nanocrystals in glasses and glazes produce a yellow to orange coloration depending on the size of the particles. As the ruby red colour is rendered by the formation of metallic copper nanoparticles, the glass must undergo a reduction process that promotes the precipitation of metallic copper while preventing the precipitation of other copper compounds, such as cuprite (Cu_2O), or the formation of large Cu^0 particles, which result in a liver-red coloration. The reduction can be controlled by various methods, including the addition of reducing agents, the regulation of atmospheric conditions and firing, and the control of the copper content. The influence of the firing atmosphere on the production of red glazes in Changsha ware is widely acknowledged. If the reducing atmosphere is rather light, an excess of copper can result in green rather than red colour (Yang 2005). However, this can hardly explain the presence of green and red decorations in the same piece. In addition, the effect that the presence of other elements such as iron, sulphur, or tin may have on the red coloration remains an area of research that requires further investigation. Lead and tin are commonly added to increase the solubility of copper in the melt, and tin and iron may also act as reducing agents (Weyl 1951, Ishida 1987, Bring 2007). Zhang (Zhang 1985) proposed that dissolved stannous oxide (SnO) facilitates the reduction of cuprous oxide, leading to the formation of colloidal copper. Some recent studies of red glazes and glasses suggest that sulphur may also act as a reducing agent (Jia 2021, Yuan 2023). These questions highlight the need for further research into the various factors influencing the production of red glazes in Changsha ware.

In addition, the ongoing controversy over the application technique of Changsha ware, whether underglaze, overglaze, or even in-glaze, remains a topic of debate. Prior to the discovery of Changsha ware, examples of underglaze decoration from previous dynasties were scarce, and mainly associated with the white and blue porcelain (**Figure 5.7**) of the Yuan dynasty (1271-1368 C.E.). Subsequently, with the excavation of Changsha ware, the decorations appeared to be mainly executed underglaze, establishing the Changsha ware as the first known instance of underglaze application in Chinese ceramic history. Since the 1980s, however, debate and controversy have persisted, with some scholars claiming that Changsha ware was painted overglaze (Sun 2008, Zhang 2020). In reality, the choice of glazing depends not only on the aesthetic preferences of different dynasties and regions, but also on the expertise acquired over time. Technological developments and the development of specific painting techniques warrant further study.



Figure 5.7. (A) White and blue porcelain, Yuan dynasty (c. 1271-1368), The British Museum, https://www.britishmuseum.org/collection/object/A_1924-0114-1; (B) One example of the cross-section image of Xuande (1426-1435) imperial blue-and-white porcelain in backscattering mode. (Jiang 2019)

5.2 Objective

The beautiful designs and colours of the Changsha ware have attracted a lot of attention, but some questions are still being debated or have yet to be answered: what is the reason for the differences in the colour and opacity/transparency? Were the decorations applied overglaze or underglaze? The Changsha potters are also credited with the beginnings of copper red decoration and red, but there are still many questions to be answered: were they produced in a controlled manner, or were they the result of chance? Did the Changsha potters master the copper reds production technology? By studying a selection of Changsha ware fragments from the Palace Museum collection we will contribute to answering some of these questions: the production of the red designs, the origin opacity/transparency of the glaze, the colourants and the painting technique.

5.3 Materials

The selected glazes, **Figure 5.8**, belong to a collection of pieces which have been previously studied from a chemical point of view by Energy Dispersive X-Ray Fluorescence analysis directly on the surface of the glazes (Hou 2022a). They show the typical transparent and opaque lime glazes of the Changsha kiln, dated to the late Tang dynasty (8th-10th century). CS2 was excavated from the Huangsipu site in Zhangjiagang (Suzhou, Jiangsu Province) and CS7, CS8, CS10 and CS28 were unearthed from the Tongguan kiln site in Changsha. CS2, CS7 and CS8 have an opaque glaze, while CS10 and CS28 have a transparent glaze. CS8 has a plain green glaze, CS2 and CS7 have a white glaze with green decoration, CS10 has a transparent glaze with brown and green decoration, CS28 also has a transparent glaze with red decoration.

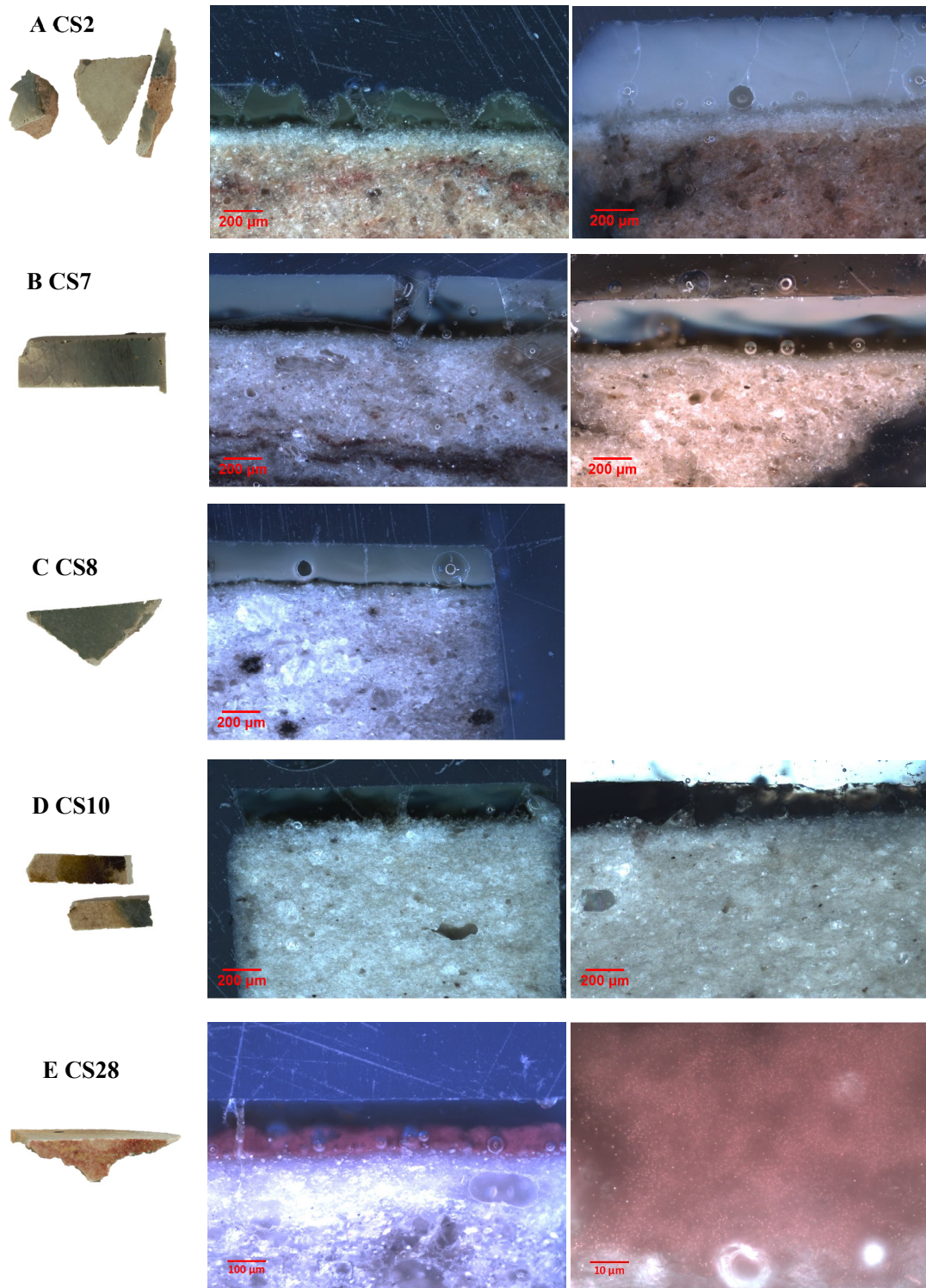


Figure 5.8. (A) CS2; (B) CS7; (C) CS8; (D) CS10; (E) CS28 sample and optical microscope darkfield image.

5.4 Chemical and microstructural analysis

The chemical composition of the glazes as measured by microprobe data taken from cross sections of the glazes is given in **Table 5.1**.

Table 5.1. Major and minor element composition of the glazes determined by Microprobe (-bd: below detection limit).

Sample	colour	SiO ₂	Al ₂ O ₃	TiO ₂	CaO	Na ₂ O	MgO	BaO	MnO	FeO	CuO	K ₂ O	SnO ₂	SO ₃	P ₂ O ₅	Tot
CS2	white	58.2	8.0	0.79	21.6	0.24	3.89	0.15	0.73	1.11	b.d.	2.39	b.d.	0.01	2.45	99.7
	green	55.4	9.0	0.74	16.5	0.22	2.86	0.13	0.54	1.11	6.34	3.08	1.23	0.03	2.02	99.2
CS7	white	58.7	9.3	0.88	19.8	0.17	3.72	0.19	0.66	1.23	0.25	1.46	0.19	0.10	2.51	99.2
	turquoise	56.5	8.5	0.86	20.7	0.18	3.90	0.21	0.67	1.11	1.37	1.55	0.94	0.05	2.77	99.3
CS8	green	55.3	6.5	0.62	22.2	0.38	3.62	0.23	0.80	0.95	3.07	2.12	1.12	0.01	2.15	99.1
CS10	colourless	58.9	12.6	0.85	17.8	0.14	2.20	0.11	0.49	1.54	b.d.	1.90	b.d.	b.d.	1.32	97.9
	turquoise	56.9	8.3	0.73	18.0	0.39	3.46	0.19	0.64	1.11	4.36	2.02	1.49	0.04	1.92	99.6
	brown	52.5	10.2	0.84	18.4	0.13	2.35	0.20	0.51	8.64	0.11	1.63	b.d.	0.02	1.47	97.0
CS28	backside colourless	60.8	12.6	0.79	18.4	0.14	2.40	0.06	0.47	2.05	b.d.	1.46	b.d.	b.d.	1.37	100.5
	colourless	59.4	12.3	0.86	19.8	0.24	2.19	b.d.	0.45	1.81	0.41	1.65	b.d.	0.01	1.29	100.6
	red	59.6	14.0	0.85	18.3	0.26	1.85	b.d.	0.37	1.99	0.43	1.99	b.d.	b.d.	0.93	100.7

The glazes are typical lime glazes (between 16%-23% CaO) with relatively high contents of MgO, MnO, K₂O and P₂O₅ associated with the use of wood ash (Hou 2022a, Wood 1999). In terms of colourants, the brown glaze contains iron (8.6% FeO), the green and turquoise glazes contain copper (1-6% CuO) and tin (0.9-1.5% SnO₂), and also a few hundred ppm of As, Sb and Pb as determined by LA-ICP-MS, indicating the use of a bronze alloy as the copper source. The red glaze contains a lower copper content than the green glazes (0.4% CuO), and also a 400 ppm of Sn, and a few tens of ppm of As, Sb and Pb, suggesting the use of the same bronze alloy as the copper source. The red decoration analysed directly on the surface by Energy Dispersive X-Ray Fluorescence (Hou 2022b), also showed the presence of around 0.10% SO₃ in the red decoration, but only 0.02% SO₂ in the lime glaze. We did not detect sulphur in the red glaze by microprobe analysis because, as we will see later, it is mainly concentrated in copper sulphide particles. Sulphur is also present in the other glazes, but at very low levels (around 0.02%). The CS28 glaze has a slightly higher iron content than the other glazes particularly the backside glaze, mainly due to its reduced thickness (60 µm), as it is thought to be incorporated into the glaze by diffusion from the underlying ceramic body.

The formulation of high lime glazes involves the use of two calcareous materials: wood ash and limestone. Wood ash, known for its high calcium and low potassium compounds, typically with a potash-to-lime ratio of 0.2 to 0.8 (Stern 2004), with additional traces of sodium, magnesium, manganese, phosphorus, and other oxides and carbonates has been used since very early in Chinese ceramic history. Limestone, on the other hand, has served as the primary flux in glaze formulation in Jingdezhen since the 10th century. As shown in **Table 5.1**, all samples have high lime and low potash contents, confirming the use of wood ash in Changsha ware.

Table 5.2. Trace elements of the glazes measured by LA-ICP-MS.

ppm	Li	B	Cl	V	Cr	Co	Ni	Zn	Ga	As	Se	Rb	Sr	Y	Zr	Nb	Ag	Sn	Sb	Cs	La	Ce	Nd	Pb	Th
CS2 white	119	186	456	65	54	10	41	188	14	40	22	114	556	30	216	15	1	393	3	7	42	73	29	57	11
CS2 green	131	199	544	65	51	66	107	335	16	123	23	140	448	25	227	14	4	9324	65	10	43	75	31	571	12
CS8 green	152	194	483	47	42	41	81	161	13	160	10	96	660	26	271	12	12	7782	81	7	48	82	35	340	11
CS28 backside colourless	110	139	275	79	63	9	47	50	23	2	82	101	353	22	160	14	0	13	1	13	36	63	26		10
CS28 colourless	168	117	1378	67	61	9	68	43	18	16	306	115	379	31	181	14	24	454	6	13	35	61	25		9
CS28 red	146	131	450	80	67	10	43	77	20	15	54	93	411	59	164	16	1	353	4	11	46	82	36	54	13

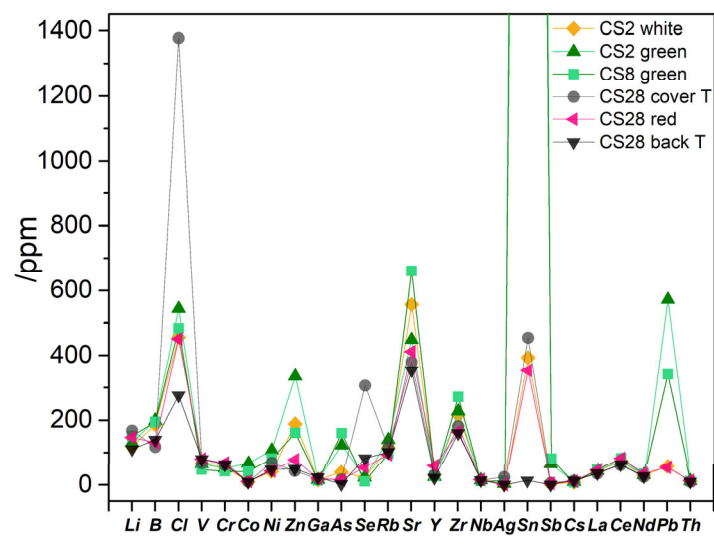
**Figure 5.9.** Trace elements of the glazes measured by LA-ICP-MS (Laser Ablation-Inductively Coupled Plasma Mass Spectrometry)

Table 5.2 and **Figure 5.9** show the trace elements present in the glazes obtained by LA-ICP-MS analysis, which reveals notable differences in the composition of the CS28 transparent glaze compared to the other glazes, in particular, shows higher levels of chlorine (Cl) among other elements, possibly indicating surface contamination. Both strontium (Sr) and zirconium (Zr) show relatively high levels in all glazes. Sr is primarily associated with calcium (Ca). Zr, on the other hand, is likely to be derived from Si-rich minerals.

Table 5.3. Summary of the properties and microstructure of the glazes

Sample	Colour		Thickness (μm)	$\text{SiO}_2/\text{Al}_2\text{O}_3$ (wt%)	Glaze nanostructure	Crystalline particles
CS2	white	opaque	470	7.3	23% 140 nm	$\text{Ca}_5(\text{PO}_4)_3\text{F}$ (fluorapatite)
	green	opaque	200	6.5	25%, 247 nm	SnO_2 (cassiterite), CaSnSiO_5 (malayaite)
CS7	turquoise	opaque	250	6.7	21%, 114 nm	
CS8	green	opaque	260	8.5	26%, 217 nm	
CS10	turquoise	opaque	200	6.9	25%, 109 nm	SnO_2 (cassiterite), CaSnSiO_5 (malayaite)
	colourless	transparent	180	4.7	none	
	brown	transparent	300	5.1	none	
CS28	backside colourless	transparent	30	4.8	none	
	colourless	transparent	60	4.8	none	
	red	opaque	60	4.2	none	$\text{Ca}_5(\text{PO}_4)_3\text{F}$ (fluorapatite), Cu_2S (chalcocite), Cu^0

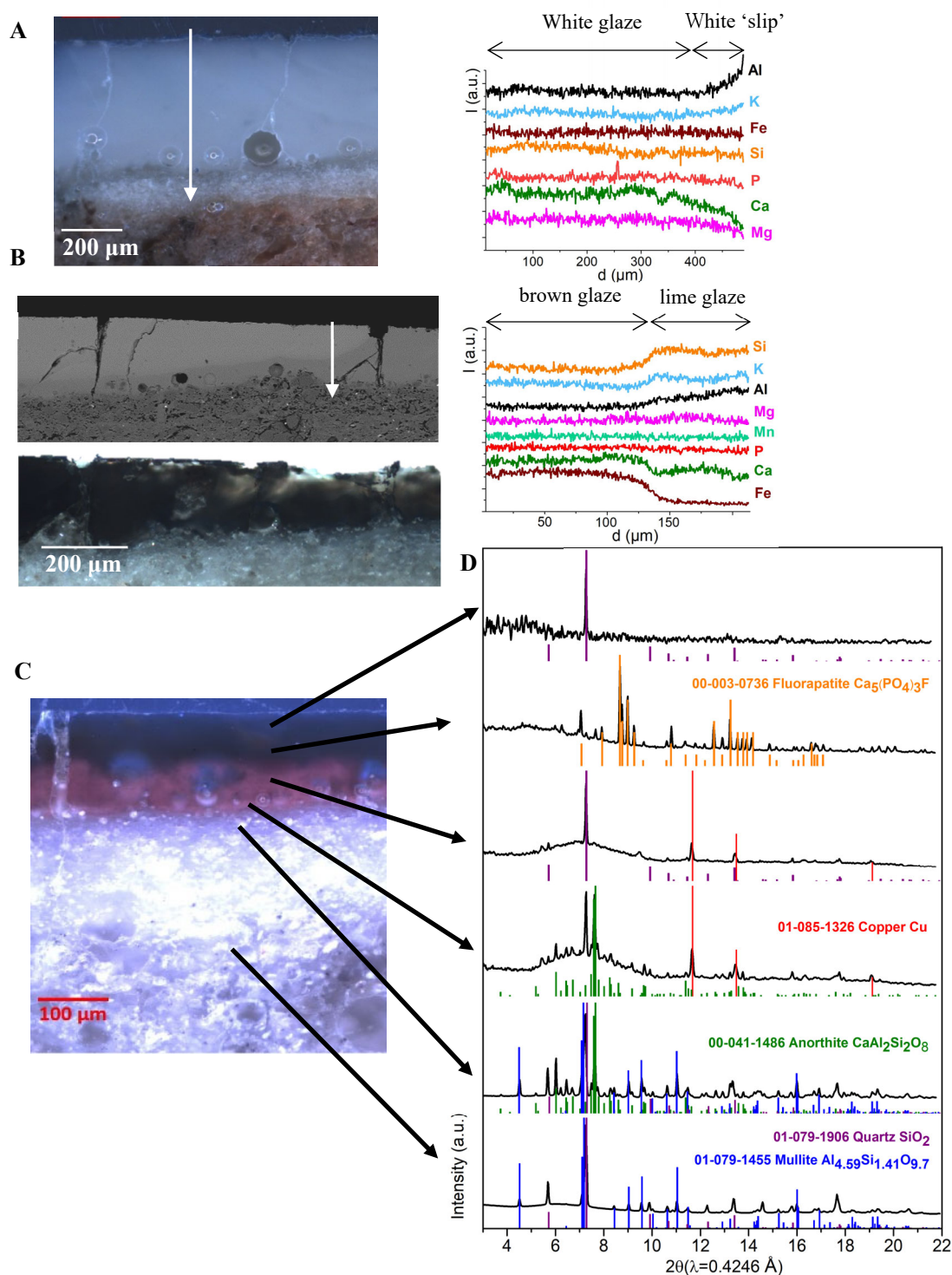
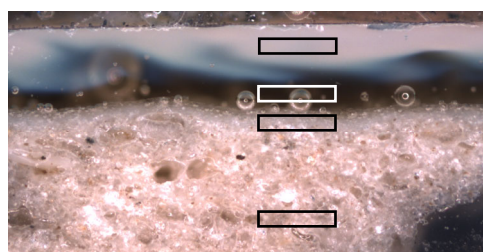


Figure 5.10. (A) OM image and line-scan through the white opaque glaze and white 'slip' of CS2, (B) SEM-BSD and OM image and line-scan through the iron-rich brown glaze over the colourless lime glaze of CS10, (C) OM image of a section of the red glaze and (D) micro-XRD patterns corresponding to different areas of CS28.

The glazes have a layered microstructure (**Figure 5.10A**), the glaze, a thin glaze-ceramic interaction layer consisting of a dark transparent glass layer (100 μm thick) enriched with Si, Al and K and precipitates of calcium-rich feldspar crystals, anorthite ($(\text{Ca},\text{Na})\text{Si}_2\text{Al}_2\text{O}_8$), and a white mainly crystalline layer (200 μm thick) with mullite ($\text{Al}_{4.5}\text{Si}_{1.5}\text{O}_{9.75}$), quartz (SiO_2) and few anorthite crystallites and finally, the stoneware

body containing mullite and quartz (**Figure 5.10D**). The interface layer is the result of the interaction of the lime glaze with the stoneware, resulting in the precipitation of calcium-rich feldspars (white background, about 200 μm thick) and a K- and Al-rich transparent dark vitreous phase with a few anorthite crystallites (about 80 μm size). Aluminium and potassium are incorporated into the glaze due to the interaction with the ceramic body; as is shown by the diffusion profile of Al and K, **Figure 5.10B**. In fact, as shown in **Table 5.4**, the white interface is richer in Al_2O_3 and K_2O and poorer in SiO_2 and FeO than the stoneware, which is consistent with the use of a fine clay on the surface, a white ‘slip’, to hide the colour of the stoneware. This ‘slip’ was probably obtained by washing the stoneware clay and selecting the fine clay fraction. **Figure 5.10B** also shows the brown glaze is applied over the transparent lime glaze.

Table 5.4. SEM-EDX data obtained on different areas of CS7, turquoise glaze, brown glaze interface, white ceramic interface and body.



wt%	Na ₂ O	MgO	Al ₂ O ₃	SiO ₂	P ₂ O ₅	K ₂ O	CaO	TiO ₂	MnO	FeO	CuO	Si ₂ O/Al ₂ O ₃
glaze	0.1	4.0	8.7	57.3	2.5	1.2	21.4	1.0	0.7	1.6	1.4	6.6
dark interface	0.3	2.5	13.7	59.2	1.7	2.8	16.0	1.0	0.4	1.3	1.2	4.3
white interface	0.4	0.3	31.6	57.8	0.2	5.0	2.4	0.7		1.3	0.4	1.8
body	0.3	0.9	19.1	72.0		3.6	0.5	0.7		2.8		3.8

The glazes with a $\text{SiO}_2/\text{Al}_2\text{O}_3$ ratio above 6 (CS2 white and green, CS7 turquoise, CS8 green and CS10 turquoise) show a glass nanostructure with darker spherical droplets in a lighter matrix (**Figure 5.11**) and are opaque. The droplets are rich in Si and K and the matrix is richer in Ca, Mg, P, Mn, Fe and Cu. The volume fraction of the droplets is more or less the same, $\approx 25\%$, while the size of the droplets varies between them from ≈ 100 nm for the turquoise glazes to over ≈ 200 nm for the green glazes and ≈ 140 nm for the white glaze. The opacity is due to the scattering of the light by the glaze droplets. The glass nanostructure is opposite to that of the Jun ware glazes, where the droplets are richer in Ca and the matrix is rich in Si (Hou 2018). This is because the Changsha glazes are richer in calcium than the Jun glazes, around 20% and 10% respectively, and consequently, the calcium-rich glass phase dominates.

Glazes characterised by a $\text{SiO}_2/\text{Al}_2\text{O}_3$ ratio below 6 show transparency and no discernible glaze nanostructure. An interesting exception is the red region of the red glaze, which appears opaque appearance. It is important to note that the opacity in this case is not due to the presence of a glass nanostructure, but rather arises from a significant concentration of metallic copper nanoparticles. The nanoparticles scatter light, resulting in the observed opacity. In this case, it is the presence of metallic copper nanoparticles,

rather than a glass nanostructure that makes the glaze opaque.

The interaction of the glaze with the ceramic surface increases the aluminium content of the interface area, reduces the $\text{Si}_2\text{O}/\text{Al}_2\text{O}_3$ ratio and, is therefore responsible for the development of a droplet-free transparent glaze. It also contains iron and titanium, which diffused from the ceramic, giving a dark appearance.

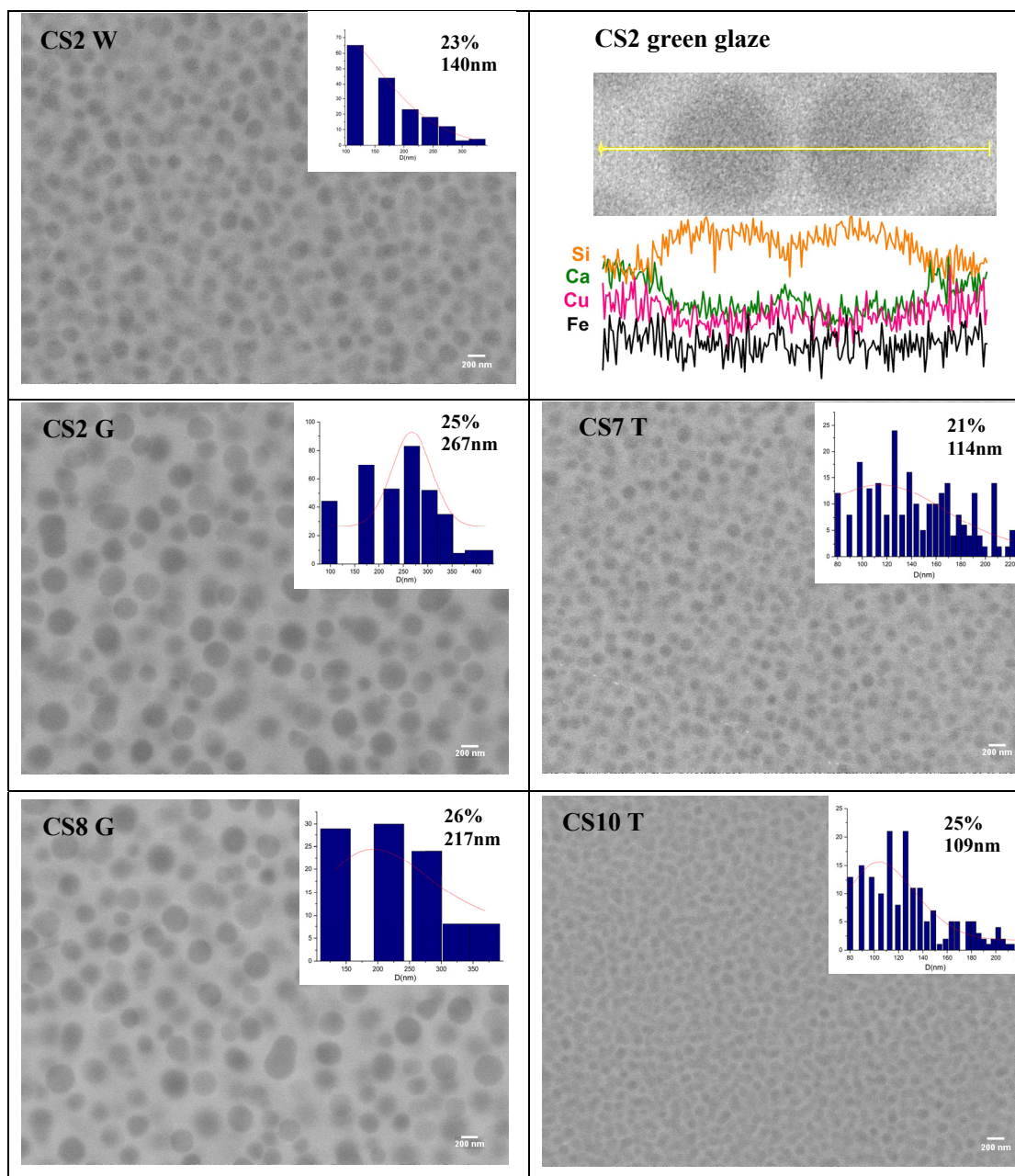


Figure 5.11. Glaze nanostructure of the opaque glazes showing the presence of spherical glass droplets (dark) and the glaze the matrix (light). W (white), G (green), T (turquoise). The line-scan shows that the droplets are richer in Si and poorer in Ca, Fe and Cu than the matrix.

The glazes also show crystalline precipitates, the white glaze of CS2 and the red area of the CS28 glaze show the presence of $\text{Ca}_5(\text{PO}_4)_3\text{F}$ (fluorapatite) (**Figure 5.12A**, **Figure 5.9D**), fluorapatite is by far the most common species in the apatite group and is often found in small amounts in igneous rocks or calcium-rich

metamorphic rocks.

The green and turquoise glazes show SnO_2 (cassiterite) and CaSnSiO_5 (malayaite), **Figure 5.12B**, both associated with the presence of tin in the copper-containing glazes. Malayaite precipitates have been documented in calcium rich areas of the glazes, often associated with copper green and blue glazes (Coentro 2014).

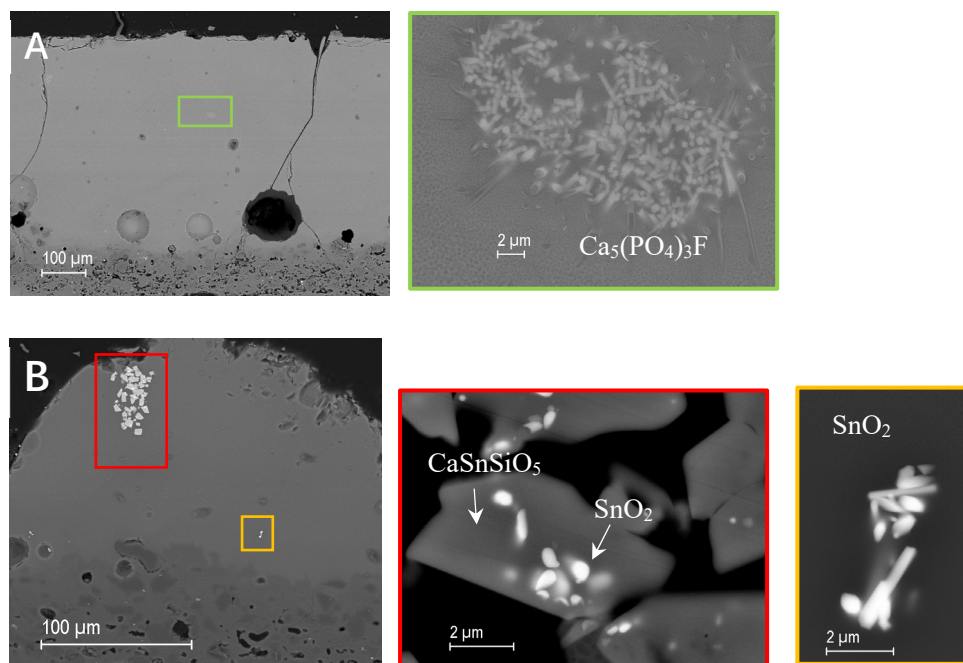


Figure 5.12. (A) CS2W (white) glaze showing precipitates of fluorapatite. (B) CS2G (green) glaze showing precipitates of malayaite and cassiterite.

The red decorated area of CS28 has a thin glaze, approximately 100 µm thick, and shows two coloured layers, a red opaque layer (60 µm thick) in contact with the ceramic surface and a colourless transparent layer (60 µm thick) on top, **Figure 5.13**. The colourless transparent layer shows the presence of a few copper sulphide microcrystallites, while the red opaque layer also contains a large amount of copper nanocrystallites, **Figure 5.13B** and **Figure 5.13C**. **Figure 5.14** shows some images and line scans corresponding to the particles. The larger particles (microcrystallites) have copper and sulphur with variable copper/sulphur content, while the nanoparticles are mainly metallic copper although they are often surrounded by copper and sulphur. The composition of the larger particles is close to Cu_2S , chalcocite. Fluorapatite crystals and calcium-rich feldspar crystals (anorthite) are also seen at the ceramic-glaze interface, both surrounded by metallic copper nanoparticles, **Figure 5.13D** and **Figure 5.13E**.

The presence of metallic copper nanoparticles is also confirmed by micro-XRD (**Figure 5.10D**), while the copper sulphide particles are not determined; in fact, the relatively scarce presence and the variable composition of the copper sulphide particles, together with the presence of other crystalline phases such as anorthite and fluorapatite with many reflections limit their identification.

In fact, the presence of copper sulphide has recently been found in the copper red glazes of early Ming

porcelain (Jia 2021). Its relevance in the development of the red colour has also been noted in the production of medieval red glass (Yuan 2023).

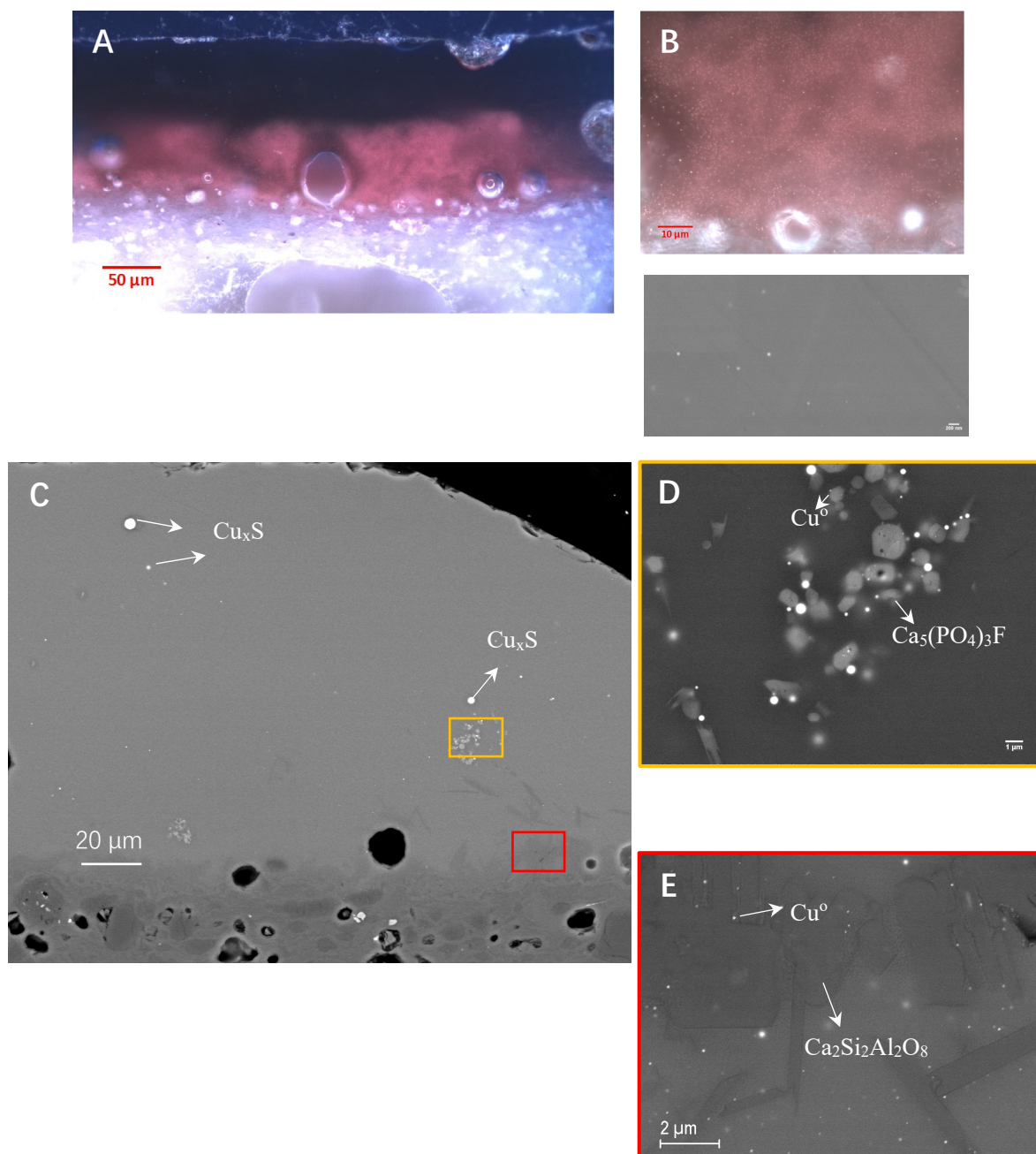


Figure 5.13. CS28 red decorated glaze (A) dark field OM image showing the red and colourless layers (B) magnification of the red area showing metallic copper nanoparticles. (C) SEM BSD image of a cross section of CS28 showing several crystalline precipitates, (D) magnification of the yellow framed area showing the presence of fluorapatite crystallites surrounded by metallic copper nanocrystallites and copper sulphide microcrystallites, (E) magnification of the red framed area showing the presence of anorthite crystals growing along the interface and metallic copper nanocrystallites.

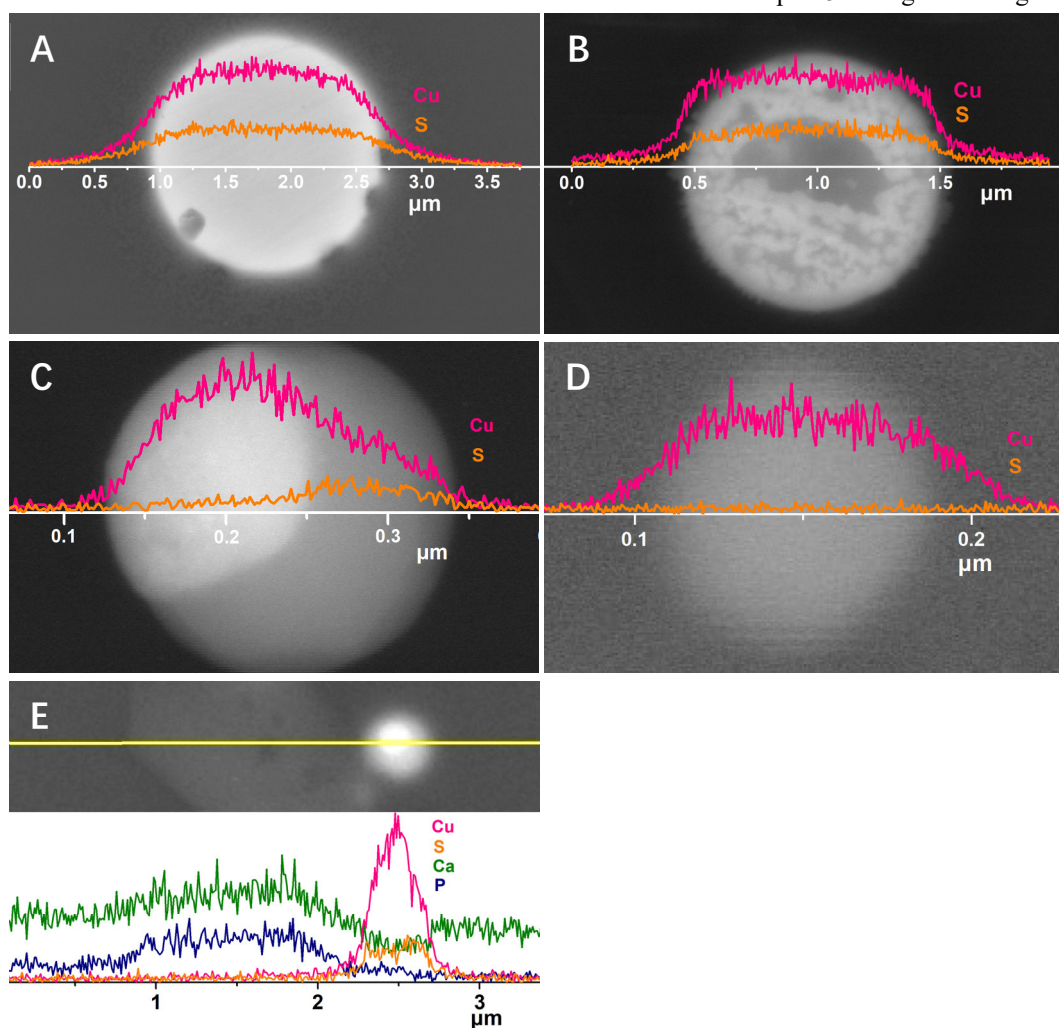


Figure 5.14. SEM-BSD and line-scans of (A) copper sulphide (Cu_2S) microparticle, (B) copper sulphide with some copper-rich areas microparticle, (C) partly copper sulphide partly metallic copper nanoparticle, (D) metallic copper nanoparticle, (E) metallic copper surrounded by copper sulphide nanoparticle growing near a fluorapatite microcrystal.

The colour of glazes is caused either by the absorption of light by chromophores (ions of transition metals) or by the absorption of light by nanoparticles. The colour and opacity of the glazes is studied using UV-Vis-NIR spectroscopy. The opaque glazes are shown in **Figure 5.15A** and the transparent glazes in **Figure 5.15B**. The glass has a characteristic exponential decrease in absorbance (increase in reflectance) with the photon wavelength (Urbach's edge) that kills the ultraviolet light. The cut-off wavelength depends on the composition of the glaze. For a lime glaze, the cut-off wavelength is at $\lambda \approx 350$ nm. The opaque glazes show an increase in the reflectance in the visible region (between 500 nm and 800 nm) due to scattering by the glass nanostructure which is partially counteracted in the green glazes by the Cu^{2+} absorption band at 800 nm. A faint tetrahedral Fe^{3+} absorption band between 400 nm and 500 nm is also visible. The white CS2 glaze also shows the broad near-infrared absorption band of Fe^{2+} in octahedral coordination at around 1100 nm.

Scattering from the glass nanostructure is therefore responsible for the opacity (high reflectance in the visible), partly counteracted by the broad absorption band at 800 nm due to the presence of Cu^{2+} . The size

of the droplets affects the total amount of light scattered, but it also shifts the scattered light to a lower wavelength (increasing the blue component). A larger number of droplets will produce more scattered light, the reflectance; the size of the droplets also affects the scattered light, the larger the droplets the larger the wavelength of the scattered light but because the surface area of the droplet is larger ($S \approx d^2$) the reflectance also increases. A high volume fraction of droplets in the glaze produces multiscattering, which broadens and red-shifts the reflectance.

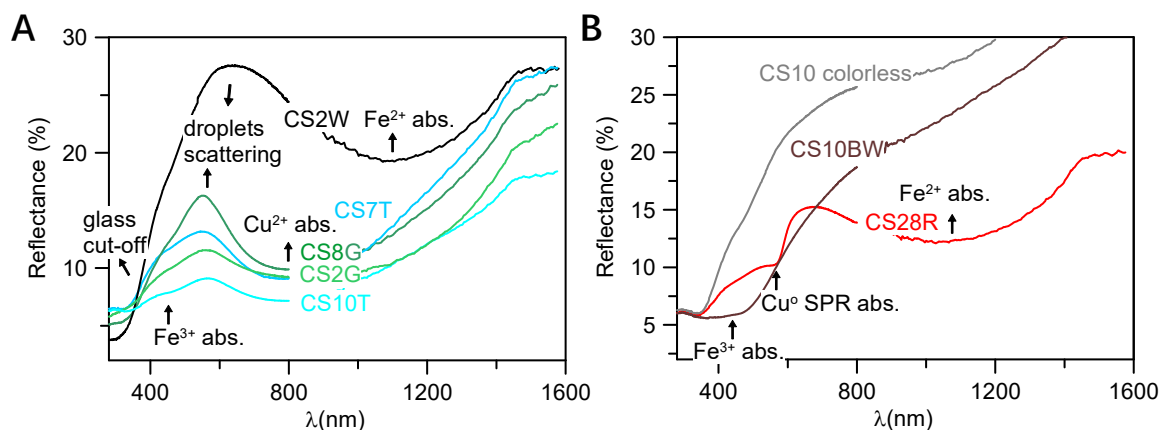


Figure 5.15. UV-Vis-NIR spectra of (A) the opaque and (B) the transparent glazes. W: white, T: turquoise, G: green, BW: brown, R: red. The scattering glass droplet nanostructure, the Fe^{2+} , Fe^{3+} and Cu^{2+} absorption bands and the Surface Plasmon Resonance (SPR) absorption of the Cu^0 nanoparticles are shown.

The transparent glazes are characterised by the absence of the glass droplet nanostructure and hence scattering, **Figure 5.15B**, and also by the near-infrared absorption band of Fe^{2+} in octahedral coordination. The brown glaze shows large absorption between 350 and 500 nm associated with tetrahedral Fe^{3+} responsible for the brown colour, a faint tetrahedral Fe^{3+} band in the colourless glaze gives a yellowish colour to the glaze. The red glaze shows the characteristic Surface Plasmon Resonance (SPR) absorption band at 560 nm, associated with the presence of metallic copper nanoparticles and responsible for the red colour and opacity. In addition, the reflectance of the CS28 glaze also shows the absorption band of Fe^{2+} in the red-NIR region.

In general, the green colour is due to the presence of Cu^{2+} and Fe^{3+} combined with the scattering ($\approx 25\%$ volume fraction) of large droplets ($\approx 200\text{-}250$ nm). The same combination of chromophores, almost the same volume fraction but of smaller droplets ($\approx 120\text{-}150$ nm) results in a blue colour. The droplet size of the CS2G is larger than that of CS8G, therefore the reflectance of the CS2G has a slight red shift compared to that of CS8G. In addition, the presence of some undissolved cassiterite (SnO_2) and malayaite (CaSnSiO_5) particles in CS2G and CS10T also increases the reflectance. The copper in CS2 is mainly present as Cu^{2+} . The presence of Fe^{2+} and Fe^{3+} , the absence of copper and the higher droplet volume fraction are responsible for the white colour in CS2W.

5.5 XAS study

The oxidation state of copper, iron and tin and sulphur was investigated from the cross section of the green glazes (CS2G and CS8G), as well as the red and colourless transparent areas, and from some particles of the red glaze CS28 (CS28R, CS28T, CS28 particle). The spectra are shown in **Figure 5.16**.

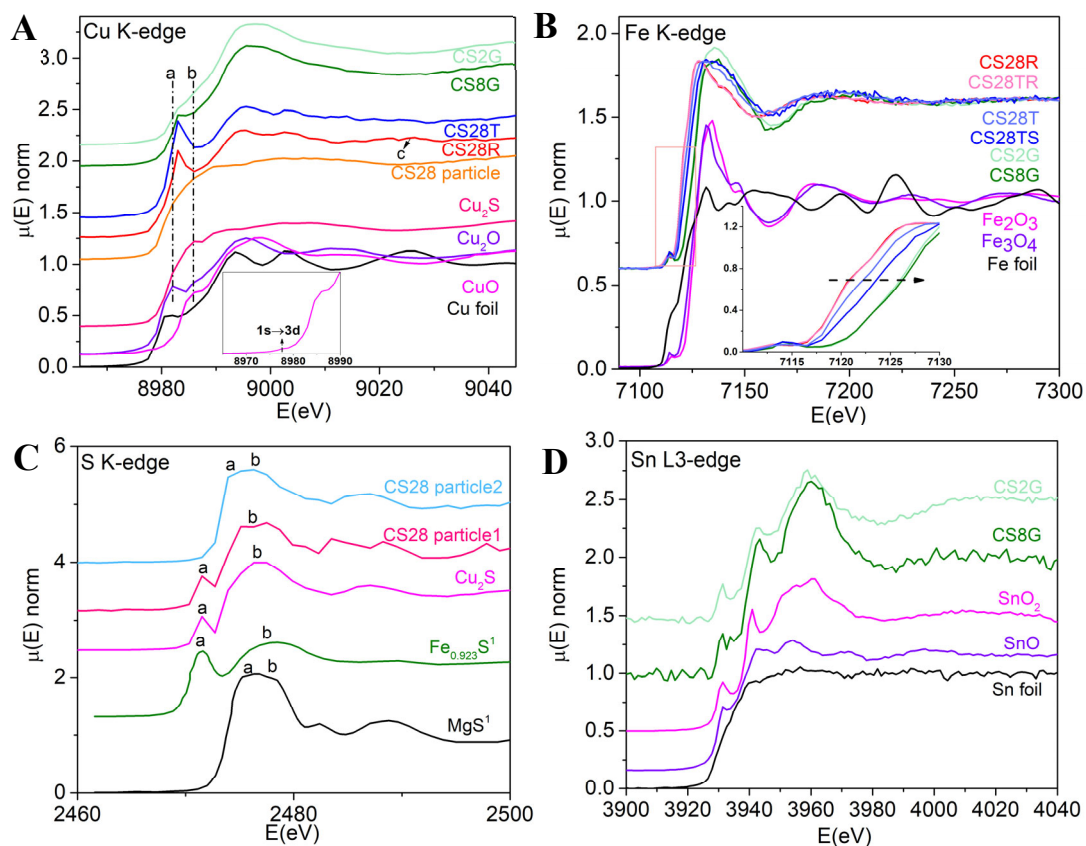


Figure 5.16. (A) Cu K-edge and (B) Fe K-edge XAS data corresponding to the green glazes (CS2G and CS8G) and to the red glass and colourless transparent layers (CS28R, CS28T) and to the copper and iron standards; (C) S K-edge of some particles of the transparent glaze (particle 1) and the interface between transparent and red glaze (particle 2), and corresponding Cu_2S reference and $\text{Fe}_{0.923}\text{S}$ and MgS after Fleet et al. (Fleet 2005) (D) Sn L3-edge corresponding to the green glazes and tin standards.

In both CS28 glazes (CS28T and CS28R) and in CS8G, the absence of the $1s \rightarrow 3d$ transition (see inset in **Figure 5.16A**) and the prominent feature observed around 8983 eV (the sharp peak between **a** and **b**) strongly suggest the prevalence of Cu^+ . In the case of CS2G, the broad peak around 8985 eV is characteristic of Cu^{2+} . In addition, the spectrum of CS28 red glaze (CS28R) shows a small peak around 9025 eV (**c**) characteristic of metallic Cu.

The Cu K-edge EXAFS fitted data are shown in **Table 5.5** and **Figure 5.17**. The data confirm that in CS2G copper is mainly present as Cu^{2+} while in CS8G Cu^+ dominates. In the red glaze Cu^{2+} is absent and Cu^+ and Cu^0 are present, 82% Cu^+ and 18% Cu^0 in the red area (CS28R) and 96% Cu^+ and 4% Cu^0 in the colourless area (CS28T).

For the copper sulphide particles present in the red glaze (CS28 particles) both the Cu and S K-edges were measured. **Figure 5.16C** shows the S K-edge corresponding to two different particles. The prominent

absorption edge features **a** and **b** are attributed to the transition of the S 1s core electron to the lowest unoccupied antibonding states on the S atom, while feature **b** is also attributed to multiple scattering resonances (Fleet 2005). Although the transition of a 1s core electron to unoccupied 3d states is forbidden by the dipole selection rules ($L=\pm 1$), p-d hybridisation makes the transition became possible. Becoming stronger at both the metal and S K-edges of metal sulphides by hybridisation of S antibonding and metal 3d states (Tossell 1977). This *p-d* hybridization is particularly strong for 3d(e_g) states. As a result, the absorption edge of most transition-metal monosulfides is complex. The increase in the area of peak **a** with increasing in metallic character, reflecting increase in the number and availability of empty e_g orbitals and covalence of metal-S bonds which aligns with the finding of Farrell et al. (Farrell 2001). Consequently, the lower absorption feature **a** of particle 2 corresponds to a weak metal signal. However, it is important to note that no distinction in the oxidation state of sulphur is evident between both particles. The data show the characteristic features of a sulphide, although not corresponding to chalcocite (Cu_2S). The copper sulphide particles analysed by SEM-EDS show a composition closer to Cu_2S in the clear glaze and closer to CuS in the red glaze, this change in composition suggests the use of more oxidising conditions in the clear glaze compared to the red glaze.

Comparing the green glazes of CS2 and CS8 (CS2G and CS8G) the latter contains significantly more CaO (22.2% instead of 16.5%) and less CuO (3.07% instead of 6.34%). When the copper content is relatively high (>3%), it tends to be present mainly as Cu^{2+} , which enhances the green colour, whereas in the CS8 green glaze (CS8G) copper is present mainly as Cu^+ , **Table 5.5**.

Table 5.5. Cu EXAFS fitting results of Changsha ware glazes.

sample	shell	Model for fit	Model parameters	Bond length	at. fraction	R factor
		R(Å)	N	R(Å)	(%)	(%)
CS28R	Cu-O	Cu_2O	2	1.83(0)	82(2)	2.8
	Cu-Cu	Cu^0	12	2.52(0)	18(2)	
CS28T	Cu-O	Cu_2O	2	1.85	96(4)	3.1
	Cu-Cu	Cu^0	12	2.55	4(4)	
CS8G	Cu-O	Cu_2O	2	1.93(2)	98(21)	3.1
	Cu-O	CuO	4	2.03(2)	2(21)	
CS2G	Cu-O1	CuO	4	1.94(1)	100	1.3
	Cu-O2	CuO	2	2.76(1)		

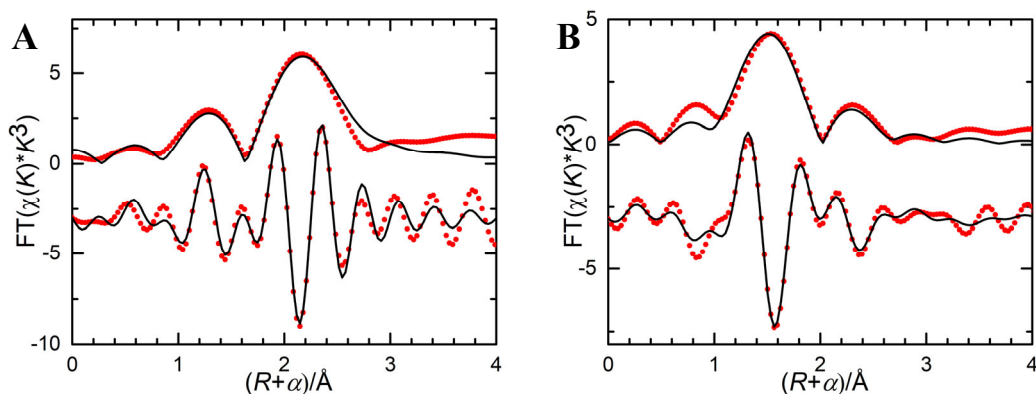


Figure 5.17. Cu K-edge EXAFS R-space (FT magnitude and imaginary part), data (points) and fit (line) of (A) red glaze of CS28 and (B) blue glaze of CS2. The data are k^3 -weighted and not phase-corrected.

Tin was measured only in the green glazes and after comparing with the measured standards (SnO and SnO₂) and also with the literature of Sn²⁺ and Sn⁴⁺ in glasses, tin appears present mainly as Sn⁴⁺, **Figure 5.16D**.

Iron was measured in the green glazes (CS2G and CS8G) and also at various depths in the red glaze; the colourless area near the surface (CS28TS), in the centre of the colourless area (CS28T), near the red area (CS28TR) and in the red area (CS28R). **Figure 5.18** and **Table 5.6** show the Fe K-edge pre-edge fitted data. In the green glazes CS2G and CS8G, iron is mainly oxidised, 80-100% Fe³⁺. In the red glaze CS28, the iron is more oxidised in the colourless area near the surface of the glaze (49% Fe³⁺/Fe_{tot}), with the Fe³⁺ content decreasing towards the red glaze, in the red area of the glaze the iron is completely reduced to Fe²⁺.

In summary, in the green glazes (CS2G and CS8G) both copper, tin and iron appear oxidised, while the red glaze (CS28) shows two distinct areas, colourless and red, with copper and iron more reduced in the red area than in the colourless area. The red area also shows the presence of large amounts of copper sulphide particles of a composition closer to Cu₂S, while the colourless area shows a few large copper sulphide particles of a composition closer to CuS.

Table 5.6. Fe K-edge fitting of the pre-edge peak of the Changsha ware glazes.

*Iron speciation calculated according to A. Fiege et al. (Fiege 2017).

	CE	A	Fe ³⁺ /Fe _{tot}
	(eV)	(eV)	(%)
	$\epsilon \approx 0.1$		
CS2G	7113.5	0.20(1)	100
CS8G	7113.4	0.19(1)	80
CS28TS	7113.2	0.22(2)	49
CS28T	7112.6	0.15(3)	20
CS28TR	7111.9	0.10(1)	0
CS28R	7112.0	0.11(1)	0

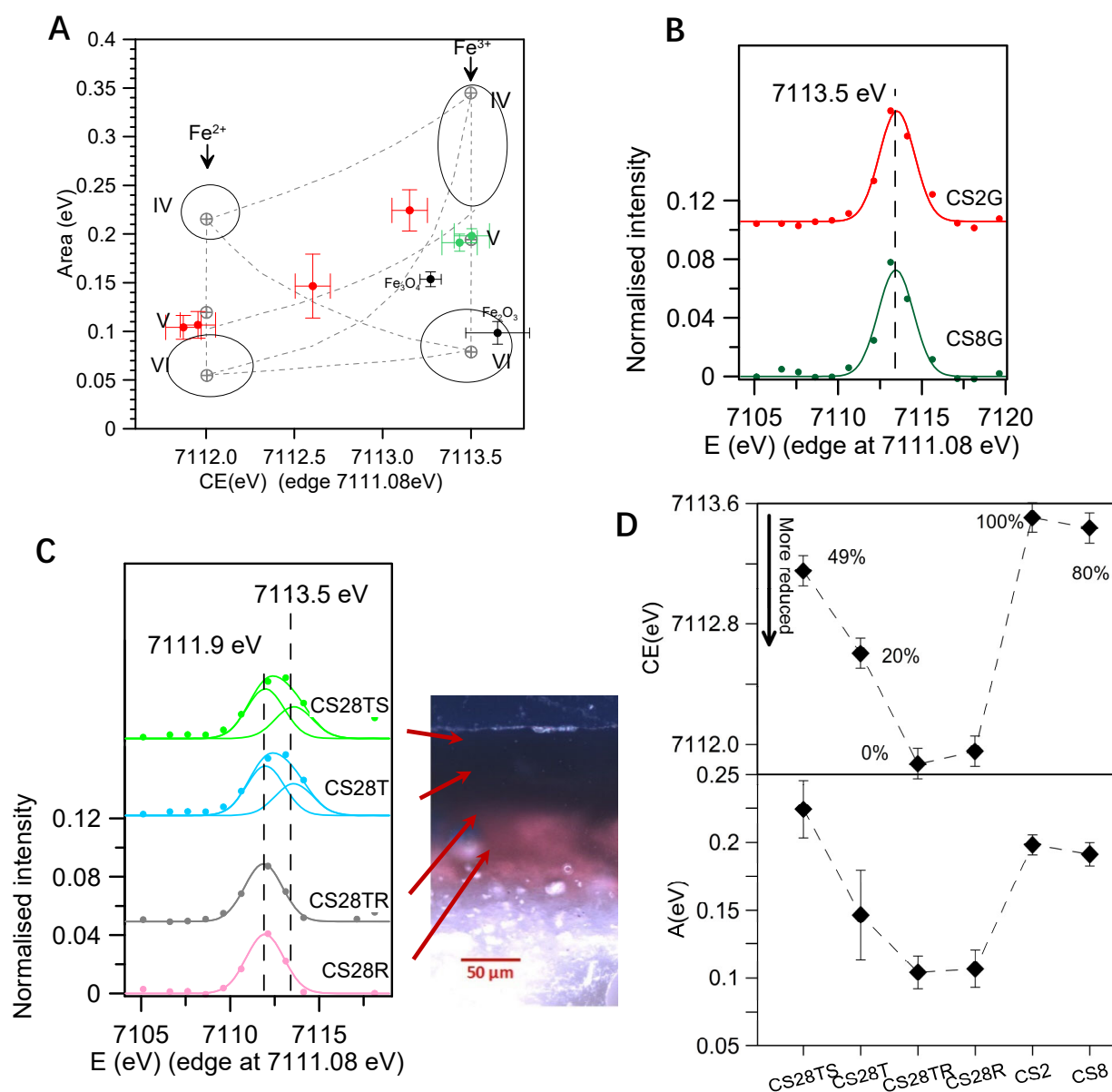


Figure 5.18. Fe K-edge XAS pre-edge peak fitting. **(A)** Variogram showing the green glazes (CS2G and CS8G) (green dots) and measurements taken at different depths of the red glaze (CS28) (red dots) showing that iron is more oxidised near the surface and appears completely reduced in the red areas of the glaze. **(B)** Fitted pre-edge peak of the green glazes (CS2G and CS8G) and **(C)** of the red glaze at different depths (CS28TS, CS28T, CS28TR, CS28R). The peak at 7111.9 eV corresponds to Fe^{2+} and at 7113.5 to Fe^{3+} . **(D)** Centre Shift and Area of the pre-peak of CS28.

5.6 Discussion

5.6.1 Colour and opacity of Changsha glazes

We have shown that visible light scattering by the glass nanostructure is responsible for the opacity of the glazes, similar to what happens in Jun ware glazes (Hou 2018, Yuan 2022). The droplet nanostructure results from the high Si/Al ratio ($\text{SiO}_2/\text{Al}_2\text{O}_3 > 6$), which causes a Si-rich liquid and a Ca-rich liquid separation at high temperature. Ca^{2+} with an ionic potential of 1.89 is strongly linked to O^{2-} , causing the phase separation in calcium rich and silica rich areas of the glaze melt at high temperature (Schuller 2018). Furthermore, the elemental distribution between the two immiscible phases followed the Nernst distribution law. It was found

that the Si-rich liquid is rich in K and Na, while the Ca-rich liquid is also rich in Mg, Fe, P and Ti as in Jun glazes. The main difference is that the droplets are Si-rich and the matrix is Ca-rich, whereas in Jun glazes it is the other way round. This is due to the high CaO content of the Changsha glazes ($\approx 20\%$ CaO) compared to Jun glazes ($\approx 10\%$ CaO). Consequently, the volume fraction of calcium-rich areas in the Changsha glazes is $\approx 75\%$, whereas it is only $\approx 25\%$ in the Jun glazes. The Changsha glaze droplets are spherical and larger (between 100 and 250 nm) than the Jun glaze droplets, which are smaller (between 70-120 nm) and show spherical, worm-like and largely interconnected shapes.

Jun glazes are reduced and show cream-coloured millimetre-sized calcium-rich areas (25% volume fraction of 120 nm droplets) with blue calcium-poor areas ($<20\%$ volume fraction of 70 nm droplets). The creamy and blue areas are the result of using of a coarse-grained material. The opacity and colour result from the light scattering of calcium-rich droplets with more oxidised iron (Fe^{3+} giving a slight yellowish colour) in the silica-rich glass with more reduced iron (Fe^{2+} giving the blue colour) (Yuan 2022). On the contrary, the Changsha glazes are oxidised, the nanostructure is homogeneous and the calcium-rich glass areas dominate with a volume fraction of calcium-rich areas of $\approx 75\%$, the iron content is lower than in the Jun glazes ($\approx 1\%$ for Changsha and $\approx 2\%$ for Jun) and consequently, the colour of the copper-free opaque glazes is creamy. Iron and copper are reduced in Jun glazes, $\approx 70\%$ Fe^{2+} , which has a broad absorption band at about 1100 nm, giving to the glaze its characteristic blue background; copper is mainly present as Cu^+ , which is colourless, but the presence of very few metallic copper nanoparticles (strong SPR absorption band at 560 nm) gives a red tinge to the cream-coloured clouds and a purple tinge to the bluish background. In contrast, Changsha glazes are oxidised and both copper and iron are mainly present in their most oxidised state, Cu^{2+} and Fe^{3+} . Cu^{2+} has a broad absorption band at 800 nm which gives the glazes their characteristic green colour.

The size of the droplets affects the total amount of light scattered, increasing the opacity but also shifting the scattered light to a longer wavelength. The combination of glass scattering and Cu^{2+} absorption is responsible for the final profile in the visible part of the UV-Vis spectrum and therefore the colour. Smaller droplets will tend to produce a green more bluish (turquoise) colour, while larger droplets will produce a green more yellowish colour.

In the Changsha opaque samples, a few different colour layers can be observed. A droplet-free transparent glaze under the opaque glaze is due to the increase in Al_2O_3 content, resulting from the interaction of the glaze with the stoneware or the 'slip'. It contains iron and titanium and appears dark. This also happens in Jun ware. Consequently, the thickness of the glaze layer also plays a significant role in opacity. If the glaze layer is too thin, the diffusion of Al from the stoneware body or the 'slip' will result in a reduced Si/Al ratio within the glaze, leading to transparency. Conversely, when the glaze layer reaches a sufficient thickness, the influence of the stoneware body or the 'slip' diminishes. Below, the white 'slip' that hides the colour of the stoneware (richer in Al and K and poorer in Si than the stoneware).

The transparent lime glazes are characterised by the absence of the glass droplet nanostructure scattering and show the characteristic exponential-like absorption/reflectance of glass. The weak tetrahedral Fe^{3+}

absorption band gives the colourless glaze a yellowish hue, which is also influenced by the colour of the stoneware surface underneath. As a result, it is also common to find the white 'slip' layer, especially over the reddish ceramic bodies.

Table 5.7 gives a summary of the stoneware and glaze composition of ceramics from different kilns in the Tang dynasty, as found in the literature. It can be seen that the Si/Al is higher in all the opaque samples than in the transparent samples. However, it can not be definitively concluded that the glaze and stoneware composition have been deliberately formulated. We have seen that if the glazes are applied very thinly the interaction between the stoneware and the glaze results in an increase in the aluminium and potassium and decrease in the calcium content of the glaze which would reduce the $\text{SiO}_2/\text{Al}_2\text{O}_3$ ratio, and consequently in a transparent glaze.

The opacity of glazes can be enhanced by the presence of undissolved or newly formed particles. In CS2 white (CS2W) and CS28 transparent and red (CS28T, CS28R) glazes, the presence of fluorapatite, a most common apatite mineral associated with animal bone ash, while in CS2 green (CS2G) and CS7 (CS7W, CS7T) and CS10 turquoise (CS10T) glazes, the presence of undissolved cassiterite or newly formed malayaite crystals also contributes to opacity. The opacity of the glazes is mainly due to the presence of a glass nanostructure, but the presence of undissolved crystals also contributes.

The brown designs were made with an iron-rich pigment; the high absorption between 350 and 500 nm associated with tetrahedral Fe^{3+} is responsible for the brown colour.

Table 5.7. Chemical composition of ceramics from different kilns of the Tang dynasty

	No.\(wt%)	SiO ₂	Al ₂ O ₃	TiO ₂	Fe ₂ O ₃	K ₂ O	Na ₂ O	CaO	MgO	MnO	FeO	P ₂ O ₅	Total	Si/Al
Body Opaque samples	TD-15 ^[1]	74.2	19.6	1.0	2.1	2.4	0.12	0.19	0.48	0.05			100.1	3.8
	TD-16 ^[1]	74.2	18.9	1.1	2.0	2.9	0.15	0.24	0.62	0.03			100.1	3.9
	TD-17 ^[1]	71.4	21.4	1.0	2.6	2.7	0.13	0.16	0.53	0.01			99.9	3.3
	L8 ^[2]	80.6	14.7	0.5	0.5	3.1	0.38	0.19	0.22	0.03			100.2	5.5
	Q1 B ^[3]	76.6	14.5	1.0	3.5	1.6	0.37	0.32	1.63			0.29	99.9	5.3
	Q2 B ^[3]	72.3	15.6	1.1	3.4	2.2	0.50	0.48	3.92			0.32	99.9	4.6
Body Transparent samples	TG15 ^[4]	67.1	26.1	0.5	2.0	2.7	0.13	0.35	0.57	0.01		0.08	99.8	2.6
	TG1 ^[4]	71.8	20.4	0.9	1.7	2.8	0.11	0.18	0.65				99.1	3.5
	OT4 ^[5]	73.3	18.7	0.9	1.5	2.9	0.40	0.50	1.10	0.03		0.10	99.4	3.9
	OT5 ^[5]	74.0	18.5	1.1	1.3	2.8	0.30	0.60	0.80	0.02		0.10	99.5	4.0
	OT6 ^[5]	71.6	18.6	1.0	1.4	2.9	0.50	3.40	0.90	0.05		0.20	99.6	3.8
	OT7 ^[5]	75.2	16.8	1.0	1.4	3.5	0.20	0.60	0.70	0.03		0.10	99.5	4.5
Glaze Opaque samples	TD-15 ^[1]	59.4	9.8	0.64	1.0	2.5	0.39	20.8	3.2	0.56	0.24	2.2	100.6	6.1
	TD-16 ^[1]	60.5	8.9	0.70	0.8	2.1	0.41	19.7	3.5	0.76	0.37	2.4	100.2	6.8
	TD17 ^[1]	57.6	8.1	0.67	0.9	2.2	0.30	23.7	3.6	0.83	0.25	2.2	100.3	7.1
	L8 ^[2]	62.8	11.0	0.81	1.5	3.8	0.68	16.3	2.1	0.34		1.2	100.4	5.7
	Q1 G ^[3]	60.8	9.3	0.60	1.6	1.1	0.29	19.5	5.4			1.2	99.7	6.6
	Q2 G ^[3]	61.8	7.9	0.50	1.8	1.3	0.23	18.8	5.9			1.4	99.6	7.8
Glaze Transparent samples	TG15 ^[4]	62.1	12.3	0.88	1.4	2.0	0.11	14.9	2.3	0.47		1.3	97.7	5.1
	TG1 ^[4]	57.0	12.1	0.87	5.2	1.7	0.23	15.7	2.4	3.31			98.4	4.7
	OT4 ^[5]	61.9	14.1	0.70	2.3	2.1	0.70	12.2	3.3	0.50		1.6	99.4	4.4
	OT5 ^[5]	59.5	14.9	0.80	2.5	2.0	0.60	13.8	3.0	0.60		1.8	99.5	4.0
	OT6 ^[5]	58.0	15.4	0.70	2.0	1.9	0.70	15.8	2.7	0.70		1.6	99.5	3.8
	OT7 ^[5]	64.1	12.7	0.60	1.6	2.3	0.50	14.2	2.1	0.40		1.0	99.5	5.0

[1] Chen XQ, Zhang ZG, Huang RQ (1991). Opaque glaze of the Changsha Tongguan ware-Another Tang dynasty's phase separated glaze. J. Chin. Ceram. Soc., 19(3): 234-240.

- [2] Chen XQ, Huang RQ, Chen SP (1986). Phase-separation glazed porcelain in the 6th century A.D.- A study on Huaian ware of the Liang and the Tang dynasty. *Journal of Chinese Ceramic Society*, 14(2): 147-152.
- [3] Li WD, Li JZ, Wu J, Guo JK (2003). Study on the phase-separated opaque glaze in ancient China from Qionglai kiln. *Ceram. Int.*, 29: 933-937.
- [4] Zhang FK. Study on Changsha ware (1986). *J. Chin. Ceram. Soc.*, 14(3): 339-346.
- [5] Chen YC, Jin BD (1991). A preliminary study of Ou kiln brown coloured celadon (甌窑褐彩青瓷的初步研究). *Relics From Jiangxi(江西文物)*, 4 : 37-40.

5.6.2 The red design

The fine decoration in sample CS28, has both green and red areas. It should be noted that the occurrence of red colouring is relatively rare in Changsha ware, and is typically found in conjunction with green motifs. The red colour appears normally on the periphery of the green areas, as well as in the form of discrete red spots or flowers interwoven with green (as shown in **Figure 5.3C**), and sometimes requires close inspection to be seen with the naked eye. This has led many to believe that red was a sporadic by-product of the primary green colour in Changsha ware. However, the Changsha red designs are the first copper reds and therefore their study is highly relevant for the understanding of the beginnings of copper reds. In the case of CS28, the painted decoration (**Figure 5.19A**) reveals the presence of a central green area surrounded by a red rim, as is commonly found in Changsha red designs. In some places, the green glaze has flaked off, exposing the ceramic body, a common problem also in Changsha red designs.

The UV-Vis spectrum analysis of CS28 shows a prominent absorption band at 560 nm, corresponding to the surface plasmon resonance (SPR) absorption of the metallic copper nanoparticles present in the red area (CS28R). These nanoparticles are responsible for the distinctive red colour and opacity of the glaze, as shown in **Figure 5.15B**. In general, copper red glazes can be obtained by a low temperature glaze reduction. A reducing gas is introduced during the cooling (below 800°C) to convert Cu^{2+} to cuprite (Cu_2O) and to metallic copper. However, this process results in a more reduced glaze surface, whereas our red glaze has a more oxidised surface.

Moreover, the red design has green and red areas (**Figure 5.19**), green in the centre of the design and red at the edges (Hou 2022b). The glaze of the green area is thinner and contains much more copper (2.5% CuO) than the glaze of the red area (0.36% CuO). The difference in the thickness between the green and red areas is due to the application of a high concentration of pigment in the centre of the design. It is well known that a high concentration of pigment with little or no glazing-mixture or clay added will repel the glaze towards the edges, resulting in a thinner glaze in the centre and thicker edges. Some of the copper in the centre of the design will diffuse to the edges. Therefore, using a high concentration of pigment will result in a thin, copper-rich glaze with thick, copper-poor glaze edges, as shown in **Figure 5.20**.

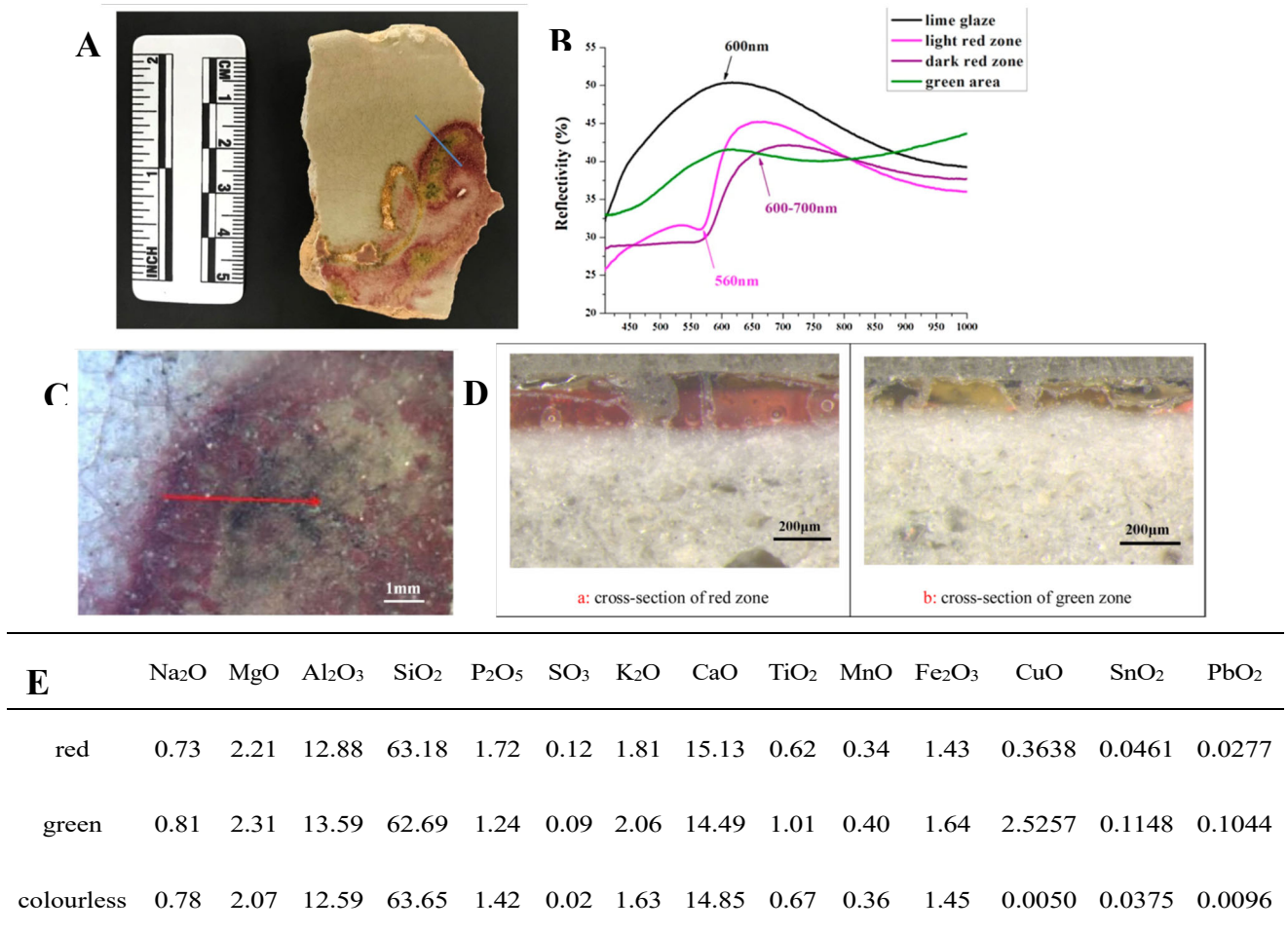


Figure 5.19. (A) Image of the decorated fragment studied (B) UV-Vis spectra of the green, red and colourless glaze (C) image of the red and green areas of the decoration, (D) OM image of the cross sections of the green and red areas and (E) chemical composition determined with XRF on the surface of the different colour areas according to Hou et al. (Hou 2022b).

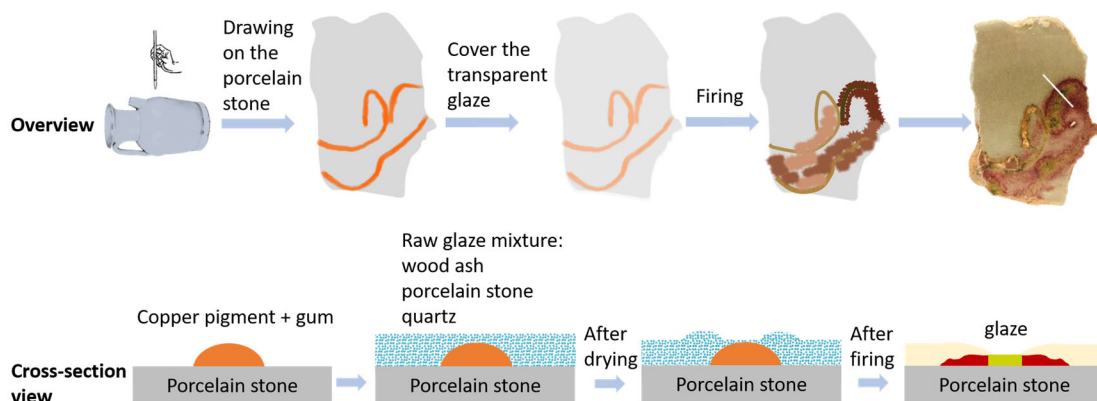


Figure 5.20. From top to bottom, application of the copper pigment, the raw glaze mixture, after drying and after firing.

The thin copper-rich central area of the design is completely oxidised and copper is present as Cu²⁺ (except

for a few red spots) as shown in **Figure 5.19** (Hou 2022b). The thick copper-poor edge has a more oxidised surface colourless layer over a red more reduced layer, **Figure 5.19A**. There is a progressive oxidation of iron towards the surface of the glaze is observed, from 100% Fe^{2+} in the red layer to 51% Fe^{2+} near the surface of the colourless layer, **Figure 5.18** and **Figure 5.19D**. Copper in the glaze is mainly present as Cu^+ even in the red area (82% Cu^+ and 18% Cu^0 in the red area), metallic copper nanoparticles are responsible for the red colour, while the copper sulphide particles present both in the red and colourless areas do not give colour to the glaze (Yuan 2022).

The presence of sulphur has also been detected in the coloured areas of the glaze (≈ 0.1 wt% SO_2) as is shown in **Figure 5.19E** (Hou 2022b), although we have seen that in the red area the sulphur appears to be mainly concentrated in the copper sulphide particles. The colourless glaze contains very little sulphur (≈ 0.02 wt% SO_2) (Hou 2022b). The glaze areas that have turned red are the edge areas of the design, which contain a low copper/sulphur ratio compared to the green area of the drawing, 2.4 and 22.6 respectively (Hou 2022b). This is in good agreement with a recent study showing that red glass contained a Cu/S atomic ratio between 2 and 2.5 (Yuan 2022).

If the atmosphere is reducing at high temperature (around 1100°C), most of the copper is retained as copper sulphide and as few metallic copper precipitates, while iron is reduced to Fe^{2+} . If more oxidising conditions then follow, they would favour the oxidation of Fe^{2+} to Fe^{3+} and the oxidation of copper sulphide, sulphur is lost as $\text{SO}_2(\text{g})$, copper dissociates as Cu_2O and Cu^0 with the consequent precipitation of metallic copper nanoparticles and dissolution of Cu^+ in the glaze.

Oxidising conditions are introduced during cooling after a reducing firing to avoid the darkening of the glaze associated with carbon deposition that occurs at around 500°C. This final oxidation process will re-oxidise the glaze, but this is a diffusion-controlled process through the glaze, the oxidation will reach a certain depth depending on the cooling rate. Therefore, thin glaze areas will appear fully oxidised, while thicker glaze areas will show a more oxidised surface layer. Consequently, the appropriate Cu/S ratio and reducing then oxidising conditions were only met at the edges of the design.

There are two ways in which sulphur could have been added to the glaze, either with the copper pigment or with the raw glaze mixture. As sulphur is highly insoluble in a silicate melt, it is mainly lost as a gas. However, in copper-containing glazes that have undergone a reducing process, copper being a highly chalcocitic element, copper sulphide particles are formed and sulphur is retained in the glaze. As higher levels of sulphur are only found in the copper design of CS28, which has undergone a reducing process, it

is difficult to say whether the sulphur was added with the raw glaze mixture or with the copper pigment. However, as the copper-free glazes also contain sulphur, albeit in very small amounts, it is possible that some of the sulphur came with the raw glaze mixture, which does not exclude the possibility that some of the sulphur also came with the copper pigment.

It is worth noting that Chinese painting made significant progress during the Tang dynasty. In particular, the depiction of flowers, birds, and animals in painting emerged as a separate category during this period (as shown in **Figure 5.21**). The elaborate decoration of Changsha ware encompassed a wide range of motifs, including figures, flora, fauna, landscapes, abstract geometric patterns, and even poetry (Changsha ware research group 1991, p116; Li 1998, p394). These decorative elements relied predominantly on line drawings to depict intricate details, complemented by the occasional use of dots for additional ornamentation. Changsha ware are one of the first wares in which the Chinese painting in a variety of colours was applied to ceramic decoration (as shown in **Figure 5.22**). Fine painting requires a great deal of skill, but also a fine background, so detailed painting is usually done on the ceramic surface rather than on the raw glaze. The painting of fine details may have led the potters to paint underglaze. If this was the case, the use of an over-concentrated pigment with little glaze or clay binder resulted in a thin design with thicker edges. The use of alternating oxidising and reducing atmospheres during the firing may have been responsible for the red-edged green designs. It is worth noting that the lack of a good binder in the design may also be responsible for the flaking off of the central parts of the design so often encountered in Changsha ware.



Figure 5.21. One example of the flower and bird painting, painter: Cui Bai(崔白), the North Song dynasty (960-1127), The

Palace Museum, <https://www.dpm.org.cn/collection/paint/228138.html>.

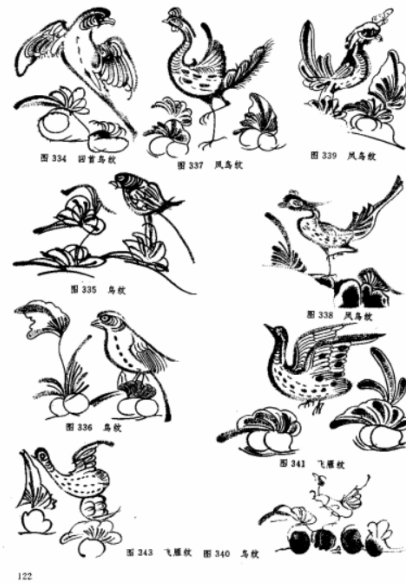


Figure 5.22. Parts of the animal painting of Changsha ware (Changsha ware research group 1991, p122)

It is also important to note that in Changsha, the ceramics were fired in a wood-fired dragon kiln common in southern China. One of the kilns located at Tanjiapuo in Wazhaping, had a large chamber measuring 41m in length and 3.5-2.8m in width. The chamber sloped upwards from the fire chamber at an angle of 90 to 230 degrees. Firing operations took place in a controlled atmosphere that alternated oxidising, reducing, and oxidising atmospheres, typically within the temperature range of 1150-1200°C (Changsha ware research group 1991, Rangika Madhumali 2021). The high inclination of the kiln indicates that the temperature was relatively easily raised, but the control of the atmosphere was difficult (Li 1998 p396). For this reason, they used saggars, evidenced by the archaeological excavations. These protective vessels played a crucial role in shielding the ceramic products from external contaminants, thereby ensuring a more stable chamber atmosphere and minimising the impact of gas impurities.

A distinctive feature of many Changsha wares is the presence of a thin white layer between the ceramic body and the glaze, particularly noticeable on finely decorated polychrome objects. This layer, known as the ‘slip’ or ‘make-up clay’, served multiple purposes. Firstly, it served to conceal any imperfections in the body, such as low temperature sintering, coarse elutriation, or undesirable red colouration. In addition, the slip was used to highlight the decorative motifs. The practice of applying such coatings can be traced back to the late Western Jin dynasty (265-317 C.E.), first found at the Wuzhou kiln in Zhejiang province.

The source of the copper used to colour the glazes in Changsha ware can be related to various geological ores, minerals, metal alloys, or copper smelting and smelting by-products. The analyses indicate that the green glazes contain copper, tin, and trace amounts of arsenic, antimony, and lead. These elements are commonly associated with natural copper ores and processed copper (Wayne Richardson 1997). The excavation of the "鄂君启节" objects in Shouxian (Anhui province) and the documents from the renowned Tang poet Dufu confirm that Tongguan was an important centre for copper casting during this period. Given the advanced state of metallurgical processes in ancient China since the Shang dynasty (2nd millennium BC), the use of copper bronze is highly plausible. It is highly probable that the copper pigment used in the glazes was obtained by roasting bronze objects. For decorative purposes, the pigment was either applied directly to the surface of the raw glaze to create designs, or mixed with the raw glaze to create monochrome glazes.

Mastering the red glaze technique has long been recognised as a challenging endeavour, the intricacies of which require considerable skill and expertise. In fact, it was not until the Tang dynasty that much progress was made in the production of red decorated glazed ceramics. The Changsha kilns in Hunan province and the Qiong kiln in Sichuan province proved to be pioneers in the successful firing of red glazes.

5.6.3 Underglaze or overglaze?

The study of the opalescent and red decorated Changsha glazes has provided valuable insights into the ongoing scholarly debate about underglaze and overglaze decoration techniques.

The historical development of underglaze decoration can be traced back to the Three Kingdoms Wu dynasty (222-280 C.E.), where the earliest examples of this technique were observed. In particular, a celadon artefact with brown decoration, as shown in **Figure 5.23A**, is considered to be one of the earliest known underglaze objects. Unfortunately, the lack of scientific analysis conducted on this object has limited our understanding of its decoration technique. Subsequently, the appearance of the dotted brown decoration gained prominence during the late West Jin dynasty (265-317 C.E.) and continued to be prevalent during the East Jin dynasty (317-420 C.E.) (an example can be seen in **Figure 5.23B**). In particular, the Ou kiln in Zhejiang province witnessed the widespread adoption of brown decoration from the East Jin period to the early South dynasty (317-589 C.E.) (**Figure 5.23 B, C, D**). These brown decorations can be divided into two distinct categories: the direct application of pigment over the glaze which is overglaze and the incorporation of pigment into the glaze to facilitate its complete dissolution. (Chen 1991b).

Furthermore, the Qiong kiln (**Figure 5.23E, F**) in Sichuan province played a pivotal role in the development of colourful ceramic decoration, despite the scarcity of fine paintings from this period. Notably, it is considered to be almost contemporary with, and even earlier than Changsha ware. It is also worth noting that the Tang dynasty witnessed the simultaneous emergence of underglaze blue and white (**Figure 5.23G**). Therefore, the ongoing debate surrounding the distinction between underglaze and overglaze techniques necessitates a reevaluation of the ambiguous definition.



Figure 5.23. (A) This celadon was defined as the first underglaze celadon, Three-kingdom Wu dynasty (222-280), Six Dynasties Museum, <http://liuchao.njmuseumadmin.com/Collections/detail/id/16>; (B) Ou Kiln, the seventh year of Yonghe reign of the East Jin dynasty (351 CE), Wenzhou Museum, https://www.wzmuseum.cn/Art/Art_28/Art_28_3272.aspx; (C) Ou Kiln, South Dynasty (420-589), Wenzhou Museum, https://www.wzmuseum.cn/Art/Art_28/Art_28_3289.aspx; (D) Ou Kiln, Tang dynasty (618-907)

Wenzhou Museum, https://www.wzmuseum.cn/Art/Art_28/Art_28_3280.aspx; (E) Qiong Kiln, Sichuan province, Tang dynasty (618-907), <https://www.dpm.org.cn/collection/ceramic/227102.htm>; (F) Qiong Kiln, Tang dynasty, Yang 2013, Master thesis, page 20. (G) Blue and white dish, probably Gongxian kilns, ca 830s, Belitung Shipwreck, c. 830s, Asian Civilisations Museum, <https://www.nhb.gov.sg/acm/galleries/maritime-trade/tang-shipwreck>.

Based on our research findings, we can conclude that both underglaze and overglaze techniques were used in the production of Changsha ceramics. Overglaze decoration is found in CS2, CS7 and CS10, while CS28 has underglaze decoration.

It can be inferred that the application of fine paintings and poems are applied directly over the body or 'slip', over which a thin, glaze layer is applied. Due to the high concentration of pigment in the central area and low concentration towards the periphery caused by diffusion, a distinct darkening effect can be observed. However, it is worth noting that the adhesion of these painted layers to the body is relatively weak, making them prone to detachment, as exemplified in the case of CS28.

The mixture of the pigments with wood ash onto the glaze has been found in CS2, CS7 and CS10. The scholarly discourse surrounding this topic has been extensively explored and discussed (Li 2021).

Furthermore, recent systematic excavations have revealed the presence of at least 57 kiln sites scattered across the southern region of Shizhu Lake and its surroundings, including numerous family workshops (Zheng 2019). Considering the evidence of commercial advertisements found on the products, it is clear that different workshops producing Changsha wares were engaged in commercial competition, which in turn facilitated the exploration and adoption of different decoration techniques. In conclusion, the flourishing of underglaze decoration in Tang Changsha wares can be attributed to the development of underglaze technique, advances in Chinese painting, and the competitive dynamics of the overseas market. At the same time, the overglaze technique used in Changsha wares has its origins in the Tang tree-colour decorated wares and the Yuezhou kilns.

5.7 Conclusions

The formation of droplet nanostructures in Changsha ware glazes can be attributed to the high Si/Al ratio ($\text{SiO}_2/\text{Al}_2\text{O}_3 > 6$), resulting in the segregation of Si-rich droplets within a Ca-rich matrix at high temperatures, contributing to the opacity of the glaze. In some samples, the presence of particles such as fluorapatite, cassiterite, and malayaite also increases opacity. The interaction between the glaze and the stoneware body

promotes an increase in aluminium content at the interface, resulting in a droplets-free transparent glaze. However, a white 'slip' gives enriched in Al, K, and relatively low Si content compared to the body was also applied with the purpose of concealing the colour of the stoneware body and also facilitating future painting.

The glazes used in Changsha ware are predominantly oxidised, with both copper and iron present mainly in their oxidised states, Cu^{2+} and Fe^{3+} respectively. The green colour of the glaze is attributed to the absorption band of Cu^{2+} at 800 nm. The presence of smaller droplets enhances the bluish hue, while larger droplets produce a more yellowish-green hue.

Regarding the underglaze/overglaze controversy, Changsha potters used both techniques to paint designs. However, it is possible that the interest in painting fine, intricate designs led the potters to switch from overglaze to underglaze painting. It is known that the application of over-concentrated pigment with little binder (clay or glaze) expels the glaze towards the edges of the painting, resulting in a thin design with thick edges. This lack of binder is also responsible for the for the flaking off of the central parts of the design so often encountered in Changsha ware.

In the case of the fine red painting, CS28, the application of a high concentration of pigment to the porcelain surface, followed by the application of a transparent glaze, resulted in the formation of a thinner design with a high copper content surrounded by a thick edge with lower copper content. The red colour develops when the glaze has a low copper content and an atomic ratio of copper to sulphur of 2.4. The red colour occurs after an initial reducing atmosphere followed by a final oxidising atmosphere, and this specific oxidation state plays a key role in the formation of copper nanoparticles. This result explains the beginning of the red designs, but leaves open the question of how much control the potters had over the process. However, even if it is the result of chance, the potters could have learnt the basic skills for making red decorations: low copper content and alternation of reducing and oxidising firings.

References

- Bring T, Jonson B, Kloo L and Rosdahl J (2007), Colour development in copper ruby alkali silicate glasses. Part 1. The impact of tin oxide, time and temperature, *Glass. Technol.: Eur. J. Glass Sci. Technol. A*. 48(2): 101-108.
- Changsha ware research group (1991). *Changsha ware (长沙窑)*. Forbidden City press. ISBN: 7-80047-174-8/K-74.
- Chinese Ceramics History (1982) (*中国陶瓷史*). Editor-in-Chief of Chinese Ceramic Society. Cultural Relics Press, Beijing. ISBN 7-5010-0953-8
- Chen XQ, R.F. Huang, S.P. Chen, X. Zhou (1989), Chinese Phase Separated Glazes in Successive Dynasties-their Chemical Composition, Immiscible Structure and Artistic Appearance, In: J. Li & X. Chen (Eds.), *Proceedings of the 1989 International Symposium on Ancient Ceramics Shanghai*, 31-37.
- Chen XQ, Zhang ZG, Huang RF (1991). Opaque glaze of the Changsha Tongguan ware- Another Tang Dynasty's Phase separation glaze (长沙窑乳浊釉-又一种唐代的分相釉). *Journal of The Chinese Ceramics Society (硅酸盐学报)*. 19(3): 234-240.
- Chen YC, Jin BD (1991b). A preliminary study of Ou kiln brown coloured celadon (瓯窑褐彩青瓷的初步研究). *Relics From Jiangxi(江西文物)*, 4: 37-40.
- Coentro S, Trindade RAA, Mirão J, Candeias A, Alves LC, Silva RMC, and Muralha VSF (2014), Hispano-Moresque ceramic tiles from the Monastery of Santa Clara-a-Velha (Coimbra, Portugal), *J. Archaeol. Sci.*, 41, 21–8. <https://doi.org/10.1016/j.jas.2013.07.031>
- Farrell SP, Fleet ME (2001). Sulfur K-edge XANES study of local electronic structure in ternary monosulfide solid solution [(Fe, Co, Ni)_{0.923}S]. *Phys. Chem. Miner.*, 28: 17–27. <https://doi.org/10.1007/s002690000129>
- Fiege A, Ruprecht P, Simon AC, Bell AS, Göttlicher J, Newville M, Lanzirotti T, Moore G (2017), Calibration of Fe XANES for high precision determination of Fe oxidation state in glasses: Comparison of new and existing results obtained at different synchrotron radiation sources, *Am. Mineral.* 102: 369–380. <https://doi.org/10.2138/am-2017-E102410>
- Fleet ME, Liu XY, Harmer SL, King PL (2005). Sulfur K-edge XANES spectroscopy: Chemical state and

content of sulfur in silicate glasses. *Can. Mineral.*, 43(5): 1605-1618.
<https://doi.org/10.2113/gscanmin.43.5.1605>

Hou JY, Pradell T, Li Y, Miao JM (2018), Jun ware glazes: Chemistry, nanostructure and optical properties, *J. Eur. Ceram. Soc.* 38 (2018) 4290-4302. <https://doi.org/10.1016/j.jeurceramsoc.2018.05.010>

Hou JY, Hu YF, Zhang XG, Zhou RK, Liu HW, Li H, Lei Y, Kang BQ (2022c), Discussion on the porcelain technology of Changsha kiln opaque glaze (长沙窑乳浊釉制瓷技术的科技研究). *Sciences of Conservation and Archaeology (文物保护与考古科学)*. 34(5): 13-21.

Hou JY, Zhang XG, Wood N, Zhou RK, Hu YF, Li H, Kang BQ, Ding YZ, Lei Y (2022a). New insights into Changsha glaze (9–10 century) based on chemical composition and strontium isotope ratio. *J. Archaeol. Sci.: Rep.* 43: 103455 <https://doi.org/10.1016/j.jasrep.2022.103455>

Hou JY, Jia C, Zhang XG, Li H, Li G, Liu HW, Kang BQ, Lei Y (2022b). The birth of copper-red glaze: Optical property and firing technology of the glaze from Changsha Kiln (8th–9th century), *J. Europ. Ceram. Soc.* 42: 1141-1148 <https://doi.org/10.1016/j.jeurceramsoc.2021.11.002>

Ishida S, Hayashi M, Takeuchi N, Wakamatsu M (1987), Role of Sn^{2+} in development of red colour during reheating of copper glass, *J. Non-Cryst. Solids.* 95-96: 793-800. [https://doi.org/10.1016/S0022-3093\(87\)80683-X](https://doi.org/10.1016/S0022-3093(87)80683-X).

Jiang XCY, Weng YJ, Wu XH, Cui JF, Lyu HS, Jiang JX, Song GD, Jin HT, Qin DS, Wang CS (2019). Early globalized industrial chain revealed by residual submicron pigment particles in Chinese imperial blue-and-white porcelains. *PNAS*, 117(12):6446-6452.
www.pnas.org/cgi/doi/10.1073/pnas.1916630117

Jia C, Li G, Guan M, Zhao J, Zheng Y, Wang G, Wei X, Lei Y (2021), A short but glorious porcelain glaze of Early Ming Dynasty: New finding of raw material and colorants in the copper red glaze, *J. Europ. Ceram. Soc.* 41 (2021) 3809–3815. <https://doi.org/10.1016/j.jeurceramsoc.2021.01.018>

Kingery WD, Vandiver PB, Huang IW, Chiang YM (1983), Liquid-liquid immiscibility and phase separation in the quaternary systems $\text{K}_2\text{O}-\text{Al}_2\text{O}_3-\text{CaO}-\text{SiO}_2$ and $\text{Na}_2\text{O}-\text{Al}_2\text{O}_3-\text{CaO}-\text{SiO}_2$, *J. Non-Cryst. Solids* 54 (1983) 163-171. [https://doi.org/10.1016/0022-3093\(83\)90090-X](https://doi.org/10.1016/0022-3093(83)90090-X).

Li G, Lei Y (2022), The computational simulation of the reflection spectra of copper red glaze. *AIP*

Advances 12(9): 095319. <https://doi.org/10.1063/5.0095570>.

Li YQ, Yang YM, Zhu J, Zhang XG, Jiang S, Zhang ZX, Yao ZQ, Solbrekken G (2016). Colour-generating mechanism of copper-red porcelain from Changsha Kiln (A.D. 7th–10th century), China. *Ceram. Int.*, 42: 8495–8500. <http://dx.doi.org/10.1016/j.ceramint.2016.02.07>

Li JZ (1998). *History of Science and Technology in China (中国科学技术史)*, Volume: Ceramic (陶瓷卷). Science press.

Li JM, Fang ZY, Shen BL, Zhu TQ, Zhang ML, Zhou SH (2021). Revisiting the Techniques of the Colored Porcelain of Changsha Kiln in the Tang and Five Dynasties (唐五代长沙窑彩饰工艺再探讨). *Journal of National Museum of China (中国国家博物馆馆刊)*, (11).

Pradell T (2019). Lustre and Nanostructures-Ancient Technologies Revisited. In: Dillmann, P., Bellot-Gurlet, L., Nenner, I. (eds) *Nanoscience and Cultural Heritage*. Atlantis Press, Paris. https://doi.org/10.2991/978-94-6239-198-7_1

Rangika Madhumali AK, Asanka Buddikasiri PR (2021). Changsha ceramics trade in ancient silk rout. *Journal of History, Art and Archaeology*, 1(1): 63-73.

Rehren T, Yin M (2012). Melt formation in lime-rich proto-porcelain glazes. *J. Archaeol. Sci.*, 39:2969-2983. <https://doi.org/10.1016/j.jas.2012.04.050>

Schuller S (2018). Phase separation in glass.

https://www.researchgate.net/publication/323692362_Phase_separation_in_glass

Stern WB, Gerber Y (2004). Potassium–Calcium Glass: New Data and Experiments. *Archaeometry*, 46(1): 137-156. <https://doi.org/10.1111/j.1475-4754.2004.00149.x>

Sun Y, Mao ZW, Zhou SR, Wang CS, Dong JQ, Yuan CX, Xu J, Yao ZQ (2008). Linear-scanning Analysis of the coloured drawing craft of Changsha-kiln porcelain by EDXRF probe (能量色散 X 射线荧光光谱法探针线扫描分析“长沙窑”彩绘工艺). *PTCA (Part B: Chem. Anal.) (理化分析-化学分册)*. 44(9): 807-814.

Tossell JA (1977): SCF- $X\alpha$ scattered wave MO studies of the electronic structure of ferrous iron in octahedral coordination with sulfur. *J. Chem. Phys.* 66, 5712-5719. <https://doi.org/10.1063/1.433845>

- Wayne Richardson H (1997). *Handbook of Copper Compounds and Applications*, CRC press. ISBN 9780824789985
- Weyl WA, 1951. *Coloured Glasses*. Reprint by Society of Glass Technology, Sheffield, 2016.
- Wood N (1999), *Chinese Glazes: Their Origins, Chemistry and Recreation*, A&C Black, London, UK, 1999.
- Yang CW (2013). *Under the glaze painted porcelain in the Tang dynasty and its comparative study of the relationship* (唐代釉下彩瓷及其相互关系的比较研究). Master thesis, Chongqing University.
- Yang YM, Feng M, Ling X, Miao ZW, Wang CS, Sun XM, Guo MS (2005). Microstructural analysis of the color-generating mechanism in Ru ware, modern copies and its differentiation with Jun ware. *J. Archaeol. Sci.* 32: 301–31. <https://doi.org/10.1016/j.jas.2004.09.007>
- Ye ZM (2011), *History of Chinese Pottery and Porcelain* (中国陶瓷史), SDX Joint Publishing Company, Beijing, China, 2011.
- Yin M, Rehren T, Zheng JM (2011). The earliest high-fired glazed ceramics in China: the composition of the proto-porcelain from Zhejiang during the Shang and Zhou periods (c. 1700e221 BC). *J. Archaeol. Sci.*, 38: 2352-2365. <https://doi.org/10.1016/j.jas.2011.04.014>
- Yuan MY, Hou JY, Gorni G, Crespo D, Li Y, Pradell T (2022), Jun ware glaze colours: An X-ray absorption spectroscopy study, *J. Eur. Ceram. Soc.* 42(6): 3015–3022. <https://doi.org/10.1016/j.jeurceramsoc.2022.02.016>
- Yuan MY, Bonet J, Cotte M, Schibille N, Gratuze B, Pradell T (2023). The role of sulphur in the early production of copper red stained glass. *Ceram. Int.*, 49(11), part B: 18602-18613. <https://doi.org/10.1016/j.ceramint.2023.02.236>
- Zhang ZG, Guo YY (1985), A study on Changsha Tongguan coloured glaze and painted wares (长沙铜官窑色釉和彩瓷的研究). *Journal of Jingdezhen Ceramic Institute* (景德镇陶瓷学院学报). 6(1): 11-17. DOI: 10.13957/j.cnki.txcb.1985.01.003.
- Zhang XG, Jiang XCY, Cui JF, Lyu HS, Qiu Y (2020). Detection and analysis of high-temperature glazed colored porcelain in Changsha kiln (长沙窑高温釉上彩瓷的检测分析). *Palace Museum Journal* (故宫博物院院刊), 5: 071-085.

Zheng JM (2019). New progress in the archaeology of high-temperature and coloured porcelain kiln sites in the Tang Dynasty since the 21st century (21 世纪以来唐代高温加彩瓷窑址考古的新进展). *Cultural Relics World* (文物天地), 1: 94-99.

Chapter 6 Copper red stained glass

Aeris rubra vitri



Chapter 6 Copper red stained glass

6.1 Introduction

The manufacture of translucent or ‘ruby’ red glass presented a significant technological challenge for early glassmakers. In ancient times, translucent red glass was extremely rare, with only a few Roman vessels from the 4th century AD known to have been coloured with gold nanoparticles (Barber 1990). However, the colour red is symbolically important and translucent red glass became an important component of ‘stained’ glass windows in cathedrals and other major buildings in northern Europe from the 12th century onwards. This achievement represented a significant advance, given that earlier red glass was predominantly opaque (Noirot 2022). Despite its significance, the precise origins of this red glass technology remain uncertain, as early coloured windows discovered in ecclesiastical buildings in the region, dating back to the 8th century AD, do not appear to have included red glass. Therefore, a comprehensive study is warranted to elucidate the technological and methodological changes underlying the production of red glass.

Medieval production of red glass relied on the controlled formation of copper nanoparticles (Weyl 1951, Ishida 1987, Freestone 1987, Freestone 1992, Nakai 1999, Farges 2006, Kunicki-Goldfinger 2014). To achieve the desired transparent red colour, it was crucial to obtain very small nanoparticles, typically less than 50 nm in size, as larger particles imparted a liver-red hue and increased opacity by scattering light (Pradell 2019, Li 2022). In addition, the volume fraction of nanoparticles had to be kept very low, ranging between 0.02% and 0.05%, as the absorption and scattering of light by the particles significantly reduced the transparency of the glass. The production of red glass aimed to achieve a vibrant red colour, but when used in the thickness of a window pane, the resulting glass would have appeared opaque and lacked the necessary transparency required for window applications. To overcome this, glassmakers developed techniques that allowed them to produce panes consisting mainly of a transparent glass substrate, with one or more extremely thin, translucent layers of red glass. In addition, red stained glass is blown glass, that is, a molten glass is gathered on an iron cane and blown into a cylinder, which is then cut and flattened while still hot. Different morphological categories of red stained window glass have been identified from the Middle Ages to the early 20th century (Farges 2006, Kunicki-Goldfinger 2014, Alonso 2009). The first category, known as ‘*striated*’ red glass, consisted of several thin layers of red and colourless glass interleaved (**Figure 6.4**). This type of glass is predominantly dated to the 12th century and gradually gave

way to the second category, known as '*sandwich*' glass. *Sandwich* glass consisted of a single layer of red glass, typically less than 0.2 mm thick, covered with a layer of clear glass of similar thickness, applied over a thick clear substrate glass (**Figure 6.1**). The third category, '*flashed*' glass, consisted of a thin surface layer of red glass applied directly to a clear glass substrate, and has been found in red window glass from the 18th, 19th, and early 20th centuries (**Figure 6.2**). Over time, the use of *striated* glass declined and was gradually replaced by *sandwich* glass, ultimately with *flashed* glass becoming the only remaining technique by the 17th century.

The solubility of metallic copper in a silicate melt is known to be extremely limited, resulting in an equilibrium of copper species primarily involving Cu^+ and Cu^{2+} . The solubility of metallic copper can vary between different glass compositions, and the addition of Pb^{2+} has been observed to increase its solubility. However, regardless of the composition, copper is predominantly present in its oxidised forms in the melt. In order to achieve the desired ruby red colour by promoting the formation of metallic copper nanoparticles, it is imperative to initiate precipitation of metallic copper nanoparticles by glass reduction while mitigating the formation of other copper compounds such as cuprite (Cu_2O), which can result in a yellow to orange hue depending its size or the formation of larger metallic copper particles which impart a livery red colour. Common methods employed for the precipitation of copper nanoparticles involve the use of a reducing atmosphere or the introduction of reducing agents into the melt. Modern red glass is obtained by adding lead, tin and iron; lead and tin increase the solubility of copper in the glass and tin and iron act as reducing agents (Weyl 1951, Ishida 1987, Bring 2007). The use of tin and iron in red glass has been documented from the mid-17th century onwards. However, in the case of medieval and Renaissance stained glass, tin is present in only trace amounts, and the iron content is comparatively lower than in later glass compositions (Kunicki-Goldfinger 2014, Pradell 2016). It is therefore important to consider the potential impact of other factors in this context.

Several studies have been conducted to investigate the production mechanisms of red stained glass in the Middle Ages, shedding light on its complex nature (Farges 2006, Kunicki-Goldfinger 2014, Colombari 2009). In general, the reduction of copper to its metallic state has been linked to the oxidation of iron during the glass firing process. For the *striated* glass type (**Figure 6.5**), a proposed mechanism suggests the precipitation of metallic copper nanoparticles in the interphase between layers of oxidised copper-rich glass and reduced copper-poor glass (Farges 2006, Kunicki-Goldfinger 2014). Detailed study of this glass type using electron microscopy and laser ablation mass spectrometry has revealed the presence of multiple

alternating layers of coloured glasses, characterized by varying copper content. The formation of micrometric red layers containing copper nanoparticles occurs in close proximity to the boundaries between the high- and low-copper areas (Kunicki-Goldfinger 2014). It has been hypothesised that copper ions diffuse from the oxidised high-copper glass into the reduced low-copper glass with low intrinsic f_{O_2} conditions, where they undergo reduction and subsequently precipitate as metallic nanoparticles. This type of red glass involves a complex technology (Kunicki-Goldfinger 2014). Nevertheless, given the greater thickness (approximately 200 μm) and uniformity observed in the red layers, this particular process seems less likely to occur in *sandwich* and *flashed* red glasses.

Valuable insights are also obtained from historical records, which provide additional information about the production and distribution of red glass at different times. Between the 13th and 16th centuries, workshops in central Europe played a prominent role in manufacturing of red glass, which was exported throughout Europe. The earliest known documentation of stained glass production can be traced back to the manuscript *De diversis artibus* (1090-1125) authored by the German monk Theophilus (Freestone 1992, Hawthorne 1979). However, this text contains little information about coloured glass, including red glass the workshops kept the information secret. It was not until the 17th century that concern about the decline of coloured glass production and the potential loss of knowledge led to the proliferation of several treatises. The first and most detailed was the manuscript *L'art vetraria* by Neri (1612) (Cable 2001). It was soon followed by Kunckel's *Ars Vitraria Experimentalis* (1679) (Kunckel 1679), ending with Pierre Le Vieil's *L'Art de la Peinture sur verre et de la Vitrierie* (Vieil 1774), both based on Neri's earlier work. These treatises aimed to preserve and extend the understanding of glassmaking techniques, including the production of coloured glass.

Recently, several attempts have been made to reproduce the glassmaking techniques described in historical treatises. Despite some inconsistencies in the chemical composition of the glass, it has been possible to successfully produce red glass using Kunckel's recipes (Vilarigues 2022), with firing temperatures of up to 1100°C. The production process involves combining a frit of a soda-rich mixed alkali glass known as *crystal* with copper and reducing agents. Two main recipes are described, one involving the addition of sulphur (actually of gunpowder, a mixture of sulphur, carbon and potassium nitrate) and the other with the addition of tin and lead *calx* (an ash of molten lead and/or tin calcined at around 600°C), burned iron or iron treated with vinegar, aqua fortis, aqua regia, and calcined cream of tartar ($\text{K}_2\text{CO}_3 \cdot 1.5\text{H}_2\text{O}$) to burnt copper. The main results of the first studies suggest that the addition of sulphur played a key role in achieving the desired

red colour, while maintaining an appropriate temperature control (around 1100°C) proved to be more important than regulating the furnace atmosphere.

Furthermore, a document written by Juan Danis in 1676, entitled *Tratado de la fábrica del vidrio* (Nieto 1967), describes also mixing *crystal* with added old copper and iron scrap, but he also mentions that the glass turns green and it is necessary to reheat it in order to obtain the red colour.

Based on the analysis of some *sandwich* red glasses from the Medieval (13th-14th centuries) and Renaissance (15th and 16th centuries) periods, the absence of tin and lead (or their presence in trace amounts only) and the presence of copper sulphide precipitates were observed (**Figures 6.13, 6.14**). This observation seems to confirm the role of sulphur in the formation of metallic copper nanoparticles, in line with the findings of Vilarigues (Vilarigues 2022). However, the specific role of sulphur in the precipitation of metallic copper nanoparticles has not been thoroughly investigated, nor has its relationship with the role of iron previously proposed in some studies (Farges 2006, Colomban 2009).

While early treatises mention the use of tin and lead *calx*, their use has been identified only in the production of small objects between the 15th and 18th centuries (Bandiera 2021, Dussubieux 2012). These glasses, characterised by a reddish-brown colour, belong to the soda-lime glass category and typically contain iron (2% to 6% Fe₂O₃), lead (0.2% to 5.5% PbO), tin (0.1% to 4.7% SnO₂), and also often antimony (0.2% to 1.1% Sb₂O₃). However, their primary purpose was decorative rather than to colour the whole glass objects, and none of them were intended for flat window glass applications. An 18th century document written by Francisco Sánchez Martínez (1718) entitled *Tratado del Secreto de pintar al fuego las Vidrieras de colores de esta Sta. Iglesia Primada de Toledo* (Iglesia 1994) describes how red glass was made by adding to clear glass a red paste made from quartz pebbles, ‘varrilla’ (ash of salicornia plants) and old copper scrap, to which were added lead and tin ashes and gunpowder (a mixture of sulphur, carbon and potassium nitrate) with old iron scrap. Although the addition of tin-lead *calx* (3.8%PbO+SnO) is mentioned, the analysis of a red fragment from the cathedral of Toledo did not reveal the presence of lead or tin (Iglesia 1994).

Finally, contemporary descriptions of red glass production emphasise the preference for using a lead potash frit, although a soda-lime frit containing some boron was also used. In the formulation, copper oxide, tin oxide, and/or antimony oxide (Bring 2007) were added to the glass frit, while in some cases, tin metal and magnetite were introduced (Weyl 1951). The resulting mixture was then fired at the melting temperature, followed by a cooling and reheating process between 500°C and 650°C to achieve the desired red colour. Higher temperatures or prolonged firing times may result in loss of the red colour. There is no specific

information available on the materials used to make the red window *flushed* glass in the 18th, 19th, and early 20th centuries.

In summary, several treatises describe the production of red glass by melting together a clear glass with old copper and iron scrap, in some cases the use of lead and tin ashes and/or of gunpowder (sulphur, carbon and potassium nitrate) is indicated. The need of reheating the glass to achieve the red colour is also mentioned.

6.2 Objective

The formation of copper nanoparticles in *striated* red glass has been proposed to occur through the diffusion of copper ions from an oxidised high-copper (Cu) glass into a low-copper glass with a low intrinsic oxygen fugacity (f_{O_2}), where the ions are subsequently reduced and precipitated as metallic nanoparticles (Kunicki-Goldfinger 2014). However, the production of the *striated* glass is less straightforward. Furthermore, while the presence of sulphur has been found to play a significant role in the formation of metallic copper nanoparticles, its specific involvement in the precipitation process has not been thoroughly investigated, nor has its potential connection with the previously suggested role of iron (Colomban 2009). In addition, there is limited knowledge of the materials used in the production of red window glass, particularly *flushed* glass, in the 18th, 19th, and early 20th centuries. As a result, an investigation is carried out on a collection of red window glasses, including *striated* glass, *sandwich* type glass, and *flushed* glass, dating from the 13th to the early 20th centuries. This chapter uses a combination of microanalytical techniques, such as laser ablation inductively coupled plasma mass spectrometry (LA-ICP-MS), field emission scanning electron microscopy (FESEM), microprobe analysis, ultraviolet and visible spectroscopy (UV-Vis), micro X-ray diffraction (micro-XRD), and micro X-ray absorption spectroscopy (micro-XAS) using synchrotron light, to determine the chemical composition, oxidation states, nature of colourants, and crystalline precipitates within the studied glass samples.

6.3 Materials

A comprehensive study is conducted on a selection of historical glass samples, including one *striated* red glass from the 13th century from the York Minster (UK), twelve *sandwich* glass samples spanning from the 13th to the 17th centuries, from Catalonia, along with one fragment from the 16th century from the cathedral of Segovia. Additionally, nine *flushed* glasses ranging from the 18th to the 20th centuries from Catalonia

and another from the 17th century from the cathedral of Segovia are examined.

The *striated* red glass sample under investigation (Ch9n-YM-5b-R3) is specifically chosen from a set of ten similar fragments obtained from the removal of glass from Window n9 of the Chapter House Vestibule in York Minster, dating back to approximately 1290-1300 (Kunicki-Goldfinger 2014).

The *sandwich* type glasses predominantly are obtained from various places in Catalonia, with the incorporation of a piece of 16th century red glass from the cathedral of Segovia of Flemish origin. Although local stained glass was produced in Catalonia since the Romanesque period, red glasses seem to have been imported from central Europe at least in the Middle Ages and Renaissance (Gimeno 2008, Domínguez Rodés 2008). In this periods, red glass was also imported from Central Europe also in Italy and Spain, the difficulties of producing red glass being the most probable reason. Similar composition and structure of red glass found in the UK further suggest a shared origin (Kunicki-Goldfinger 2014). Notable stained glass examples in Catalonia include the earliest known stained glass from the 11th century at the Museu d'Historia de la Ciutat in Barcelona, the earliest *in-situ* figurative windows at the Monastery of Santes Creus from around 1200, and recent discoveries of panels at the cathedral of Girona. The collection studied includes fragments of red glass from the Royal window from the Monastery of Santes Creus (Tarragona) dating back to approximately 1284-1320 (Ainaud i de Lasarte 1992), along with one fragment from a 16th century restoration at the same location, eight samples from the cathedral of Barcelona, three samples from the Santa Eulalia window dated 1330 of unknown authorship, three samples from the Sant Silvestre window dated 1386, also of unknown authorship, potentially rearranged by Nicoli de Maraye, and two samples from the Sant Andreu & Sant Llorenç window dated 1398-1408, created by Nicoli de Maraye (Ainaud i de Lasarte 1997), see **Figure 6.1**. Additionally, a sample from the church of Sant Joan Baptiste at Valls, part of the rose window crafted by Giacomo Carnobali in 1609 (Velasco 2017) and restored in the 17th century reusing earlier glass fragments, is included in the collection. To complement the range of samples, a fragment of red glass from the cathedral of Segovia is added, originating from the panel glasses created by the Flemish master glaziers Pierres d'Hollande and Pierres de Chiverry between 1544 and 1548.

The *flushed* glasses selected for study are primarily sourced from historic buildings in Catalonia and one fragment from the end of the 17th century from the cathedral of Segovia due to Juan de Danis, with available documentation on the production and subsequent restoration of the stained-glass windows. However, some of the fragments selected belonging to 18th century buildings ended up being from the 19th century. Details can be seen in **Table 6.1 and Figure 6.2**.

Table 6.1. Details on the red glass studied.

sample	dating	original location/collection	window/artist	glass type
Ch9n-YM-5b-R3	1290-1300	York Minster	Window n9. Chapter House Vestibule	<i>striated</i>
SC13	1284-1320	Monastery of Santes Creus. Tarragona	Royal window/ attributed to Pere d'Insa	<i>sandwich</i>
CB8, CB9, CB10	1330	Cathedral. Barcelona	Santa Eulalia window unknown authorship	<i>sandwich</i>
CB3, CB4, CB5	1386	Cathedral. Barcelona	Sant Silvestre window Nicoli de Maraye	<i>sandwich</i>
CB1, CB2	1398-1408	Cathedral. Barcelona	Sant Andreu & Sant Llorenç window Nicoli de Maraye	<i>sandwich</i>
PS15	1544-1548	Cathedral. Segovia	Pierres d'Hollande & Pierres de Chiverri	<i>sandwich</i>
SC14	1560	Monastery of Santes Creus. Tarragona	Fragment from a 16 th c. restoration	<i>sandwich</i>
Valls	1609	Church of Sant Joan Baptiste. Valls	Rose window/ Giacomo Carnobali Restauration using old glass fragments	<i>sandwich</i>
JD16	1670	Segovia cathedral	Juan Danis, Segovia	<i>flashed</i>
SM	1790	Basilica of Santa Maria del Mar	Campmajor workshop, Barcelona	<i>flashed</i>
TDM	17 th -c. building 19 th c. glass	Torroella de Montgri	lower part of the window	<i>flashed</i>
SDC	14 th -c. building reformed in the 18 th c. Destroyed 1810. Closure 1835.19 th c. glass	Church of Sant Domenec.Cervera	apse	<i>flashed</i>
Vic	Building 1748-1753 Renewal 1883 19 th c. glass	Hospital Santa Creu. Vic	dome	<i>flashed</i>
LGA	1876	Casa d'Empara. La Geltrú	fragment	<i>flashed</i>

CB6	1880	Barcelona cathedral	Santa Tecla & Sant Jordi	<i>flashed</i>
SDPDM	1889	Seu de Palma de Mallorca	Trinity window	<i>flashed</i>
CBCB	1905	Casa Bures. Barcelona	Skylight	<i>flashed</i>
CB7	1905	Museu del Disseny Barcelona. Càtedra Gaudí	Trichromacy fragment/ Gaudí	<i>flashed</i>

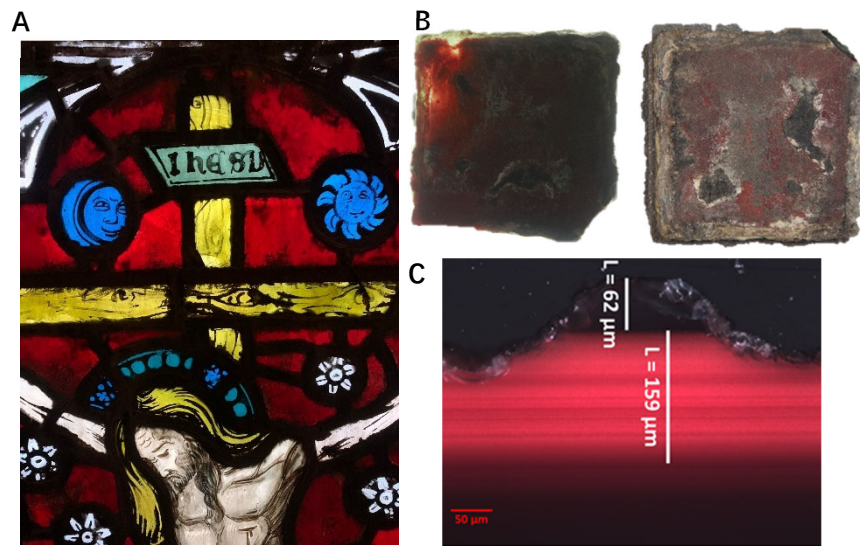


Figure 6.1. Red glass of sandwich type. (A) Fragment of Santa Eulalia window, cathedral of Barcelona, c. 1330. (B) transmission and reflection image and (C) dark field optical image of a cross section of CB1 from Sant Andreu & Sant Llorenç window, cathedral of Barcelona c. 1398-1408 by Nicoli de Maraye.

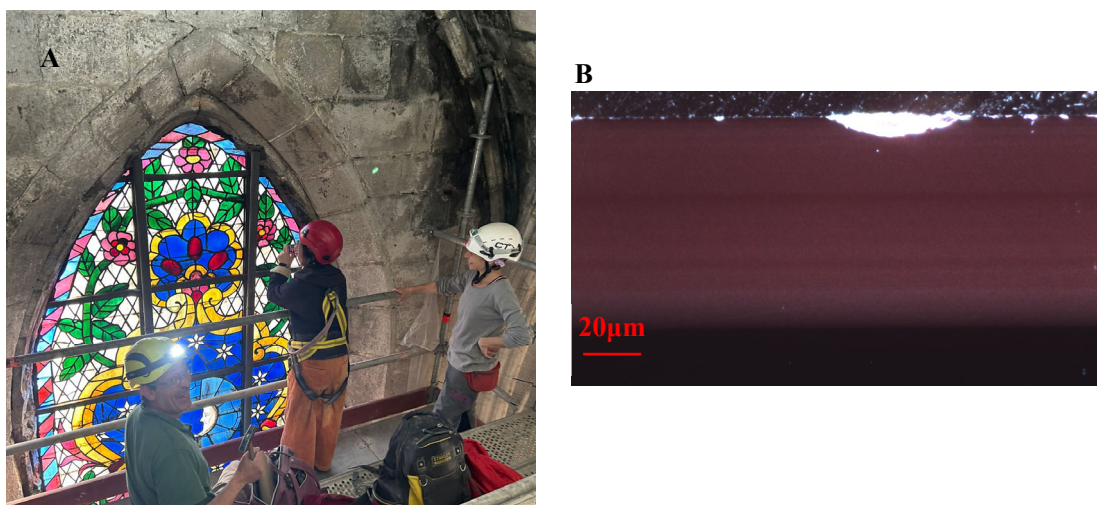


Figure 6.2. Red glasse of flashed types. (A) Stained glass window from Santa Maria del Mar made by the Campmajor workshop dated in 1790. Dark field reflection optical microscope image of (B) CB6.

Figure 6.3 shows the changes in the chemical composition of the red and base clear glasses over time. A number of features emerge from the chemical analysis of the glasses, which are summarised below.

13th -14th century: potash lime clear glass made from forest ash; the red glass has the same composition as the clear glass except for copper. Sandwich type.

15th century: potash lime-rich clear glass made from forest ash; the red glass has the same composition as the clear glass except for copper. Sandwich type.

16th - 17th century: high lime-low potash clear glass made from plant ash; the red glass has the same composition as the clear glass except for copper. Sandwich type.

Late 17th - early 19th century: soda and potash-low lime clear glass made from plant ash; the red glass has the same composition as the clear glass except for copper. Flashed type.

19th - 20th century: soda-lime glass made from artificial soda, contains less P and more Cl. The red glass is poorer in poorer and richer in soda than the clear glass and contains, copper, tin and iron, the 20th century the red glass contains less iron. Flashed type.

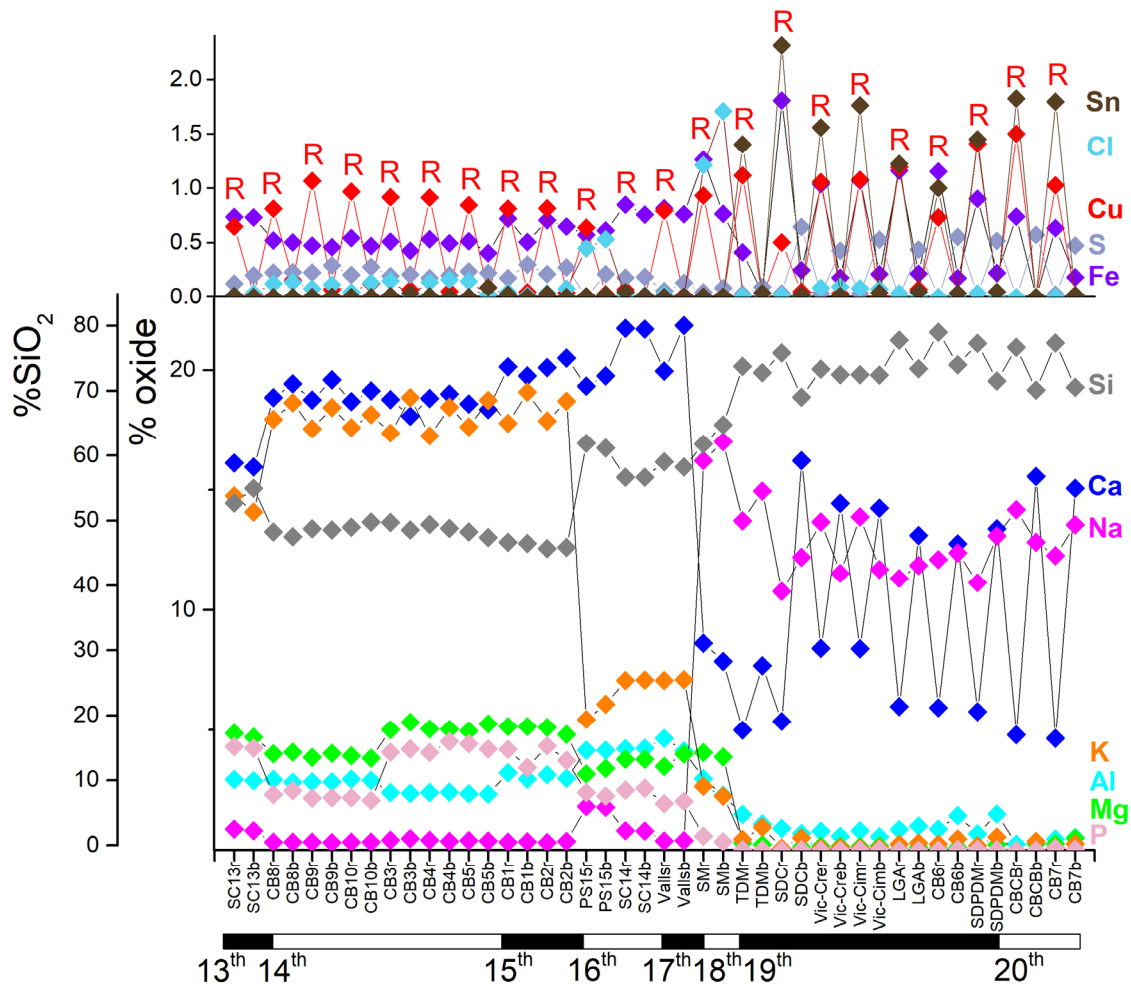


Figure 6.3. Chemical composition of the red (r) and base (b) glasses from the 13th to the 20th analysed by Microprobe.

6.4 Red glass-one case study of *striated* red glass in the 13th century

6.4.1 Results

Figure 6.4A displays a cross-sectional view of the layered structure of the examined glass, with the analysed area highlighted. In **Figure 6.4B**, both transmission and reflectance optical images of the analysed area are provided. The transmission optical image reveals the presence of colourless and red glass layers, whereas the dark field reflection image showcases the light scattering phenomenon caused by copper nanoparticles, with brighter areas indicating larger nanoparticles. The images provide visual evidence of the variable hue observed in the red layers, which consist of multiple thin layers of copper nanoparticles between colourless glass layers.

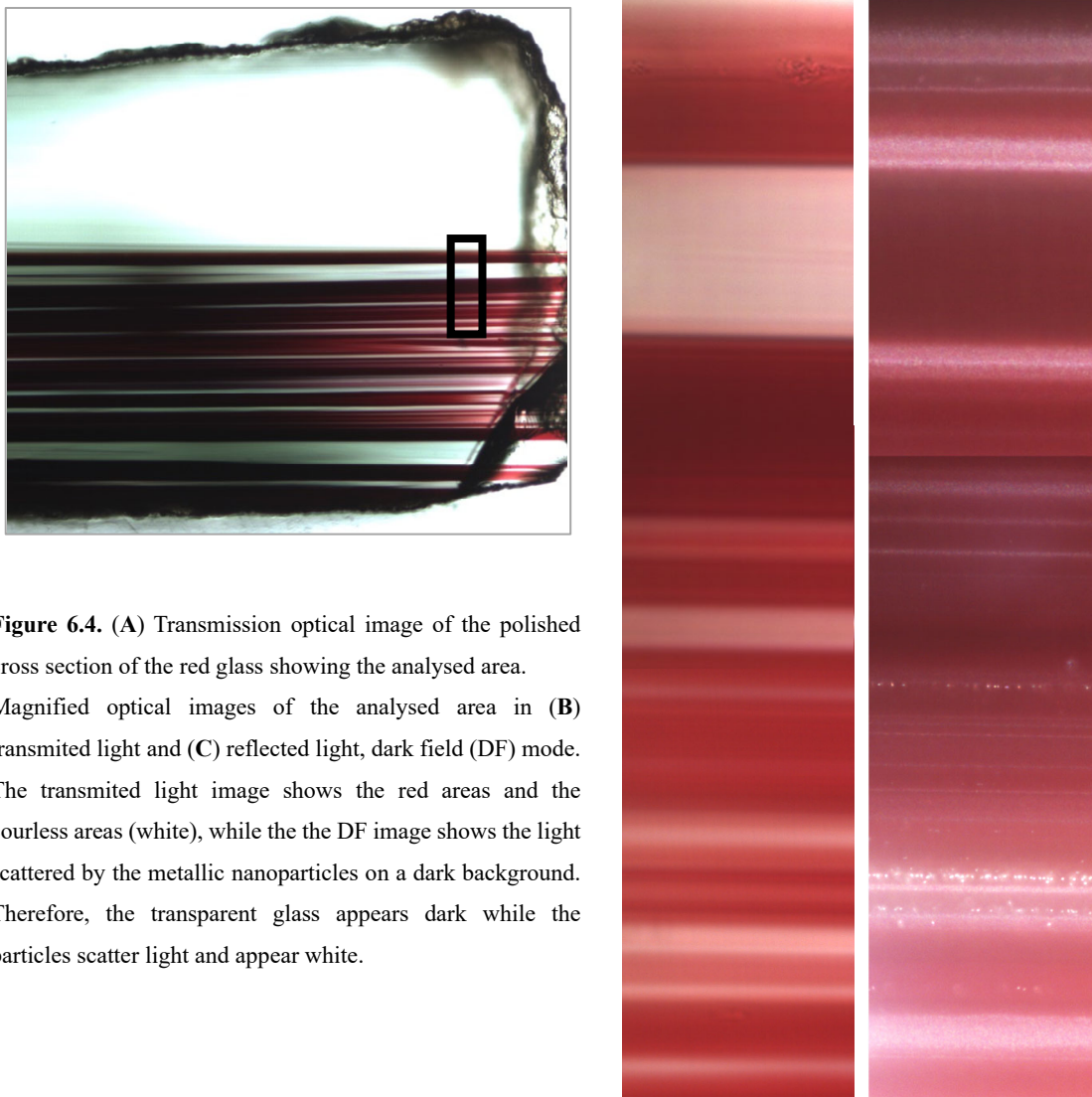


Figure 6.4. (A) Transmission optical image of the polished cross section of the red glass showing the analysed area. Magnified optical images of the analysed area in (B) transmitted light and (C) reflected light, dark field (DF) mode. The transmitted light image shows the red areas and the colourless areas (white), while the DF image shows the light scattered by the metallic nanoparticles on a dark background. Therefore, the transparent glass appears dark while the particles scatter light and appear white.

The red glass comprises multiple layers of nanoparticles, each layer being remarkably thin. **Figure 6.5** exhibits a FESEM-BSD image focusing on one of these nanoparticle layers, which typically measures

around 1 μm in thickness. The particles within the layer exhibit varying sizes, ranging from 20 to 40 nm.

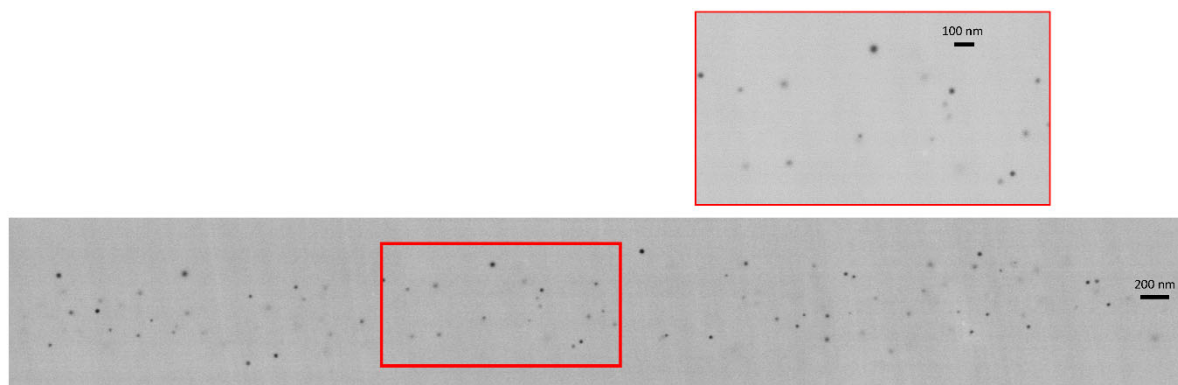


Figure 6.5. SEM-BSD image of one of the metallic copper nanoparticle layers. The particle sizes vary between 20 and 40 nm and form layers less than 1 μm thick.

Figure 6.6 shows the micro-XRF maps of copper (**Figure 6.6E**) and iron (**Figure 6.6F**) were obtained and the corresponding line-scans (**Figure 6.6A**) were extracted from the mapped area. The corresponding transmission and reflectance optical images are also shown in **Figure 6.6C** and **Figure 6.6D**. Other elements of interest were also checked but they did not show any significant changes across the section. Different glass layers were identified in the glass cross section according to their colour and iron and copper content (**Figure 6.6A**). The iron and copper contents of the different areas were measured by SEM-EDX:

1. Cu-free colourless substrate glass, 0.45% Fe, contains no copper. Blue in **Figure 6.6B**.
2. Cu-rich colourless glass, $\approx 0.5\%$ Cu and $\approx 0.5\%$ Fe. Green in **Figure 6.6B**.
3. Cu-rich red glass, between $\approx 0.4\%$ Cu and $\approx 0.45\%$ Fe. Red in **Figure 6.6B**.
4. Cu-poor reddish glass, $\approx 0.2\%$ Cu and $\approx 0.45\%$ Fe. Pink in **Figure 6.6B**.
5. Cu-poor colourless glass, below $\approx 0.2\%$ Cu and $\approx 0.5\%$ Fe. Grey in **Figure 6.6B**.

Over the copper-free colourless substrate glass (blue) a copper-rich colourless glass (green) is applied. This copper-rich layer is then followed by a series of glass areas in varying shades, including red (red), reddish (pink), and colourless (grey), all of which contain certain amounts of copper. Additionally, iron is present in all of the glass areas.

For the further analysis of the oxidation state, several points were chosen from the different glass areas, and corresponding spectra for the Cu K-edge and Fe K-edge were obtained.

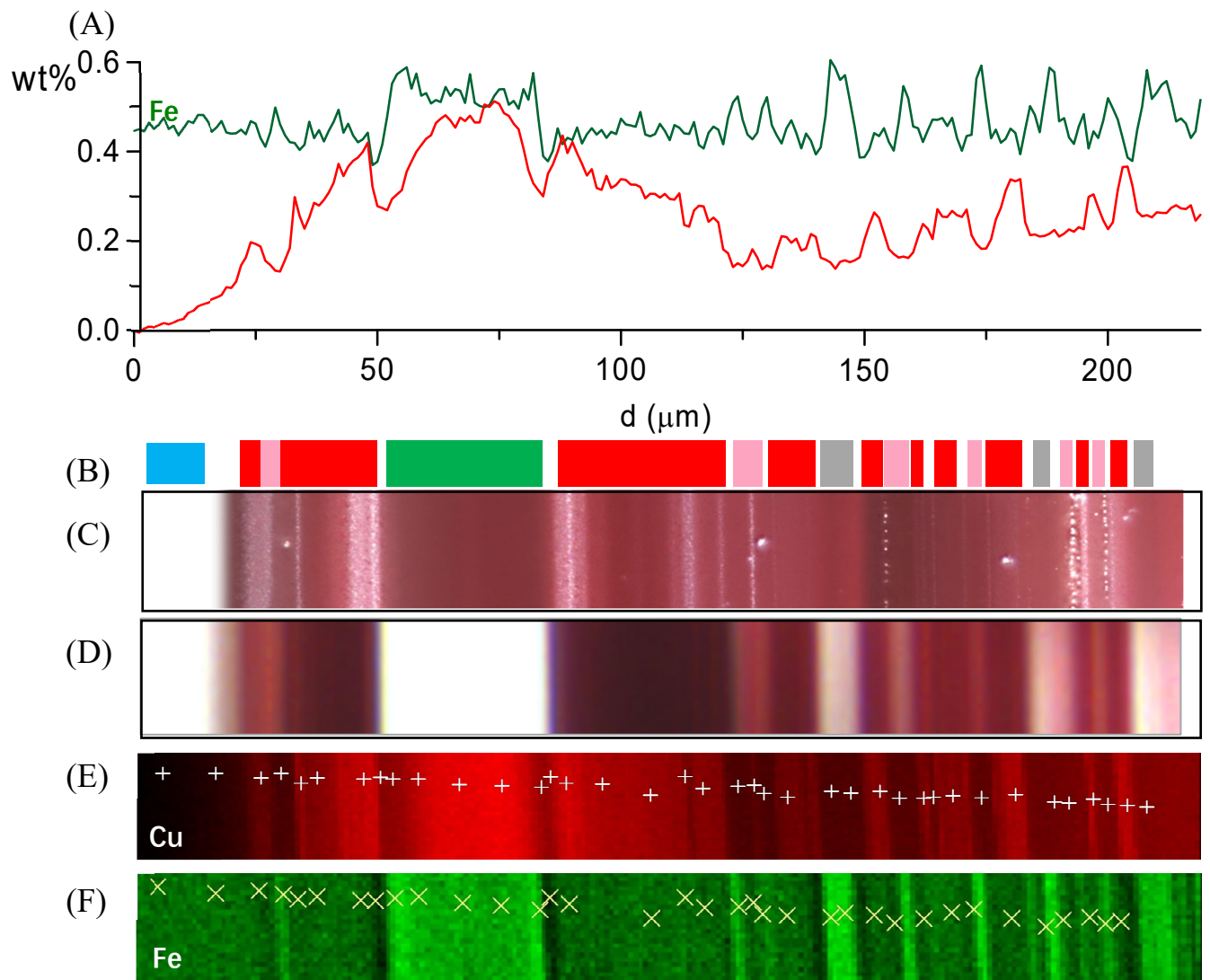


Figure 6.6. (A) Cu and Fe XRF line scan, (B) glass areas determined as a function of the copper and iron content and colour, (C) Dark field reflection optical image (D) transmission optical image, (E) Cu XRF map and (F) Fe XRF map. + and x correspond to the measured copper and iron points, respectively.

The normalized absorption spectra for the Cu K-edge and Fe K-edge, representing different glass areas and reference compounds, are presented in **Figure 6.7A** and **Figure 6.7B**, respectively. Each spectrum corresponds to the designated colours indicated above for the respective glass areas.

It is important to note that the colourless substrate glass (blue) does not contain any copper and thus only the presence of iron is plotted. The substrate glass is of particular significance as it can be taken as the original oxidation state of the copper-free glass. In contrast, the thin iron-rich colourless areas (grey) do contain traces of copper, likely due to copper diffusion from the adjacent copper-rich glass areas.

The EXAFS Cu K-edge spectrum associated with the red areas exhibits distinct oscillations characteristic

of metallic copper, which are notably absent in the copper-rich colourless glass (green).

In **Figure 6.7B**, the spectra corresponding to the Fe K-edge are displayed. The inset in **Figure 6.7B** highlights that the most oxidized iron is observed in the copper-rich colourless glass (green), while the most reduced iron is found in the copper-free colourless substrate glass (blue).

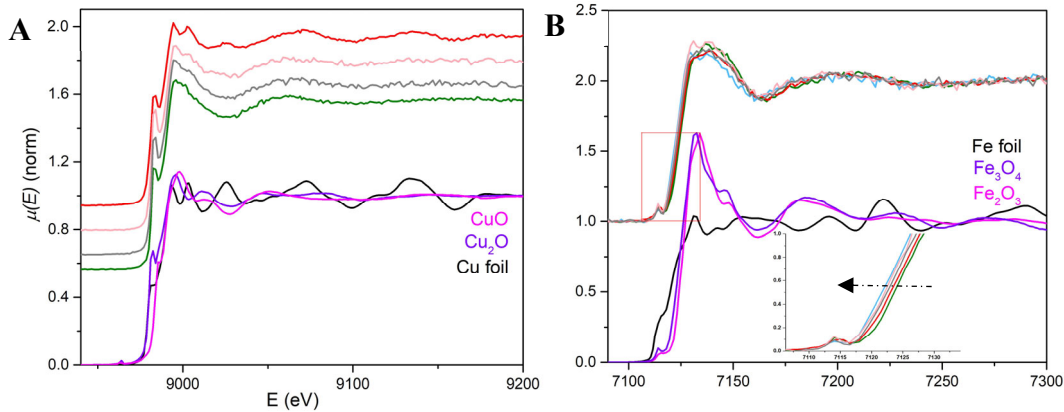


Figure 6.7. (A) Cu K-edge and (B) Fe K-edge absorption spectra corresponding to the four and five glass areas respectively, and reference compounds. Green: copper-rich colourless glass, red: copper rich red glass, pink: copper-poor reddish glass, grey: copper-poor colourless glass, blue: copper-free colourless substrate glass. The shift to a lower energy of the Fe K-edge (arrow) indicates that the iron is more reduced.

Table 6.2. Copper EXAFS fitted parameters of the *Striated* glass.

Glass areas (number of points)	Model for fit	shell	Model parameters		Bond length R(Å)	Fraction (at%)	R factor (%)
			N	R(Å)			
Green (3 points)	CuO (tenorite)	Cu-O	4	1.956	1.95(1)	20(1)	1.6
	Cu ₂ O (cuprite)	Cu-O	2	1.857	1.85(1)	80(1)	
Pink (6 points)	CuO	Cu-O	4	1.956	1.98(1)	3(12)	1.6
	Cu ₂ O (cuprite)	Cu-O	2	1.857	1.88(1)	92(12)	
	Cu ⁰	Cu-Cu	12	2.556	2.58(1)	4(12)	
Red (14 points)	Cu ₂ O (cuprite)	Cu-O	2	1.857	1.85(1)	63(7)	2.7
	Cu ⁰	Cu-Cu	12	2.556	2.55(1)	37(7)	
Grey (4 points)	Cu ₂ O (cuprite)	Cu-O	2	1.857	1.86(1)	100(2)	3.2

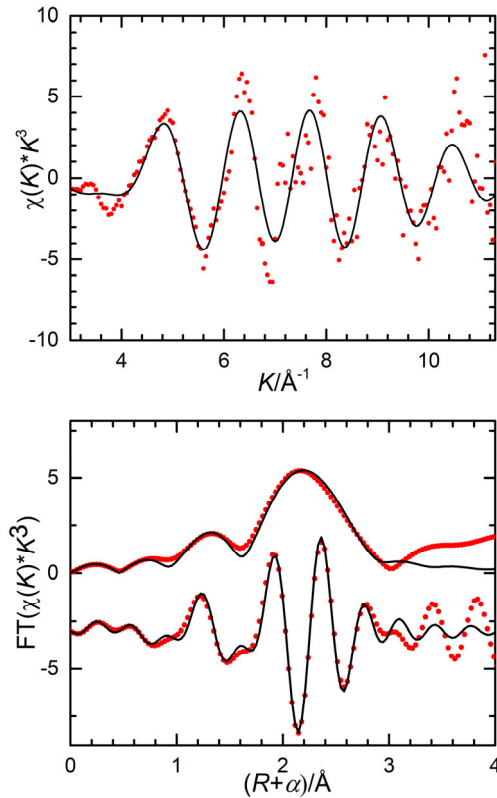


Figure 6.8. Cu K-edge experimental data (points) and curvefit (line) of red area (upper) k^3 -weighted phase-uncorrected data. (below) R-space (FT magnitude and Imaginary component).

Figure 6.8 shows the EXAFS oscillations and the corresponding Fourier transform (points) and the fitted data (line) corresponding to the red areas of the glass. **Table 6.2** shows the fitted data for the spectra of the different glass areas of the glass and the atomic fraction of copper atoms present as Cu^+ , Cu^{2+} and Cu^0 .

The data show that Cu^+ is the dominant species in all the glass areas. The copper-rich transparent colourless glass (green) is the most oxidised, with copper present only as Cu^{2+} and Cu^+ ; metallic copper is detected in the red and pink glass areas, in greater amounts in the red than in the pink area. Finally, metallic copper is absent in the colourless areas of the glass (grey).

Information about the oxidation state of iron can be extracted from the pre-peak features, a weighted position or centre shift (CE) and total area (A), and the fitted data is shown in **Table 6.3** and plotted in the variogram (Wilke 2001, Wilke 2005) in **Figure 6.9**.

The copper-rich colourless glass (green) is the most oxidised, while the copper-free colourless substrate glass (blue) is the least oxidised. The iron from the other glass areas shows an intermediate oxidation state.

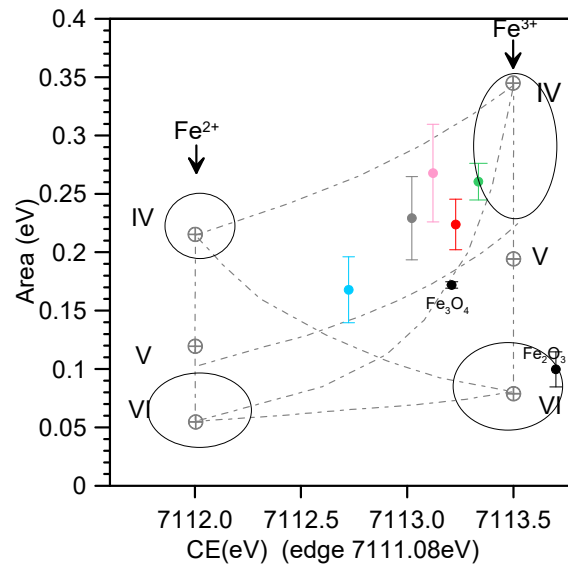


Figure 6.9. Variogram (Wilke 2001, Wilke 2005, Boubnov 2015), area (A) versus center shift (CE) showing the fitted standards (Fe_2O_3 and Fe_3O_4) and coloured glass areas.

Table 6.3. Fitted centroid and area of the Fe K-edge pre-peak for the different glass areas.

^aFirst inflection of the metallic iron edge at 7111.08 eV. ^bIron speciation (Fiege 2017).

Glass areas (number of points)	CE (eV) ($\epsilon=0.15$)	A(eV) ($\epsilon=0.06$)	% $\text{Fe}^{3+}/\Sigma\text{Fe}^b$ ($\epsilon=10\%$)
Green (3 points)	7113.3	0.26	65
Red (13 points)	7113.2	0.22	55
Pink (6 points)	7113.1	0.27	47
Grey (3 points)	7113.0	0.23	41
Blue (2 points)	7112.7	0.17	26

6.4.2 Discussion

Figure 6.10 shows a summary of the copper and iron speciation in the different glass areas of Ch9n-YM-5b-R3 (*striated* red glass). We can see that the Cu-rich colourless glass (green) is the most oxidised, 20% Cu^{2+} and 80% Cu^+ and 65% Fe^{3+} . Conversely, the copper-free colourless substrate glass (blue) is the most reduced, with 26% Fe^{3+} . This shows that a copper-rich oxidised glass layer was applied over a copper-free reduced substrate glass.

Then we have a sequence of red, reddish and colourless (red, pink and grey) glass layers. Copper is present in all of them mainly as Cu^+ . The red glass areas contain 37% Cu^0 , while the reddish glass areas (pink)

contain only 4% Cu^0 . In the colourless glass areas (grey) all the copper is present as Cu^+ , which gives no colour to the glass.

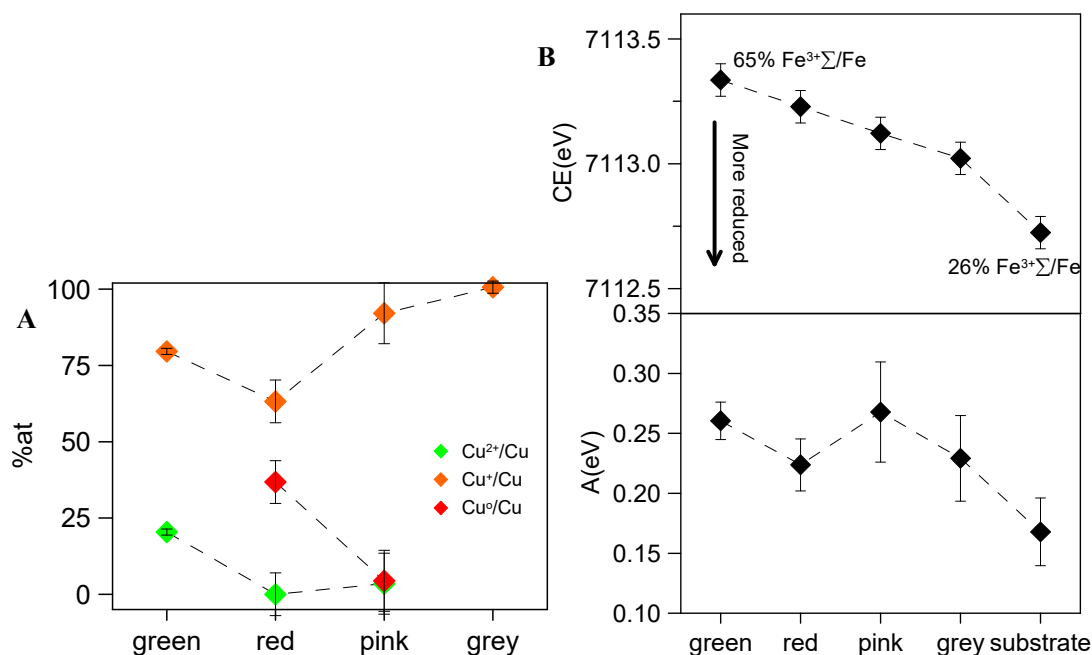


Figure 6.10. (A) Copper speciation determined by fitting of the Cu K-edge EXAFS data and (B) fitted centroid and area from the Fe K-edge pre-peak for different areas of the glasses.

This means that more metallic copper particles (or larger nanoparticles) are formed in the red glass areas than in the reddish glass areas (pink) and none in the colourless (grey) glass areas. The red colour is due to the reduction of copper to the metallic state. In addition, as shown in **Figure 6.10B**, iron shows an intermediate oxidation in the red (red), reddish (pink) and colourless (grey) areas between the copper-free substrate glass (blue).

We can assume that the glass originally consisted of a succession of copper-rich oxidised (green) and copper-free reduced (blue) glass layers. Both (Fe^{3+} and Fe^{2+}) are present in both glasses, but Fe^{2+} is the dominant species in the copper-free glass (blue) and Fe^{3+} in the copper-rich glass (green). Therefore, Fe^{2+} will diffuse from the copper-free glass to the copper-rich glass and Fe^{3+} will diffuse from the copper-rich glass to the copper-free glass. Fe^{2+} can reduce Cu^{2+} to Cu^+ and Cu^+ to Cu^0 . Therefore, metallic copper nanoparticles precipitate at the interface between the two glasses, but ionic copper species (Cu^+ and Cu^{2+}) will continue to diffuse towards the copper-poor glass, where new thin layers of copper nanoparticles will form. Iron ions will also diffuse, but because some of the Fe^{2+} will change to Fe^{3+} , the diffusion will slow down.

When the layers are thin, the interdiffusion of ions is important, so the iron-rich colourless glass layers

(grey) between the red layers contain some Cu^+ , and the iron is also more oxidised than in the original copper-free reduced glass.

The results obtained show that the diffusion of copper from a copper-rich oxidised glass into a copper-free reduced glass results in the reduction of copper and the precipitation of a succession of thin layers of copper nanoparticles. Interdiffusion of iron ions (Fe^{3+} and Fe^{2+}) between the two glasses also occurs and the data has shown that the reduction of copper is associated with the oxidation of Fe^{2+} to Fe^{3+} in the interlayers.

6.5 Red glass-from the 13th to the 18th century

6.5.1 XAS methods

To investigate the role of sulphur of *sandwich* glass, the copper speciation was obtained from the analyses of the Cu K-edge XAS spectra. Copper in magmas has been found to form complexes similarly to copper in aqueous solutions (Lanzirotti 2019). Cu K-edge XANES spectra for copper aqueous solutions appeared as copper-oxygen complexes in a distorted octahedral symmetry. Cu(I)-oxygen complexes have a very characteristic spectrum that displays a strong, rising resonance peak at $\approx 8983\text{--}8984$ eV while Cu (II)-complexes have no pre-edge peak but the absorption maximum near 9000 eV (Fulton 2000). Similarly, copper is present as a Cu(I)-oxide complex in sulphur-free and Low-S basaltic glasses obtained under reducing conditions (Lanzirotti 2019). Copper is considered a strongly chalcophile element and, consequently, it can also form complexes with S, Cu(I)-sulphide, the Cu K-edge spectral features of High-S basaltic glasses is similar to those of CuS (covellite) but smoother as corresponds to an amorphous structure (Lanzirotti 2019). In fact, various studies have shown that Cu^{2+} ions are not present in CuS, but that it has a pyrite-type structure where Cu^{1+} and S^{1-} undergo pairing (Vegeius 2012). Consequently, in our S-bearing glasses we may expect the presence of Cu(I)-oxide and Cu(I)-sulphide complexes besides the presence of crystalline metallic copper and copper sulphide particles. **Figure 6.11A** shows the Cu K-edge XANES spectra corresponding to the different model compounds used in this study. Thanks to the micrometric beam size, the copper sulphide microparticles, and selected areas of the red glass near and far away from the particles were analysed. The red glass spectra fitting was carried out with Athena software (Ravel 2005) as a linear combination of model compounds, Cu(I)-oxide, Cu(I)-sulphide (Lanzirotti 2019) and metallic Cu, each weighted by the compound fraction. The three-component fitting was done in the normalized $\mu(\text{E})$ space over an energy range of 8960-9060eV. The calculated R factors (**Table 6.3, Table**

6.6 and Table 6.8) are a measure of residuals between the fitted and measured spectra, lower R-factors correspond to a better fit (Ravel 2005).

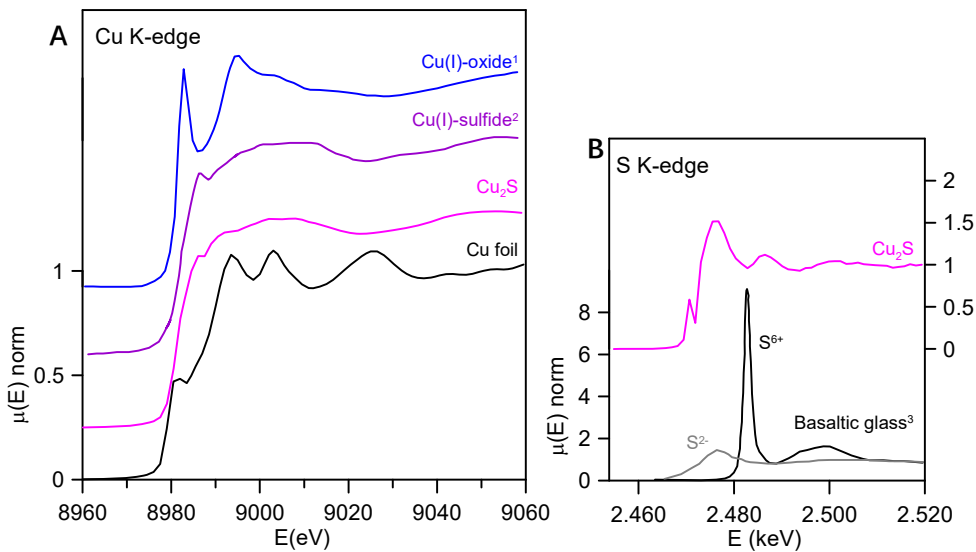


Figure 6.11. (A) Cu K-edge XANES of the model compounds, ¹Cu(I)-oxide, Low-S basaltic glass spectrum and ²Cu(I)-sulphide, High-S basaltic glass spectrum after Lanzirotti (Lanzirotti 2019), Cu foil and Cu₂S (chalcocite); (B) S K-edge XANES, of the model compounds, ³completely oxidised (black) and reduced (grey) basaltic glass after Jugo (Jugo 2010) and Cu₂S, chalcocite, (magenta) used to fit the red glasses.

6.5.2 Results

All the glasses show a characteristic sandwich-like structure (**Figure 6.1C**, **Figure 6.12B**), except those from the end of the 17th century and 18th century which show a single layer of red glass. The sandwich glasses show a red glass layer of about 100-300 μm thickness is applied over a transparent base glass of about 1-3 mm thickness and covered by a transparent glass of about 50-300 μm thickness. The cover layer is often highly corroded, with crystalline precipitates formed on many areas of the surface (**Figure 6.1B**) making the glasses opaquer, and sometimes it is even missing.

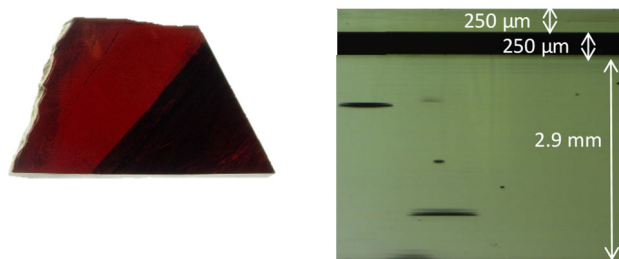


Figure 6.12. (A) Sample PS15 (B) Optical transmission image of the cross section of PS15.

Table 6.4 and **Figure 6.3**, show the chemical composition of the base, red and cover glasses. The composition of the three glasses is basically the same with the exception of copper; this indicates that copper was added to a transparent glass of similar composition to obtain the red glass. Between the 13th and the beginning of the 16th century the glasses are of the potash-lime type with increasing K₂O and CaO content in the 14th and 15th centuries (**Figure 6.3**). In the 16th century a sudden change in the glass composition happens in the form of an increase in the SiO₂, CaO and Al₂O₃ and decrease in the K₂O, P₂O₅ and MgO content (**Figure 6.3**). The amount of iron and manganese is low (below 0.9%FeO and below 1.1% MnO) in all the glasses. Tin is present in amounts below the detection limit of the microprobe, it has been determined by Laser-Ablation ICP Mass spectrometry (LA-ICP-MS) (details on the analytical methods are found in Gratuze (Gratuze 2016)). Some of the samples (CB1, CB2, CB3, CB4, PS15 and Valls) tin contents vary between 2 and 50 ppm. Similarly, As varies between 10-50 ppm, Zn and Rb between 150 and 250 ppm, Zr between 100-150 ppm and Sr between 500-700 ppm. A few ppm of Ni, Co, Ag, Sn, Sb, Pb, As and Bi are also present (data can be seen in **Appendix 2**). Potash-lime glasses were produced mixing sand which usually contains some clay and feldspars with forest wood ashes which are potash and lime rich but also contain small amounts of sulphur, phosphorous, chlorine, magnesium and manganese. Consequently, Ni, Co, Zn, Ag, Sn, Sb, Pb, As and Bi may be related to the source of copper while Zr, Sr and Rb to the sand.

Table 6.4. Major and minor elements composition of the glasses. Microprobe analysis. bd: below detection limit.

*cover glass was missing

Sample	colour	Na ₂ O	MgO	Al ₂ O ₃	SiO ₂	P ₂ O ₅	SO ₃	Cl	K ₂ O	CaO	TiO ₂	MnO	FeO	CuO	BaO	Tot
SC13	cover	0.83	4.76	2.86	54.3	4.21	0.20	bd	14.1	16.0	0.16	0.98	0.68	bd	0.31	99.4
	red	0.87	4.87	2.94	52.7	4.30	0.13	bd	14.8	16.1	0.19	1.05	0.73	0.65	0.34	99.7
	base	0.81	4.70	2.88	55.0	4.25	0.20	bd	14.1	16.0	0.22	0.94	0.73	bd	0.28	100.1
CB8*	red	0.33	4.01	2.93	48.3	2.30	0.23	0.12	18.0	18.9	0.23	1.24	0.52	0.81	0.90	98.7
	base	0.34	4.07	2.83	47.6	2.47	0.23	0.14	18.7	19.4	0.20	1.28	0.50	0.16	0.83	98.7
CB9	cover	0.30	4.05	2.84	48.7	2.36	0.21	0.13	18.3	19.6	0.18	1.26	0.51	0.09	0.91	99.4
	red	0.33	3.85	2.84	48.8	2.17	0.23	0.08	17.6	18.8	0.20	1.19	0.48	1.07	0.87	98.4
	base	0.32	4.02	2.83	48.6	2.18	0.29	0.11	18.5	19.6	0.17	1.21	0.46	0.07	0.84	99.1
CB10	cover	0.29	3.87	2.89	49.0	1.99	0.24	0.10	18.0	19.1	0.20	1.31	0.54	0.09	0.76	98.3
	red	0.33	3.92	2.96	49.0	2.18	0.21	0.04	17.6	18.7	0.20	1.23	0.54	0.97	0.94	98.8
	base	0.34	3.83	2.90	49.8	2.06	0.28	0.13	18.2	19.2	0.20	1.22	0.47	0.12	0.72	99.4
CB3	cover	0.40	5.04	2.37	49.0	4.60	0.23	0.16	18.0	19.2	0.11	1.06	0.49	bd	0.36	101.1
	red	0.42	5.01	2.40	49.7	4.06	0.19	0.15	17.4	18.8	0.12	1.07	0.51	0.92	0.37	101.1
	base	0.48	5.32	2.37	48.6	4.21	0.21	bd	18.9	18.1	0.09	1.00	0.43	bd	0.49	100.2
CB4	cover	0.38	5.03	2.40	49.0	4.33	0.27	0.15	18.3	19.0	0.14	1.09	0.50	bd	0.39	101.0
	red	0.42	5.05	2.39	49.4	4.05	0.18	0.14	17.3	18.8	0.12	1.07	0.53	0.91	0.39	100.8
	base	0.37	5.03	2.41	48.8	4.51	0.20	0.16	18.5	19.0	0.11	1.11	0.50	bd	0.40	101.1
CB5*	red	0.38	4.97	2.37	48.2	4.37	0.22	0.15	17.6	18.6	0.11	1.03	0.51	0.81	0.37	99.7
	base	0.38	5.26	2.32	47.4	4.20	0.22	bd	18.7	18.4	0.16	0.99	0.40	bd	0.50	99.1
CB1	cover	0.33	4.71	3.08	46.9	3.50	0.28	bd	18.3	20.4	0.20	1.19	0.64	0.25	0.36	100.2
	red	0.33	5.15	3.21	46.7	4.18	0.18	bd	17.8	20.1	0.16	0.98	0.72	0.81	0.33	100.7
	base	0.36	5.15	2.95	46.5	3.44	0.30	bd	19.1	19.8	0.27	1.10	0.51	bd	0.35	99.9
CB2	cover	0.33	4.94	3.01	45.9	3.43	0.26	bd	18.3	20.5	0.21	1.17	0.65	0.30	0.37	99.3
	red	0.31	5.12	3.13	45.7	4.33	0.21	bd	17.9	20.1	0.14	0.98	0.71	0.81	0.36	99.9
	base	0.36	4.82	2.98	45.9	3.73	0.27	bd	18.7	20.5	0.12	1.19	0.65	bd	0.42	99.8
PS15	cover	1.92	3.33	4.16	61.2	2.33	0.18	0.52	5.50	19.6	0.21	0.83	0.60	0.16	0.25	100.8
	red	1.81	3.17	4.15	61.9	2.39	bd	0.45	5.44	19.3	0.22	0.71	0.57	0.64	0.20	101.0
	base	1.79	3.39	4.16	61.2	2.24	0.21	0.53	6.08	19.8	0.21	0.99	0.61	bd	0.27	101.5
SC14	cover	0.80	3.80	4.23	57.0	2.65	0.18	bd	7.09	22.0	0.27	0.97	0.72	bd	0.41	100.1
	red	0.81	3.77	4.22	56.7	2.49	0.18	bd	7.07	21.7	0.20	0.98	0.85	bd	0.40	99.5
	base	0.79	3.78	4.23	56.7	2.57	0.19	bd	7.09	21.7	0.31	1.02	0.76	bd	0.30	99.5
Valls	cover	0.39	3.70	4.01	58.9	2.03	0.27	bd	6.78	21.2	0.23	0.94	0.84	bd	0.41	99.8
	red	0.38	3.47	4.66	59.1	1.94	bd	bd	7.07	20.0	0.24	1.02	0.82	0.79	0.41	99.9
	base	0.40	3.99	4.12	58.2	2.03	0.13	bd	7.11	21.9	0.20	1.03	0.76	bd	0.38	100.3
JD16	red	10.45	3.77	1.66	63.2	0.22	0.29	0.32	9.20	7.6	0.08	0.20	1.87	0.99		
	base	14.02	3.75	0.98	63.8	0.36	0.13	0.58	7.98	7.5	0.05	0.20	0.31			
SM	red	16.23	4.06	2.97	61.8	0.59	0.04	1.21	2.66	8.6	0.18	0.41	1.26	0.93	0.01	101.0
	base	17.03	3.88	2.28	64.8	0.34	0.08	1.71	2.25	7.9	0.11	0.43	0.76	0.01	0.00	101.5

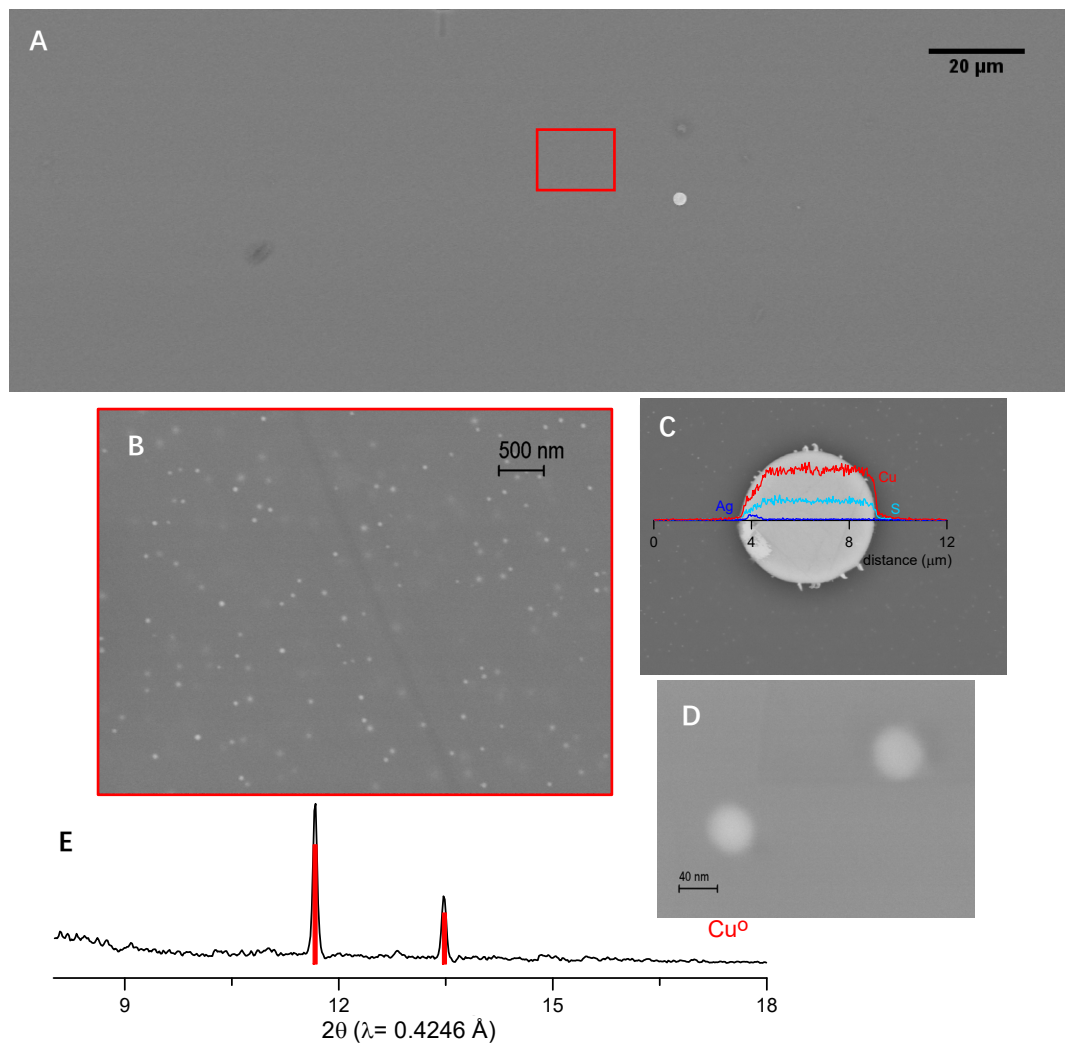


Figure 6.13. (A) SEM-BSD image of SC13 red glass showing the presence of a micrometric Cu_2S particle (B) Magnification of the red square from (A) showing the presence of small metallic copper nanoparticles. (C) magnification and chemical linescan of one of the Cu_2S particles showing the presence of Ag_2S precipitated at the edge and (D) magnification and linescan of the metallic copper nanoparticles. (E) Micro-XRD pattern taken from a cross section of the red glass.

A Cu/S atomic ratio ≈ 2 is determined for the Medieval glasses (2.5, 2.3, 2.6, 1.8, 2.3 and 1.9 ± 0.2 for SC13, CB3, CB4, CB5, CB1 and CB2 respectively) and in some very few copper sulphide particles are identified (**Figure 6.13A**). On the contrary, the Renaissance glasses (PS15, SC14 and Valls) have a similar amount of copper but lower sulphur (for PS15 and Valls below detection limits of the Microprobe) and profuse copper sulphide particles (typical volume fraction of about 0.6%) are identified (**Figure 6.14A**). We have to mention, that the analyses of the red glasses were performed in areas free of copper sulphide particles, thanks to the small beam size of the Microprobe $\sim 1 \mu\text{m}^2$ and large size of the copper sulphide particles (between $0.5 \mu\text{m}$ and $7 \mu\text{m}$).

SEM images (**Figure 6.13B** and **Figure 6.13D**) of the Medieval red glass layers show the presence of metallic copper nanoparticles (typical sizes varying between 20 nm and 50 nm); SC13 shows also the presence of a few micron sized copper sulphide particles (**Figure 6.13A** and **Figure 6.13C**). In the Renaissance (PS15, SC14 and Valls) both micron sized copper sulphide particles (between 0.5 μm to 7 μm) (**Figure 6.14A**, **Figure 6.14C** and **Figure 6.14D**), and metallic copper nanoparticles (typical sizes varying between 20 nm and 50 nm) (**Figure 6.14B** and **Figure 6.14E**), are found. The micro-XRD patterns taken from the Medieval red glass layers show the presence of metallic copper nanoparticles (ICCD file 01-85-1326) and in the Renaissance glasses (PS15, SC14 and Valls) also of tetragonal Cu_2S (chalcocite) (ICDD file 01-72-1071) particles (**Figure 6.13E** and **Figure 6.14F**).

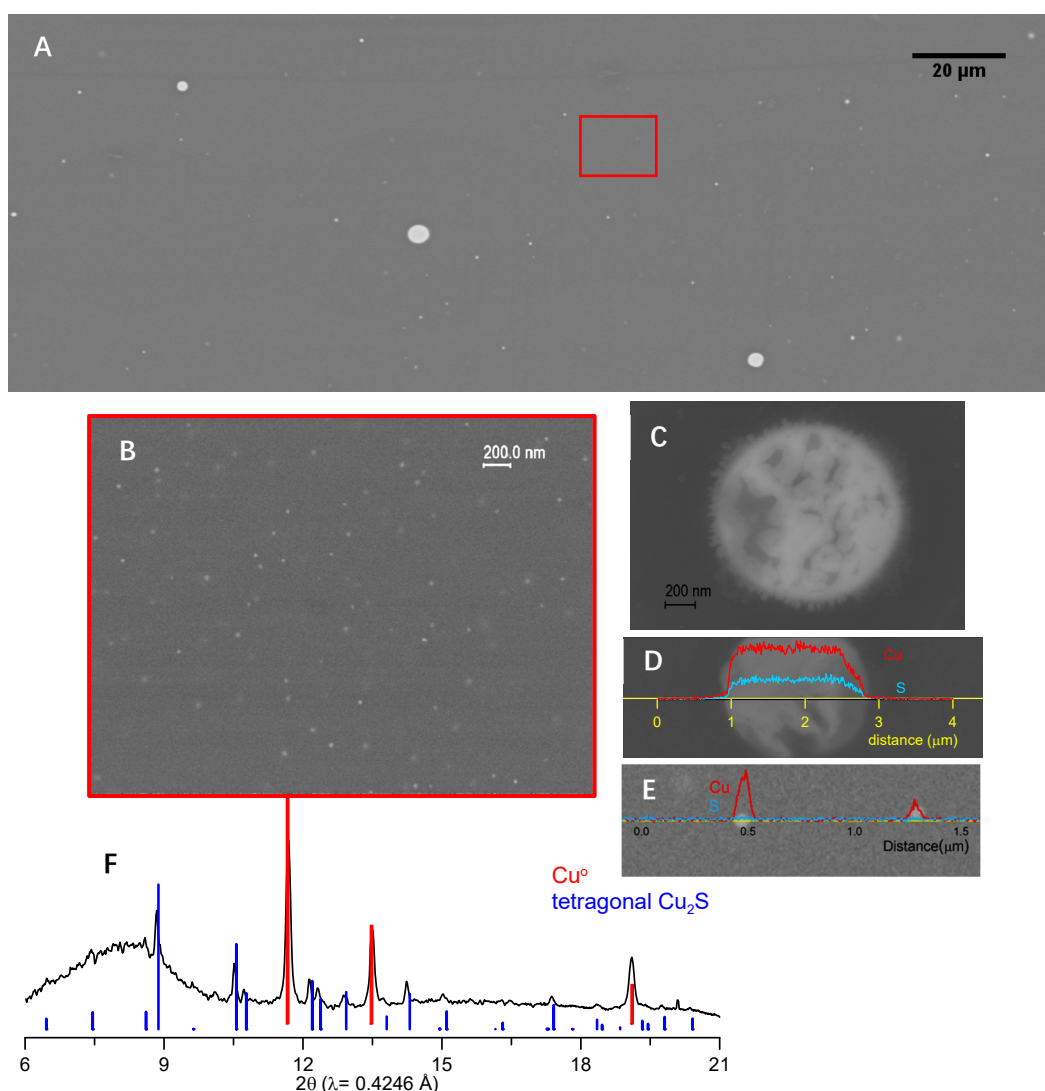


Figure 6.14. (A) SEM-BSA image of Valls red glass showing the presence of many micrometric Cu_2S particles (B) Magnification of the red square from (A) showing the presence of small metallic copper nanoparticles. (C) magnification and (D) linescan of some large micrometric Cu_2S particles and (E) linescan of small nanometric metallic copper particles. (F) Micro-XRD pattern taken from a cross section of the red glass, tetragonal Cu_2S , chalcocite, ICDD pattern 01-72-1071.

The presence of copper sulphide precipitates is not unexpected in silicate melts. Copper is a high chalcophilic element and sulphur has very low solubility in a silicate melt. Consequently, a sulphide-silicate melt partition happens at high temperature in the melt with the precipitation of solid copper sulphide blebs (spherical inclusions) after cooling. The temperature at which copper sulphide separates from a basaltic melt depends also on the pressure; at low pressure, the temperature may be extrapolated (Li 2012) between 1050°C and 1100 °C. The experiments performed (Li 2012, Ripley 2002) provided also evidence for oxide or oxy-sulphide complexing of Cu in the silicate melts, showing a decrease in the solubility of copper increasing the sulphur content of the melt (between some tens of ppm up to about 10^3 ppm). Among the impurities present in the glass which may produce sulphide precipitates Ni, Ag, Bi are the most probable and Co, Pb, Sn and Sb less probable (Li 2012). In our case, from a few to some tens of ppm of Ni, Co, Ag, Sn, Sb, Pb and Bi are determined in the red glasses. In fact, in our glasses silver sulphide precipitates are also found (Figure 6.13C). Although no other elements are found in the particles studied, they could also be present in the sulphide precipitates.

In order to understand the role of sulphur in the development of the red colour of the glasses Cu K-edge and S K-edge (only for SC13) micro-XANES spectra were obtained in different areas of the glasses and particles (Figure 6.15).

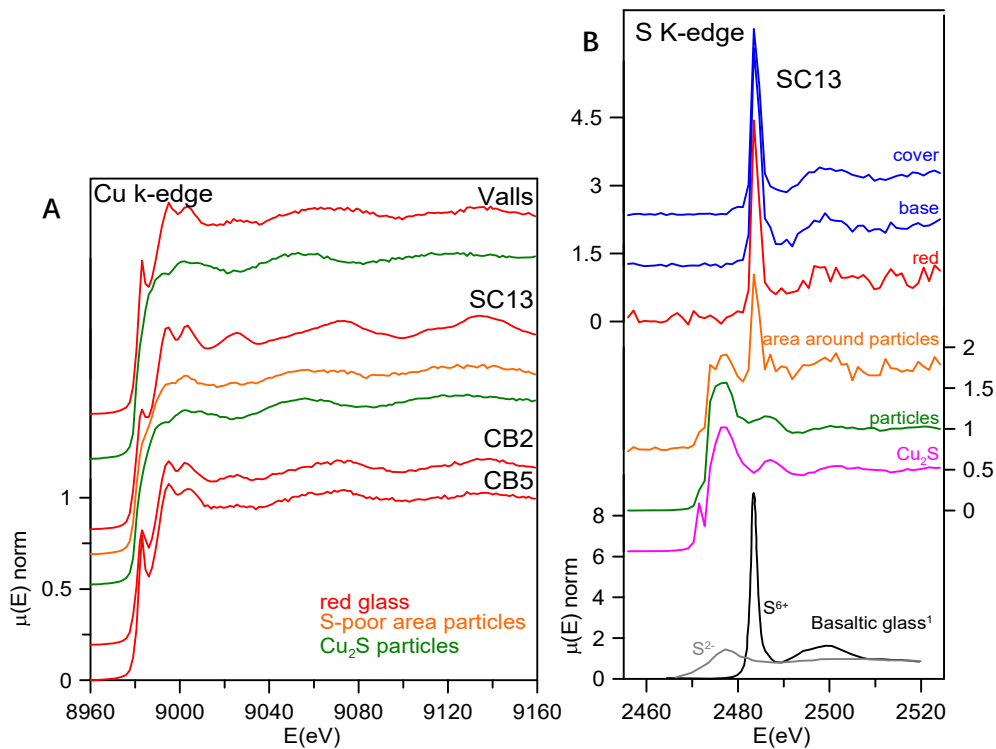


Figure 6.15. (A) Copper K-edge EXAFS of the red glasses and copper sulphide particles from SC13 and Valls. (B) S K-edge XANES from SC13 transparent and red glasses and copper sulphide particles. Reference spectra corresponding to Cu_2S (magenta) and a completely oxidised (black) and reduced (grey) basaltic glass after Jugo (Jugo 2010).

Cu K-edge spectra were obtained from the red glass far from the copper sulphide particles, in the copper sulphide particles and in sulphur-poor areas of the copper sulphide particles (**Figure 6.15A**). The data show that the red glass contains a large number of small metallic copper particles, and a few larger ones, of a composition consistent with Cu_2S ; the spectra of the sulphur-poor areas in the particles show also mainly a copper sulphide shape but with some contribution of metallic copper. The red glass spectra can be fitted by a linear combination of metallic copper, copper(I)-oxide and copper(I)-sulphide complexes model compounds (Lanzirotti 2019) following the procedure indicated in the **6.4 XAS Methodology** section. The results are shown in **Figure 6.16** and **Table 6.5**.

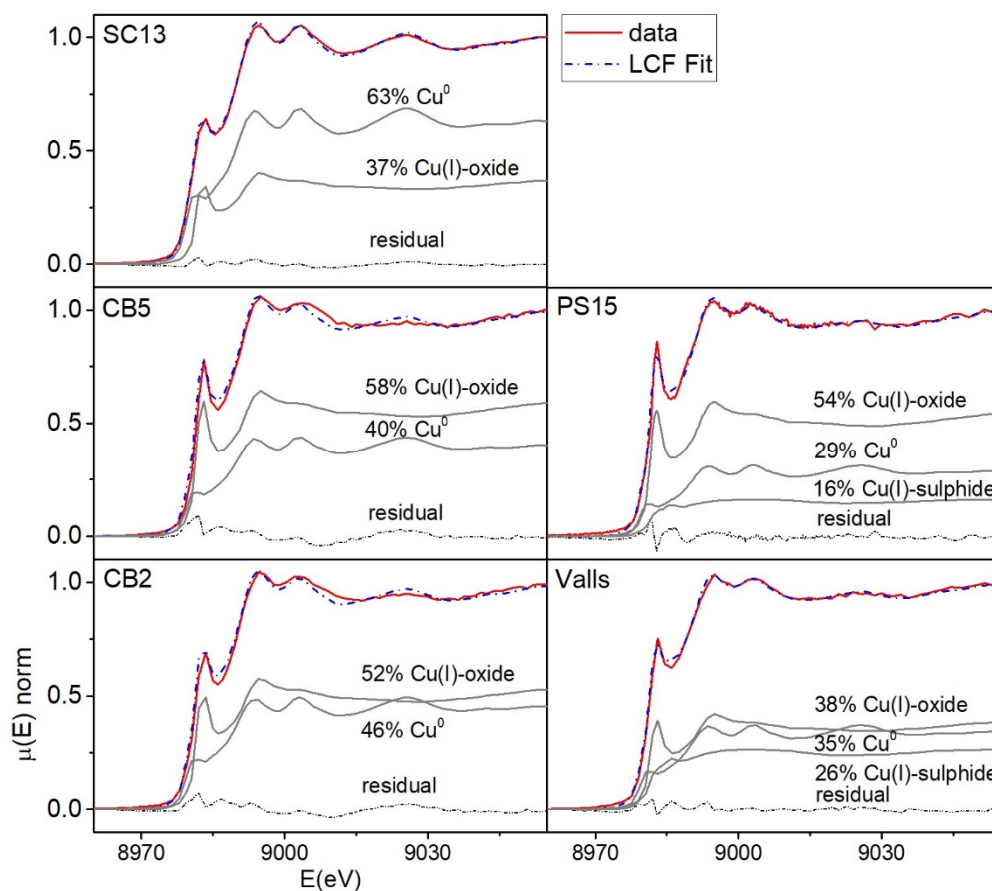


Figure 6.16. Linear combination fitting Cu k-edge XANES data of the red glasses using metallic copper (Cu^0), Cu(I)-oxygen and Cu(I)-sulphide complexes after Lanzirotti (Lanzirotti 2019).

Table 6.5. Copper XANES speciation calculated using a linear combination of Cu(I)-oxide (Low-S basaltic glass) and Cu(I)-sulphide (High-S basaltic glass) after Lanzirrotti (Lanzirrotti 2019) and metallic Cu.

Red glass	Cu(I)-sulphide (%)	Cu(I)-oxide (%)	Cu ⁰ (%)	R factor (%)
SC13	--	37(1)	63(1)	0.05
CB5	--	58(3)	40(3)	0.50
CB2	--	52(2)	46(2)	0.30
PS15	16(2)	54(1)	29(1)	0.20
Valls	26(3)	38(2)	35(2)	0.10

The data show that metallic copper and Cu(I)-oxide are present in all the red glasses analysed while Cu(I)-sulphide is also present in the Renaissance glasses (PS15 and Valls). S K-edge spectra were also obtained from different areas of SC13; the red and transparent glasses, the copper sulphide particles and around the copper sulphide particles (**Figure 6.15B**). The data show that the sulphide particles spectra are consistent with Cu₂S. S⁶⁺ is determined in the transparent glass and in the red glass far away from the copper sulphide particles, while a mixture of S²⁻ and S⁶⁺ is found in the area around the copper sulphide particles. This result is in good agreement with the literature (Backnaes 2008, Jugo 2010), S²⁻ and S⁶⁺ coexist in silicate melts while S⁴⁺ is absent or insignificant. The result is also consistent with the fact that S²⁻ is pretty insoluble compared to S⁶⁺ in a silicate melt and, consequently, a higher concentration of S⁶⁺ can be present in the silicate melt without saturation or precipitation of sulphate compounds, while relatively low S contents (as S²⁻) is required to reach sulphide saturation (Jugo 2010).

Moreover, the transition from S²⁻ to S⁶⁺ in silicate melts occurs over a very narrow interval of oxygen fugacity contrarily to the transition from Fe²⁺ to Fe³⁺ which expands over 16 orders of magnitude (Jayasuriya 2004). Consequently, a slight increase in the oxygen fugacity results in a fast transformation of S²⁻ into S⁶⁺ with the consequent reduction of the Cu⁺ to the metallic state. Finally, although sulphur occurs as sulphide (S²⁻), sulphate (S⁶⁺) or a combination of both in the silicate melts, it can also be released as SO₂ (S⁴⁺), secondly as H₂S and in minor amounts as S₂ and COS (Jugo 2010). Therefore, the release of S to the atmosphere during the glass firing cannot be withdrawn.

To investigate the role of iron in the process, Fe K-edge spectra were also obtained from the red and transparent glasses from the Medieval (SC13, CB5) and Renaissance (PS15 and Valls) periods. **Figure 6.17** shows also a different behaviour for the Medieval and Renaissance glasses. While in the Medieval glasses SC13 and CB5, the red glass is more oxidised than the transparent glass, in the Renaissance glasses PS15

and Valls, the transparent glass is more oxidised than the red glass. The data indicates a more oxidising atmosphere for the red Medieval glasses and a more reducing atmosphere for the red Renaissance glasses.

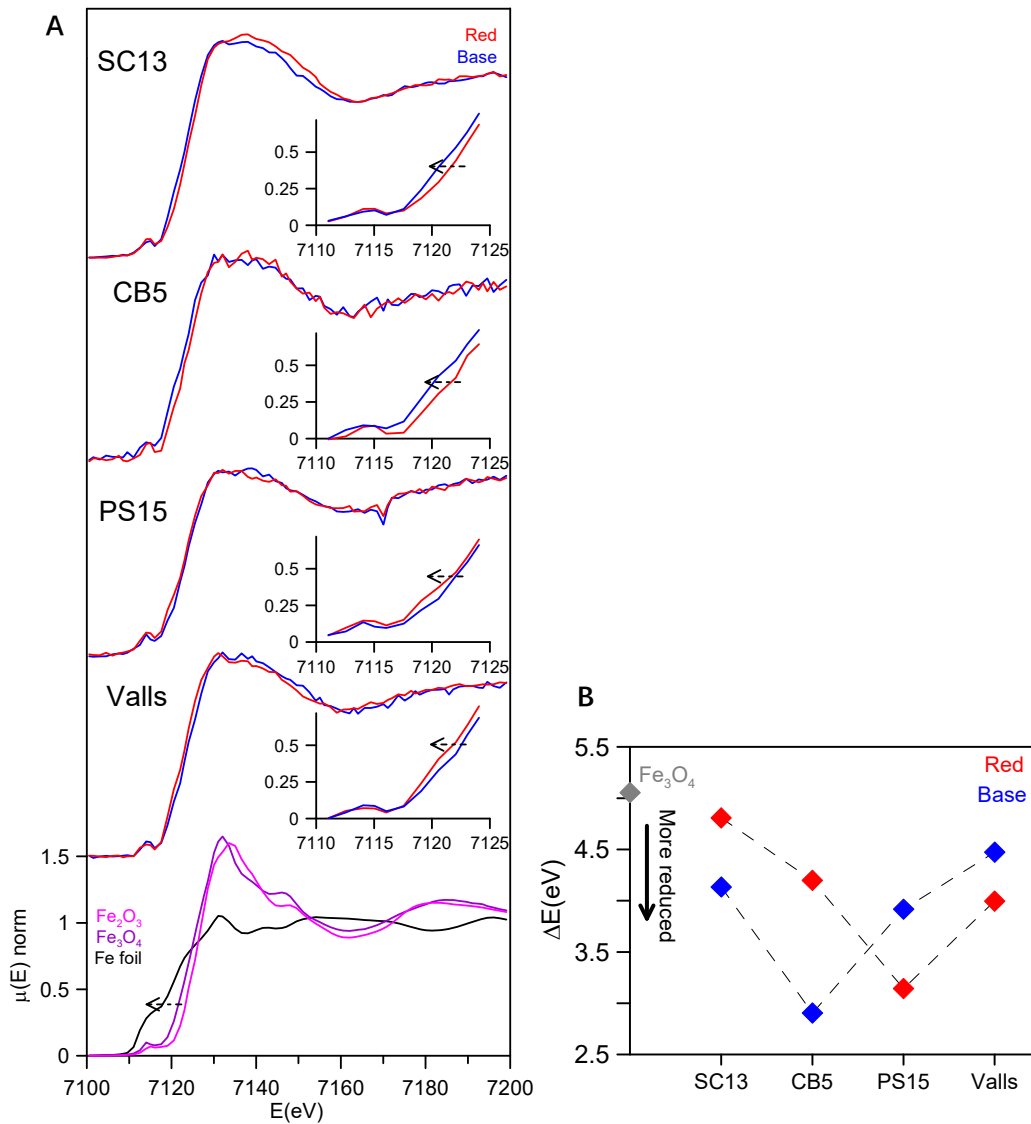


Figure 6.17. (A) Fe K-edge spectra corresponding to the transparent and red glasses from SC13, CB5, PS15 and Valls and to the standards. (B) Fe K-edge shift calculated using the Integral method.

These data suggest that more oxidising conditions at a temperature above 1050°C were attained probably during the reheating of the Medieval red glasses which resulted in the oxidation of S^{2-} to S^{6+} , with the consequent reduction of copper from Cu^+ to Cu^0 . On the contrary, less oxidising conditions or a lower temperature did not favour this process in the Renaissance red glasses, where many copper sulphide precipitates are still present, and less metallic copper nanoparticles were formed than in the Medieval red glasses (about 30%-35% for the Renaissance glasses compared to 40-63% for the Medieval glasses) (Table 6.5). Nevertheless, the higher silica and lower potassium content of the Renaissance glasses increases the

viscosity of the melt and, consequently, it may also have some influence on the decomposition of the copper sulphide particles. The data demonstrates also that, at least in the Medieval red glasses, the oxidation of iron is not responsible for the reduction of copper to the metallic state.

Although the precipitation of copper sulphide is expected in silicate melts containing sulphur, the precipitation of tetragonal chalcocite was not expected. Chalcocite at room temperature is monoclinic and inverts to hexagonal at 103°C; at 435°C the cubic high polymorph forms continuous solid solution with cubic $\text{Cu}_{9+x}\text{S}_5$ (Fleet 2006). At low-temperature, a high-pressure polymorph stable only above ~ 0.8 kbars has tetragonal symmetry (Skinner 1970). Therefore, at room temperature and pressure, monoclinic chalcocite should be formed. However, some studies have demonstrated the stabilization of tetragonal chalcocite in presence of Fe^{3+} (Machani 2011). The stabilisation of tetragonal chalcocite seems therefore related to the presence of iron in the melt.

The cubic crystallographic structure of tetragonal chalcocite is particularly interesting as while S atoms maintain a rigid sublattice, interstitial Cu atoms are distributed throughout many possible positions (up to 25). This high degree of structural disorder is also related to a high mobility of copper ions with temperature, resulting in a ‘liquid-like’ behaviour of copper ions around a crystalline sublattice (Liu 2012, Qiu 2016). Consequently, as soon as the sulphide is oxidised to sulphate and dissolves into the melt, small clusters of Cu^0 atoms are more easily formed. In fact, *striking* refers to the sudden appearance of the red colour due to the precipitation of metallic nanoparticles during the reheating of the glass (Weyl 1951).

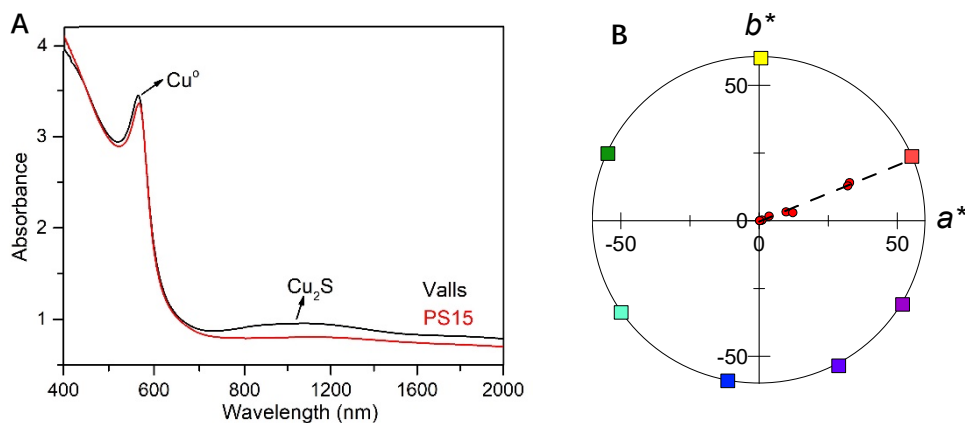


Figure 6.18. (A) UV-Vis and NIR absorbance corresponding to Renaissance glasses containing Cu_2S precipitates. (B) CIE $L^*a^*b^*$ colour coordinates, a^* and b^* and fitted h^* line.

Finally, UV-Vis-NIR analysis of the red glasses was also performed to assess the nature of the particles present (Figure 6.18A), and colour coordinates (a^* and b^*) of the red glasses, Figure 6.18B. Small metallic

copper nanoparticles have a strong Surface Plasmon Resonance absorption band (SPR) at about 560 nm, responsible for the red colour of the glasses. On the contrary, copper sulphide particles absorb light in the Near-Infrared (NIR) region (above 800 nm) and, therefore, they do not contribute to the red colour of the glasses. The hue calculated by the slope of the line, in the colour wheel, **Figure 6.18B**, is similar for all the red glasses (fitted value $h^* = 22.0(9)^\circ$, $r^2=0.998$). This indicates that copper nanoparticles present have a similar size for all the glasses studied (below 50 nm). Lightness (L^*) and saturation (c^*) vary among the samples depending on the thickness and fraction of metallic copper nanoparticles of the red glass layer, but also on the thickness of the transparent base and cover glasses and the presence of alteration compounds at the surface which strongly reduce the light transmitted.

6.5.3 Discussion

The presence of small metallic copper nanoparticles, the absence of other copper precipitates such as cuprite is responsible for the ruby red colour of the glasses. Due to the limited solubility of metallic copper into a silicate melt, copper has to be previously oxidised. Consequently, in order to render the ruby red colour, reducing agents have to be incorporated in the melt to induce the precipitation of metallic copper.

Small amounts of sulphur were present (associated to the plant ashes) in the glasses from the Medieval and Renaissance period. The presence of sulphur in the silicate melt is responsible for a sulphide-silicate melt partition at temperature above $\sim 1100^\circ\text{C}$. As copper is a highly chalcophilic element, copper accumulates in the sulphide partition where tetragonal chalcocite (Cu_2S) particles are formed. The presence of Fe^{3+} in the melt may be responsible for the stabilisation of the high-pressure tetragonal polymorph of chalcocite (Machani 2011) instead of the low temperature/pressure form.

Cooling and reheating the glass at the working temperature ($\sim 1050^\circ\text{C}$) under slightly oxidising conditions results in the decomposition of the tetragonal chalcocite particles by oxidation of sulphide into sulphate, dissolution of sulphate into the melt, reduction of Cu^+ to Cu^0 and the formation of small clusters of metallic copper (*striking*). In fact, the transition from S^{2-} to S^{6+} in silicate melts occurs over a very narrow interval of oxygen fugacity. Consequently, slightly increasing the oxygen fugacity results in a fast transformation of S^{2-} into S^{6+} with the consequent reduction of the Cu^+ to the metallic state. The cubic structure of copper sulphide with high mobility of the copper atoms is likely to favour the formation of small metallic copper nanoparticles once the sulphide is oxidised to sulphate.

This process has been more effective in Medieval glasses than in Renaissance glasses for which

considerable amounts of tetragonal chalcocite particles still exist and a lower fraction of metallic copper nanoparticles is present. This may be due to the use of less oxidising conditions or a lower temperature in the reheating of the glass (below 1050°C), or to the higher silica and lower potassium content of the Renaissance glasses which increases the viscosity of the melt and may delay the transformation.

The presence of Fe^{3+} in the melt may be responsible for the stabilisation of tetragonal chalcocite, and the crystallographic structure of this phase is probably better suited to induce the formation of small clusters of metallic copper nanoparticles. Furthermore, the transition from Fe^{2+} to Fe^{3+} expands over a large oxygen fugacity range contrarily to the transition from S^{2-} to S^{6+} . Therefore, it is more likely that iron acts as an oxidation/reduction buffer, becoming more reduced or oxidised by the atmosphere rather than directly intervening in the reduction of copper to the metallic state and consequent precipitation of the copper nanoparticles. Consequently, iron has only a secondary role in the production of red glass. In conclusion, our data has confirmed the main conclusions obtained from the replication of red glass following some historical recipes described in the Kunkel treatise (Vilarigues 2022) namely that the incorporation of sulphur is fundamental to attain the red colour of the glass and that an adequate control of the temperature ($\sim 1100^\circ\text{C}$) is more important than controlling the furnace atmosphere.

6.6 Red glasses-from the 19th to the 20th century

6.6.1 Results

Table 6.6 shows the chemical composition of the glasses, red glass layer and colourless substrate glass. All the colourless substrate glasses are of the soda-lime type (10-15% Na_2O and CaO); they contain only about 0.5% SO_2 , 0.1% Cl and 50 ppm P , indicating the use of synthetic soda (Na_2CO_3) in their production, which replaced plant ashes as a source of sodium. Synthetic soda was invented by the French chemist Nicholas Leblanc in 1791, an innovative process for making soda ash from salt and calcium carbonate, which was first used in the glass industry in 1835 (Aftalion 1991, Dungworth 2011). This process was highly polluting (it produced hydrochloric acid) and was later replaced by the Solvay process patented in 1861 by Ernest and Alfred Solvay, which used salt, calcium carbonate, ammonia and charcoal (Kostick 1998). In addition, the substrate glasses TDM, SDC and Vic contain relatively high amounts of arsenic (between 0.1 and 0.2% As_2O_3). The use of As_2O_3 as a refining agent was discovered a few years after the invention of Leblanc's salts (Muspratt 1860). Arsenic oxide was replaced by saltpetre (KNO_3) around 1870. Thermal decomposition of KNO_3 at 400°C produces KNO_2 and O_2 (g) (Kramer 1981) which favours the release of

bubbles. Consequently, SDC and Vic should be dated before 1870, LGA, CB6 and SDPDM after 1870. TDM contains many impurities, Mn, Zn, As, Sb, Ba, Pb, which seems to indicate a glass of low quality and probably an earlier date. Finally, CB7 and CBCB contain very few impurities, no more than a few dozen ppm of P, Cl, Mn, Zn, As, Sb, Ba, Pb. This is consistent with the dating of the glasses to the first decades of the 20th century. The working temperature (temperature required to blow the glass, T_w) of the 19th-century glasses is about 1050°C, while for the 20th-century glasses it is slightly lower, about 1040°C.

All the glasses show a single layer of red glass on the surface, i.e. *flushed* glasses. There are some important differences between the chemical composition of the red glass layers and the corresponding substrate colourless glasses. The red glasses contain copper and tin (≈ 0.5 -1.4% CuO, 1-2 % SnO₂), they also have a higher iron content (1-2 % FeO in the 19th-century glasses and 0.7 % FeO in the 20th-century glasses) and lower calcium content (5-8% CaO) than the corresponding substrate glasses (0.2% FeO and 8-16% CaO). Therefore, copper, tin and probably iron were added to obtain the red colour. The most important change is the addition of tin instead of sulphur (used before the 19th century) in the red glass, and also the addition of Fe (more in the 19th century than later in the 20th century red glasses). Both Sn²⁺ and Fe²⁺ are known reducing agents in glass, and may be involved in the reduction of copper to the metallic state.

In all the cases, the red colour of the glasses is due to the presence of small copper nanoparticles of typical sizes between 20 and 50 nm for all the red glass layers with the exception of TDM which has larger particles, between 50 and 150 nm, as shown in **Figure 6.19**. No other crystalline precipitate was found.

Table 6.6. Major, minor elements measured by Microprobe and trace elements measured by LA-ICP-MS. *CBCB was measured by LA-ICP-MS. T_w: the working temperature is the optimal temperature for blowing the glass has been calculated using the approximation given in Fluegel (Fluegel 2007).

Sample	colour	Na ₂ O	MgO	Al ₂ O ₃	SiO ₂	Cl	K ₂ O	CaO	FeO	CuO	SnO ₂	SO ₃	T _w
TDM	red	13.7	0.31	1.48	73.8	0.01	0.45	5.0	0.41	1.12	1.40	bd	1060
	base	15.0	0.24	1.08	72.8	0.03	0.96	7.7	0.04	0.00	0.04	bd	1022
SDC	red	10.8	0.09	0.92	75.9	0.02	0.09	5.4	1.81	0.50	2.32	bd	1106
	base	12.2	0.14	0.69	69.0	0.00	0.51	16.2	0.25	0.05	0.02	0.64	1007
Vic	red	13.7	0.17	0.80	73.4	0.09	0.09	8.4	1.04	1.06	1.56	bd	1031
	base	11.5	0.17	0.58	72.5	0.10	0.12	14.5	0.18	0.03	0.01	0.43	1035
LGA	red	11.3	0.04	0.85	77.8	0.03	0.25	6.0	1.16	1.19	1.22	bd	1088
	base	11.9	0.13	1.01	73.4	0.01	0.30	13.1	0.22	0.07	0.05	0.44	1039
CB6	red	12.1	0.07	0.88	79.0	0.00	0.26	5.9	1.15	0.73	1.00	bd	1080
	base	12.4	0.11	1.43	74.0	0.01	0.47	12.8	0.18	0.02	0.03	0.55	1033
SDPDM	red	11.2	0.05	0.68	77.3	0.03	0.19	5.8	0.90	1.41	1.45	bd	1093
	base	13.1	0.23	1.50	71.6	0.00	0.55	13.4	0.22	0.05	0.05	0.52	1015
CBCB*	red	14.5	0.13	0.35	76.8	0.09	0.11	4.40	0.73	1.26	1.54	-	1030
	base	13.3	0.20	0.57	69.8	0.05	0.38	15.4	0.23	0.01	0.00	0.57	999
CB7	red	12.3	0.27	0.47	77.4	0.00	0.10	4.7	0.63	1.02	1.80	bd	1089
	base	13.6	0.50	0.53	70.6	0.01	0.27	15.1	0.18	0.01	0.02	0.47	998

sample	colour	Li	B	P	Ti	Mn	Zn	As	Rb	Sr	Zr	Sn	Sb	Ba	Pb
TDM	red	8	794	5	236	77	32	44	23	32	36	9140	14	68	705
	subs	12	100	41	189	689	849	1596	8	84	30	82	899	1179	3706
SDC	red	11	8	78	522	56	43	39	5	28	63	15358	7	83	101
	subs	9	25	56	378	66	8	189	4	68	54	299	4	59	36
Vic	red	12	24	128	452	43	48	36	5	39	27	10527	9	33	23
	subs	10	23	53	196	39	7	788	4	164	18	118	2	29	26
LGA	red	22	10	77	200	158	22	35	7	16	28	7838	6	40	60
	subs	11	10	32	198	168	8	8	8	48	28	273	1	79	11
CB6	red	14	12	94	239	395	25	41	8	21	39	7301	11	81	-
	subs	10	6	50	179	82	9	15	12	61	28	372	1	104	8
SDPDM	red	20	7	39	182	230	41	28	4	16	17	9941	6	54	29
	base	14	7	52	188	989	9	8	12	98	29	398	7	459	61
CBCB	red	8	15	-	181	82	18	26	4	22	19	12125	2	35	104
	subs	11	23	52	206	32	10	2	6	136	21	21	0	40	31
CB7	red	10	16	38	192	41	107	24	4	31	19	11870	2	30	34
	subs	10	25	35	187	48	10	8	5	83	18	97	0	33	10

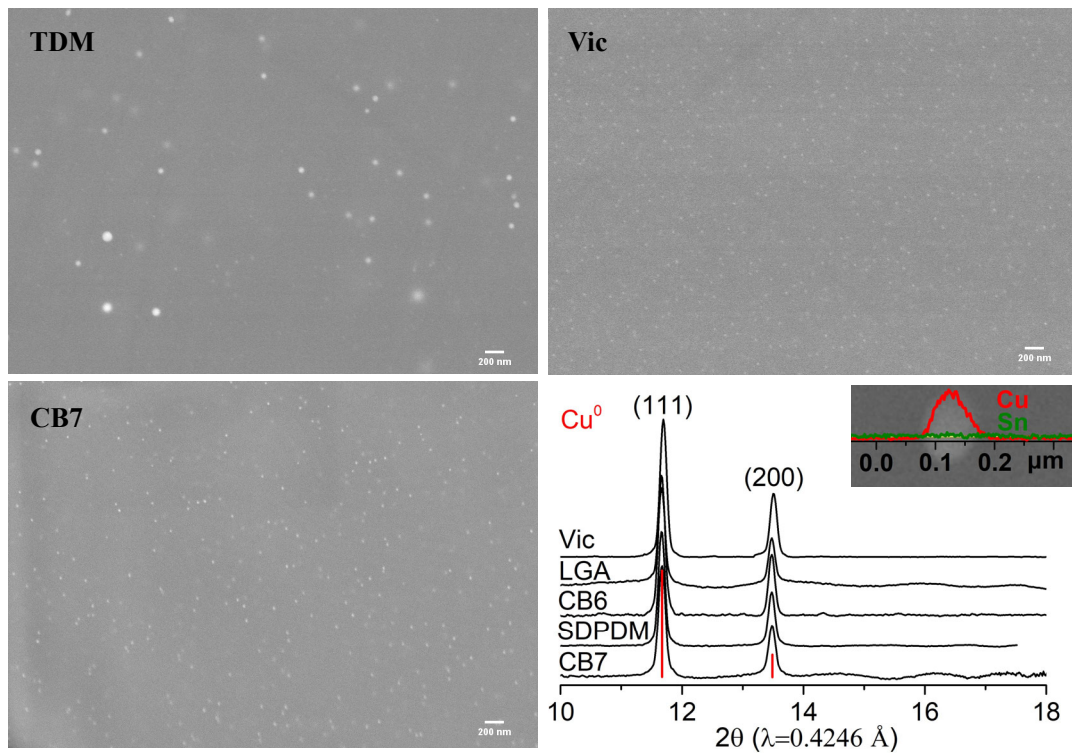


Figure 6.19. Secondary electrons FE-SEM images (TDM, Vic, CB7), micro-XRD patterns of the red glasses and line scan of a metallic copper nanoparticle of TDM.

UV-Vis is particularly useful for the identification of the presence of colouring cations in the glass, as well as the presence of cuprite and metallic copper nanoparticles. The UV-Vis absorption spectra corresponding to the glasses are shown in **Figure 6.20**. Metallic copper nanoparticles show a Surface Plasmon Resonance (SPR) extinction band around 560 nm. The band is slightly red shifted (570 nm) for TDM, due to the larger particle sizes of the metallic copper nanoparticles.

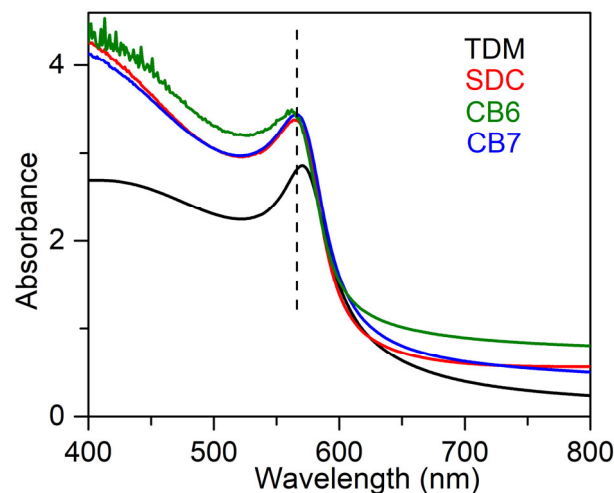


Figure 6.20. UV-Vis absorption spectra taken in transmission mode showing the SPR extinction band at 560 nm characteristic of metallic copper nanoparticles (20 to 50 nm). The spectrum corresponding to TDM appears slightly red shifted due to the large particle size (50 to 150 nm)

In order to see the role of iron and tin in the formation of the metallic copper nanoparticles, the absorption spectra at the Fe and Cu K-edge and Sn L₃-edge were measured for some of the red and corresponding colourless substrate glasses, SDC from the 19th century and CB7 from the 20th century. The Cu K-edge XAFS taken from the red glasses and from the copper standards, Cu⁰, Cu₂O and CuO are shown in **Figure 6.21A**. In both spectra, the dominant contribution corresponds to metallic copper. **Figure 6.21B** and **Table 6.7** show the fit of the first shell data of the EXAFS region. Within the spectral resolution of XAS, SDC red glass is mostly metal while CB7 contains half of the copper as Cu⁰ and the other half as Cu⁺. Cu²⁺ is not found in the red glasses.

Figure 6.22 and **Table 6.8** show the Fe K-edge spectra and fitted data corresponding to the SDC and CB7 red glass layers and the substrate glasses. Iron is more reduced in the red glass than in the substrate glass and in the red glass layers iron is also more oxidized in CB7 than in SDC.

Finally, Sn L₃-edge spectra from the substrate glass and red coloured layer were acquired from SDC and are shown in **Figure 6.23** together with the corresponding tin standards. The uncoloured substrate glasses contain only trace amounts of tin, 299 ppm for SDC, this is the reason why the corresponding data is very noisy. The Sn L₃-edge spectra corresponding to Sn²⁺ and Sn⁴⁺ in glass are similar to those of the crystalline oxides, SnO and SnO₂, but with smoother and broader absorption peaks (Masai 2018). We can clearly see that Sn⁴⁺ predominates in the red glass layer while Sn²⁺ predominates in the colourless substrate glass.

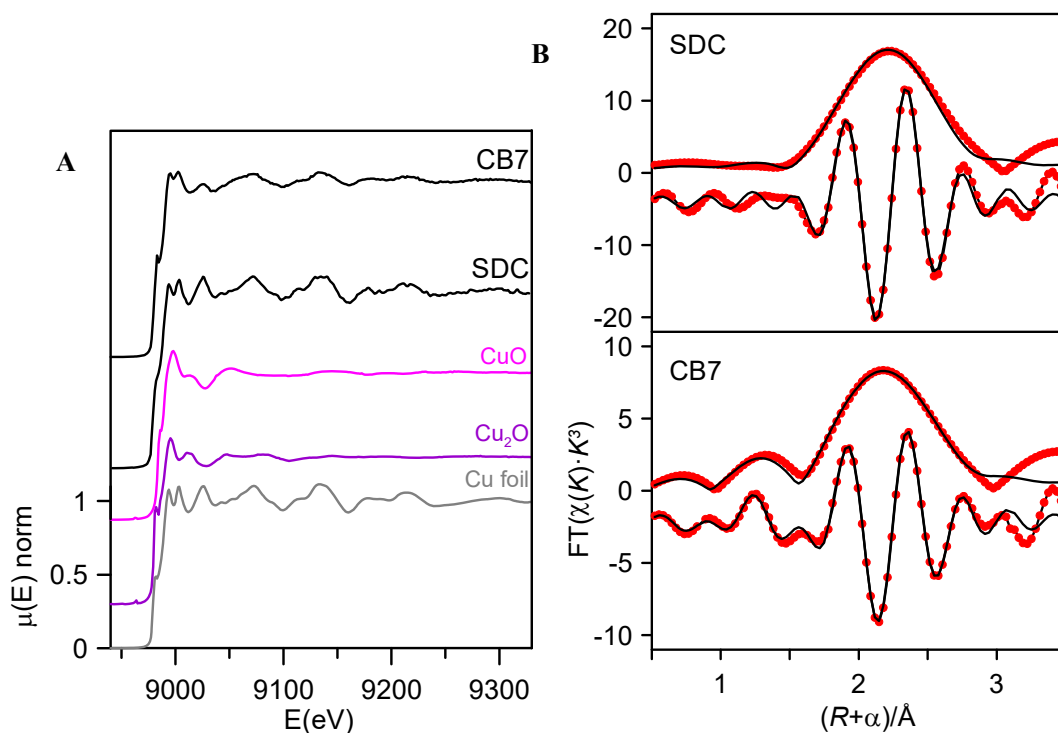


Figure 6.21. (A) Cu K-edge spectra of SDC, CB7 and Cu standards; (B) Cu K-edge EXAFS (dots) and curve fitting (line) for SDC and CB7 red glasses in R-space (FT magnitude and imaginary component). Data are k^3 -weighted and not phase-corrected.

Table 6.7. Fitted Cu K-edge EXAFS data of SDC and CB7 red glass layers

sample	shell	Model compound	Model parameters		Bond length R(Å)	at. fraction (%)	R _{factor} (%)
			N	R(Å)			
SDC	Cu-Cu	Cu ⁰	12	2.556	2.54(0)	100(16)	1.4
CB7	Cu-O	Cuprite	2	1.857	1.84(0)	49(6)	1.2
	Cu-Cu	Cu ⁰	12	2.556	2.53(0)	51(6)	

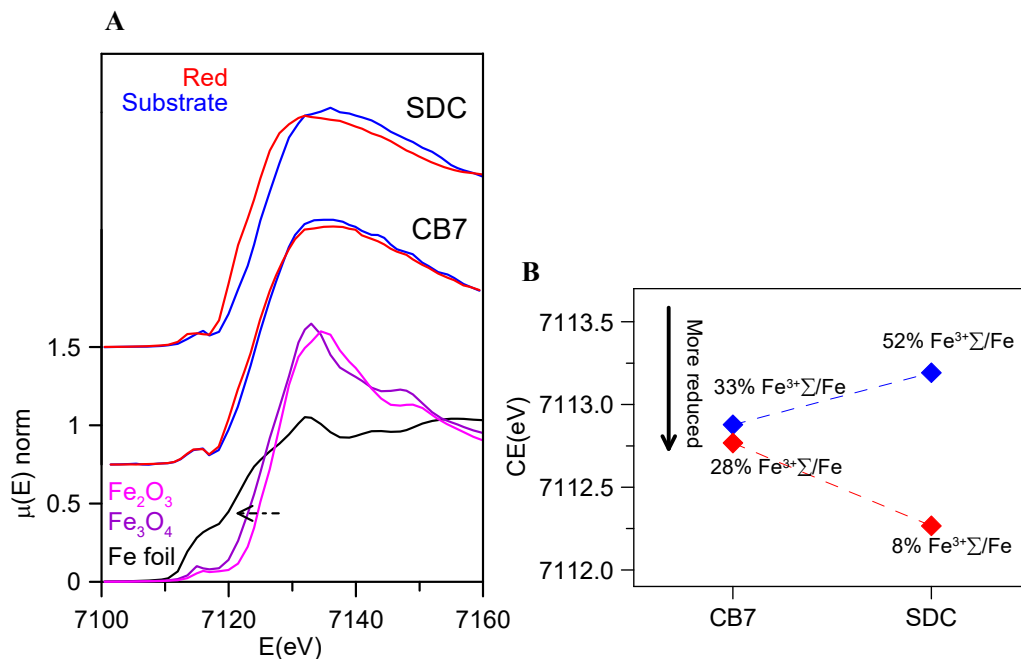


Figure 6.22. (A) Fe K-edge spectra of CB7 and SDC colourless substrate glasses and red glass layers (the red line and dots correspond to the red layer and the blue line and dots to the substrate transparent glass) and Fe standards. The edge shifts to higher energy as the iron becomes more oxidized; (B) pre-edge Center Shift (CE) of the glasses. The CE increases as the iron becomes more oxidized. The Fe³⁺ fraction has been calculated using the expression in A. Fiege et al (Fiege 2017).

Table 6.8. Fitted pre-edge peak Center shift and Area of SDC and CB7 colourless substrate glasses and red glass layers, ϵ is the standard deviation of the fitted data. *Iron speciation calculated according to A. Fiege et al. 2017 (Fiege 2017).

		CE (eV)	A(eV)	%Fe ³⁺ /ΣFe*
		($\epsilon=0.15$)	($\epsilon=0.01$)	($\epsilon=5\%$)
SDC	substrate	7113.2	0.20	52
	red	7112.3	0.14	8
CB7	substrate	7112.9	0.24	33
	red	7112.8	0.22	28

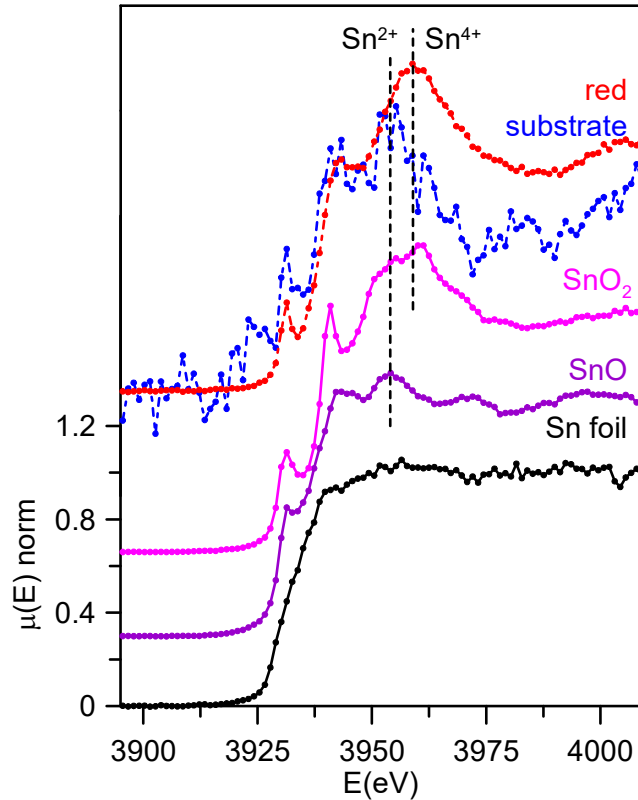


Figure 6.23. Sn L_3 -edge spectra of SDC colourless substrate glass and red glass layer and Sn standards. Sn^{4+} predominates in the red glass layer while Sn^{2+} predominates in the colourless substrate glass.

6.6.2 Discussion

All the red flashed glasses from the 19th and 20th centuries are of the soda-lime type, and considering the low presence of ash components (P, S and Cl) manufactured from synthetic soda that was used in the glass industry since 1835 (Aftalion 1991, Dungworth 2011). In addition, TDM, SDC and Vic glasses can be dated before 1870, while LGA, CB6 and SDPDM after 1870 (in good agreement with the official dating of the windows). Finally, CBCB and CB7 are dated to the very beginning of the 20th century, in 1905.

All the glasses have a single layer of red glass on the surface and are *flashed* glasses. The red glass layers contain copper and tin (≈ 0.5 -1.4% CuO, 1-2 % SnO_2), they also contain higher iron (1-2% FeO in the 19th-century glasses and 0.7% FeO in the 20th-century glasses) and lower calcium (5-8% CaO) than the corresponding substrate glasses (0.2% FeO and 8-16% CaO).

In a previous study, we demonstrated that copper and iron are more oxidised in Ca-rich glasses fired under the same conditions, oxidizing and then reducing (Yuan 2022). The $\text{Cu}^+ / (\text{Cu}^+ + \text{Cu}^{2+})$ was 70% in Ca-rich areas (about 23%CaO) and 90% in the Ca-poor areas (9% CaO) and the $\text{Fe}^{2+} / (\text{Fe}^{2+} + \text{Fe}^{3+})$ was 20% and 70%, respectively. In addition, a Mössbauer spectroscopy study of lime glasses (Iwamoto 1978) showed that the

Fe^{3+} fraction increases with the CaO content of the glasses or the oxygen partial pressure of the firing. Therefore, decreasing the calcium content of red glasses favours both copper and iron to be present in a more reduced form.

The oxidation state of tin in soda-lime glasses has also been studied by Mössbauer spectroscopy (Krohn 2005). A set of soda-lime glasses was produced by adding either a Sn^{4+} or a Sn^{2+} compound. Interestingly, when tin was added as Sn^{4+} , tin was present as Sn^{4+} in the glass whereas if it was added as Sn^{2+} , only half of the tin was still present as Sn^{2+} in the glass, the other half was already as Sn^{4+} . No differences in the behaviour were found for tin contents ranging from 0.4 to 6% SnO_2 or SnO .

Due to the extremely low solubility of metals in silicate glass, copper must be incorporated into the glass in its ionic form, Cu^+ and/or Cu^{2+} , which requires an oxidizing atmosphere during the firing. The process of red glass production described in the historical and modern documents involves mixing the glass with copper and reducing agents such as tin, lead, iron and/or calcined cream of tartar ($\text{K}_2\text{CO}_3 \cdot 1.5\text{H}_2\text{O}$) and firing at high temperatures (Weyl 1951, Cable 2001, Kunckel 1679, Vilarigues 2022). According to historical treatises, the ingredients were pretreated (burned copper, vinegar, aqua fortis, or aqua regia treated iron, tin-lead ashes), while more recent descriptions indicated the addition of tin oxide, magnetite and in some cases directly as metal (Sn^0) (Weyl 1951, Bring 2007). Our glasses do not contain lead, and only tin and iron were added as reducing agents.

Our data have shown that in the red glass, copper appears as Cu^+ and Cu^0 while tin is present mainly in its oxidized form Sn^{4+} . Consequently, tin acted as a reducing agent, which requires tin to be incorporated into the glass as Sn^{2+} . The addition of other reducing agents, such as $\text{K}_2\text{CO}_3 \cdot 1.5\text{H}_2\text{O}$ to the glass melt, as described in historical and modern documents, would favour the incorporation of tin as Sn^{2+} into the glass. It has been found (Krohn 2005) that when tin is added in the form of SnO , only half of the tin remains in the glass as Sn^{2+} , so that a tin to copper ratio of 2:1 is required to reduce all the copper. Therefore, the relative amount of the different ions involved must be taken into account. **Table 6.9** shows the atomic concentration of tin, iron and copper in the red glasses. In CB7 with a Sn:Cu = 1:1, only half of the copper is reduced to the metallic state, while in SDC with Sn:Cu = 2:1, all copper is reduced to the metallic state. To obtain a red glass, it is therefore necessary to use a Sn^{2+} compound or metallic tin, or to add some reducing agents such as $\text{K}_2\text{CO}_3 \cdot 1.5\text{H}_2\text{O}$ to the melt, as described in the documentation. Once tin is oxidised to Sn^{4+} , it is quite soluble in alkaline glasses (Farges 2006) and remains dissolved in the red glass. The predominance of Sn^{2+} in the substrate glass indicates reducing conditions during production, which is

probably also aided by the low tin content (200-300 ppm).

Table 6.9. Chemical composition of the red glasses

	at%Sn	at%Fe	at%Cu	Sn/Cu
TDM	0.24	0.11	0.27	0.9
SDC	0.37	0.54	0.13	2.7
Vic	0.24	0.30	0.28	0.9
LGA	0.19	0.34	0.31	0.6
CB6	0.15	0.33	0.19	0.8
SDPDM	0.23	0.26	0.37	0.6
CBCB	0.25	0.21	0.39	0.6
CB7	0.28	0.18	0.27	1.0

Iron in SDC is mainly present in its reduced form (about 90% Fe^{2+}) and cannot have acted as a reducing agent for copper. Consequently, the role of iron is less clear. However, since iron in a calcium poor soda-lime glass tends to be present in its more reduced state Fe^{2+} , copper may be more likely present in the glass as Cu^+ rather than Cu^{2+} , as we have seen occurring (Yuan 2022). Iron may then have an indirect role in the production of red glass by preventing the presence of copper as Cu^{2+} , thus facilitating the reduction of copper to the metallic state. In addition, we have observed that the iron content of red glasses decreases slightly in the 20th century.

The 19th century marks an important change in the production technology of copper red glasses. This coincides with scientific advances in glass production such as the use of synthetic soda, the use of As_2O_3 and later of KNO_3 as refining agents.

6.7 Conclusions

The compositional analysis reveals a significant transition in glass composition from the 13th to the 20th century, coinciding with advancements in glassmaking technology.

The ruby red colour of the glasses is due to the presence of small metallic copper nanoparticles.

The study of 13th century *striated* glass reveals a distinctive glass structure, in which a copper-rich oxidised glass layer is applied to a copper-free reduced substrate glass. Copper diffusion from the oxidised layer into the reduced glass induces copper reduction and the formation of a sequence of fine layers composed of copper nanoparticles. Simultaneously, interdiffusion of iron ions (Fe^{3+} and Fe^{2+}) takes place between the two glasses, and the results indicate that the reduction of copper is associated to the oxidation of Fe^{2+} to

Fe^{3+} within the interlayers.

The study of red glass spanning from the 13th to the 17th centuries highlights the important role of sulphur in the reduction of metallic copper. Analysis reveals the presence of trace amounts of sulphur in medieval and Renaissance red glasses. Sulphur is responsible for a sulphide-silicate melt partition at low pressure and temperatures above 1100°C; copper is a highly chalcophilic element and accumulates in the sulphide partition. The presence of iron in the melt may be responsible for the precipitation of tetragonal rather than monoclinic chalcocite (Cu_2S) particles. The cooling and reheating of the glass under mildly oxidising conditions promotes the oxidation of the sulphide and the loss of sulphur (probably as SO_2) and the sudden reduction of copper to the metallic state (*striking*). The crystalline structure of tetragonal chalcocite with a high mobility of copper ions is more likely to favour the precipitation of metallic copper nanoparticles. The differences found between Medieval and Renaissance red glasses may be related to the different composition, the Renaissance glasses being richer in silica, or to a less oxidising or lower reheating temperature of the red glass.

The analysis of the red glass from the 13th to the 18th centuries suggests that sulphur was a key ingredient in the production of red glass of that period, in agreement with the main conclusions obtained from the replication of red glass according to some historical recipes. On the contrary, iron does not seem to play a direct role in the reduction of copper and the precipitation of copper nanoparticles, but rather an indirect role, stabilising the tetragonal chalcocite and acting as an oxidation/reduction buffer.

Ultimately, the analysis of the 19th and 20th century glass produced compelling results, shedding light on the complex process of copper red formation and providing valuable insights into its underlying mechanisms. The chemical composition of the substrate colourless and red glasses indicated that they were all made from synthetic soda, which was not used before 1835; the presence/absence of arsenic added to the glass as a fining agent, allowed dating three of them to be dated before 1870 and the other after 1870, the other two were produced in 1905. The red colour of the glass is due to the presence of metallic copper nanoparticles (size 20-50 nm). Unlike the red copper glasses produced between the 13th and 18th centuries, the composition of the red glass layers is different from that of the substrate glasses. The red glass has a low calcium content (about 5% CaO), which causes both copper and iron to be present in the glass mainly in their reduced form, Cu^+ and Fe^{2+} . The red glasses contained copper, tin and iron, while lead, described in historical and modern documentation was absent.

The data showed that in the red glass, tin is mainly present in its oxidised form Sn^{4+} , while copper is present

as Cu^+ and metallic copper; the more the copper is reduced, the more the iron in the glass is reduced. Consequently, tin acted as a reducing agent, requiring tin to be incorporated into the glass as Sn^{2+} . The addition of other reducing agents such as $\text{K}_2\text{CO}_3 \cdot 1.5\text{H}_2\text{O}$, as described in historical and modern documents, would promote the incorporation of tin into the glass as Sn^{2+} . The role of iron is less clear, but as iron is also preferentially incorporated into a low-calcium glass as Fe^{2+} , it may prevent the incorporation of copper as Cu^{2+} , thereby facilitating the reduction of copper to the metallic state.

References

- Aftalion F (1991), *A History of the International Chemical Industry (Chemical Science in Society)*, O.T. Bentey (Transl.) University of Pennsylvania Press, Philadelphia, pp. 11–13. ISBN 13: 978-0-8122-1297-6
- Ainaud i de Lasarte J, Vila-Grau J, Virgili MJ (1992), *Els vitralls del monestir de Santes Creus i la Catedral de Tarragona. Corpus vitrearum medii aevi. Catalunya, Vol. 3*, Institut d'Estudis Catalans, Barcelona. ISBN: 84-7283-209-0.
- Ainaud i de Lasarte J, Mundó AM, Vila-Grau J, Escudero I Ribot MA, Cañellas S, Vila i Delclòs A (1997), *Els vitralls de la Catedral de Barcelona i del monestir de Pedralbes. Corpus vitrearum medii aevi. Catalunya, Vol. 4*, Institut d'Estudis Catalans, Barcelona. ISBN: 84-7283-335-6.
- Alonso MP, Capel F, Valle Fuentes FJ, Pablos AD, Ortega I, Gómez B, Respaldiza MA (2009), *Caracterización de un vidrio rojo medieval procedente de las vidrieras del Monasterio de las Huelgas de Burgos*, *Bol. Soc. Esp. Ceram.* 8(4): 179-186.
- Barber DJ, Freestone IC (1990). *An investigation of the origin of the colour of the Lycurgus Cup by analytical transmission electron microscopy.* *Archaeometry*, 32,33-45.
- Backnaes L, Stelling J, Behrens H, Goettlicher J, Mangold S, Verheijen O, Beerkens RGC, Deubener J (2008), *Dissolution mechanisms of tetravalent sulphur in silicate melts: evidences from sulphur K edge XANES studies on glasses.* *J. Amer. Ceram. Soc.* 91(3): 721-727. <https://doi.org/full/10.1111/j.1551-2916.2007.02044.x>
- Bandiera M, Verità M, Zecchin S, Vilarigues M (2021). *Some secrets of Renaissance Venetian opaque red glass revealed by analyses and glassmaking treatises.* *Glass Technol. : Eur. J. Glass Sci. Technol., Part A*, 62(1) : 24-33. <http://doi.org/10.13036/17533546.62.1.001>
- Boubnov A, Lichtenberg H, Mangold S, Grunwaldt JD (2015), *Identification of the iron oxidation state and coordination geometry in iron oxide- and zeolite-based catalysts using pre-edge XAS analysis*, *J. Synchrontron Radiat.* 22: 410–426. <https://doi.org/10.1107/S1600577514025880>
- Bring T, Jonson B, Kloo L and Rosdahl J (2007), *Colour development in copper ruby alkali silicate glasses. Part 1. The impact of tin oxide, time and temperature*, *Glass. Technol.: Eur. J. Glass Sci. Technol. A.* 48(2): 101-108.

Cable M (2001), *The World's Most Famous Book on Glassmaking: The Art of Glass* by Antonio Neri, Christopher Merrett (Transl.), Michael Cable (Eds), The Society of Glass Technology, Sheffield. ISBN: 090068237X.

Colomban P, Tournié A, and P. Ricciardi (2009), Raman spectroscopy of copper nanoparticle-containing glass matrices: ancient red stained-glass windows. *J. Raman Spectrosc.* 40: 1949-1955. <https://doi.org/1949–1955> 10.1002/jrs.2345

Domínguez Rodés MC and Cañellas S (2008), Materials for stained glass windows in Catalonian documentation (14th and 15th centuries). *J. Cult. Herit.* 9: e85-e88. <https://doi.org/10.1016/j.culher.2008.05.004>

Dussubieux L, Gratuze B (2012). Chemical Composition of 16th- to 18th-Century Glass Beads Excavated in Paris. *BEADS: J. Soc. Bead Researchers* 24: 6. <https://surface.syr.edu/cgi/viewcontent.cgi?article=1212&context=beads>

Dungworth D (2011), The value of Historic Window Glass, *The Historic Environment*, 2(1) 21–48. <https://doi.org/10.1179/175675011X12943261434567>

Farges F, Etcheverry MP, Scheidegger A, Grolimund D (1999), Speciation and weathering of copper in “copper red ruby” medieval flashed glasses from the Tours cathedral (XIII century). *Appl. Geochem.* 21: 1715-1731. <https://doi.org/10.1016/j.apgeochem.2006.07.008>

Farges F, Etcheverry MP, Scheidegger A, Grolimund D (2006). Speciation and weathering of copper in “copper red ruby” medieval flashed glasses from the Tours cathedral (XIII century). *J. Appl. Geochem.*, 21:1715–1731. <https://doi.org/10.1016/j.apgeochem.2006.07.008>

Fiege A, Ruprecht P, Simon AC, Bell AS, Göttlicher J, Newville M, Lanzirotti T, Moore G (2017), Calibration of Fe XANES for high precision determination of Fe oxidation state in glasses: Comparison of new and existing results obtained at different synchrotron radiation sources, *Am. Mineral.* 102: 369–380. <https://doi.org/10.2138/am-2017-E102410>

Fleet ME, Liu XY, Harmer SL and King PL (2005), Sulfur K- edge XANES spectroscopy: chemical state and content of sulfur in silicate glasses. *Can. Mineral.* 43: 1605-1618. <https://doi.org/10.2113/gscanmin.43.5.1605>

Fleet ME (2006), Phase Equilibria at High Temperatures, *Rev. Mineral. Geochem.* 61(1): 365-419. <https://doi.org/10.2138/rmg.2006.61.7>

Fluegel A (2007). Glass viscosity calculation based on a global statistical modelling approach. *Glass Technol.: Eur. J. Glass Sci. Technol. A*, 48(1): 13–30. <https://glassproperties.com/viscosity/>

Freestone IC (1987), Composition and microstructure of early opaque red glass in Early Vitreous Materials, in: M. Bimson, I.C. Freestone (Eds.), *British Museum Occasional Paper 56*, London, pp. 173-191. ISBN 13: 9780861590568.

Freestone IC (1992), Theophilus and the composition of medieval glass, *MRS Online Proceedings Library 267*: 739–745. <https://doi.org/10.1557/PROC-267-739>

Fulton JL, Hoffmann MM and Darab JG (2000), An X-ray absorption fine structure study of copper (I) chloride coordination structure in water up to 325°C. *Chem. Phys. Lett.* 330(3-4): 300–308. [https://doi.org/10.1016/S0009-2614\(00\)01110-6](https://doi.org/10.1016/S0009-2614(00)01110-6)

Gimeno D, Garcia-Valles M, Fernandez-Turiel JL, Bazzocchi F, Aulinas M, Pugès M, Tarozz C, Riccardi MP, Basso E, Fortina C, Mendera M, Messiga B (2008), From Siena to Barcelona: Deciphering colour recipes of Na-rich Mediterranean stained glass windows at the XIII-XIV century transition. *J. Cult. Herit.* 9: e10-e15. <https://doi.org/10.1016/j.culher.2008.08.001>

Gratuze B, (2016). Glass characterization using laser ablation-inductively coupled plasma-mass spectrometry methods, in: L. Dussubieux, M. Golitko, B. Gratuze (Eds.), *Recent Advances in Laser Ablation ICP-MS in Archaeology*, Springer Verlag, Berlin Heidelberg, *Natural Sciences in Archaeology*, Chap 12, pp. 179-196. <https://doi.org/10.1007/978-3-662-49894-1>

Hawthorne JG, Smith CS (1979), *Theophilus: On Divers Arts. The Foremost Medieval Treatise on Painting, Glassmaking and Metalwork*, Dover Publications Inc., New York. ISBN 13:9780486237848.

ICDD. web site of the International Centre for Diffraction Data. <https://www.icdd.com/>

Iglesia AL, López de Azcona MC, Martín FM (1994). El “Tratado secreto de pintar a fuego las vidrieras de colore” de F. Sánchez Martínez, 1718. *Composición Química de algunos vidrios antiguos de la Catedral de Toledo. Bol. Soc. Esp. Cerám. Vidrio*, 33(6), 327-331. <http://boletines.secv.es/upload/199433327.pdf>

Ishida S, Hayashi M, Takeuchi N, Wakamatsu M (1987), Role of Sn^{2+} in development of red colour during reheating of copper glass, *J. Non-Cryst. Solids.* 95-96: 793-800. [https://doi.org/10.1016/S0022-3093\(87\)80683-X](https://doi.org/10.1016/S0022-3093(87)80683-X)

Iwamoto N, Tsunawaki Y, Nakagawa H, Yoshimura T, Wakabayashi N (1978), Investigation of calcium-iron-silicate glasses by the Mössbauer method, *J. Non-Cryst. Solids*, 29(3): 347-356. [https://doi.org/10.1016/0022-3093\(78\)90155-2](https://doi.org/10.1016/0022-3093(78)90155-2)

Jayasuriya KD, Neill HSC, Berry AJ and Campbell SJ (2004), A Mössbauer study of the oxidation state of Fe in silicate melts, *Am. Mineral.* 89: 1597-1609. <https://doi.org/10.2138/am-2004-11-1203>

Jugo PJ, Wilke M, and Botcharnikov RE (2010), Sulfur K-edge XANES analysis of natural and synthetic basaltic glasses: Implications for S speciation and S content as function of oxygen fugacity, *Geochim. Cosmochim. Acta*, 74(20): 5926-5938. <https://doi.org/10.1016/j.gca.2010.07.022>

Kostick DS (1998), The origin of the U.S. natural and synthetic soda ash industries, *Proceedings First International Soda Ash Conference, Vol I, Laramie, Wyoming*: 11-35.

Kramer CM, Munir ZA (1981). Thermal decomposition of NaNO_3 and KNO_3 , *Proc.* Vol. 9: 494-505. <https://doi.org/10.1149/198109.0494PV>

Krohn MH, Hellmann JR, Mahieu B, Pantano CG (2005), Effect of tin-oxide on the physical properties of soda-lime-silica glass, *J. Non-Cryst. Solids*, 351(6-7): 455-465. <https://doi.org/10.1016/j.jnoncrysol.2005.01.050>

Kunicki-Goldfinger JJ, Freestone IC, McDonald I, Hobot JA, Gilderdale-Scott H, Ayers T (2014), Technology, production and chronology of red window glass in the medieval period-rediscovery of a lost technology, *J. Archaeol. Sci.* 41: 89-105. <https://doi.org/10.1016/j.jas.2013.07.029>

Kunckel J (1679), *Ars Vitrarya Experimentalis, Oder Vollkommene Glasmacher-Kunst* (Franckfurt und Leipzig) http://www.deutschestextarchiv.de/kunckel_glasmacher_1679

Lanzirotti A, Lee L, Head E, Sutton SR, Newville M, McCanta M, Lerner AH, Wallace PJ (2019), Direct measurements of copper speciation in basaltic glasses: understanding the relative roles of sulfur and oxygen in copper complexation in melts, *Geochim. Cosmochim. Acta*, 267: 164-178. <https://doi.org/10.1016/j.gca.2019.09.029>

- Li G, Lei Y (2022), The computational simulation of the reflection spectra of copper red glaze. *AIP Advances* 12(9): 095319. <https://doi.org/10.1063/5.0095570>
- Li Y, Audetat A (2012), Partitioning of V, Mn, Co, Ni, Cu, Zn, As, Mo, Ag, Sn, Sb, W, Au, Pb, and Bi between sulfide phases and hydrous basanite melt at upper mantle conditions. *Earth Planet. Sci. Lett.* 355-356: 327-340. <https://doi.org/10.1016/j.epsl.2012.08.008>
- Liu HL, Shi X, Xu FF, Zhan LL, Zhang WQ, Chen LD, Li Q, Uher C, Day Tand Snyder GJ (2012), Copper ion liquid-like thermoelectrics, *Nat. Mater.* 11: 422-425. <https://doi.org/10.1038/NMAT3273>
- Machani T, Rossi DP, Golden BJ, Jones EC, Lotfipour M and Plass KE (2011), Synthesis of Monoclinic and Tetragonal Chalcocite Nanoparticles by Iron-Induced Stabilization, *Chem. Mater.* 23, 24: 5491–5495. <https://doi.org/10.1021/cm2022196>
- Masai H, Ina T, Okumura S, Mibu K (2018), Validity of Valence Estimation of Dopants in Glasses using XANES Analysis, *Sci Rep.* 8: 415. <https://doi.org/10.1038/s41598-017-18847-0>
- Muspratt S (1860), *Chemistry, Theoretical, Practical and Analytical, as Applied and Relating to the Arts and Manufactures*, Vol. 2. Glasgow, Scotland: William Mackenzie. <https://digital.sciencehistory.org/works/ysz6nva>
- Nakai I, Numako C, Hosono H, Yamasaki K (1999), Origin of the red color of satsuma copper-ruby glass as determined by EXAFS and optical absorption spectroscopy. *J. Am. Ceram. Soc.* 82(3): 689-695. <https://doi.org/10.1111/j.1151-2916.1999.tb01818.x>
- Nieto V (1967), El tratado de la fabrica del vidrio de Juan Danis y el Modo de hacer vidrieras de Francisco Herranz, *Archivo español de Arte*, 40(159), 273-303.
- Noirot C, Cormier L, Schibille N, Menguy N, Trcera N, Fonda E (2022), Comparative Investigation of Red and Orange Roman Tesserae: Role of Cu and Pb in Colour Formation, *Heritage*. 5(3) 2628-2645. <https://doi.org/10.3390/heritage5030137>
- Pradell T (2019). Lustre and Nanostructures-Ancient Technologies Revisited. In: Dillmann, P., Bellot-Gurlet, L., Nenner, I. (eds) *Nanoscience and Cultural Heritage*. Atlantis Press, Paris. https://doi.org/10.2991/978-94-6239-198-7_1

Pradell T, Molina G, Murcia S, Ibañez R, Liu C, Molera J, Shortland AJ (2016), Materials, Techniques, and Conservation of Historic Stained Glass “Grisailles”, *Int. J. Appl. Glass Sci.* 7(1): 41–58. <https://doi.org/10.1111/ijag.12125>

Qiu PF, Shi X and Chen LD (2016), Thermoelectric Properties of $\text{Cu}_{2-\delta}\text{X}$ (X = S, Se, and Te), in: Uher, C. (Eds.), *Materials Aspect of Thermoelectricity*, CRC Press, Boca Raton, pp. 289-316. <https://doi.org/10.1201/9781315197029>

Ravel B and Newville M (2005), ATHENA, ARTEMIS, HEPHAESTUS: Data Analysis for X-Ray Absorption Spectroscopy Using IFEFFIT, *J. Synchrotron Rad.* 12: 537-541. <https://doi.org/10.1107/S0909049505012719>

Ripley EM, Brophy JG and Li C (2002), Copper solubility in a basaltic melt and sulfide liquid/silicate melt partition coefficients of Cu and Fe. *Geochim. Cosmochim. Acta*, 66(15): 2791–2800. [https://doi.org/10.1016/S0016-7037\(02\)00872-4](https://doi.org/10.1016/S0016-7037(02)00872-4)

Skinner BJ (1970), Stability of the tetragonal polymorph of Cu_2S , *Economic Geology*, 65(6): 724–730. <https://doi.org/10.2113/gsecongeo.65.6.724>

Velasco A, Cañellas S (2017), El pas per Tàrrrega del vitraller Jaume Carnoval (1608). *URTX revista cultural de l’Urgell* 31: 166-177. <https://raco.cat/index.php/Urtx/article/view/326036>

Vegelius JR, Kvashnina KO, Hollmark H, Klintonberg M, Kvashnin YO, Soroka IL, Werme L and Butorin SM (2012), X-ray spectroscopic study of Cu_2S , CuS , and copper films exposed to Na_2S solutions, *J. Phys. Chem. C* 116: 22293–22300. <https://doi.org/10.1021/jp302390c>

Vilarigues M, Ruivo A, Hagendijk T, Bandiera M, Coutinho M, Alves LC, Dupré S (2022), Red glass in Kunckel’s *Ars Vitraria Experimentalis*: The importance of temperature. *Int. J. Appl. Glass Sci.* 1–15. <https://doi.org/10.1111/ijag.16605>

Vieil PL (1774), *L’Art de la Peinture sur verre et de la Vitrierie*, France. ISBN 10: 2019937972

Weyl WA, 1951. *Coloured Glasses*. Reprint by Society of Glass Technology, Sheffield, 2016.

Wilke M, Farges F, Petit PE, Brown GE, Martin F (2001), Oxidation state and coordination of Fe in minerals: An Fe K-XANES spectroscopic study, *Am. Mineral.* 86 (5): 714–730. <https://doi.org/10.2138/am-2001-5-612>

Wilke M, Partzsch GM, Bernhardt R, Lattard D (2005), Determination of the iron oxidation state in basaltic glasses using XANES at the K-edge, *Chem. Geol.* 220: 143–161.
<https://doi.org/10.1016/j.chemgeo.2005.03.004>

Yuan MY, Hou JY, Gorni G, Crespo D, Li Y, Pradell T (2022), Jun ware glaze colours: An X-ray absorption spectroscopy study, *J. Eur. Ceram. Soc.* 42(6): 3015–3022.
<https://doi.org/10.1016/j.jeurceramsoc.2022.02.016>

Yuan MY, Bonet J, Cotte M, Schibille N, Gratuze B, Pradell T (2023), The role of sulphur in the early production of copper red stained glass, *Ceram. Int.* 49(11) B: 18602-18613.
<https://doi.org/10.1016/j.ceramint.2023.02.236>

Appendix 1 Microprobe data of the red glass

SC13-Valls: *Sandwich* glass; SM-CB7: *flash* glass. bd: below detection limit., *cover glass was missing

Dating	type	wt%	Na ₂ O	MgO	Al ₂ O ₃	SiO ₂	P ₂ O ₅	SO ₃	Cl	K ₂ O	CaO	TiO ₂	MnO	FeO	CuO	SnO ₂	BaO	Tot
1284-1320	SC13	cover	0.83	4.76	2.86	54.3	4.21	0.20	0.03	14.1	16.0	0.16	0.98	0.68	0.00	0.00	0.31	99.4
		red	0.87	4.87	2.94	52.7	4.30	0.13	0.01	14.8	16.1	0.19	1.05	0.73	0.65	0.01	0.34	99.7
		base	0.81	4.70	2.88	55.0	4.25	0.20	0.03	14.1	16.0	0.22	0.94	0.73	0.02	0.00	0.28	100.1
1330	CB8*	red	0.33	4.01	2.93	48.3	2.30	0.23	0.12	18.0	18.9	0.23	1.24	0.52	0.81	0.00	0.90	98.7
		base	0.34	4.07	2.83	47.6	2.47	0.23	0.14	18.7	19.4	0.20	1.28	0.50	0.16	0.00	0.83	98.7
	CB9	cover	0.30	4.05	2.84	48.7	2.36	0.21	0.13	18.3	19.6	0.18	1.26	0.51	0.09	0.00	0.91	99.4
		red	0.33	3.85	2.84	48.8	2.17	0.23	0.08	17.6	18.8	0.20	1.19	0.48	1.07	0.00	0.87	98.4
		base	0.32	4.02	2.83	48.6	2.18	0.29	0.11	18.5	19.6	0.17	1.21	0.46	0.07	0.01	0.84	99.1
	CB10	cover	0.29	3.87	2.89	49.0	1.99	0.24	0.10	18.0	19.1	0.20	1.31	0.54	0.09	0.00	0.76	98.3
red		0.33	3.92	2.96	49.0	2.18	0.21	0.04	17.6	18.7	0.20	1.23	0.54	0.97	0.00	0.94	98.8	
base		0.34	3.83	2.90	49.8	2.06	0.28	0.13	18.2	19.2	0.20	1.22	0.47	0.12	0.00	0.72	99.4	
1386	CB3	cover	0.40	5.04	2.37	49.0	4.60	0.23	0.16	18.0	19.2	0.11	1.06	0.49	0.05	0.02	0.36	101.1
		red	0.42	5.01	2.40	49.7	4.06	0.19	0.15	17.4	18.8	0.12	1.07	0.51	0.92	0.01	0.37	101.1
		base	0.48	5.32	2.37	48.6	4.21	0.21	0.02	18.9	18.1	0.09	1.00	0.43	0.07	0.04	0.49	100.2
	CB4	cover	0.38	5.03	2.40	49.0	4.33	0.27	0.15	18.3	19.0	0.14	1.09	0.50	0.06	0.00	0.39	101.0
		red	0.42	5.05	2.39	49.4	4.05	0.18	0.14	17.3	18.8	0.12	1.07	0.53	0.91	0.01	0.39	100.8
		base	0.37	5.03	2.41	48.8	4.51	0.20	0.16	18.5	19.0	0.11	1.11	0.50	0.05	0.00	0.40	101.1
CB5*	red	0.38	4.97	2.37	48.2	4.37	0.22	0.15	17.6	18.6	0.11	1.03	0.51	0.81	0.00	0.37	99.7	
	base	0.38	5.26	2.32	47.4	4.20	0.22	0.02	18.7	18.4	0.16	0.99	0.40	0.01	0.09	0.50	99.1	
1398-1408	CB1	cover	0.33	4.71	3.08	46.9	3.50	0.28	0.06	18.3	20.4	0.20	1.19	0.64	0.25	0.00	0.36	100.2
		red	0.33	5.15	3.21	46.7	4.18	0.18	0.04	17.8	20.1	0.16	0.98	0.72	0.81	0.02	0.33	100.7
		base	0.36	5.15	2.95	46.5	3.44	0.30	0.02	19.1	19.8	0.27	1.10	0.51	0.04	0.00	0.35	99.9
	CB2	cover	0.33	4.94	3.01	45.9	3.43	0.26	0.08	18.3	20.5	0.21	1.17	0.65	0.30	0.00	0.37	99.3

		red	0.31	5.12	3.13	45.7	4.33	0.21	0.04	17.9	20.1	0.14	0.98	0.71	0.81	0.02	0.36	99.9
		base	0.36	4.82	2.98	45.9	3.73	0.27	0.08	18.7	20.5	0.12	1.19	0.65	0.04	0.00	0.42	99.8
Dating		wt%	Na₂O	MgO	Al₂O₃	SiO₂	P₂O₅	SO₃	Cl	K₂O	CaO	TiO₂	MnO	FeO	CuO	SnO₂	BaO	Tot
1544-1548	PS15	cover	1.92	3.33	4.16	61.2	2.33	0.18	0.52	5.50	19.6	0.21	0.83	0.60	0.16	0.01	0.25	100.8
		red	1.81	3.17	4.15	61.9	2.39	0.00	0.45	5.44	19.3	0.22	0.71	0.57	0.64	0.01	0.20	101.0
		base	1.79	3.39	4.16	61.2	2.24	0.21	0.53	6.08	19.8	0.21	0.99	0.61	0.02	0.02	0.27	101.5
1560	SC14	cover	0.80	3.80	4.23	57.0	2.65	0.18	0.00	7.09	22.0	0.27	0.97	0.72	0.00	0.00	0.41	100.1
		red	0.81	3.77	4.22	56.7	2.49	0.18	0.01	7.07	21.7	0.20	0.98	0.85	0.07	0.05	0.40	99.5
		base	0.79	3.78	4.23	56.7	2.57	0.19	0.01	7.09	21.7	0.31	1.02	0.76	0.00	0.01	0.30	99.5
1609	Valls	cover	0.39	3.70	4.01	58.9	2.03	0.27	0.04	6.78	21.2	0.23	0.94	0.84	0.01	0.00	0.41	99.8
		red	0.38	3.47	4.66	59.1	1.94	0.05	0.02	7.07	20.0	0.24	1.02	0.82	0.79	0.00	0.41	99.9
		base	0.40	3.99	4.12	58.2	2.03	0.13	0.00	7.11	21.9	0.20	1.03	0.76	0.01	0.00	0.38	100.3
1670	JD16	red	10.45	3.77	1.66	63.2	0.22	0.29	0.32	9.20	7.6	0.08	0.20	1.87	0.99			
		base	14.02	3.75	0.98	63.8	0.36	0.13	0.58	7.98	7.5	0.05	0.20	0.31				
c. 1791	SM	red	16.23	4.06	2.97	61.8	0.59	0.04	1.21	2.66	8.6	0.18	0.41	1.26	0.93	0.01	0.01	101.0
		base	17.03	3.88	2.28	64.8	0.34	0.08	1.71	2.25	7.9	0.11	0.43	0.76	0.01	0.00	0.00	101.5
19 th c.	TDM	red	13.73	0.31	1.48	73.8	0.01	0.03	0.01	0.45	5.0	0.02	0.01	0.41	1.12	1.40	0.04	97.8
		base	14.96	0.24	1.08	72.8	0.02	0.09	0.03	0.96	7.7	0.05	0.07	0.04	0.00	0.04	0.21	98.3
c. 1835	SDC	red	10.78	0.09	0.92	75.9	0.00	0.03	0.02	0.09	5.4	0.10	0.01	1.81	0.50	2.32	0.01	97.9
		base	12.21	0.14	0.69	69.0	0.01	0.64	0.00	0.51	16.2	0.08	0.01	0.25	0.05	0.02	0.02	99.9
Renewal of the building c. 1883	Vic-cre Vic-cim	red	13.67	0.17	0.80	73.4	0.01	0.03	0.09	0.09	8.4	0.07	0.01	1.04	1.06	1.56	0.02	100.4
		base	11.54	0.17	0.58	72.5	0.01	0.43	0.10	0.12	14.5	0.03	0.02	0.18	0.03	0.01	0.02	100.2
1876	LGA	red	13.89	0.15	0.81	72.5	0.02	0.03	0.08	0.09	8.4	0.08	0.01	1.07	1.08	1.76	0.01	100.0
		base	11.70	0.18	0.56	72.4	0.04	0.53	0.07	0.10	14.2	0.04	0.00	0.21	0.00	0.04	0.01	100.1
1880	CB6	red	11.32	0.04	0.85	77.8	0.00	0.00	0.03	0.25	6.0	0.03	0.02	1.16	1.19	1.22	0.04	100.0
		base	11.86	0.13	1.01	73.4	0.01	0.44	0.01	0.30	13.1	0.06	0.01	0.22	0.07	0.05	0.01	100.7
1880	CB6	red	12.11	0.07	0.88	79.0	0.00	0.00	0.00	0.26	5.9	0.06	0.05	1.15	0.73	1.00	0.04	101.3

flashed

		base	12.40	0.11	1.43	74.0	0.04	0.55	0.01	0.47	12.8	0.01	0.00	0.18	0.02	0.03	0.02	102.0
1889	SDPDM	red	11.15	0.05	0.68	77.3	0.04	0.03	0.03	0.19	5.8	0.04	0.02	0.90	1.41	1.45	0.02	99.1
		base	13.10	0.23	1.50	71.6	0.02	0.52	0.00	0.55	13.4	0.03	0.15	0.22	0.05	0.05	0.05	101.4
1905	CB7	red	12.28	0.27	0.47	77.4	0.08	0.02	0.00	0.10	4.7	0.05	0.00	0.63	1.02	1.80	0.00	98.8
		base	13.56	0.50	0.53	70.6	0.03	0.47	0.01	0.27	15.1	0.01	0.01	0.18	0.01	0.02	0.02	101.3

Appendix 2 LA-ICP-MS data of the red glass

ppm	Li	B	P	Cl	Ti	V	Cr	Mn	Fe	Co	Ni	Cu	Zn	As	Se	Rb	Sr	Y	Zr	Ag	Sn	Sb	Ba	La	Ce	Nd	Pb	Bi
CB3 red	17	153	16869	1927	841	11	9	7790	3778	24	34	6891	204	4		245	720	8	82	4	9	24	3241	27	43	18	19	2
CB4 red	16	152	16780	1956	844	11	9	7818	3798	24	34	6868	204	4		245	718	8	82	4	9	24	3257	27	43	18	14	2
CB5 red	14	155	17913	1885	824	10	8	8102	3615	23	32	3193	214	3		239	748	8	80	7	6	11	3299	27	43	19	11	1
CB1 red	28	117	17678	759	1161	16	11	7501	5269	9	48	6037	202	9		248	675	8	108	3	81	55	3055	13	25	10	250	1
CB2 red	24	119	17496	806	1177	16	11	7632	5224	8	47	5059	198	9		258	676	9	110	2	74	49	3096	14	26	10	253	0
PS15 red	19	172	9784	5017	1381	14	13	5437	4360	21	54	5109	195	26		79	656	12	185	4	6	10	1886	21	41	17	22	3
Valls cover	12	182	9020	1426	1410	18	14	7409	6933	37	44	119	182	58	-	127	518	11	146	1	49	1	3681	17	35	14	3500	38
Valls red	16	156	9275	665	1520	19	13	8012	6429	21	61	7041	138	45	-	128	550	12	150	33	18	31	3738	18	36	15	15	4
TDM red	8	794	5	1040	236	19	11	77	3495	4	8	8209	32	44	106	23	32	2	36	0	9140	14	68	2	3	1	705	0
TDM base	12	100	41	2256	189	8	6	689	614	2	2	14	849	1596	146	8	84	2	30	0	82	899	1179	2	3	2	3706	1
SDC red	11	8	78	1999	522	8	35	56	15524	11	8	3700	43	39	34	5	28	3	63	0	15358	7	83	4	5	3	101	0
SDC base	9	25	56	591	378	7	24	66	2125	3	3	99	8	189	25	4	68	4	54	0	299	4	59	3	5	3	36	1
Vic-Cre red	12	24	128	1011	452	12	14	43	7413	5	11	7513	48	36	19	5	39	2	27	1	10527	9	33	3	6	2	23	2
Vic-Cre base	10	23	53	667	196	6	10	39	1399	2	2	97	7	788	17	4	164	2	18	0	118	2	29	2	5	2	26	0
Vic-Cim red	13	25	121	956	452	13	17	43	7406	5	11	7570	49	36	42	5	40	2	27	1	10617	9	34	3	6	2	28	2
Vic-Cim base	11	23	47	630	193	6	12	39	1386	2	2	97	7	782	41	4	168	2	18	0	117	1	30	2	5	2	30	0
LGA red	22	10	77	1929	200	10	51	158	9137	2	11	8582	22	35	-	7	16	2	28	0	7838	6	40	2	3	1	60	2
LGA base	11	10	32	505	198	5	15	168	1771	1	2	351	8	8	5	8	48	2	28	0	273	1	79	3	5	2	11	0
CB6 red	14	12	94	1915	239	10	10	395	9182	2	11	6016	25	41		8	21	2	39	0	7301	11	81	2	3	2		1
CB6 base	10	6	50	574	179	4	11	82	1934	2	2	371	9	15	5	12	61	3	28	0	372	1	104	4	7	3	8	0
SDPDM red	20	7	39	2121	182	8	10	230	7781	4	10	10997	41	28	26	4	16	1	17	0	9941	6	54	1	2	1	29	1
SDPDM base	14	7	52	1403	188	5	16	989	2063	2	3	491	9	8	17	12	98	3	29	0	398	7	459	4	7	3	61	0
CBCB red	8	15	-	919	181	6	12	82	5073	4	10	10049	18	26	36	4	22	1	19	1	12125	2	35	2	4	2	104	4
CBCB base	11	23	52	484	206	8	11	32	1642	1	3	44	10	2		6	136	3	21	0	21	0	40	3	5	2	31	0
CB7 red	10	16	38	1626	192	6	22	41	4884	7	5	6729	107	24	-	4	31	1	19	0	11870	2	30	2	4	2	34	1

CB7 base	10	25	35	406	187	7	17	48	1719	1	2	76	10	8	28	5	83	2	18	0	97	0	33	2	4	2	10	0
-----------------	----	----	----	-----	-----	---	----	----	------	---	---	----	----	---	----	---	----	---	----	---	----	---	----	---	---	---	----	---

Chapter 7 Conclusions

Chapter 7 Conclusions

The role of iron and copper in the production of coloured glazes and glasses and the technology of production have been studied.

Chapter 3 examines the imperial yellow porcelains. Some differences are determined in the composition and glazing techniques between the Ming (1368-1644) and Qing (1616-1912) periods. The scarcity of raw materials led to changes in porcelain composition, resulting in higher firing temperatures (from 1200 °C to 1300 °C). In addition, advances in kiln design, from the *hulu yao* (double-gourd kiln) to the *zhen yao* (egg-shaped kiln), allowed better control of the temperature and atmosphere. The yellow glaze was applied over a transparent lime glaze in the Ming dynasty and directly onto the porcelain in the Qing dynasty. Despite these differences, the optical properties, valence state (predominantly Fe³⁺), and coordination state (average fivefold coordination) of the glazes did not show any significant variation between the Ming and Qing dynasties.

Replication under controlled laboratory conditions showed that the final colour of the yellow glaze is influenced by four interrelated parameters: glaze thickness, firing temperature, substrate composition, and firing atmosphere. Achieving a pure yellow colour requires a thin glaze layer and oxidising conditions. Historic yellow glazes were remarkably thin, typically around 50µm, resulting in an almost pure yellow colour. The presence of calcium had a more pronounced effect on enhancing the yellow colour compared to other elements. In the Ming yellow glazes, the presence of a high-lime transparent glaze under the yellow glaze increased the calcium content compared to the Qing glazes.

Higher firing temperatures also contributed to a deeper yellow colour, with typical firing temperatures of historic yellow glazes estimated to be slightly below 1000°C, for the Ming glazes and above for the Qing glazes. However, as the firing and cooling times of the historic glazes were significantly longer than those of the laboratory replicas, the estimated firing temperatures may be lower in both cases.

The presence of Fe²⁺ was also detected even in glazes fired in an oxidising atmosphere and the relative Fe²⁺ content increased with higher firing temperatures. The colour of the glazes shifts from yellow-gold in air fired glazes to yellow-green in air-free fired glazes, with lower b* and L* values that decrease with increasing firing temperature. The results suggest that the historic glazes were fired under oxidising conditions, but slightly more reducing than the electric kilns used in the replicas. A small amount of Fe²⁺

had a positive effect on brightness by increasing transparency.

Chapter 4 examines the pale blue and red/purple glaze colours of Jun ware a stoneware produced since the North Song dynasty (960-1127). The study showed that the opacity of the glaze in Jun ware is due to the glass nanostructure resulting from a liquid-liquid phase separation at around 1200°C, facilitated by a high SiO₂:Al₂O₃ ratio (above 7:1). A double glass nanostructure, consisting of lime-rich droplets enriched in Fe, Mg, P, and Ti within a silica-rich matrix enriched in K and Na. X-ray absorption spectroscopy analysis revealed that iron is more oxidised in the calcium-rich areas than in the calcium-poor areas of the glaze.

Jun glazes were fired under reducing conditions and, the striking sky-like appearance of the blue Jun ware blue glazes is the result of a combination of light absorption in the transparent-dark-blue Fe²⁺-richer areas, and predominantly light scattering in the white-yellowish Fe³⁺-richer areas. Copper was also added to the glazes to impart red/violet colours. The presence of small copper nanoparticles and the predominance of Cu⁺ and Cu²⁺ species were observed in the glaze, with the ratio between them depending on the glaze composition and atmosphere. In particular, iron was more oxidised in the red glaze, where copper metal nanoparticles were present, than in the blue glaze where they were absent. This phenomenon was more pronounced in calcium-poor areas (with higher Fe²⁺ content) than in calcium-rich areas (with higher Fe³⁺ content). The results suggest a simultaneous reduction of copper from Cu⁺ to Cu⁰ and oxidation of iron from Fe²⁺ to Fe³⁺ in the glaze. The precipitation of metallic copper nanoparticles imparted a red colour to the creamy lime-rich areas and a violet colour to the blue lime-poor areas.

The colours of Changsha ware glazes, late Tang dynasty (9th - 10th century) in China, are examined in **Chapter 5**. The study reveals remarkable similarities and differences with Jun ware. Similar to Jun ware, the opacity of some Changsha ware glazes is attributed to a high Si/Al ratio when fired at high temperatures. However, due to its higher Ca content, Changsha glaze exhibits Si-rich droplet segregation within a Ca-rich matrix. In addition, the glazes show the presence of microparticles of fluorapatite, cassiterite and malayaite, which contribute to opacity. As with the Jun ware, the interaction between the glaze and the stoneware increases the aluminium content at the glaze interface, resulting in a droplets-free transparent glaze. As the opacity was not so commonly achieved, a white 'slip,' enriched in Al, K, and relatively low in Si compared to the body, was applied to hide the colour of the stoneware. Unlike Jun ware, Changsha ware was often decorated and the white slip enhanced the colours.

X-ray absorption spectroscopy of the glazes revealed the predominant presence of Cu²⁺ and Fe³⁺. The green and turquoise colour of the glazes is due to the presence of Cu²⁺, with smaller droplets intensifying the

bluish hue and larger droplets giving a more yellowish-green hue. Therefore, unlike Jun ware Changsha ware was fired under oxidising conditions.

A reducing firing followed by an oxidising firing was used to produce the fine red painting seen on some Changsha wares. Typical designs with a green (often flaking) coloured area surrounded by red were produced by applying a highly concentrated copper pigment directly to the raw ceramic surface, followed by a lime glaze applied over the entire surface. The highly concentrated pigment pushed the glaze towards the edges of the design, resulting, in a thin copper-rich glaze surrounded by a thicker copper-poor glaze. The copper in the glaze near the surface ($\approx 50 \mu\text{m}$) is oxidised while the copper present in the glaze below remains reduced. The development of the red colour is due to the precipitation of copper nanoparticles, which are favoured by the low copper and a copper/sulfur atomic ratio of 2.4 present at the edges of the design. Although the potters may not have mastered control of the process, they may have learnt some of the basics of producing a copper red design, such as the need for a low copper content in the glaze and the use of a combined reducing and oxidising firing.

Regarding the underglaze/overglaze controversy, our study has shown that both techniques were used. The preference for fine, intricate designs may have influenced the switch from overglaze to underglaze painting, and the use of a thinner glaze. However, the application of a highly concentrated paint without the appropriate addition of binder (clay or glaze) was also responsible for the flaking.

In the final chapter, **Chapter 6**, the study of red window glass provides an insight into the production of red glass between the 13th and the 20th centuries. In particular, the composition shows significant changes over the period, corresponding to advances in glassmaking technology. Three types of red glass are examined: *striated* glass, *sandwich* glass, and *flash* glass.

The study of the *striated* glass has shown that the ruby red colour of the glass is due to the presence of small metallic copper nanoparticles, and the absence of cuprite particles. X-ray absorption spectroscopy of the copper and iron in the 13th-century *striated* glass reveals a unique glass structure, in which a sequence of copper-rich oxidised glass layers were applied to copper-free reduced glass layers. Copper diffusion from the copper-rich oxidised layer into the copper-free reduced glass and simultaneous interdiffusion of Fe^{3+} and Fe^{2+} occurs resulting in the reduction of copper to the metallic state and precipitation of copper nanoparticles and simultaneous oxidation of Fe^{2+} to Fe^{3+} within the layers.

The study of *sandwich* red glasses from the 13th to the 17th centuries highlighted the role of sulphur in the precipitation of metallic copper nanoparticles. The presence of trace amounts of sulphur in medieval and

Renaissance red glasses was found to be responsible for a sulphur-silicate melt partition at low pressures and temperatures around 1100°C; copper is a highly chalcophilic element and accumulates in the sulphide partition. The presence of iron in the melt may favour the precipitation of tetragonal chalcocite (Cu_2S) particles instead of monoclinic chalcocite. The cooling and reheating of the glass under mildly oxidising conditions resulted in the oxidation of the sulphur and loss of sulphur (probably as SO_2), leading to the sudden reduction of copper to its metallic state (striking) and the formation of metallic copper nanoparticles. The differences observed between medieval and renaissance red glasses may be due to differences in the composition, with renaissance glasses being richer in silica, or to a less oxidising or lower reheating temperature of the red glass.

In addition, the results obtained by other researchers on the replication of red glass using historical recipes align are consistent with the main conclusions obtained from our analysis. Rather than being directly involved, iron appears to play an indirect role in the reduction of copper and the precipitation of copper nanoparticles, stabilising the tetragonal chalcocite and acting as an oxidation/reduction buffer.

The chemical composition of 19th and 20th century *flashed* red glass, has shown that both the clear substrate and the red layer glasses were made using synthetic soda ash, first commercialised in 1835. The presence/absence of arsenic, used as a fining agent, allowed three of the glasses to be dated before 1870 and the others after 1870, two of which were dated in 1905. Unlike the red copper glasses produced between the 13th and 18th centuries, the composition of the red glass layers differs from that of the substrate glasses. The red glass has a low calcium content (about 5% CaO), which favours the presence of copper and iron, mainly in their reduced forms, Cu^+ and Fe^{2+} . In addition, the red glasses contained copper, tin, and iron, but no lead, contrary to what describes historical and modern documentation.

X-ray absorption spectroscopy data indicate that in the red glass, tin is mainly present in its oxidised form Sn^{4+} , while copper is present as Cu^+ and metallic copper and iron as Fe^{2+} . This suggests that tin initially added to the glass in its reduced form acted as a reducing agent for copper and iron. The addition of other reducing agents, such as $\text{K}_2\text{CO}_3 \cdot 1.5\text{H}_2\text{O}$, as described in historical and modern documents, promotes the incorporation of tin into the glass as Sn^{2+} . The role of iron is less clear, but its preferential incorporation into the low calcium glass as Fe^{2+} may prevent the incorporation of copper as Cu^{2+} , thereby facilitating the reduction of copper to its metallic state.